Molecular Simulation of Processes at Fluid Interfaces and Electrolyte Solutions

Vom Fachbereich Maschinenbau und Verfahrenstechnik

der Rheinland-Pfälzischen Technischen Universität Kaiserslautern-Landau

zur Verleihung des akademischen Grades

Doktor-Ingenieur (Dr.-Ing.)

genehmigte

Dissertation

von

M. Sc. Dominik Schäfer

aus Koblenz

"Sometimes there is more to life than just livin'."

Danksagung

Bachelor-, Studien- und Masterarbeiten und/oder als studentischen Hilfskräfte tatkräftig unterstützt haben. Ohne euch wäre diese Arbeit deutlich weniger umfangreich geworden und hätte deutlich weniger Spaß gemacht.

Der Großteil der Ergebnisse dieser Arbeit ist auf dem heimischen Hochleistungsrechner "Elwetritsch" der RPTU Kaiserslautern entstanden. Dementsprechend möchte ich mich herzlich bei dem Team der "Elwe" für die verlässliche Bereitstellung und Erweiterung der Recheninfrastruktur, die unkomplizierte Kommunikation und die grandiose technische Unterstützung über die Jahre bedanken.

Zudem möchte ich mich bei allen wissenschaftlichen und nicht-wissenschaftlichen Mitarbeiterinnen und Mitarbeitern des LTD bedanken. Ihr alle habt den Arbeitsalltag mit so vielen schönen Gesprächen, Diskussionen, wilden Spekulationen, Konferenzreisen, Feierabendaktionen, Urlauben und Feiern bereichert. Obwohl wir inhaltlich oft an komplett unterschiedlichen Baustellen gearbeitet haben, ist der kollegiale Zusammenhalt am LTD etwas ganz Besonderes. In diesem Sinne: "Cheers, mates!"

Ich möchte außerdem meiner Familie danken, die mich seit jeher unterstützt und mir den Freiraum geschaffen hat, mein Leben nach meinen eigenen Vorstellungen zu verwirklichen. Zu guter Letzt möchte ich meiner Frau Katharina danken. Danke dafür, dass du mir in schwierigen Zeiten so viel Rückhalt gibst, immer an mich glaubst, gerade wenn ich selbst den Glauben verloren habe, und ich mit dir die guten Zeiten so wunderbar feiern kann.

Bad Kreuznach, August 2023

Dominik Schäfer

Abstract

Molecular simulation is an important tool for investigating the behavior of fluids and solids. Nanoscopic processes and physical properties of the material can be studied predictively based on the description of the molecular interactions by force fields. This is used in the present work to tackle engineering questions that are hard to answer with other methods. First, mass transfer at fluid interfaces was investigated on the nanoscopic level. Therefore, two distinct simulation methods were developed and used to systematically investigate the mass transfer in mixtures of simple model fluids, described by the 'Lennard-Jones truncated and shifted' (LJTS) potential. The research question was whether the adsorption of components at the interface, which is observed also in many simple fluid mixtures, has an influence on the mass transfer. Such an influence was indeed found in the studies with both scenarios. Furthermore, explosions of nanodroplets caused by a spontaneous evaporation of the liquid phase were investigated with non-equilibrium molecular dynamics (NEMD) simulations. In these simulations, the interior of an LJTS droplet was superheated by a local thermostat, so that a vapor bubble nucleated inside of the droplet. Depending on the degree of superheating, different phenomena were observed, ranging from a simple evaporation of the droplet over oscillatory behavior of the bubble to an immediate droplet explosion. For molecular simulations of real mixtures, suitable force fields are needed. In this work, a set of molecular models for the alkali nitrates was developed and systematically compared to experimental data of thermophysical and structural properties of aqueous alkali nitrate solutions from the literature. Lastly, the structure and clustering of 1:1 electrolytes in aqueous solution was investigated for a broad concentration range starting from near infinite dilution up to high supersaturation. Based on the simulation results, an empirical rule was proposed to provide estimates of the solubility of salts with standard molecular dynamics simulations without the need of elaborate calculation schemes or significant additional computational effort.

Kurzfassung

Die molekulare Simulation ist ein wichtiges Werkzeug zur Untersuchung des Verhaltens von Fluiden und Feststoffen. Nanoskopische Prozesse und physikalische Stoffeigenschaften können basierend auf der Beschreibung der molekularen Wechselwirkung der verwendeten Kraftfelder prädiktiv untersucht werden. Dies wird in der vorliegenden Arbeit verwendet, um technische Fragen zu anzugehen, die mit anderen Methoden nur schwer zu beantworten sind. Zunächst wurde der Stofftransport an Phasengrenzflächen auf der nanoskopischen Ebene untersucht. Hierfür wurden zwei unterschiedliche Simulationsmethoden entwickelt und verwendet, um systematisch den Stofftransport in Mischungen einfacher Modellfluide zu untersuchen, die durch das 'Lennard-Jones truncated and shifted' (LJTS) Potential beschrieben werden. Die Leitfrage war, ob die Adsorption von Komponenten an der Grenzschicht, welche für viele Mischungen einfacher Fluide beobachtet wird, einen Einfluss auf den Stofftransport hat. Ein solcher Einfluss wurde in den Studien mit beiden Szenarien gefunden. Des Weiteren wurden Explosionen von Nanotropfen, die durch das spontane Verdampfen der Flüssigphase verursacht wurden, in moleculardynamischen Nichtgleichgewichtssimulationen (NEMD) untersucht. In diesen Simulationen wurde das Innere eines LJTS-Tropfens durch ein lokales Thermostat überhitzt, sodass sich eine Gasblase im Inneren des Tropfens bildete. Abhängig vom Grad der Überhitzung wurden verschiedene Phänomene beobachtet: von einfacher Verdampfung über ein oszillatives Verhalten der Gasblase bis hin zu der sofortigen Explosion des Tropfens. Für die molekulare Simulation realer Mischungen werden geeignete Kraftfelder benötigt. In dieser Arbeit wurde ein Satz molekularer Modelle für die Alkalinitrate entwickelt und systematisch mit experimentellen Daten thermophysikalischer und struktureller Eigenschaften der wässrigen Lösung von Alkalinitraten aus der Literatur verglichen. Abschließend wurde die Struktur und Clusterbildung von 1:1 Elektrolyten in wässriger Lösung in einem breiten Konzentrationsbereich beginnend bei nahezu unendlicher Verdünnung bis hin zu hoher Übersättigung untersucht. Auf Basis der Simulationsergebnisse wurde eine empirische Regel aufgestellt, um die Salzlöslichkeit abzuschätzen, ohne dedizierte und rechenzeitintensive Samplingverfahren anwenden zu müssen.

Contents

List of Symbols

Latin symbols

A	Parameter for the water activity correlation
a_g	Gaussian peak height
a_{W}	Water activity
B	Adjustable parameter of the water activity correlation
$\tilde{b}_{\mathrm{AB}}$	Molality of the salt AB
C	Adjustable parameter of the water activity correlation
c_g	Gaussian standard deviation
d	Diameter
D_{ij}	Binary Fick diffusion coefficient
$Ð_{ij}$	Binary Maxwell-Stefan diffusion coefficient
D_i	Self-diffusion coefficient
E_i	Enrichment of component i in the interface
f_{Gauss}	Sum of Gaussians
G	Total number of Gaussian functions
g_{i-j}	Radial distribution function
j_i	Molar flux
k	Force constant of the harmonic potential of the soft repulsive wall
k_{B}	Boltzmann constant
l	Length
m	Mass of a particle
$\bar{M}^{\mathrm{C}}$	Mean number of clusters
M_i	Total number of interaction sites of particle i
M_i	Molar mass
N	Number of particles
N_{avo}	Avogadro constant
n	Bin index
N^{C}	Number of particles in a cluster
n_{CIP}	Number of contact ion pairs (equivalent to n_{i-j} in the case of the coordination of cations and anions)
N^{drop}	Number of particles in a droplet
n_{i-j}	Number of particles of type i in the first coordination shell around the central particle of type j

p	Pressure
p_N	Normal pressure at interface
p_T	Tangential pressure at interface
q	Magnitude of point charges
r	Distance between interaction sites
r_α	Alpha shape radius
r^C	Neighbor search radius for the cluster algorithm
r_G	Radius of gyration
r^IF	Interface position
r_max1	Position of the first maximum of the RDF
r_min1	Position of the first minimum of the RDF
R	Universal gas constant
T	Temperature
$u(r)$	Intermolecular potential energy
v	Velocity of a particle
V	Volume
x	Spatial coordinate
x_i	True mole fraction of the component i
$x_\mathrm{A^+}^\mathrm{sol}$	Solubility limit
$x_\mathrm{A^+}^*$	Lowest mole fraction at which the first clusters with j or more ions are determined
$x_\mathrm{A^+}^\mathrm{sol,CIP}$	Solubility limit estimated with the *ion pair rule*
$x_\mathrm{A^+}^\mathrm{sol,C\text{-}6}$	Solubility limit estimated with the *cluster rule*
$\tilde{X}^\mathrm{C\text{-}6}$	Number of ions in clusters containing 6 or more ions divided by the overall number of ions
y	Spatial coordinate
z	Spatial coordinate

Greek symbols

α_AB	Adjustable parameter of the density correlation
β	Adjustable parameter of the water activity correlation
Γ	Thermodynamic factor
$\gamma_i^\mathrm{b*}$	Activity coefficient of ion i on the molality scale
$\tilde{\gamma}_\mathrm{AB}^\mathrm{b*}$	Mean ionic activity coefficient of the salt AB on the molality scale
ε	Lennard-Jones energy parameter
ϵ_0	Vacuum permittivity
ϵ_r	Relative permittivity
μ	Chemical potential
$\tilde{\mu}_\mathrm{AB}$	Overall chemical potential of salt AB
$\tilde{\mu}_\mathrm{AB}^\mathrm{ref\ b}$	Overall chemical potential of salt AB in the reference state
ξ_{ij}	Binary interaction parameter

ν	Stoichiometric coefficient
π	Ratio of a circle's circumference to its diameter
Π	Osmotic pressure
ρ	Density
σ	Lennard-Jones size parameter
τ	Time
Ω	Collision integral
χ	Generic observable

Subscripts and superscripts

0	Reference
$*$	Reduced
$'$	Phase $'$
$''$	Phase $''$
∞	At infinite dilution
a, b	Indices for Lennard-Jones interaction sites
bin	Bin related property
box	Simulation box related property
break	Droplet break-up
c, d	Indices for point charge interaction sites
cut	Cut-off
eq	Equilibrium state
exp.	Experimental
g	Index of Gaussian function
i, j	Component indices
IF	Interface
in	Inner interface position
j	Minimal cluster size
k	Particle index
liq	Liquid phase region
(m)	Mass-related property
max1	First maximum
min1	First minimum
(n)	Particle number related property
off	Offset
out	Outer interface position
set	Simulation setting
sim.	Simulation
therm	Thermostat
vap	Vapor phase region

Operators

$\bar{\chi}$	Arithmetic mean of χ
$\Delta\chi$	Difference of χ
$\langle\chi\rangle$	Ensemble average of χ
$\delta\chi$	Infinitesimal difference of χ
$\underline{\chi}$	Vector

Abbreviations

A^+	Cation
AB	1:1 electrolyte consisting of cation A^+ and anion B^-
B^-	Anion
CIP	Contact ion pairs
C	Cluster
COM	Center of mass
CV	Control volume
DCV	Dual control volume
DFT	Density functional theory
DGT	Density gradient theory
drop	Droplet
eCPA	Electrolyte cubic plus association EOS
EOS	Equation of state
ePC-SAFT	Electrolyte perturbed chain SAFT EOS
Eq1	Sampling phase of the first vapor-liquid equilibrium state
Eq2	Sampling phase of the second vapor-liquid equilibrium state
GCMC	Grand canonical Monte Carlo
In	Insertion phase
IniEq	Initial equilibration phase
JC	Models by Joung and Cheatham
L	Bulk liquid domain
LJ	Lennard-Jones
LJTS	Lennard-Jones truncated and shifted
MC	Monte Carlo
MD	Molecular dynamics
μVT	Grand canonical ensemble
MV	Measurement volume
NEMD	Non-equilibrium molecular dynamics
NpT	Isobaric-isothermal ensemble
NRTL	Non-random two liquid
NVT	Canonical ensemble
OPAS	Osmotic pressure for the activity of solvents

OPC	"Optimal" point charge
PC	Point charge
PeTS	Perturbed truncated and shifted EOS
RDF	Radial distribution function
RDVH	Models by Reiser et al.
Relax	Relaxation phase
SAFT	Statistical associating fluid theory
SAFT-γ Mie	Group contribution SAFT variable range Mie EOS
SD	Models by Smith and Dang
SLE	Solid-liquid equilibrium
solv	Solvent
SPC	Simple point charge
SPC/E	Simple point charge / Extended
TIP4P	Transferable intermolecular potential with 4 points
TIP4P-Ew	TIP4P - Ewald summation
TIP4P-FQ	TIP4P - fluctuating charges
V	Bulk vapor domain
VLE	Vapor-liquid equilibrium
VLLE	Vapor-liquid-liquid equilibrium
W	Water

1 Introduction

Molecular simulation has become a major asset for natural scientists and engineers, since the development of the Monte-Carlo (MC) [1] and molecular dynamics (MD) [2] simulation methods in the middle of the last century. Molecular simulation helps to meet the ever-growing need of the biotechnological and chemical industry for thermophysical, structural, and transport properties of chemical compounds by replacing expensive and time-consuming laboratory experiments with fast and scalable computer experiments [3, 4]. The applicability of molecular simulations has significantly increased due to the growth and the broad availability of computational resources in the last decades. Molecular simulations are used for predicting the behavior of systems under equilibrium and non-equilibrium conditions. Furthermore, molecular simulations provide insights into processes on the nanoscopic scale, which currently cannot be gained experimentally. The molecular models used in these simulations are built on a strong physical background and, hence, enable robust extrapolations with comparatively few adjustable parameters. Furthermore, they basically yield all thermodynamic and transport properties as well as information on structural properties. In the present work, engineering challenges are addressed by molecular simulations: mass transfer through fluid interfaces, droplet explosions caused by spontaneous evaporation of the liquid phase, thermophysical and structural properties of electrolyte in aqueous solution as well as the estimation of the solubility of electrolytes.

Mass transfer through vapor-liquid interfaces is a highly important phenomenon: it is ubiquitous in nature and applied in many technical processes, including fluid separation processes such as absorption and distillation. Interesting phenomena occur in the interfacial region, such as the enrichment of components [5–18]. The vapor-liquid interfacial region has been studied extensively in equilibrated systems, but only little is known about the influence of mass transfer in that region and, vice versa, on the influence of that region on mass transfer. That influence is usually neglected in macroscopic mass transfer theories, but recently, doubts on the validity of that assumption have been raised [11, 14, 19–25], which makes such studies all the more important.

Given the importance of this phenomenon, it is astonishing that, up to recently, no MD simulation methods for studying mass transfer through vapor-liquid interfaces driven by

a gradient of the chemical potential have been described in the literature. Therefore, two simulation methods for inducing such a mass transfer were developed in the present work. In the first method, a stationary molar flux through interfaces [26] is induced, while in the second method [27], a non-stationary molar flux is induced by the temporary insertion of particles in an equilibrated system. Both methods were tested using the same Lennard-Jones truncated and shifted (LJTS) model mixtures. In these simulations, the question is addressed whether an interfacial enrichment has an influence on the mass transfer rates. The approach taken for this is straightforward: results for fluxes through interfaces in a model mixture with a high interfacial enrichment were compared with those obtained for a similar mixture that has no enrichment.

Coupled mass and heat transfer also plays a crucial role for processes in which liquid droplets are exposed to a hot atmosphere, resulting in the coupled heating and evaporation of the droplets. Examples include combustion engines as well as spray flame synthesis for the production of functional nanomaterials. If the liquid in the droplet is a mixture, explosions of the droplets may occur in that process [28–30], which obviously have important consequences for the process in which the evaporating droplets are used. For example, it is known that they lead to an improvement of the synthesis product. It is hence of great importance to know under which circumstances and how such explosions occur for being able to design such processes. In particular, it is practically impossible to obtain information on what happens inside the droplet before the explosion or to get detailed information on the explosion from experiments. Therefore, such information must be gained from simulations. To investigate these phenomena, in the present work, non-equilibrium molecular dynamics simulations were used for studying droplet explosions of simple fluids. In these simulations, a liquid droplet was exposed to a sudden rise in temperature in its center, which led to the formation of a vapor bubble that eventually tears the droplet apart (if the temperature is high enough). A series of simulations was carried out with that scenario, using the same model fluid as in the aforementioned mass transfer simulations to describe intermolecular interactions.

The droplets that combust and explode in the spray flame synthesis are electrolyte solutions containing a combustible solvent and a metal-containing precursor salt. Thermophysical properties of such electrolyte solutions are difficult to model due to the strong electrostatic interactions between the ions as well as the strong interaction between the ions and the solvent molecules. In the present work, molecular simulations were used for predicting properties of alkali nitrates in aqueous solution. The used molecular models of the ions and the solvent were developed by different research groups and have never before been used in the combinations studied here.

In many technical applications concerning electrolyte solutions, such as the spray flame synthesis [31] or desalination plants for drinking water purification [32], the solvent is

evaporating rapidly and, hence, thermophysical properties have to be predicted in a broad concentration range up to the solubility of the salt. As shown for the example of alkali nitrates, these properties can be obtained by molecular simulations. However, with molecular simulations of electrolyte solutions there is always one potential issue: the salt solubility. Since the time span that can be covered in typical molecular dynamics simulations is far too short for establishing the stable equilibrium state between a saturated solution and a salt crystal, one may actually simulate what could be considered a metastable state. In the worst case, simulations are carried out at concentrations beyond the solubility, which can lead to invalid results of properties which are assumed to be determined for a homogeneous solution. Knowledge of the salt solubility of the studied system would of course solve this problem. However, calculating the solubility rigorously is computationally demanding and, hence, for most molecular models for electrolyte solutions, even popular ones, the solubility is not known. Therefore, in this work, structural properties and ion clustering were rigorously investigated for models of 1:1 electrolytes in aqueous solution with known solubility. From the simulation results, an empirical rule for the estimation of the solubility is proposed, which can be used on the fly or as a simple post-processing step in standard MD simulations.

The presented work is structured as follows: The fundamentals of molecular simulations, the used models, and investigated observables are discussed in Chapter 2. The stationary and non-stationary simulation scenarios and the corresponding results for mixtures of simple fluids are presented in Chapters 3 and 4, respectively. In Chapter 5, the results of droplet explosions of simple fluids are presented. A molecular model set for alkali nitrates in aqueous solution is presented and rigorously compared to available experimental data in Chapter 6. Finally, in Chapter 7, the method for estimating the solubility of 1:1 electrolytes in aqueous solution based on the structure of the solution is presented.

2 Fundamentals

The fundamentals of molecular modeling and simulation are covered extensively in the literature, for example in the books of Rapaport [33], Frenkel and Smit [34], and Allen and Tildesley [35]. In this chapter, only concepts that are useful in the context of the present work are briefly discussed. For more details, please refer to the aforementioned books and the list of references.

2.1 Molecular Models

In the presented work, two different modeling approaches are used: in the Chapters 3, 4, and 5, simulation scenarios developed in the scope of this work are systematically tested with pure substances or mixtures of simple model fluids, namely the Lennard-Jones truncated and shifted (LJTS) model fluid, while in Chapters 6 and 7, thermophysical and structural properties of models representing a real solvent, i.e., water, and real solutes, i.e., ions, are investigated.

The LJTS fluid is chosen since it is computationally inexpensive, allowing for parametric studies in which process parameters and simulation settings are systematically varied, and, therefore, is a suitable candidate for testing new simulation scenarios. The properties of pure LJTS fluids and mixtures have been investigated rigorously in the literature, e.g., the bulk phase [36–39] and interfacial properties [36, 40, 41]. Furthermore, mass and heat transfer processes at vapor-liquid interfaces of the pure substance and mixtures of different LJTS fluids have been thoroughly investigated recently [15, 27, 42–45]. Furthermore, the LJTS fluid is an appropriate model for representing simple fluids, such as noble gases and methane [36, 40, 46]. The LJTS potential u_{ij}^{LJTS} is defined as

$$u_{ij}^{\mathrm{LJ}}(r_{ij}) = 4\varepsilon_{ij}\left[\left(\frac{\sigma_{ij}}{r_{ij}}\right)^{12} - \left(\frac{\sigma_{ij}}{r_{ij}}\right)^{6}\right] \tag{1}$$

$$u_{ij}^{\mathrm{LJTS}}(r_{ij}) = \begin{cases} u_{ij}^{\mathrm{LJ}}(r_{ij}) - u_{ij}^{\mathrm{LJ}}(r_{\mathrm{cut}}) & r_{ij} \leq 2.5\,\sigma \\ 0 & r_{ij} > 2.5\,\sigma \end{cases} \tag{2}$$

Herein, $u_{ij}^{\mathrm{LJ}}(r_{ij})$ is the Lennard-Jones (LJ) potential between the particles i and j with the distance r_{ij}, ε_{ij} is the energy parameter, and σ_{ij} is the length parameter. Truncating and shifting the potential at the cut-off radius $r_{\mathrm{cut}} = 2.5\,\sigma$ means that no long-range corrections are needed. This is convenient for simulating heterogeneous systems with planar and curved interfaces, such as the ones investigated in this work, since handling long-range corrections in such simulation settings is not trivial and, depending on the type of intermolecular interaction, might additionally be computationally quite demanding. As is common for studies for LJ-type model fluids, all properties shown Chapters 3, 4, and 5 concerning the LJTS model fluid were reduced with respect to the the LJTS fluid with the parameters $\sigma = 1$, $\varepsilon = 1$, and the mass $m = 1$ as well as the Boltzmann constant k_{B} [35].

The models used in Chapters 6 and 7 representing real solvents and solutes consist of two types of interaction sites: the aforementioned LJ and the point charge (PC) interaction site. The potential interaction energy u_{ij} between two such particles i and j is given by

$$u_{ij} = u_{ij}^{\mathrm{LJ}} + u_{ij}^{\mathrm{PC}}$$

$$= \sum_{a=1}^{M_i^{\mathrm{LJ}}} \sum_{b=1}^{M_j^{\mathrm{LJ}}} 4\varepsilon_{ijab} \left[\left(\frac{\sigma_{ijab}}{r_{ijab}} \right)^{12} - \left(\frac{\sigma_{ijab}}{r_{ijab}} \right)^{6} \right] + \sum_{c=1}^{M_i^{\mathrm{PC}}} \sum_{d=1}^{M_j^{\mathrm{PC}}} \frac{1}{4\pi\epsilon_0} \frac{q_{ic} q_{jd}}{r_{ijcd}} \ . \tag{3}$$

Here, a–d are indices for the interaction sites, M_i is the total number of interaction sites of a particle i, σ_{ijab} and ε_{ijab} are the LJ size and energy parameters corresponding to the LJ interaction site a of particle i and site b of particle j, while q_{ic} and q_{jd} denote the magnitudes of the point charges in an analogous manner. Furthermore, ϵ_0 is the vacuum permittivity. Results of simulations using models representing real molecules in Chapters 6 and 7 and their corresponding Appendices are given in SI units. To reduce the computational effort, the LJ and PC interactions are evaluated up to a distance of $r_{\mathrm{cut}} = 15$ Å. The standard tail corrections [35] is applied for the correction of the LJ interaction and the Ewald summation [47] is applied for the long-range electrostatics.

In both cases - mixtures of LJTS model fluids and mixtures of models for real solvents and solutes - the interactions between unlike LJ-type interaction sites are described using the modified Lorentz-Berthelot combining rules [48, 49]

$$\sigma_{ijab} = \frac{\sigma_{ia} + \sigma_{jb}}{2} \tag{4}$$

$$\varepsilon_{ijab} = \xi_{ijab} \sqrt{\varepsilon_{ia} \varepsilon_{jb}} \ . \tag{5}$$

Herein, ξ_{ijab} is an adjustable parameter for the cross interaction energy. In the case of the models of real solvents and solutes, ξ_{ijab} was set to unity and, thus, the unmodified Lorentz-Berthelot rules apply for simulations in Chapters 6 and 7. ξ_{ijab} is adjusted only

in the case of LJTS fluid mixtures, which are investigated in Chapters 3 and 4. The cross interaction energy parameter ξ_{ijab} has a major influence on the phase behavior and the bulk phase and interfacial properties of fluid mixtures [14, 20, 26, 27, 50–52].

2.2 Thermophysical and Structural Properties

2.2.1 Self-Diffusion Coefficients

The self-diffusion coefficient D_i is a measure for the Brownian movement of a single particle of the species i in a fluid under equilibrium. In this work, D_i was determined using the Green-Kubo formalism [53–55]

$$D_i = \frac{1}{3N_i} \int\limits_0^\infty \Big\langle v_{k,i}(\tau{=}0) \cdot v_{k,i}(\tau) \Big\rangle \mathrm{d}\tau \ ,$$ (6)

where N_i is the total number of particles of component i, $v_{k,i}(\tau)$ is the velocity of a particle k of component i at time τ, and the angular brackets denote the ensemble average.

2.2.2 Radial Distribution Function

The radial distribution function $g_{i-j}(r)$ of particles of type j around particles of type i is used for quantifying the microscopic structure of the studied fluids. It is defined as [35]

$$g_{i-j}(r) = \frac{1}{\rho_j^{(\mathrm{n})}} \frac{\mathrm{d}N_j}{4\pi r^2 \mathrm{d}r} \ ,$$ (7)

where r is the distance between the center of mas of the particle i and an infinitesimally thin shell with a thickness $\mathrm{d}r$, $\mathrm{d}N_j$ is the number of particles of component j inside this shell, and $\rho_j^{(\mathrm{n})}$ is the number density of particles of component j in the bulk.

2.2.3 Number of Particles in the First Coordination Shell

The number of particles of type j around the central particle of type i in the first coordination shell n_{i-j} is determined by

$$n_{i-j} = 4\pi \rho_j^{(\mathrm{n})} \int\limits_0^{r_{\mathrm{min1}}} g_{i-j}(r)\, r^2 \mathrm{d}r \ .$$ (8)

The upper integration limit r_{min1} is the position of the first minimum in the corresponding RDF. In the case of the 1:1 electrolytes studied in Chapter 7, $n_{\mathrm{A^+-B^-}}$ of the cation 'A$^+$' and the anion 'B$^-$' corresponds to the number of contact ion pairs (CIP) [56–58], which is referred to as n_{CIP}.

2.3 Composition Measures for Electrolyte Solutions

For a strong 1:1 electrolyte 'AB' that fully dissociates into the cation 'A$^+$' and the anion 'B$^-$' upon solution in the solvent 'solv', the true mole fraction of the cation $x_{\mathrm{A^+}}$ is given by

$$x_{\mathrm{A^+}} = \frac{n_{\mathrm{A^+}}}{n_{\mathrm{A^+}} + n_{\mathrm{B^-}} + n_{\mathrm{solv}}} \ , \tag{9}$$

in which n_i is the true mole number of species i. The overall molality of the salt $\tilde{b}_{\mathrm{AB}}$ is defined as

$$\tilde{b}_{\mathrm{AB}} = \frac{\tilde{n}_{\mathrm{AB}}}{m_{\mathrm{solv}}} \ , \tag{10}$$

in which $\tilde{n}_{\mathrm{AB}}$ is the overall mole number of the salt and m_{solv} is the mass of the solvent. For strong 1:1 electrolytes, both properties are related by

$$\tilde{b}_{\mathrm{AB}} = \frac{x_{\mathrm{A^+}}}{(1 - 2x_{\mathrm{A^+}}) M_{\mathrm{solv}}} \tag{11}$$

$$x_{\mathrm{A^+}} = \frac{\tilde{b}_{\mathrm{AB}}}{2\tilde{b}_{\mathrm{AB}} + 1/M_{\mathrm{solv}}}, \tag{12}$$

where M_{solv} is the molar mass of the solvent.

3 Quasi-Stationary Mass Transfer through Vapor-Liquid Interfaces

3.1 Introduction

In the present chapter, the first of two developed simulation methods for inducing mass transfer through a vapor-liquid interface driven by a gradient in the chemical potential is introduced. The simulation method employed in the present chapter is based on the so-called dual control volume (DCV) method, which has been applied before for studying diffusion in crystals, membranes, and pores [59–66], but to the best of the author's knowledge not for studies of mass transfer through vapor-liquid interfaces. Some related simulation methods have been described previously in the literature: the heat and mass transfer through vapor-liquid interfaces during evaporation and condensation has been studied extensively in the literature using molecular simulation [42, 67–84] or mesoscopic models such as density functional theory [73, 78, 82, 84–88]. Most of these studies consider a temperature gradient as the driving force of the heat and mass transfer. Furthermore, in most of these studies, only pure components are considered. Diffusion near vapor-liquid interfaces is known to be anisotropic. The available studies on this subject deal mostly with self-diffusion [89–92]. Interestingly, the diffusion parallel to the interface has been investigated more often than the diffusion perpendicular [92–94] to the interface, which is relevant for the mass transfer in fluid separation techniques.

Nagl et al. [19] recently reported a combined theoretical–experimental investigation of the mass transfer through liquid-liquid interfaces. Also Braga et al. [95] investigate diffusion at liquid-liquid interfaces. The free energy barrier of particles crossing a vapor-liquid interface has been studied by Braga et al. [93] and Garrett et al. [96]. The build up of the interfacial excess at vapor-liquid interfaces of binary mixtures in a relaxation process has been studied recently by Baidakov et al. [97, 98].

In the DCV method on which the presented method is based, the chemical potential in two sub-sections of the simulation volume is prescribed by a Monte Carlo algorithm. Particles are then inserted in one sub-section and removed from the other, causing a mass flux. The basic idea of the dual control volume method [61, 65, 99–101] is adapted

to induce a mass flux through vapor-liquid interfaces driven by a gradient of the chemical potential. This approach was applied in the present chapter on a rectangular simulation volume in which there is a liquid slab in the middle with a vapor slab on each side. In each of the vapor domains, there is a control volume near the outer boundary of the simulation volume. The chemical potential is prescribed such that there is a mass transfer through the two vapor-liquid interfaces. The developed simulation scenario is tested using simple Lennard-Jones model mixtures. In these tests, a current topic is addressed: the influence of the enrichment of components at the vapor-liquid interface on the mass transfer [102].

Results from equilibrium molecular thermodynamics show an enrichment of low-boiling components at vapor-liquid interfaces for many mixtures [5–15, 20, 52, 102–108]. This enrichment is predicted consistently by molecular simulations, i.e., Monte Carlo or molecular dynamics simulations, as well as density gradient theory (DGT) [5, 14–17, 102, 109]. Since the enrichment is a nanoscopic effect at fluctuating fluid interfaces, currently no experimental methods are available to study it directly. The enrichment of components at fluid interfaces of mixtures is believed to influence the mass transfer through fluid interfaces [11, 14, 19–23, 25, 110], but a proof is still lacking.

The new simulation scenarios are applied to two different binary Lennard-Jones mixtures (referred to as mixtures A and B from here on). Both mixtures have been studied extensively regarding thermodynamic [14, 20, 52, 103, 104] and transport properties [26, 39, 111]. Equilibrium molecular dynamics simulations and density gradient theory consistently predict a strong enrichment of the low-boiling component at the interface for mixture A, while no such enrichment is found for mixture B [14, 20, 26, 52, 103, 104]. An enrichment of low-boiling components at equilibrium conditions has been reported for many mixtures of real fluids and model fluids [5–18]; see [102] for a recent review. It has been discussed in various studies [11, 14, 19–25] that the enrichment might have an influence on the diffusive mass transfer through the interface (which would be in line with Fick's law), but to date there is no proof of this hypothesis. No experimental studies of this are available, nor are they to be expected in the foreseeable future since the enrichment occurs in the interfacial region, which is only a few nanometers wide and fluctuates, which hinders the acquisition of meaningful experimental data. Hence, corresponding studies have to rely on simulation methods.

This chapter is organized as follows: first, the simulation method is introduced. Then the two mixtures are defined and described. The simulation results for the two mixtures are then presented and compared; finally, conclusions are drawn.

3.2 Molecular Simulations

3.2.1 Overview of the Simulation Method

In the present section, the molecular simulation method for studying the mass transfer at vapor-liquid interfaces driven by a gradient in the chemical potential is described in a general way. The actual settings that were used for the simulations in the present chapter are reported below.

The simulation scenario is schematically shown in Figure 1. It contains a liquid domain in the middle and two vapor domains on each side. Each of the vapor domains contains a control volume (labeled CV+ and CV−), in which the chemical potential is prescribed such that the chemical potential difference causes a mass flux in $+z$-direction, which passes through both vapor-liquid interfaces. This mass flux is the most important observable in the simulation. Periodic boundary conditions are applied in x- and y-direction perpendicular to the interfaces. In z-direction, the simulation volume is confined by soft repulsive walls.
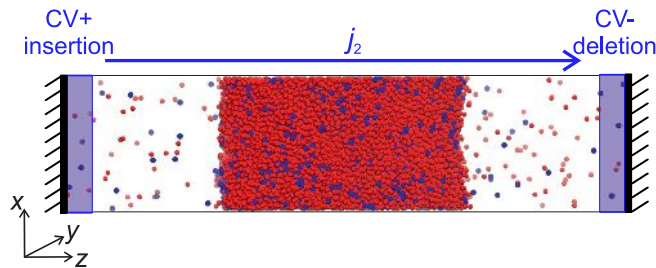
Figure 1: Scheme of the simulation set-up used in the present chapter for studying the mass transfer through vapor-liquid interfaces in binary mixtures. Red spheres indicate the high-boiling component 1 and blue spheres the low-boiling component 2. A liquid domain in the middle is surrounded by two vapor domains. The simulation box has periodic boundaries in x- and y-direction and soft repulsive walls in z-direction. The chemical potential of component 2 is adjusted to prescribed values in the control volumes CV+ and CV− (shaded blue) by a Monte-Carlo algorithm. The resulting flux j_2 of component 2 is measured.

As described in more detail in the next section, binary Lennard-Jones mixtures were studied in the present chapter for testing the simulation scenario. The high-boiling component is component 1, the low-boiling component is component 2. The chemical potential difference was only set for component 2. No action on component 1 was taken in the control volumes. The resulting flux j_2 of component 2 is defined here as the mean number of particles per time passing through a plane perpendicular to the z-axis. All fluxes are reported in the fixed laboratory frame. The flux of component 2 j_2 can also be

interpreted as a diffusive flux, when component 1 is taken as reference (as the velocity of that component is zero). The use of a number averaged mean velocity as reference for defining the diffusive fluxes is briefly discussed in Appendix A.

Quasi-stationary conditions were established before the sampling was started. The magnitude of the chemical potential difference of component 2 was chosen such that the resulting flux of component 2 was low, but still reasonably measurable. The resulting response is described well by linear theory.

The simulation was specified as follows: the temperature T was prescribed in the entire simulation volume using velocity-scaling. As the particle velocity from the Brownian movements is much larger than the averaged component velocity that causes the flux, the thermostat was simply applied to the actual velocities of all particles without subtracting the average component velocity. The error induced by this simplification is negligible. The total volume of the simulation box V was constant. Due to the boundary conditions, the number of particles of component 1 N_1 was also constant. Particles of component 2 were inserted into the control volume CV+ and removed from the control volume CV− by prescribing the number for the chemical potential of component 2 in the two control volumes μ_2^{CV+} and μ_2^{CV-}. This was achieved by a grand canonical Monte Carlo algorithm [99–101].

The simulation was carried out as follows: the initialization and an equilibration were carried out in the NVT ensemble – as it is done in direct vapor-liquid equilibrium (VLE) simulations. After that, the control volumes, which are placed next to the soft repulsive walls, were switched on. With all settings active, the simulation was run until the mass flux of component 2 through the simulation box was stationary; then, the sampling was started.

The primary measured observable during the production phase is the flux of component 2 j_2. It is measured by monitoring the number of particles of component 2 that are inserted in the control volume CV+ and those that are deleted in the control volume CV−. These numbers are equal – within their fluctuation band-width – in the stationary sampling phase. The area that is used for calculating the flux is the geometric cross section of the simulation box perpendicular to the z-direction. Besides the flux j_2, also profiles of different variables depending on the z-position in the simulation box were sampled. For that purpose, the box was divided into bins in z-direction, in which the number densities of both components $\rho_1(z)$ and $\rho_2(z)$ and the diagonal components of the pressure tensor were measured.

The pressure in the bulk domains in the simulation box is not constant in z-direction. This can be understood as a consequence of prescribing the temperature and imposing a chemical potential gradient that controls the concentration profiles. The pressure gra-

dient and the flux of the particles of component 2 act in such a way that the momentum balance is practically fulfilled in any sub-volume in the simulation box, i.e., no measures had to be taken to stabilize the position of the liquid slab in the center of the simulation volume.

The simulations with the outlined scenario pose several challenges. Unfavorable choices for the difference of the chemical potential between both control volumes can yield nucleation of droplets in the vapor domain, separation of the liquid film, movements of the liquid film during simulations, and exceedingly long simulation times to reach a quasi-stationary state. However, by choosing suitable settings, these problems can be circumvented. Further details on the simulation method are given in Appendix A.

3.2.2 Studied Lennard-Jones Mixtures

The simulation method proposed in this chapter was applied to two different binary LJTS mixtures. For both mixtures, the size parameter σ_i and mass m_i of component 1 and 2 were equal and set to unity. Also, the energy parameter of component 1 ε_1 was set to unity while ε_2 of component 2 was different for the two mixtures. The same holds true for ξ_{12}. The parameters of the two studied test mixtures are given as

- Mixture A: $\varepsilon_2/\varepsilon_1 = 0.6$ and $\xi_{12} = 0.85$

- Mixture B: $\varepsilon_2/\varepsilon_1 = 0.9$ and $\xi_{12} = 1.00$

The phase behavior and interfacial properties of these two LJTS mixtures have been investigated systematically in previous works of our group [14, 20, 52, 103, 104]. There, the thermophysical properties were found to be described well by the PeTS equation of state [14, 112]. The resulting phase equilibria of mixtures A and B at the temperatures that were studied in the present chapter are shown in Figure 2.

Mixture A exhibits an asymmetric, wide-boiling phase behavior, whereas mixture B has essentially an ideal phase behavior in the sense of Raoult's law. Mixture A also exhibits a vapor-liquid-liquid equilibrium (VLLE) at the lowest studied temperature. Examples of real mixtures, which exhibit phase behavior qualitatively resembling that of mixture A, are water + carbon dioxide, which is relevant, for example, for carbon capture technologies, nitrogen + ammonia, which occurs in the Haber-Bosch process, and water + ammonia, which, among others, is used as a disinfectant or household cleaner. In the case of mixture B, real mixtures that have comparable phase behavior are benzene + toluene and propane + propene, both of which are separated via distillation in the petrochemical industry. Even though both mixtures exhibit distinctively different phase behaviors, they have similar diffusivity (the product of density and the mutual diffusion coefficient) in the vapor and liquid phases [26]. In mixture A, the low-boiling
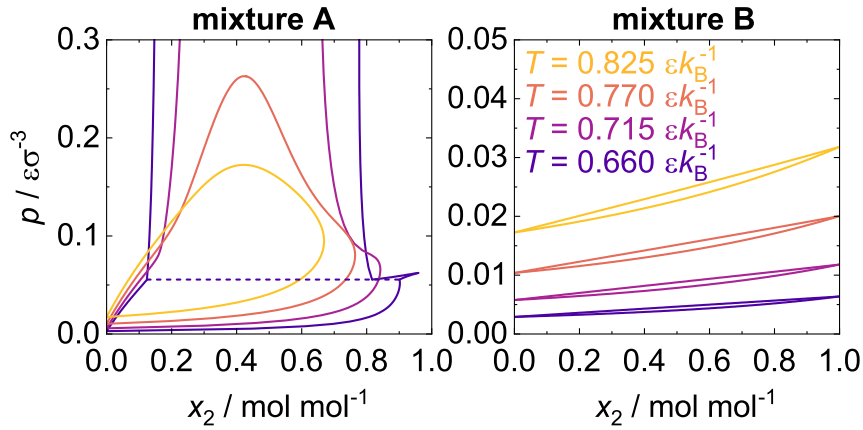
Figure 2: Phase diagrams of mixture A (left) and mixture B (right) for all investigated temperatures calculated with the PeTS EOS [14, 112].

component exhibits a large enrichment at the vapor-liquid interface in thermodynamic equilibrium [14, 52], i.e., the number density $\rho_2(z)$ shows a distinct maximum at the interface. In mixture B, no such enrichment is present. [14, 52]. The two mixtures also differ in other interfacial properties such as the surface tension, the interfacial thickness, and the relative adsorption of the low-boiling component at the interface; for details see Ref. [52].

3.2.3 Simulation Details

First, the principles are explained and then their realization is discussed. Let us start by considering an equilibrium situation (or, equivalently, assume that only a negligible gradient in the chemical potential of component 2 was applied). Then, after the equilibration, a vapor-liquid equilibrium would be established in the simulation. Let us first consider this vapor-liquid equilibrium in intensive variables. In molecular simulations, it is specified by the temperature T and the chemical potential of component 2 μ_2. Furthermore, the number of particles of component 1 N_1 as well as the simulation volume V are set (N_2 is not set and will adjust itself to meet the specification of μ_2). Hence, such a simulation can be characterized as an N_1, V, T, μ_2-simulation. These settings fully determine the vapor-liquid equilibrium in the simulation box, including the amounts of the vapor and the liquid phase and the corresponding compositions. Starting from this equilibrium, the finite gradient of the chemical potential of component 2 μ_2 is imposed by increasing μ_2 in one control volume CV+ by $\delta\mu_2$ and decreasing it by the same amount in the other control volume CV−. The resulting quasi-stationary state is then sampled in the simulation, which is near the equilibrium state described above for small $\delta\mu_2$. For a binary mixture at constant temperature, the gradients of the chemical potentials of both components and the pressure are coupled by the Gibbs-Duhem equa-

tion. As a result of the imposed gradient of the chemical potential of component 2, in general, also the gradients of the chemical potential of component 1 and the pressure are non-zero. The resulting diffusive and convective mass flux of component 1 cancel each other, as a consequence of the employed boundary conditions that do not allow a net flux of component 1 in the stationary simulation. The new simulation scenario is based on these principles; but the realization involves additional considerations, that are discussed now.

The rectangular simulation volume V used in the present chapter has a quadratic cross section in x- and y-direction with a side length $l_x = l_y$. The length of the simulation volume in z-direction was always $l_z = 170\,\sigma$. The lengths l_x and l_y were $21.1\,\sigma$ in the simulations with mixture A and $22\,\sigma$ in the simulations with mixture B. The settings were chosen such that the thickness of the liquid domain (in z-direction) was about $40\,\sigma$ and the thickness of the vapor domain was $65\,\sigma$ each, cf. Figure 3. The maximal range of the soft repulsive wall potential was $5\,\sigma$ and the thickness of the control volumes was $10\,\sigma$, such that each of the two undisturbed bulk vapor domains has a thickness of $50\,\sigma$, when these regions are excluded. The total particle number $N_1 + N_2$ was about 16,000 in all simulations. The selection of the actual choices for the initial densities and compositions was supported by preliminary calculations of the phase equilibrium using the PeTS EOS [14, 112].
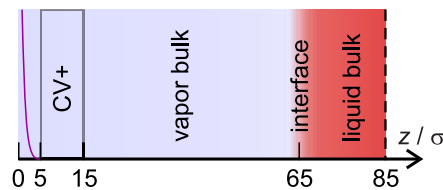
Figure 3: Geometric parameters of the scenario used in the present simulations. Only one half of the geometrically symmetric simulation box is shown; the symmetry plane is indicated by the dashed line. The cross section of the simulation box in the x, y plane was quadratic (edge length was $21.1\,\sigma$ for mixture A simulations and $22\,\sigma$ for the mixture B). The purple parable indicates the soft repulsive wall. The control volume is indicated by the gray lines.

The soft repulsion of the walls acts on both components 1 and 2 and is modeled by half a harmonic potential which starts to become effective at a distance of $5\,\sigma$ from the end of the simulation box, as indicated in Figure 3. At closer distances, a repulsive force acts on the particle that rises linearly with a force constant of $k = 20\,\varepsilon\sigma^{-2}$.

In the left control volume CV+ (cf. Figure 1) particles of component 2 were inserted; and in the right control volume CV− particles of component 2 were removed from the simulation box. The choice of the chemical potentials of component 2 μ_2 in the control volumes is not trivial. Basically, μ_2, as determined in the NVT equilibrium simulations

was increased by $\delta\mu_2$ in the control volume CV+ and decreased by the same $\delta\mu_2$ in the control volume CV−. The difference of the chemical potentials between the two control volumes was the same in all simulations and was $\Delta\mu_2 = 0.5\,\varepsilon$. Preliminary simulations showed that this is enough to ensure a reliable determination of the flux of component 2, but still well in the linear regime. It turns out that this value chosen based on computational considerations lies in the same range as the chemical potential differences that are common in chemical engineering mass transfer problems [113]. However, the chemical potential gradient, which results from this choice, is much larger than that in common chemical engineering problems, as the distance of the control volumes is of the order of 10^{-7} m whereas the boundary layers in chemical engineering mass transfer problems are of the order of 10^{-4} m [113]. The corresponding difference of 3 - 4 orders of magnitude is also found for the fluxes between engineering mass transfer problems and the fluxes obtained from the mass transfer simulations of the present chapter.

The simulation was carried out as follows: the first phase of the simulation is a pre-run in the NVT ensemble. It is used to establish an equilibrium with a liquid slab in the middle and the two surrounding vapor domains, see Figure. 1 and 3. The initial positions and velocities of the particles were chosen as it is common in direct simulations of phase equilibria; the description given in Ref. [103] applies also here, correspondingly. The time step was $\delta\tau = 0.001\ \sigma(m/\varepsilon)^{1/2}$ in all simulations; the NVT simulations were carried out for 50,000 time steps. After this, the control volumes in the vapor domains were switched on to evoke the mass flux j_2 in z-direction through the simulation box. The simulations were then run for at least 3,000,000 further time steps, until a stationary mass flux was established. The settings for the MC algorithm that was used for this purpose in the control volumes were: 50 Monte Carlo insertion/ removal trials every 40 MD time steps. The insertion and removal were steered by a grand canonical Monte Carlo algorithm, cf. Refs. [99–101] for details.

After a steady state was achieved, the sampling was started and carried out for at least 5,000,000 time steps. The simulation box was divided in 1200 equal bins by a discretization in the z-direction.

The mass flux $j_2 = \frac{\Delta N_2}{\Delta\tau\, a^2}$ was determined from the total number of inserted and removed number of particles during the production time $\Delta\tau$. The cross section of the simulation box is a^2. The number of inserted and deleted particles ΔN_2 was computed from the average of the inserted and deleted particles by the end of the production phase τ_{end}, i.e., $\Delta N_2 = \frac{N_2^{\mathrm{CV}+}(\tau_{\mathrm{end}})+N_2^{\mathrm{CV}-}(\tau_{\mathrm{end}})}{2}$. In all cases, $N_2^{\mathrm{CV}+}(\tau_{\mathrm{end}})$ and $N_2^{\mathrm{CV}-}(\tau_{\mathrm{end}})$ deviate by no more than 10%. Details are given in Appendix A.

The pressure profile and the component density profiles were sampled in these bins. Density and pressure profiles were computed in block averages of 200,000 time steps during

the production phase. During the entire simulation time, the box was temperature-controlled by velocity scaling, as discussed in Section 2.1. The velocity associated with the flux of the particles of component 2 was two to three orders of magnitude smaller than the mean thermal motion velocity. The flux j_2 of component 2 was measured by counting the insertions and deletions of particles of component 2 in the control volumes in the production phase. A detailed discussion of the sampling and the computation of the statistical uncertainties is given in Appendix A.

An inspection of the profiles (see results section) shows, that the gradients of the pressure and the component densities in the bulk domains are moderate. For the discussion, it is helpful to consider the average properties over the three bulk domains, which are labeled here V_{left} (vapor left), L (liquid), and V_{right} (vapor right). The density ρ, the pressure p, and the composition x_i were calculated as an average over the respective bulk domain excluding the area close to the interface and close to the control volumes, i.e., keeping a distance of at least $10\,\sigma$ to the control volume and to the center of the interface. The corresponding statistical uncertainties were computed from the standard deviation of the individual bin values.

Furthermore, the enrichment E_2 of the low-boiling component at the interfaces [5, 14] was computed from each density profile from the production phase as

$$E_2 = \frac{\max\big(\rho_2(z)\big)}{\max\big(\rho_2^{\text{liq}}, \rho_2^{\text{vap}}\big)} \,. \tag{13}$$

Here, ρ_2^{liq} and ρ_2^{vap} are the densities in the adjoining bulk domains. For each simulation and interface, E_2 and its uncertainty were computed as the mean value from the block averages and three times their standard deviation, respectively.

The mass transfer simulations were carried out using the molecular dynamics code *ls*1 *mardyn* [114].

3.2.4 Bulk Diffusion Coefficient Simulations

Diffusion coefficients were computed for both mixtures in the liquid and the vapor phase. For the liquid phase, molecular simulations were performed at state points slightly above the bubble line. For the vapor phase, diffusion coefficients were determined from the Chapman-Enskog theory [115].

The liquid bulk diffusion coefficients were determined with the molecular simulations code *ms*2 [116] using the Green-Kubo formalism as in previous work of our group [55, 117–120]. Simulation details are reported in Appendix A.

3.3 Results and Discussion

3.3.1 Overview

Table 6 and 7 report the numerical values for the mass flux j_2 and the enrichment E_2 in the mass transfer simulations for all considered temperatures. The numerical values of the average bulk domain state points and the interface positions are reported in Appendix A.

Also the results for the bulk diffusion coefficients are presented in Appendix A. As no unexpected findings were made, they are not discussed here.

In the following, the results of the mass transfer simulations are discussed, starting with a detailed consideration of a single temperature, before also the results for other temperatures are presented and discussed.

3.3.2 Temperature $T = 0.715\,\varepsilon k_{\mathrm{B}}^{-1}$

For the simulations at $T = 0.715\,\varepsilon k_{\mathrm{B}}^{-1}$, the mass flux sampled in the production phase was $j_2 = 0.11{\cdot}10^{-3}\,\sigma^{-3}(m/\varepsilon)^{-0.5}$ for mixture A and $j_2 = 0.26{\cdot}10^{-3}\,\sigma^{-3}(m/\varepsilon)^{-0.5}$ for mixture B (the unit of j_2 corresponds to the dimension of the number of particles per area and time). Hence, the obtained mass flux in mixture A is smaller than that for the mixture B by more than a factor of two, even though the chemical potential gradient and the bulk phase transport diffusion coefficient of both mixtures are approximately the same – see Appendix A for details. In all cases, no net flux of component 1 was observed, in accordance with the chosen simulation settings (see discussion above).

Table 6: Numeric values of the mass flux j_2, the prescribed residual chemical potential in the inserting and deleting control volume $\mu_2^{\mathrm{CV}+}$ and $\mu_2^{\mathrm{CV}-}$, respectively, and the number of component 1 particles N_1 in the performed mass transfer simulations for both mixtures A and B at all four investigated temperatures. The box size was $170\,\sigma$ in z-direction in all cases; the xy-cross section was a square with the edge length $21.1\,\sigma$ for the simulations with mixture A and $22\,\sigma$ for the simulations with mixture B.

$T/\varepsilon k_{\mathrm{B}}^{-1}$	$j_2\ /\ 10^3\,\sigma^{-3}(m/\varepsilon)^{-0.5}$		$\mu_2^{\mathrm{CV}+}\ /\ \varepsilon$		$\mu_2^{\mathrm{CV}-}\ /\ \varepsilon$		N_1	
	A	B	A	B	A	B	A	B
0.66	0.06(5)	0.23(1)	-0.75	-2.22	-0.25	-1.72	12705	12447
0.715	0.11(5)	0.26(1)	-0.8	-2.4	-0.3	-1.9	12703	12344
0.77	0.10(4)	0.21(1)	-0.95	-2.6	-0.45	-2.1	12642	12344
0.825	0.19(3)	0.24(1)	-1.1	-2.6	-0.6	-2.1	12689	12347

Here, only fluxes in the fixed laboratory frame are discussed. A brief discussion of the corresponding mean directed velocities and the diffusive fluxes in various reference systems is also given in Appendix A.

Figure 4 left and middle panel shows the density and pressure profiles obtained from the mass transfer simulations for mixtures A and B at $T = 0.715\,\varepsilon k_{\mathrm{B}}^{-1}$ during the production phase. The density profiles in Figure 4 show that the density of the low-boiling component exhibits a gradient $\frac{\partial \rho_2}{\partial z}$ in the bulk domains as a response to the gradient of the chemical potential, whereas the total density exhibits no gradient in the bulk domains. Since the diffusion coefficient is lower in the liquid phase than in the vapor phase (see Appendix A), the gradient $\frac{\partial \rho_2}{\partial z}$ is larger in the liquid bulk domain than in the vapor bulk. This holds for both mixtures.
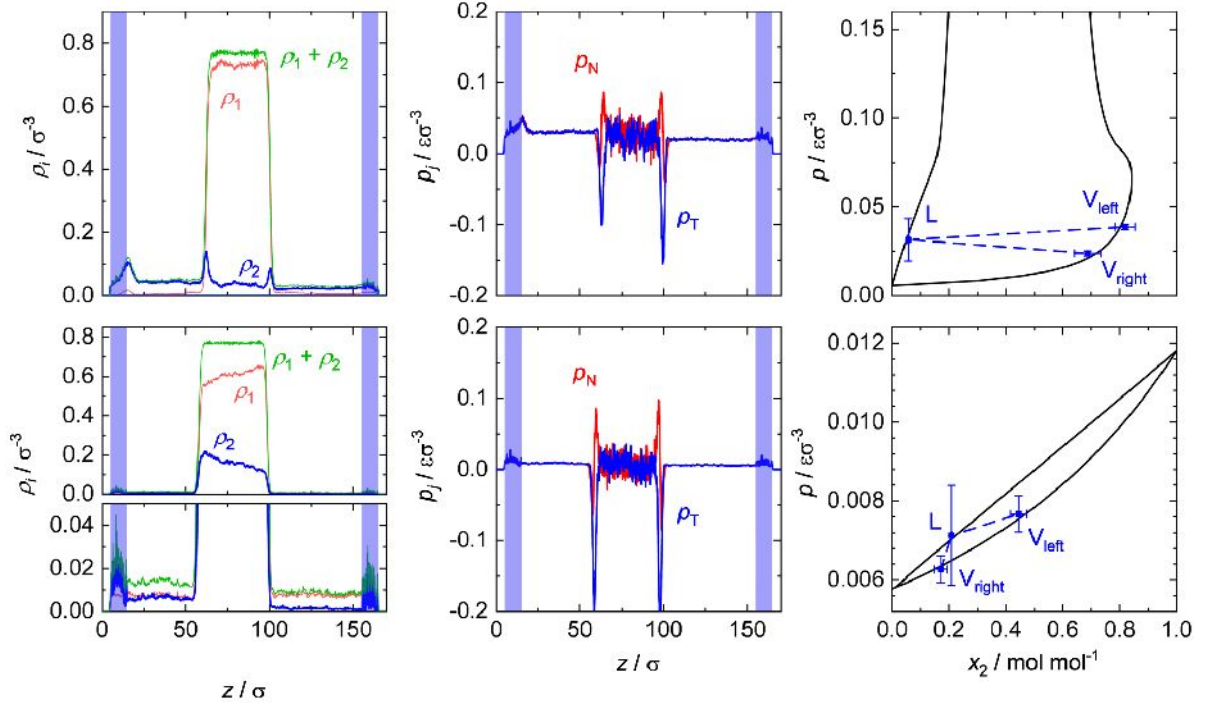
Figure 4: Density profiles (left), pressure profiles (middle), and averaged thermodynamic state points in the bulk domains (right) for the mixtures A (top) and B (bottom) obtained in mass transfer simulations at $T = 0.715\,\varepsilon k_{\mathrm{B}}^{-1}$. The lower part of the split plot (bottom-left panel) is just an expansion of the upper part. The blue shaded area indicates the control volumes. For the pressure profiles, the indices $j = N, T$ indicate the normal and tangential component of the pressure tensor, respectively. The thermodynamic state points indicated as symbols in the right plots were sampled in the three bulk domains during the production phase of the simulations. They are compared to results for the vapor-liquid equilibrium computed with the LJTS EOS [14, 112] (lines). The density and pressure profiles are from one arbitrarily selected block average during the production phase, the state points depicted in the $p - x$ diagrams (right) are the average of all blocks.

For mixture A, the low-boiling component exhibits a large enrichment at the interface,

which is not observed for the mixture B. To the best of the author's knowledge, this is the first time that the enrichment is studied under the influence of a mass transfer. This is in line with results from equilibrium simulations for these mixtures [14, 52]. The numerical values for the enrichment in mixture A at the left and right interface are compared in Table 7 with equilibrium results from the literature [52] at the same liquid phase composition. Two values are reported for the enrichment at the right interface. The evaluation of Eq. (13) requires the computation of the larger value of the density of component 2 in the adjoining bulk domains as reference in the denominator. In equilibrium simulations, the choice poses no problem as the bulk is equilibrated. In mass transfer simulations, however, gradients occur. This introduces an ambiguity in the choice of the bulk value: it could be chosen as the average value of the domain, or be selected as values at the foot of the peak. For the left peak, this makes no difference, the reference is always the vapor domain and there is no substantial difference between the average vapor density and that at the foot of the peak. For the right peak, this is different. When the average bulk densities are used for the evaluation of Eq. (13), the reference is the liquid density; when the values at the foot of the peak are used, the reference is the vapor density (for which the value at the foot of the peak is again basically the same as the average value). Hence, two values for the right peak are reported.

Table 7: Numerical values of the enrichment of the low-boiling component at the interface for mixture A at all four investigated temperatures. The column x_2^{liq} indicates the mole fraction of component 2 in the liquid bulk domain L sampled during the mass transfer simulations. The columns E_2^{left} and E_2^{right} indicate the enrichment at the left and right interface, respectively. For the right interface, vap and liq indicate the evaluation of Eq. (13) using the vapor or liquid domain as reference, respectively (details are given in the text). E_2^{eq} indicates the equilibrium enrichment at the corresponding temperature and liquid phase composition taken from Ref. [52].

$T / \varepsilon k_{\text{B}}^{-1}$	x_2^{liq} / mol mol^{-1}	E_2^{left}	$E_2^{\text{right,liq}}$	$E_2^{\text{right,vap}}$	E_2^{eq}
0.66	0.057(5)	4.4(2)	3.2(3)	5.4(4)	4.0(3)
0.715	0.056(3)	3.2(2)	2.6(2)	3.7(4)	3.1(1)
0.77	0.058(4)	2.5(1)	1.9(2)	2.9(2)	2.5(1)
0.825	0.055(3)	2.1(1)	1.6(2)	2.2(2)	1.9(1)

As a reference, the results for the enrichment obtained for the same mixture from vapor-liquid equilibrium simulations at the same temperature and the same composition of the liquid bulk domain are included in Table 7 . The results are also illustrated in Figure 5, from which it can be seen that the results for the left interface that were obtained in the mass transfer simulations agree very well with those from equilibrium simulations. For the right interface, depending on the choice of the reference, the results lie below

or above the corresponding equilibrium values. Overall, it can be concluded, that the values for the enrichment E_2 do not change strongly when mass transfer occurs, at least for moderate gradients of the chemical potential, as they were applied here.
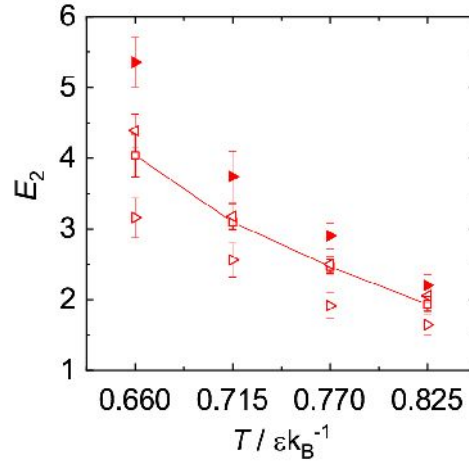
Figure 5: Enrichment of component 2 E_2 at the interface at different temperatures during the mass transfer simulations (triangles) in comparison to the enrichment at equilibrium states (squares; adapted from Ref. [52]) at the same liquid phase composition. Left triangles and right triangles indicate the enrichment obtained for the left and right interface in the mass transfer simulations, respectively. The filled and empty right triangles indicate the enrichment using the vapor or liquid domain as reference, respectively (details are given in the text). Lines are a guide for the eye.

No enrichment is found for mixture B, i.e., $E_2 = 1$ within the numeric uncertainty in all experiments, cf. component density profiles in Appendix A. This finding is in line with the findings from the equilibrium simulations [14, 52].

For both mixtures A and B, the average state points computed for the three bulk domains V_{left}, L, and V_{right} are compared with the corresponding phase equilibrium obtained from the PeTS EOS [14, 112] in the right panels of Figure 4. The averaged state points sampled in the bulk domains agree astonishingly well with the isothermal phase envelope from the EOS. The individual state points in each bin for a bulk domain show an elliptic scattering around the averaged value, cf. Figure A.2 in the Appendix. The average pressure in the bulk domains decreases from left to right with the gradient of the chemical potential, as expected.

3.3.3 Influence of the Temperature

The influence of the temperature on the mass transfer in the two mixtures A and B was studied by performing additional simulations at three further temperatures ($T/\varepsilon k_{\text{B}}^{-1}$

= 0.66, 0.77, 0.825). The numerical values obtained for the mass fluxes and the non-equilibrium enrichment are reported in Table 6 and 7, respectively.

Density profiles and isothermal $p - x$ diagrams obtained during the quasi-stationary production phase for mixture A at $T/\varepsilon k_{\mathrm{B}}^{-1}$ = 0.66, 0.77, 0.825 are shown in Figure 6. The corresponding plots for mixture B are presented in Appendix A. For all four investigated temperatures (see section above), the difference of the chemical potential applied between the two control volumes was the same for mixture A and mixture B. The density profiles obtained for mixture A (cf. Figure 6) show in all cases a gradient of the low-boiling component $\frac{\partial \rho_2}{\partial z}$, i.e., ρ_2 decreases from the left to the right side in each bulk domain. An enrichment of component 2 is observed in all cases for mixture A, but its height decreases with increasing temperature, which is in line with corresponding equilibrium results [52].

The enrichment computed from Eq. (13) for the left and right interface is depicted in Figure 5 for all temperatures. As a reference, also the equilibrium enrichment at the corresponding temperature is shown [52]. As discussed above, the enrichment of the right interface was evaluated in two different ways: using the averaged bulk liquid density (open triangles right) and using the vapor density (filled triangles right) for the evaluation of the denominator in Eq. (13). For all temperatures, the enrichment at the left interface is in fair agreement with the enrichment obtained from equilibrium simulations [52]. For the right interface, the evaluation based on the average liquid bulk density as reference, yields consistently lower enrichment than the equilibrium results. Vice versa, the evaluation based on the vapor bulk density reference yields larger enrichment. The differences between the enrichment obtained for the left and the right interface are likely due to the fact that interfacial properties strongly depend on the liquid bulk composition adjoined to the interface [103], which varies for the left and right interface in the mass transfer simulations. A comprehensive comparison of equilibrium and non-equilibrium interfacial properties is out of the scope of this work but is an interesting topic for future work.

In some of the density profiles shown in Figure 6, small peaks of the total density in the vicinity of the control volumes indicate the presence of a small droplet. This is due to the fact, that the perturbations of the control volume act as nucleation precursor. Hence, in some cases, small nucleus form in the saturated vapor domains attached to the control volume. This also produces more pronounced fluctuations for the insertion rate than the removal rate of component 2 particles in the control volumes, cf. Appendix A.

For all temperatures, the average state points computed for the three bulk domains V_{left}, L, and V_{right} are in excellent agreement with the corresponding phase equilibrium. The same holds for mixture B, see Appendix A. Also, the composition difference between the left and right bulk vapor domain is similar for the results from the different temperatures.
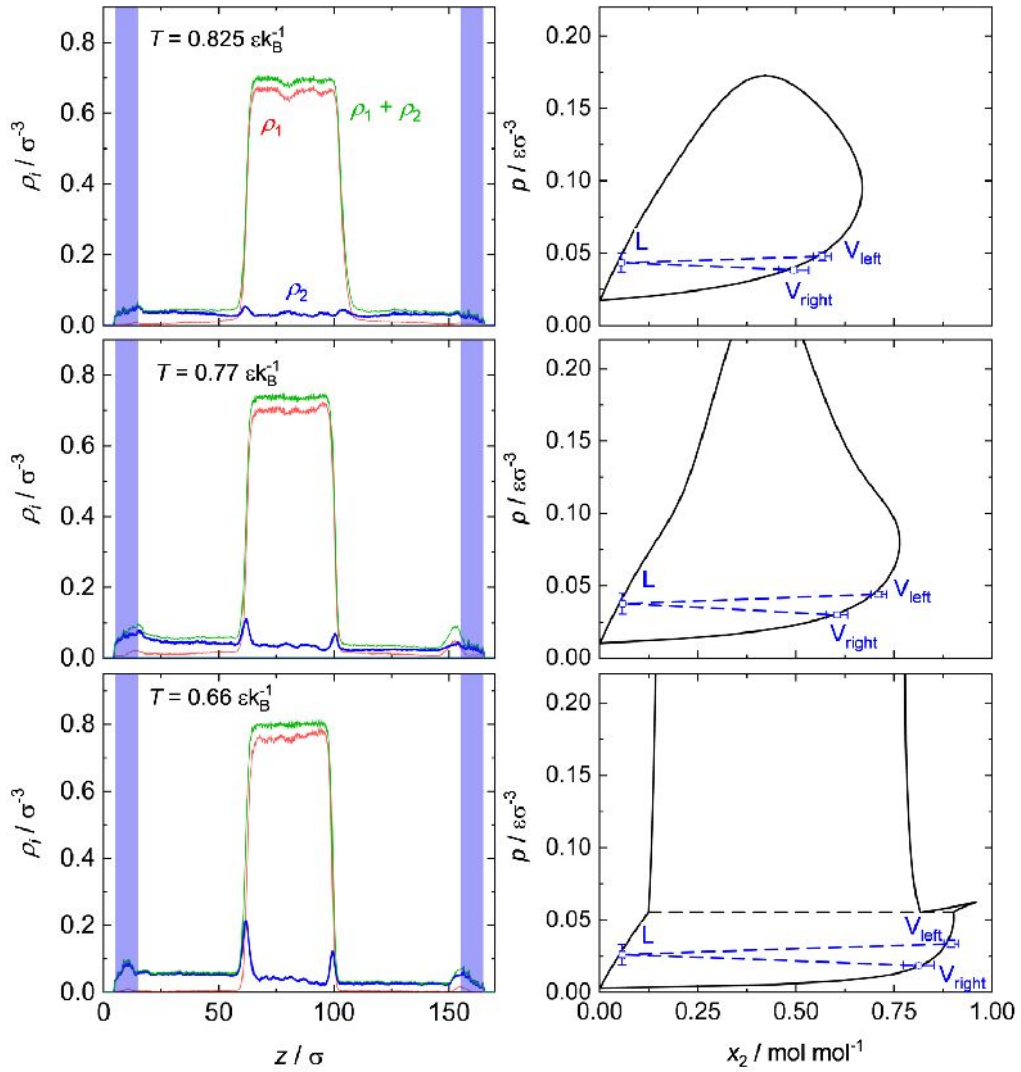
Figure 6: Density profiles (left panels) and isothermal $p – x$ diagrams (right panels) sampled during the production phase of the simulations of mixture A at different temperatures. The blue shaded area indicates the elongation of the control volumes in z-direction.

Figure 7 shows the stationary mass flux j_2 sampled during the production phase as a function of the temperature for mixture A and B. For all studied temperatures, mixture B yields a significantly larger mass flux j_2 – especially at low temperatures. The mass flux obtained for mixture B exceeds that obtained for mixture A by a factor of two to four. This is astonishing as the diffusivities of both components are similar for both mixtures, both in the vapor and liquid phase (see Appendix A), the chemical potential gradient was the same and also the geometric parameters almost identical. The major difference is that mixture A shows a high enrichment while mixture B shows almost no enrichment. Hence, the present finding might point to an influence of the enrichment on the mass transfer. A further investigation of this hypothesis would require carrying out accompanying continuum simulations, which was not in the scope of the present work.
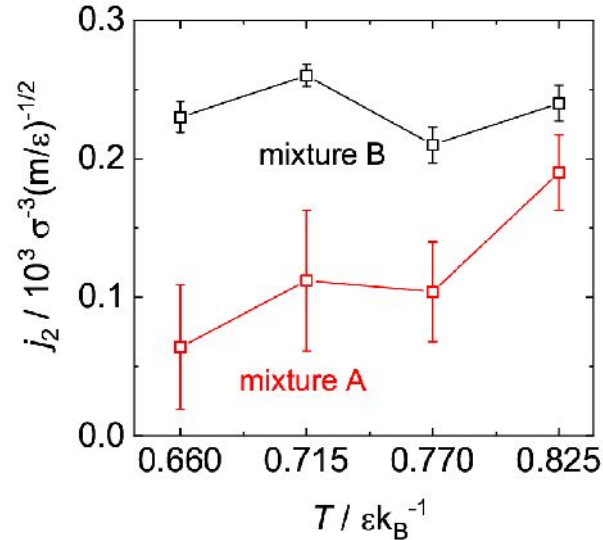
Figure 7: Mass flux j_2 sampled during the mass transfer simulations in mixture A and B at different temperatures. Lines are a guide for the eye.

3.4 Conclusions

The DCV method was applied for studying mass transfer in mixtures driven by a chemical potential difference across vapor-liquid interfaces by molecular simulations. It is based on a simulation scenario in which two vapor domains encase a liquid domain. Different values of the chemical potential of a selected component are prescribed in two control volumes in the two vapor domains and evoke a flux of that component that passes two vapor-liquid interfaces; the other components are stagnant due to the chosen boundary conditions. In isothermal simulations, the profiles of the component densities, the pressure tensor, and the flux of the selected component are measured. To the best of the author's knowledge, this is the first report on a molecular simulation method for studying mass transfer through vapor-liquid interfaces driven by chemical potential gradients. This is astonishing, as mass transfer through vapor-liquid interfaces is very important in technical and natural processes. The new simulation scenario opens the way for detailed studies of these processes on the molecular level. In particular, the new simulation scenario can be used for systematic studies of the influence of mass transfer on interfacial properties, which are presently still lacking.

The simulation method was applied to study the influence of the enrichment of components at the vapor-liquid interface on the mass transfer. Two Lennard-Jones mixtures were examined, of which the phase equilibrium properties, including the interfacial equilibrium properties, are well-known [14, 52, 103]. The first mixture exhibits a large enrichment of the low-boiling component at the interface, whereas the second mixture exhibits no enrichment. Even though both mixtures have similar bulk diffusivities and the same chemical potential gradient was applied, the mass flux observed in both systems

differs significantly. These differences might be related to the presence of an enrichment at the interface in one of the mixtures. Hence, the results support the assumption [14, 19–23, 110] that the enrichment influences the mass transfer through fluid interfaces. Further studies are, however, needed to prove or refute this hypothesis. The new scenario is a valuable tool for this. Such studies should also include simulations with continuum methods, that can be compared to the results from the molecular dynamics simulations. For such simulations, vapor and liquid bulk diffusivities are provided.

4 Non-Stationary Mass Transfer through Vapor-Liquid Interfaces

4.1 Introduction

In the present chapter, a second, non-stationary method for studying mass transfer through vapor-liquid interfaces of mixtures is proposed: First, the system containing only particles of one component is equilibrated. The initial equilibrium state consists of a vapor phase slab surrounded by a liquid bulk phase, which coexists in a rectangular simulation box with periodic boundary conditions. After the first equilibration, particles of a second component are inserted in the middle of the vapor phase during a short period of time, i.e., in a pulse-like manner. This perturbation induces a non-stationary, one-dimensional flux of the inserted particles towards the two vapor-liquid interfaces and through them into the liquid phase on both sides of the vapor phase. The process is basically symmetric with regard to these interfaces. The relaxation process caused by the perturbation is then studied, focusing on the processes in the vicinity of the interfaces. Simulations are run until a second, final equilibrium state is reached.

Non-stationary mass transfer close to and in the interfacial region has been investigated in several studies using different techniques: Baidakov et al. [97, 98] have investigated the dynamic formation of vapor-liquid interfaces in pure substances and binary mixtures and the evolution of interfacial properties in the process. In their studies, first a system containing a coexisting vapor and liquid phase was equilibrated. After the equilibration, all particles in the interface layer were instantaneously removed and the non-stationary relaxation process and formation of a new vapor-liquid interface were observed. Bucior et al. [121] studied evaporation of a pure liquid in a slit pore into a spontaneously created vacuum by moving the pore walls. Nagl et al. [19] studied the non-stationary mass transfer through liquid-liquid interfaces of different real fluid mixtures using a combination of experiments and theoretical calculations. Braga et al. investigated self-diffusion at liquid-liquid interfaces [95] and the free energy barrier at vapor-liquid interfaces [93] by moving a probe particle through the respective interface. Garrett et al. [96] observed the trajectories of single particles moving in the vicinity of a vapor-

liquid interface in aqueous systems under equilibrium conditions and categorized four different behaviors of these particle: adsorption, absorption, desorption, and reflection.

A major problem of non-stationary molecular dynamics simulations is to distinguish an actual physical process from random noise and to provide a measure of uncertainty. Therefore, this simulation study was performed using *sets of replicas*, i.e., the simulation was repeated several times using different initial velocity distributions. The simulation box and start system size, temperature, and the insertion procedure were the same for all simulations in a set of replicas. The results obtained from a set of replicas were averaged, resulting in a reduction of the noise of the signal; furthermore, a measure for the statistical uncertainties of the observables was obtained. This replica strategy based on varying starting conditions is a well-established method in non-stationary molecular dynamics simulations [40, 93, 122–124].

The new simulation method was applied to investigate non-stationary mass transfer in two binary Lennard-Jones mixtures with distinctively different phase behavior. The same mixtures have been used in the quasi-stationary mass transfer scenario presented in the previous Chapter 3.

This chapter is structured as follows: First, the simulation method is introduced. Then, the studied test mixtures are described. Next, the simulation results from one temperature are discussed in detail, comparing the results from both mixtures. Finally, results obtained for several temperatures are compared, which provide insights into the temperature dependency of the relaxation process.

4.2 Simulation Method

4.2.1 Overview

The basic concept of the simulation method is illustrated in Figure 8. The simulation box has a rectangular shape and periodic boundary conditions in all directions. At the start, the simulation box contains only particles of component 1. The conditions are chosen so that the box contains two phases: a vapor phase in the middle of the simulation box surrounded by a liquid phase. During the entire simulation run, the number of particles of component 1, the temperature, and the volume of the simulation box are kept constant. After establishing the vapor-liquid equilibrium state of the pure component 1 system, it is perturbed by the insertion of particles of component 2, which are inserted into the control volume (CV) in the middle of the vapor phase (cf. Figure 8). The response of the system to that perturbation is evaluated until the system relaxes

into a second vapor-liquid equilibrium state. Except for statistical fluctuations, the process is symmetric with respect to a plane in the middle of the simulation box.
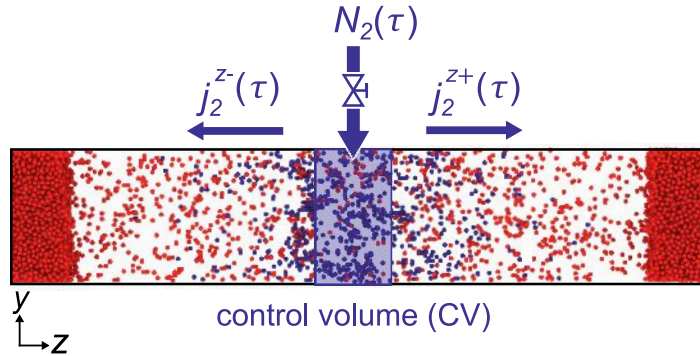
Figure 8: Scheme of the non-stationary simulation scenario. The snapshot is taken from a simulation during the insertion phase. Prior to the insertion, the system contains only particles of the high-boiling component 1 (red). Particles of component 2 (blue) are inserted into the control volume (blue shaded area), then spread through the vapor phase, cross the vapor-liquid interface, and enter into the liquid phase until a new equilibrium state is established.

Hence, a simulation run consists of the following five phases:

1. Initial equilibration phase (*IniEq*)

2. Sampling phase of the first vapor-liquid equilibrium state (*Eq1*)

3. Insertion phase (*In*)

4. Relaxation phase (*Relax*)

5. Sampling phase of the second vapor-liquid equilibrium state (*Eq2*)

The abbreviations in the parentheses are used in the following for brevity.

The first two simulation phases *IniEq* and *Eq1* are carried out in the *NVT* ensemble. Subsequently, in the *In* phase, particles of component 2 are inserted into the center of the vapor bulk domain (cf. Figure 8). The insertion of particles of component 2 inside the control volume is performed using a Monte Carlo algorithm [99, 101, 125] that adjusts the number of particles of the component 2 based on a prescribed chemical potential of that component $\mu_{2,\mathrm{CV}}$. Since the chemical potential is controlled only in a subvolume of the entire simulation box (cf. Figure 8), the *In* phase can be considered to be a quasi-μVT ensemble.

With the beginning of the particle insertion, a one-dimensional, non-stationary molar flux j_2 of particles of component 2 is established. The molar flux is positive on the right of the control volume and negative on the left of the control volume due to the

symmetry of the simulation box setup (cf. Figure 8). During the *Relax* phase the system re-equilibrates to the second equilibrium state point, which is sampled over the course of the *Eq2* phase. The *Relax* and *Eq2* phase are again carried out in the *NVT* ensemble.

4.2.2 Definition of Observables and Data Processing

The simulation box is discretized in z-direction into $1\,200$ equally sized bins. Since a planar interface is studied, no bin discretization in x- and y-direction is applied, i.e., the simulation scenario is quasi-one-dimensional. Observables $\chi(\tau, z)$ are sampled in these bins as a function of the z-direction and time τ every $10\,000$ simulation steps. The studied observables are the pressure tensor p, the density ρ_i, and the mole composition x_i of a component i. The rate of change of the density $\partial \rho_i / \partial \tau (\tau, z)$, which is needed for the determination of the molar flux j_i, is determined for each bin separately by numerical differentiation with respect to the time τ.

The position of the liquid film and its interfaces is not fixed in the simulation box and can therefore freely move during the simulation run (it fluctuates and changes slightly due to the absorption of component 2). The positions $z_{50} = z(\rho_{50})$ of the two interfaces as well as the positions $z_{10} = z(\rho_{10})$ and $z_{90} = z(\rho_{90})$ were determined by the z-position, where the local total density corresponds to 10 %, 50 %, and 90 % of the bulk density difference, i.e.

$$\begin{aligned}
\rho_{10} &= \rho^{''} + 0.1(\rho^{'} - \rho^{''}) \\
\rho_{50} &= \rho^{''} + 0.5(\rho^{'} - \rho^{''}) \\
\rho_{90} &= \rho^{''} + 0.9(\rho^{'} - \rho^{''}) \ ,
\end{aligned} \tag{14}$$

where $\rho^{''}$ indicates the total vapor bulk phase density and $\rho^{'}$ indicates the total liquid bulk phase density. Details on the procedure to determine $\rho^{''}$ and $\rho^{'}$ are given in Appendix B.

In the following, the data processing procedure is described for the right interface only (cf. Figure 8). The interface on the left is evaluated by applying an equivalent procedure and results for both interfaces are averaged. The molar flux j_2 of the inserted particles of component 2 is determined by solving the molar balance of each bin per time step. Particles of component 2 may enter or leave a bin over its two boundaries, thus there are two molar flux j_2 per bin. The molar flux j_2 is always the net molar flux here. A positive flux is directed in positive z-direction and, accordingly, a negative flux is directed in negative z-direction. In the following, the index $n = 1...N$ denotes bins and the flux at the left bin boundary has the index n while the flux at the right bin boundary has the index $n+1$. The molar balance of a bin n for particles of component 2 at a time

step τ can therefore be written as

$$\frac{\partial \rho_2}{\partial \tau}(\tau, n) = -\frac{j_2(\tau, n+1) - j_2(\tau, n)}{\Delta z_{\text{bin}}} \ , \tag{15}$$

where Δz_{bin} is the size of the bin and j_2 is the molar flux of component 2. To obtain $N+1$ unknown molar fluxes of N bins, N molar balances have to be solved (cf. Eq. (15)) with the help of a boundary condition. In this chapter, the symmetry boundary condition applies, according to which the net flux in the middle of the liquid slab is zero (cf. Figure 8). The position of the middle of the liquid slab is determined to be the midpoint between the positions z_{50} of the two interfaces in each time step and hence may fluctuate during the simulation. The gradient and molar balances are determined in a fixed reference frame in each time step. Only the position, where the symmetry boundary condition is applied, moves according to the position of the middle of the liquid slab. This is done for each simulation in a set of replicas independently and results are averaged at the position of the middle of the liquid slab. The density, composition, and pressure tensor sampled in a bin n at the same time τ are averaged over all simulations in a set of replicas. This procedure significantly reduces noise and enables the estimation of the statistical uncertainty for each sampled observable χ.

The start and end time of the *In* phase are the same for all simulations. The number of inserted particles in a set of replicas varies due to the probabilistic nature of the Monte Carlo algorithm. The number for $\mu_{2,\text{CV}}$ was chosen so that the mean number of inserted particles in a set of replicas was 1,200 particles. The distribution of the number of inserted particles in a set of replicas is quite narrow (standard deviation about 1.5 %). Preliminary tests showed that this yields a satisfactory signal-to-noise ratio for the observables of interest such as density, pressure, and molar flux during the simulation run. Details are given in the Appendix B.

The behavior of the system in the vapor phase and the liquid phase in the vicinity of the vapor-liquid interface is of particular interest. The relaxation process is sampled in two measurement volumes (MV) close to the interface: one in the bulk vapor phase and one in the bulk liquid phase (here labeled with MV_{vap} and MV_{liq}, respectively). The positions of these measurement volumes are defined with respect to the interface position, as illustrated in Figure 9.

Figure 10 illustrates the simulation procedure, the responses to the perturbation in vapor and liquid phase determined from a set of replicas as well as the five phases of the non-stationary simulation method.
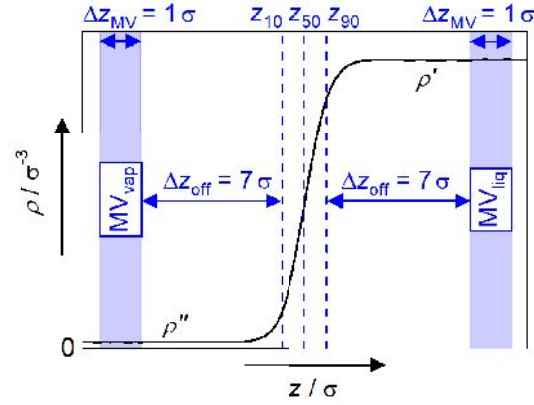
Figure 9: Schematic of the geometric configuration of the measurement volumes (MV) located in the vicinity of the interface, showing the total density at the interface as a function of the z-direction (——). The vapor and liquid measurement volumes (blue shaded areas) are located at a distance of $\Delta z_{\text{off}} = 7\,\sigma$ to the characteristic interface points z_{10} and z_{90}, respectively. The positions z_{10}, z_{50}, and z_{90} (- - -) are defined according to Eq. (14).
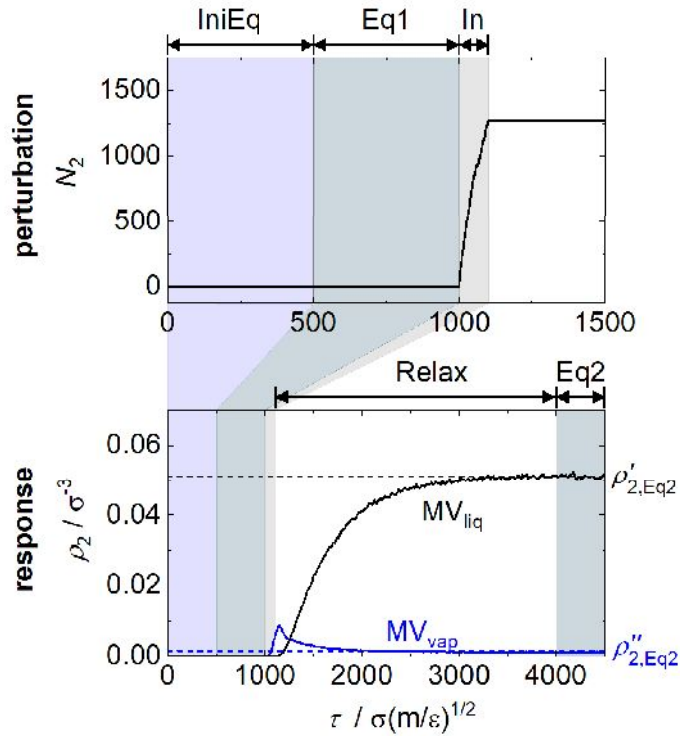
Figure 10: Example of results from the evaluation of a set of replicas of simulation runs used here for illustrating the simulation phases. Top: number of inserted particles of component 2 N_2 as a function of the simulation time (perturbation of the system); Bottom: density of component 2 in the measurement volumes MV_{vap} and MV_{liq} (cf. Figure 9) as a function of the simulation time (response of the system). The dashed lines indicate the equilibrium states at the end of the relaxation (*Eq2*).

4.3 Application of the Simulation Method

4.3.1 Binary Lennard-Jones Mixtures

The non-stationary simulation method is applied to the same LJTS mixtures A and B as in the stationary method introduced in the previous Chapter 3. In short, Mixture A exhibits an asymmetric, wide-boiling phase behavior and its low boiling component is supercritical in the investigated temperature range, while mixture B has essentially an ideal phase behavior in the sense of Raoult's law. For more details on the mixtures and their phase behavior, please refer to Section 3.2.2.

4.3.2 Simulation Details

For the simulations carried out in this chapter, the simulation box had a rectangular shape with a length l_z in z-direction of $l_z = 150\,\sigma$ and a quadratic cross section in x- and y-directions with a side length of $l_y = l_x = 27.85\,\sigma$. The temperature was controlled by the velocity scaling thermostat [35]. The control volume had a length in z-direction of $\Delta z_{\mathrm{CV}} = 10\,\sigma$ and the same quadratic cross section in x- and y-directions as the simulation box. The time step was $\Delta\tau = 0.001\,\sigma(m/\varepsilon)^{1/2}$. The total run time was $\Delta\tau_{\mathrm{Sim}} = 4\,500\,\sigma(m/\varepsilon)^{1/2}$ for all simulations. The durations of the five simulation phases was $\Delta\tau_{\mathrm{IniEq}} = \Delta\tau_{\mathrm{Eq1}} = 500\,\sigma(m/\varepsilon)^{1/2}$, $\Delta\tau_{\mathrm{In}} = 100\,\sigma(m/\varepsilon)^{1/2}$, $\Delta\tau_{\mathrm{Relax}} = 2\,900\,\sigma(m/\varepsilon)^{1/2}$, and $\Delta\tau_{\mathrm{Eq2}} = 500\,\sigma(m/\varepsilon)^{1/2}$. During the *In* phase, 50 MC insertion/removal trials were performed every 40 MD steps within the control volume to prescribe the chemical potential. The vast majority of accepted MC trials were insertion moves, as expected.

Each set of replicas contained 100 simulations. The initial configuration of a set of replicas contained $16\,000$ particles of component 1. Observables χ of bins at the same position n and time τ of each simulation in a set of replicas were arithmetically averaged and the uncertainty in each observable χ of a set of replicas was computed with the single standard deviation. Observables χ sampled in each bin were averaged at each $\Delta\tau = 10\,\sigma(m/\varepsilon)^{1/2}$ time interval. Each bin had a length in z-direction of $\Delta z_{\mathrm{bin}} = 0.125\,\sigma$ and the same quadratic cross section in x- and y-directions as the simulation box. Overall, the simulation box was discretized in the z-direction into $1\,200$ bins. The rectangular measurement volumes $\mathrm{MV}_{\mathrm{liq}}$ and $\mathrm{MV}_{\mathrm{vap}}$ had a length in z-direction of $\Delta z_{\mathrm{MV}} = 1\,\sigma$ and had a quadratic cross section with the same side length as the simulation box in the x- and y-direction. The two measurement volumes were positioned at a distance of $\Delta z_{\mathrm{off}} = 7\,\sigma$ from the characteristic interface positions z_{10} and z_{90} (cf. Eq. (14) and Figure 9), respectively. The molar fluxes in and out of the measurement volumes were sampled at the boundaries of the measurement volume in positive and negative z-direction. In the

further course of this chapter for each measurement volume, only the molar flux at the boundary closest to the interface is shown and discussed. The simulations in this chapter were carried out using the open source molecular dynamics code *ls*1 *mardyn* [114].

4.4 Results and Discussion

In this chapter, for each of the two studied mixtures, the same four temperatures were investigated, which yielded 8 sets of replicas, each containing 100 simulations. First, the results for both mixtures for the temperature $T = 0.715\,\varepsilon k_{\mathrm{B}}^{-1}$ are presented and discussed in detail. Next, an overview of the results for other temperatures is discussed, details and the corresponding numerical data are presented in the Appendix B. Table 8 summarizes the main simulation settings and some key simulation results for all studied sets of replicas: the temperature T and the chemical potential $\mu_{2,\mathrm{CV}}$ prescribed in the control volume as input parameters as well as the mean number of particles N_2 inserted in the *In* phase, the vapor pressure of *Eq1* and *Eq2*, and the vapor and liquid phase density of component 2 in the *Eq2* phase.

Table 8: Selected input parameters and results from the NEMD simulations for mixtures A and B carried out in the present chapter. Input: the temperature T in the whole simulation box and the chemical potential $\mu_{2,\mathrm{CV}}$ in the control volume during insertion phase. Results: the number of inserted particles N_2 as well as vapor-liquid equilibrium properties for the initial and the final state: Pressure p and partial density of component 2 ρ_2 in the vapor phase ($''$) and the liquid phase ($'$). The uncertainty is reported in parentheses and refers to the last digits of the value. It was obtained from the standard deviation from the results from the simulations of the set of replicas.

Mixture	T	$\mu_{2,\mathrm{CV}}$	N_2	p''_{Eq1}	p''_{Eq2}	$\rho''_{2,\mathrm{Eq2}}$	$\rho'_{2,\mathrm{Eq2}}$
	$\varepsilon k_{\mathrm{B}}^{-1}$	ε		$\varepsilon\sigma^{-3}$	$\varepsilon\sigma^{-3}$	σ^{-3}	σ^{-3}
A	0.66	-0.55	1 189(43)	0.0030(1)	0.0086(3)	0.0088(4)	0.0106(15)
	0.715	-0.675	1 199(46)	0.0058(2)	0.0122(3)	0.0092(4)	0.0104(11)
	0.77	-0.8	1 195(44)	0.0105(2)	0.0175(4)	0.0094(4)	0.0105(8)
	0.825	-0.9	1 204(45)	0.0173(3)	0.0252(4)	0.0097(5)	0.0103(9)
B	0.66	-0.8	1 194(66)	0.0030(1)	0.0032(1)	0.0007(1)	0.0538(26)
	0.715	-0.9	1 212(64)	0.0059(2)	0.0063(2)	0.0011(1)	0.0519(26)
	0.77	-1.025	1 189(65)	0.0105(2)	0.0111(2)	0.0018(2)	0.0485(26)
	0.825	-1.15	1 184(59)	0.0173(3)	0.0183(4)	0.0026(2)	0.0455(23)

4.4.1 Results for the Temperature $0.715\,\varepsilon k_{\mathrm{B}}^{-1}$

4.4.1.1 Response in the Liquid and the Vapor Phase

Figure 11 presents the results obtained in the replica studies carried out for $T = 0.715\,\varepsilon k_{\mathrm{B}}^{-1}$ with the two mixtures A and B. Besides the mean value obtained from the averaging of the replica results, the standard deviation is also depicted. Results from the sample volumes on the vapor side ($\mathrm{MV_{vap}}$) and the liquid side ($\mathrm{MV_{liq}}$) are shown for three observables: the density of component 2, the flux of component 2, and the pressure.

Let us first discuss the uncertainty of the results. For both mixtures and both measurement volumes, the noise of the results for the density is of the order of 10 % (cf. Figure 11), which is low considering the difficulty of the spatially and temporally resolved measurement of a small quantity. Results of a similar quality were obtained for the pressure in the measurement volume in the vapor phase. In contrast, the uncertainty in the results for the pressure in the measurement volume in the liquid phase is high, which is not astonishing regarding the extreme sensitivity of this property [50, 126]. As the flux of component 2 was not measured directly but derived from the results for the density, no standard deviation is reported. Fast changes in the pressure and the density of component 2, which occur during and shortly after the *In* phase, would not be recognizable as physically meaningful without the averaging procedure of the set of replicas.

In the initial equilibrium state *Eq1*, which is the same for both mixtures, only component 1 is present. Component 2, which is different for mixture A and B, is added only in the insertion phase *In*. Shortly after the beginning of the insertion, the density of component 2 and the pressure in the measurement volume $\mathrm{MV_{vap}}$ increase steeply. There is a short time delay until the first component 2 particles reach the measurement volume $\mathrm{MV_{vap}}$. As a consequence, the molar flux of component 2 j_2 in the measurement volume $\mathrm{MV_{vap}}$ also rises steeply in both simulations. All observables shown in Figure 11 peak shortly after the insertion phase has ended.

The following relaxation to the second equilibrium state *Eq2* is different for mixture A and mixture B, which is partially a consequence of the differences in the equilibrium state *Eq2* for the two mixtures. The solubility of light-boiling component 2 in the liquid component 1 is significantly lower for mixture A than for mixture B [103, 104]. This is caused by the lower value of ε_2 (causing a higher volatility of component 2) as well as by the lower value of ξ_{12} (less favorable mixed dispersive interactions) in mixture A. As a consequence, the final values of the density ρ_2 in the liquid phase are much lower for mixture A than for mixture B (cf. Figure 11 (b)) and vice versa for the vapor phase (cf. Figure 11 (a)). The larger amount of component 2 in the vapor
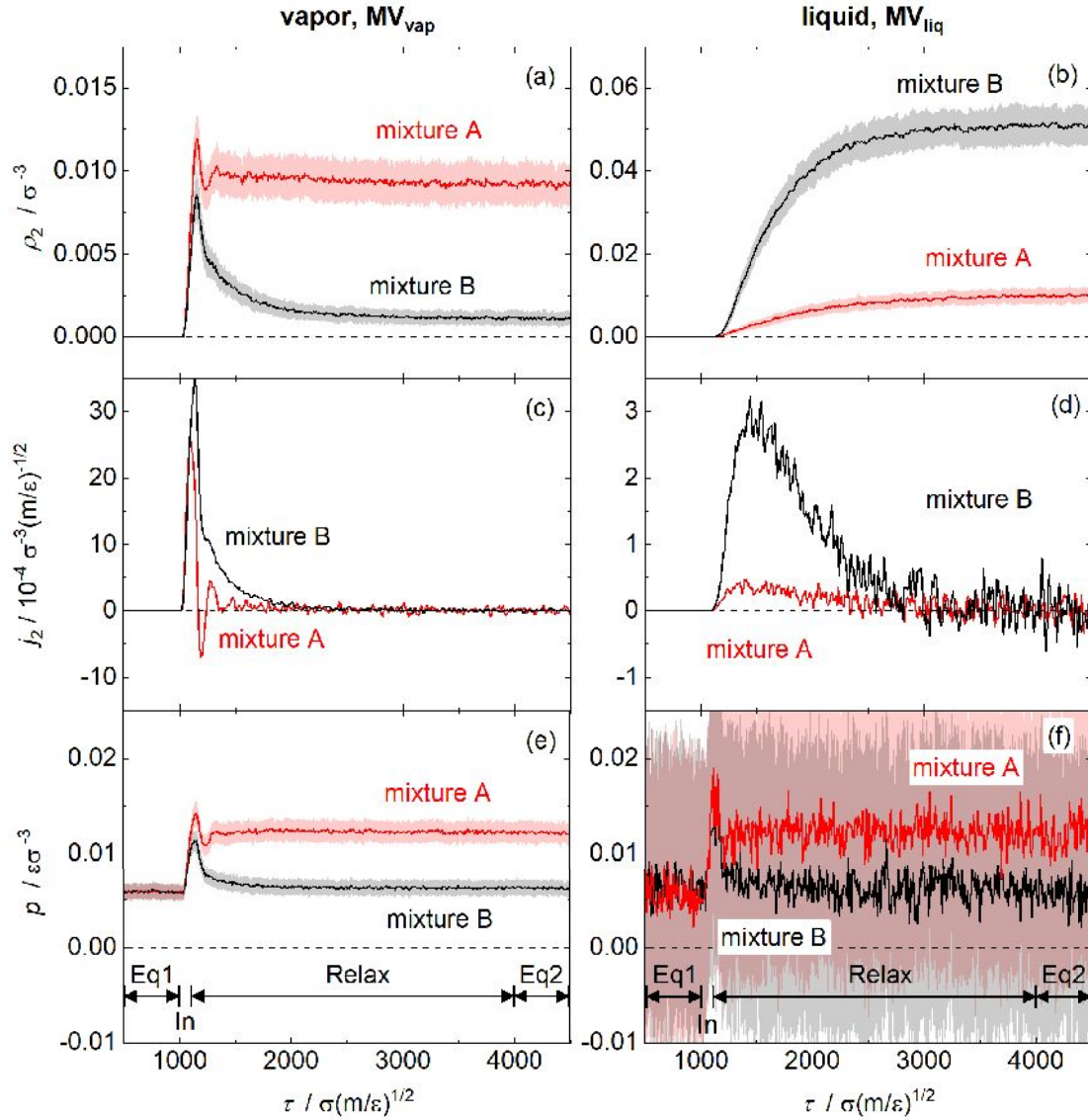
Figure 11: Observables sampled in the replica NEMD simulations in the measurement volumes in the vapor phase MV_{vap} (left) and in the liquid phase MV_{liq} (right), respectively, as a function of the simulation time: density of component 2 ρ_2, flux of component 2 j_2, and pressure p. The temperature was $T = 0.715\,\varepsilon k_B^{-1}$. Results for mixtures A are indicated in red; results for mixtures B in black. Solid lines indicate the mean value obtained from the set of replicas, the shaded area indicates standard deviation. The standard deviation is only given for the two properties that were sampled directly (ρ_2 and p); j_2 was calculated from ρ_2.

phase also causes the higher pressure observed for mixture A in the final equilibrium state *Eq2* (cf. Figure 11 (e) and (f)). As expected, the pressure is the same in both measurement volumes. The lower solubility of component 2 in mixture A also explains why the integral under the molar flux of component 2 in the measurement volume in the liquid phase MV_{liq} shown in Figure 11 (d) is much smaller than the corresponding integral for mixture B. The time constant of the relaxation process is of the same order

of magnitude for both studied mixtures. The relaxation for mixture B is slightly slower, which is attributed to the fact that more of component 2 has to be transferred into the liquid phase before the new equilibrium state is reached. The time-dependent changes in the pressure are basically a consequence of the mass transfer, as the mechanical equilibrium is established very fast.

As explained above, there is a maximum in all observables shown in Figure 11 in the vapor phase measurement volume MV_{vap} that is reached shortly after the end of the insertion phase *In* (cf. Figure 11 (a),(c),(e)). After passing through that maximum, for mixture B, all observables simply decay to their values in the second equilibrium state *Eq2*. At about $\tau = 1\,200\,\sigma(m/\varepsilon)^{1/2}$, a slight change in the way the decay takes places is noticeable, which is visible as a small hump in the signal for j_2 (cf. Figure 11 (c)).

The corresponding findings for mixture A are completely unexpected: after having passed the maximum, the density ρ_2 measured in MV_{vap} for mixture A first decreases and then rises again to approach its value in the equilibrium state *Eq2* (cf. Figure 11 (a)). This oscillating behavior translates into a net flux of component 2 that is first directed towards the vapor-liquid interface ($j_2 > 0$) but then, for a short period in time, goes in the reverse direction ($j_2 < 0$) to then turn back to the expected direction again ($j_2 > 0$) (Figure 11 (c)). The negative flux of j_2 can be interpreted as a reflection of particles of component 2 at the vapor-liquid interface, i.e., an important part of the particles of component 2 reaching the interface cannot enter the liquid phase. This is related to several effects: first, the low solubility of component 2 in the liquid phase of mixture A, which obviously hinders the uptake of component 2 by the liquid phase, and, second, the enrichment that builds up in the interfacial region in mixture A, as will be discussed below in more detail. The low affinity of the liquid phase for component 2 in mixture A is a consequence of the choice of the molecular parameters (low values of ε_2 and ξ_{12} for mixture A). In the discussion of the decay of the signals for mixture B, a slight change is observed at about $\tau = 1\,200\,\sigma(m/\varepsilon)^{1/2}$. This could be due to an effect similar to the one observed for mixture A, which, however, is much milder for mixture B, as the solubility of component 2 in the liquid phase is much better for that mixture.

The fact that particles can be repelled from a vapor-liquid interface has been reported by Garret et al. [96], who considered, however, equilibrium conditions in which they tracked individual particles (e.g., OH and O_3 radicals at water-air interfaces [127, 128]). To the best of the author's knowledge, this effect has never before been observed in mass transfer studies. Due to the symmetry of the overall simulation scenario, the repelled particles are once again repelled at the symmetry plane in the middle of the vapor phase, which could explain the small oscillations that were observed mainly in the signal for the flux j_2 in the vapor phase measurement volume MV_{vap} (cf. Figure 11 (c)).

Figure 12 shows the transient response in the pressure-composition diagram at $T =$

$0.715\,\varepsilon k_{\mathrm{B}}^{-1}$ for both studied mixtures.
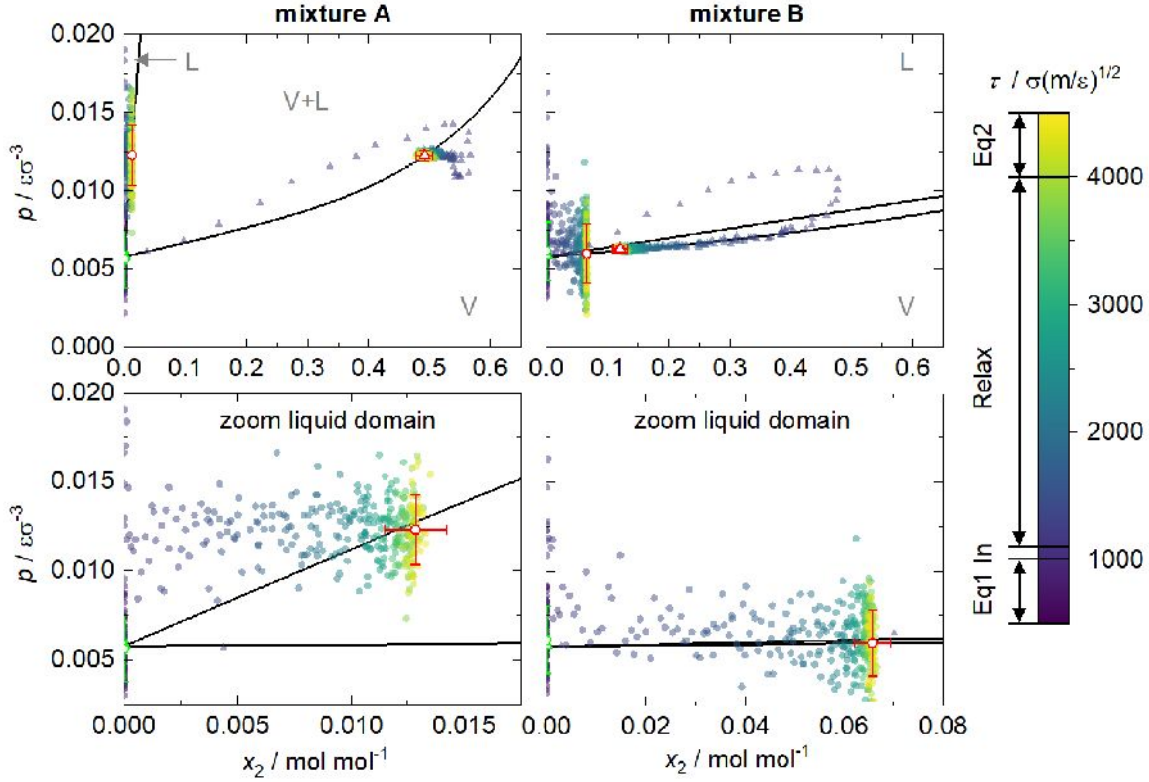
Figure 12: Pressure-composition diagram at $T = 0.715\,\varepsilon k_{\mathrm{B}}^{-1}$ for mixtures A (left) and
mixtures B (right). Circles indicate state points sampled in the measurement volume MV_{liq}; triangles indicate state points sampled in the measurement volume MV_{vap}. The bottom plots give a detailed view on the state points sampled in the liquid phase. The color scale indicates the simulation time. Each data point represents the mean value obtained from a set of replicas at a given simulation time τ. The white filled symbols indicate pressure and composition in *Eq1* (green) and in *Eq2* (red) phases. The error bars are the standard deviation obtained from a set of replicas. The black line indicates the phase equilibrium computed with the PeTS EOS [14, 112].

The pressure sampled in the liquid and vapor measurement volumes is shown as a function of composition x_2 and time τ. The liquid and vapor phase state points of both *Eq1* (before the insertion) and *Eq2* (after the insertion and relaxation) have the same pressure, as expected in a vapor-liquid equilibrium. The *Eq1* and *Eq2* points of the vapor and liquid domain agree well with the dew and bubble lines calculated with the PeTS EOS [14, 112]. The pressure sampled in the liquid phase has high noise compared to data from the vapor phase, which is typical for pressure sampled in liquid phases (cf. Figure 11 (e) and (f)).

4.4.1.2 Response at the Vapor-Liquid Interface

Figure 13 shows spatial profiles of the density ρ_2 and the molar flux j_2 of component 2 in the vicinity of the interface and the neighboring bulk phases for both mixtures at $T = 0.715\,\varepsilon k_{\mathrm{B}}^{-1}$.
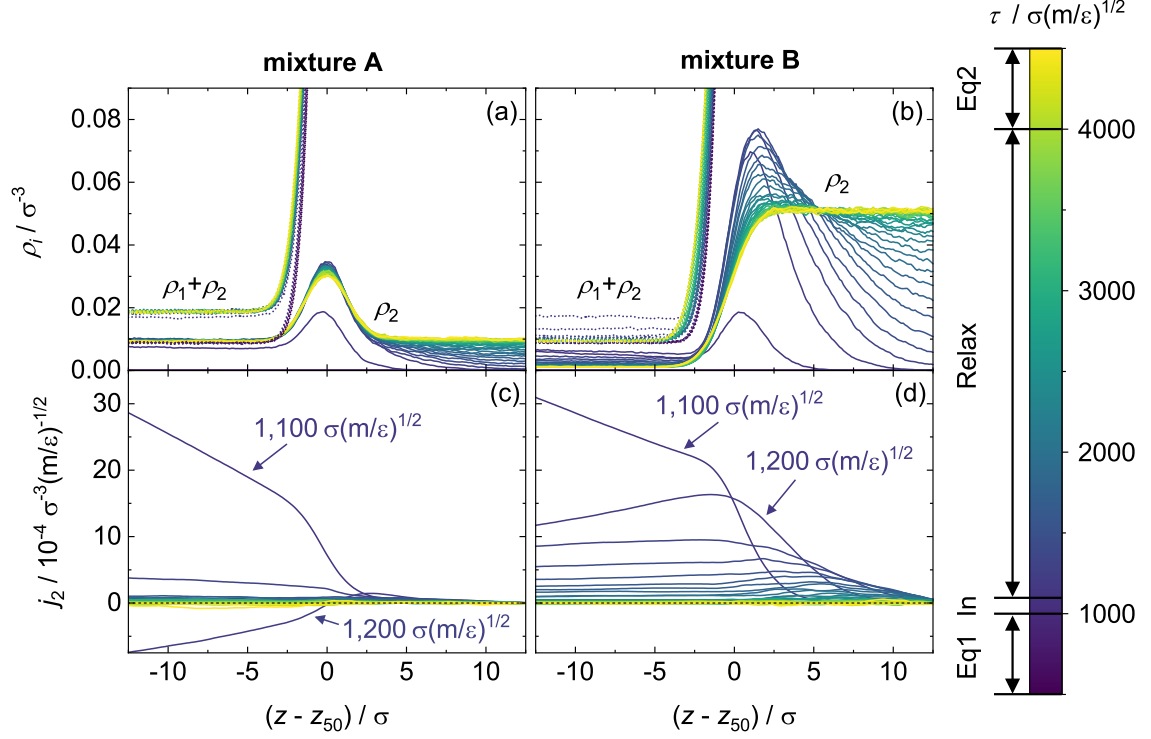
Figure 13: Spatial profiles of the observables sampled in the vicinity of the interface and the neighboring bulk phases for mixture A (left) and mixture B (right). Results for the temperature $T = 0.715\,\varepsilon k_{\mathrm{B}}^{-1}$ from sets of replicas. Top: density of the low-boiling component 2 (—) and total density (·····); Bottom: molar flux of component 2 j_2. The simulation time τ is indicated by the color. The profiles shown were measured at time intervals of $\Delta\tau = 100\,\sigma(m/\varepsilon)^{1/2}$.

The spatial profiles are discretized in time with an interval of $\Delta\tau = 100\,\sigma(m/\varepsilon)^{1/2}$. The measured spatial profiles for each time step were superimposed at the interface position $z_{50}(\tau)$ to decrease the influence from fluctuations of that position. The *In* phase starts at $\tau = 1\,000\,\sigma(m/\varepsilon)^{1/2}$. The profiles measured before this time are essentially identical and represent the initial equilibrium state *Eq1*, in which no component 2 is present.

First, the results for mixture B are discussed. For that mixture, a temporary density peak of component 2 builds up in the interfacial region (cf. Figure 13 (b)). Within the interfacial region, which is basically determined here by density profiles of component 1, this peak is shifted towards the liquid side of the interface. At about $\tau = 1\,400\,\sigma(m/\varepsilon)^{1/2}$, this temporary density peak reaches its maximum height and then decays and finally vanishes in the equilibrium density profile of component 2 for the equilibrium state *Eq2*,

which shows no extrema.

The temporary density peak of component 2 at the interface for mixture B can be interpreted as a kind of jamming. The insertion of the particles of component 2 creates an important flux j_2 in the vapor phase that is directed toward the interface. There is only little friction in the vapor phase, so the particles of component 2 reach the interface with a high directed velocity. At the interface, they are slowed down by the particles in the liquid. The transport of component 2 in the liquid phase is diffusion-controlled and slower than the vapor phase transport. This leads to a temporary accumulation of component 2 near the interface, which, however, vanishes as the overall transport goes to zero upon approaching the equilibrium state *Eq2*.

For mixture B, the molar flux j_2 is positive at all times and at all locations as expected (the flux is always directed from the vapor phase to the liquid phase). However, the flux is far from being uniform in the volume shown in Figure 13, which extends by $10\,\sigma$ to both sides of the vapor-liquid interface. The flux j_2 measured on the vapor side shortly after the insertion is very large but decays quickly ($\tau < 500\,\sigma(m/\varepsilon)^{1/2}$) by almost an order of magnitude of the process. The further decay to zero is slower.

In interpreting the j_2-flux curves, it has to be considered that a negative slope in the profile shown in Figure 13 indicates that component 2 accumulates over time in the considered bin, a constant profile indicates a steady state, and a positive slope indicates depletion. In general, as expected, depletion is observed on the vapor side and accumulation on the liquid side (disregarding the details related to the build-up and vanishing of the density peak discussed above). The exception is the profile measured at $\tau = 1\,100\,\sigma(m/\varepsilon)^{1/2}$ on the vapor side where accumulation is observed because the insertion phase just stopped.

Also for mixture A, a peak builds up in the concentration profile of component 2 near the interface shortly after the insertion phase *In* is finished. But this peak in mixture A is of different nature than the one in mixture B – it does not vanish and also persists in the equilibrium state *Eq2*. The peak observed in mixture A is caused by the well-known enrichment of light-boiling components at vapor-liquid equilibrium interfaces [5–18], which is known to be important for mixture A but not for mixture B [14, 52]. In mixture A, the enrichment peak builds up very quickly (in about $200\,\sigma(m/\varepsilon)^{1/2}$) and then undergoes only minor changes during the rest of the process (it diminishes slightly, but the difference between the maximal height and the end height are only on the order of 10 %). In contrast to the peak observed in mixture B, the enrichment peak in mixture A is almost symmetric with respect to the interface, which confirms previous findings [52].

The flux j_2 measured in mixture A shortly after the end of the insertion phase *In* (at

$\tau = 1\,100\,\sigma(m/\varepsilon)^{1/2}$) is similar to that measured in mixture B, which is not unexpected, as the disturbance is then still limited largely to the vapor phase. However, for longer times, major differences occur. First, the flux j_2 is much lower for mixture A than for mixture B, which can be interpreted as a consequence of the lower solubility of component 2 in the liquid in mixture A. Furthermore, it can be seen that at $\tau = 1\,200\,\sigma(m/\varepsilon)^{1/2}$ the flux j_2 is reversed in the vapor phase, i.e., there is a net flow of component 2 from the surface back to the vapor. This effect has already been discussed above and is interpreted as a reflection of particles of component 2 at the interface. It may be associated with the buildup of the interfacial enrichment.

The temporary density peak of mixture B at the interface position might also be caused by a higher solubility due to the increased pressure. The bubble line of mixture B has a flat positive slope (cf. Figure 12 right). Hence, an increase in pressure significantly increases the mole fraction of component 2 in the liquid phase of mixture B in an equilibrium state, i.e., the solubility of component 2 in the liquid phase increases. The pressure in the vapor phase of mixture B is higher than the pressure of the second equilibrium state $Eq2$ up to $\tau = 1\,700\,\sigma(m/\varepsilon)^{1/2}$ (cf. Figure 11 (d)) while the density peak builds up until $\tau = 1\,400\,\sigma(m/\varepsilon)^{1/2}$ (cf. Figure 13 (b)). The temporarily increased pressure raises the solubility of component 2, which in turn increases the molar flux across the interface and causes the temporary density peak. In contrast, the slope of the bubble line of mixture A is positive and very steep (cf. Figure 12 left). An increase in pressure increases the mole fraction of the liquid phase of mixture A only slightly in an equilibrium state. Mixture A shows only a slight temporary increased density at the interface (cf. Figure 13 (a)).

4.4.2 Results for Various Temperatures

The new simulation method was used to study the mass transfer process in mixture A and mixture B not only at the temperature $T = 0.715\,\varepsilon k_{\mathrm{B}}^{-1}$ but also at the temperatures $T = 0.66\,\varepsilon k_{\mathrm{B}}^{-1}$, $0.77\,\varepsilon k_{\mathrm{B}}^{-1}$, and $0.825\,\varepsilon k_{\mathrm{B}}^{-1}$. This is of particular interest since the interfacial properties of the mixtures are known to depend strongly on the temperature [14, 103], e.g., the enrichment of mixture A is known to decrease with increasing temperature.

Figure 14 shows the results for the density of component 2 as a function of time sampled in the measurement volumes in the vapor phase ($\mathrm{MV_{vap}}$, top) and liquid phase ($\mathrm{MV_{liq}}$, bottom) for both mixtures A and B, for all studied temperatures.

In all cases, the change in temperature leads to quantitative changes, but the qualitative behavior is the same for all temperatures, which is not unexpected. Overall, the influence of the temperature on the results is larger for mixture B, mainly as the solubility of
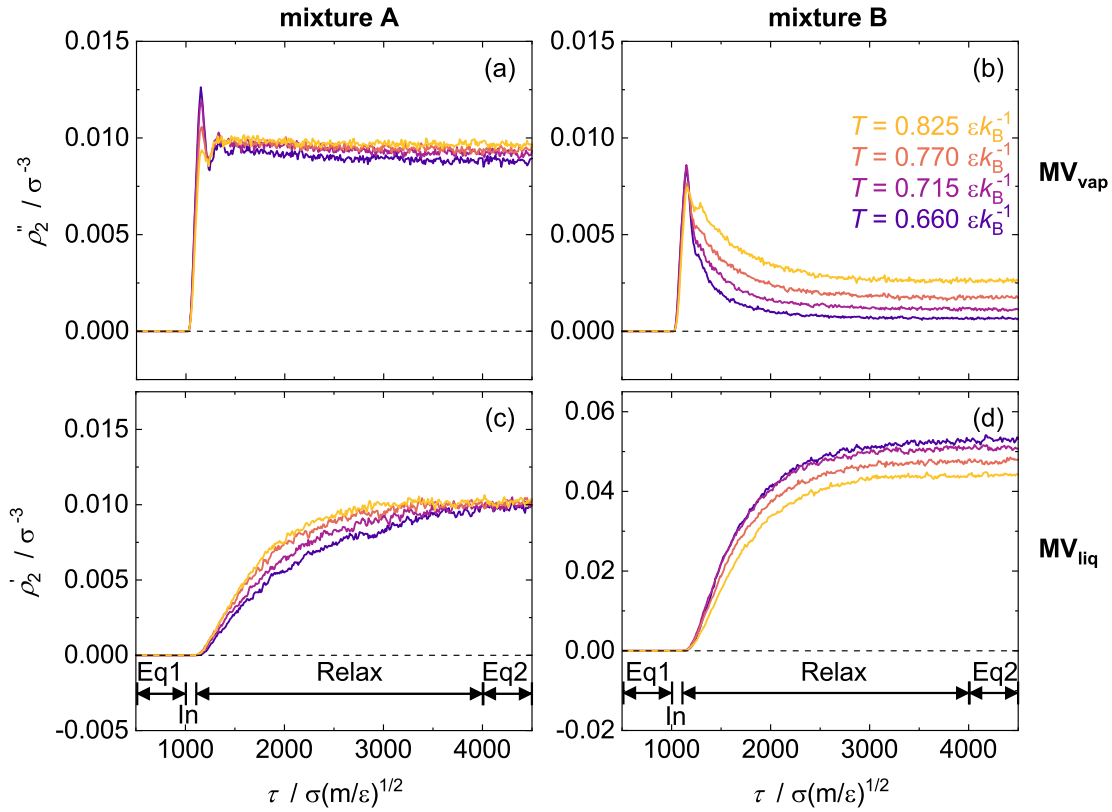
Figure 14: Density of component 2 sampled in the measurement volume in the vapor phase MV_{vap} (top) and in the measurement volume in the liquid phase MV_{liq} (bottom) as a function of the simulation time τ. Results for mixture A (left) and mixture B (right) from replica simulations at different temperatures are shown, which are indicated by color.

component 2 in the liquid depends on temperature for that mixture, whereas it is hardly temperature-dependent for mixture A (cf. Figure 14 (c)).

It is interesting that contrary to the overall trend, the height of the initial peak in the density ρ_2 measured in the vapor phase (MV_{vap}) in mixture A depends strongly on temperature: the peak is large for low temperatures and almost vanishes at the highest studied temperature. Together with the fact that the solubility of component 2 in the liquid phase is hardly temperature-dependent, this is a strong argument for the influence of the enrichment on this peak, namely, as the enrichment is known to be high at low temperatures and vice versa [14, 103]. This argument is further supported by the findings for mixture B for the density ρ_2 in MV_{vap}, where the influence of the temperature on the peak height is quite low, despite the considerable influence of the temperature on the solubility.

Figure 15 shows the flux of component 2 sampled at different positions in the simulation box as a function of time in replica simulations at various temperatures for mixture A (left) and mixture B (right). Results for three positions are reported: the measurement

volume on the vapor side (MV_{vap}), the interfacial plane ($z = z_{50}$), and the measurement volume on the liquid side (MV_{liq}).
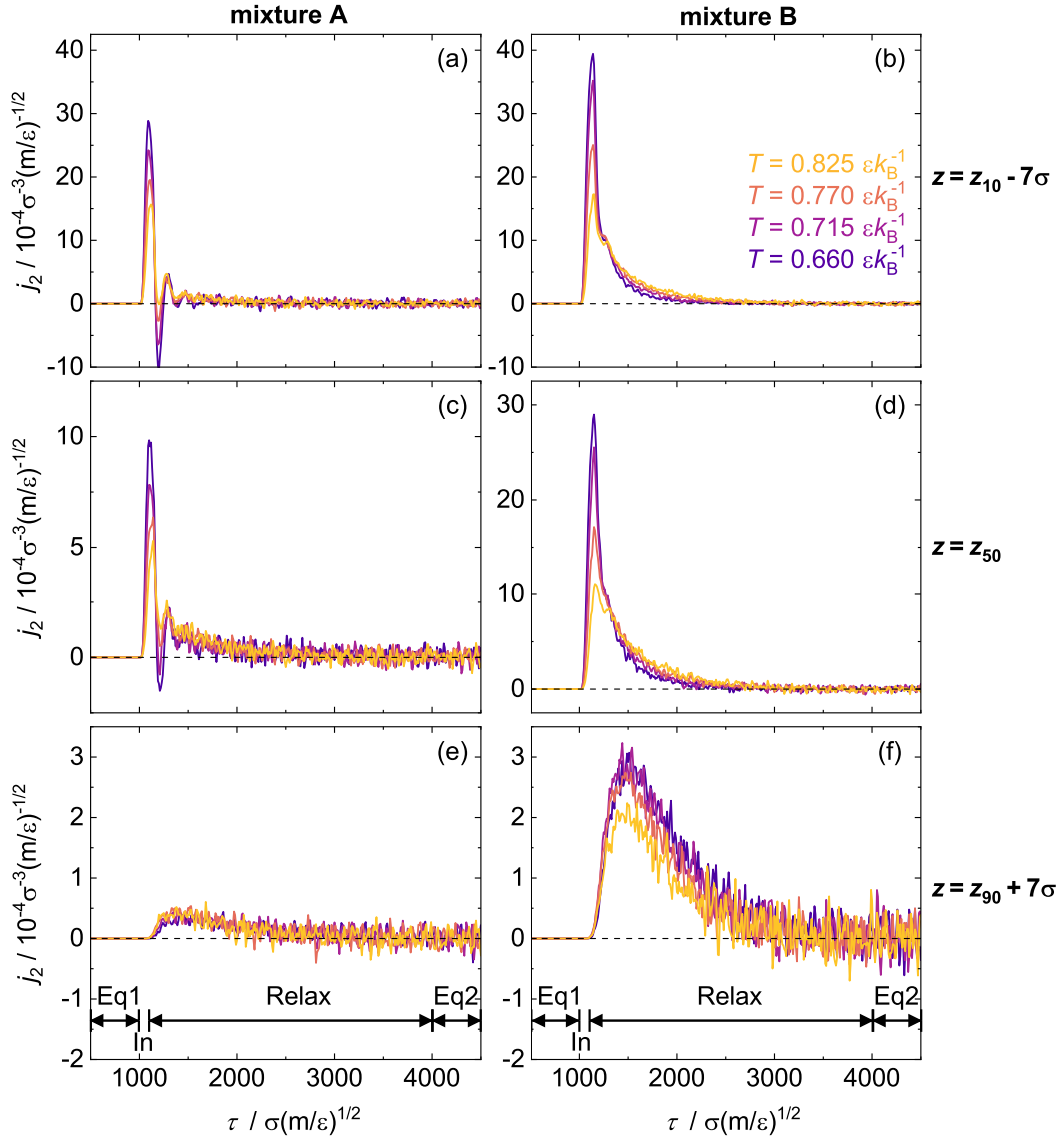
Figure 15: Molar flux of component 2 sampled at different positions as a function of time in replica simulations at different temperatures for mixture A (left) and mixture B (right). The temperature is represented by the color. Top: measurement volume on the vapor side (MV_{vap}); Middle: interface plane $z = z_{50}$; Bottom: measurement volume on the liquid side (MV_{liq}).

The results confirm that the variation in the temperature leads to quantitative changes, but the qualitative behavior remains the same. Differences in the flux of component 2 caused by a variation of the temperature are mainly limited to the first peak in the flux observed shortly after the insertion phase. In remarkable agreement, in basically all cases shown in Figure 14 the peak is highest for the lowest temperature and its height decreases steadily with increasing temperature. The only exception from this rule is the density signal from the liquid side MV_{liq} for mixture A, which exhibits only a very small

peak.

Additional results for the temperature dependency of the transient response are given in the Appendix B.

4.5 Conclusions

A non-stationary molecular dynamics simulation method is introduced for studying mass transfer through vapor-liquid interfaces. The mass transfer of a certain component through the interface is driven by a concentration gradient of the respective component that is initially built up and then the system relaxes in a new equilibrium state. During that relaxation process, the mass transfer through the vapor-liquid interface is examined in detail. The statistics of the sampling of the observables are amplified by studying sets of simulation replicas, which differ only in their initial velocity distribution.

In the proposed simulation method, particles of component 2 are inserted over a short period of time in the middle of the vapor phase of an equilibrated vapor-liquid system containing only particles of component 1. After the insertion phase, the system is re-equilibrated. During this relaxation phase, the inserted particles move from the vapor phase through the vapor-liquid interface and enter the liquid phase. Over the whole simulation run, profiles of the density, composition, and molar flux of each component as well as the pressure are sampled.

The simulation method was tested on binary mixtures of simple fluids. Two binary LJTS mixtures with the same high-boiling component and different low-boiling components were investigated. Both mixtures exhibit distinctly different phase behaviors and interfacial properties, such as the enrichment [14, 103], while having a comparable bulk diffusivity [26]. Mixture A shows a high enrichment, while mixture B shows none. The number of inserted particles is chosen to be the same for the two studied mixtures. Even though both mixtures have similar bulk phase diffusivities, the results from both mixtures from the new simulation method are distinctly different, which can be attributed to differences in the interfacial properties. The behavior of the molar flux across the interface deviates significantly between the two studied mixtures: For mixture A, an important part of the particles is repelled at the interface. The repulsion of particles at the interface causes a temporarily negative net flux back into the vapor phase. For mixture B, on the other hand, a temporary density peak is observed at the beginning of the relaxation process on the liquid side of the interface. This temporary accumulation of component 2 particles at the interface is caused by jamming due to a lower transport resistance at the interface and in the liquid bulk phase compared to that in vapor bulk phase. The different behavior of mixture A and B is attributed to three facts: (i) the

mass transfer process is governed by the bulk properties of the second equilibrium state, which in turn is dependent on the number of inserted particles and of course the mixture; (ii) a significant amount of particles of component 2 is repelled at the interface in the case of mixture A; (iii) the enrichment acts as a mass transfer resistance. However, the significance of the last two phenomena has to be evaluated in further studies.

5 Explosions of Nanodroplets Studied with Molecular Simulations

5.1 Introduction

In the field of fuel combustion, the evaporation and combustion of droplets has been studied extensively with continuum models that consider the coupled mass and heat transfer inside the droplet. Also the reason for the occurrence of droplet explosions has been investigated with this approach: in many fuel mixtures, heat conduction is much faster than mass diffusion, leading to a superheated state inside the droplet, which will eventually give rise to vapor nucleation [129–132]. Similar investigations for the field of spray flame synthesis have been carried out only recently [133], reaching a similar conclusion. A challenge in these simulations is that the results depend strongly on the properties of the studied mixtures, and that for may practical applications, the relevant properties are not known. A notable exception are some of the mixtures in spray flame synthesis, for which a good data basis has been established [134–138] and used in a recent study [133], confirming that the superheating of the droplets must be expected. However, in none of these studies, the actual explosion of the droplet induced by the sudden formation of the gas phase has been studied.

Therefore, in the present chapter, the explosions of superheated nanoscale droplets were studied by molecular dynamics simulations. Only pure fluids were studied, the superheating was induced by thermostatization of the droplet's center, using a temperature gradient that was large enough to observe the entire explosion of evaporation process induced by the heating in a reasonable simulation time. The Lennard-Jones truncated and shifted potential was used to describe the intermolecular interactions. For investigating the reproducibility of the obtained results, the series of simulations was carried out twice, using the two independent open-source MD codes *LAMMPS*[139] and *ls1 mardyn* [114].

5.2 Molecular Simulation

5.2.1 Simulation Scenario

A schematic depiction of the simulation scenario is shown in Figure 16.
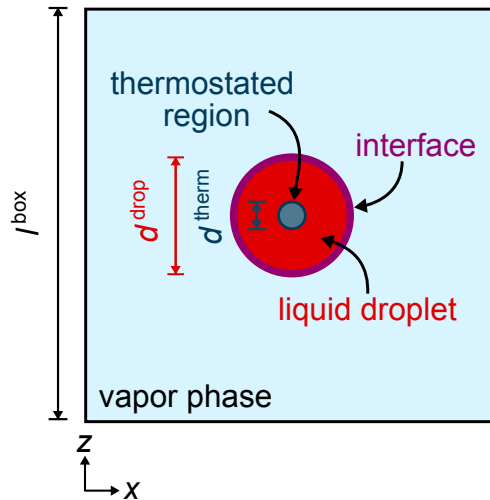
Figure 16: Scheme of the simulation scenario used in this chapter at the beginning of
the production run: the outer black square represents the cubic simulation
box with periodic boundary conditions; the red circle represents the liquid
droplet, which is surrounded by a vapor phase colored in light blue. The two
regions are separated by the vapor-liquid interfacial region colored in purple.
The small dark blue circle in the droplet center shows the thermostated
region in which the temperature is increased after the equilibration of the
system.

The simulation scenario consists of a liquid droplet in the center of a cubic simulation box
surrounded by a vapor phase. Periodic boundary conditions are applied in all Cartesian
directions. First, the system is equilibrated in the NVT ensemble at $T = 0.825\,\varepsilon k_{\mathrm{B}}^{-1}$.
This part of the simulation is referred to as the "equilibration". In the equilibration,
the temperature was held constant in the entire simulation box using a Nosé-Hoover
thermostat [140, 141], which is well-suited for heterogeneous systems. The initial values
of the liquid and vapor density were determined with the PeTS equation of state [112].
During the whole simulation, the center of mass of the system was aligned with the
center of the simulation box to keep the droplet centered.

After the equilibration, the Nosé-Hoover thermostat controlling the whole simulation
box was turned off and a velocity-scaling thermostat [35] was applied to a spherical
region in the middle of the simulation box and, hence, the center of the droplet. That
thermostat was used to impose a set temperature T^{set} that was higher than the tempe-
rature $T = 0.825\,\varepsilon k_{\mathrm{B}}^{-1}$ in the equilibrated system (cf. Figure 16). The thermostat was

active over the whole production run. The system response was studied for six values of the set temperature $T^{\text{set}} = (1, 1.5, 2, 3, 4, 5)\,\varepsilon k_{\text{B}}^{-1}$. The time step at which the equilibration is completed and the velocity-scaling thermostat is activated is denoted as the "reduced simulation time" $\tau = 0$ and the simulation for $\tau > 0$ is called the "production run". The production runs of all simulations started from the same equilibrated system, i.e., the equilibration run was carried out only once.

5.2.2 Technical Simulation Details

Results shown in the main body of this chapter were obtained from MD simulations with the open source tool *LAMMPS* [139]. Additionally, all simulations were reproduced with the open source tool *ls*1 *mardyn* [114]. The results obtained with both programs agree reasonably well. The *ls*1 *mardyn* results are presented in the Appendix C and compared to those from *LAMMPS*.

The number of time steps in the equilibration run was 5 000 000, that in the production run was 3 000 000. The damping time of the Nosé-Hoover thermostat was 100 time steps, as recommended in the *LAMMPS* documentation [139]. The equations of motion were integrated using the velocity-Verlet scheme [35, 142] with a time step of $0.0005\,\sigma(m/\varepsilon)^{1/2}$. The cubic simulation box had a side length of $l^{\text{box}} = 150\,\sigma$. The system contained 134 425 particles. At the end of the equilibration phase, the droplet had a diameter of $d^{\text{drop}} = 49.06(2)\,\sigma$, corresponding to about 18 % of the box volume. Details on the determination of the droplet radius are given in Section 5.2.3. The thermostated region inside the droplet had a diameter of $d^{\text{therm}} = 18\,\sigma$, corresponding to about 5 % of the droplet volume and about 0.1 % of the overall box volume. The change of the kinetic energy, which is interpreted as the heat supplied to the simulation box, as well as the average number of thermostated particles was written to disk every 100 time steps. The center of mass of the simulation box was aligned with the center of mass of the system every 1 000 time steps. The configuration of the particles was written to disk every 2 000 time steps. The majority of the results of this chapter stem from these configurations and the post-processing of the data is explained in detail in the following section.

5.2.3 Data Processing

During the production run, the simulation box contains a droplet (or fragments after its break-up), potentially a gas bubble inside the liquid, as well as a surrounding vapor phase. Furthermore, there are vapor-liquid interfacial regions. In order to evaluate the shape of the liquid fragments and the vapor bubbles, particles are assigned to be part of a liquid region, a vapor region, or an interfacial region. This is achieved by using (i)

Delaunay triangulation [143] in conjunction with (ii) the alpha shape method [144] as explained in the following.

In short, the Delaunay triangulation (i) works as follows: a group of four particles are connected to a tetrahedron if the sphere that is uniquely defined by their Cartesian coordinates does not contain any further particles. The vertices of the tetrahedra are assigned to the particle positions. In this evaluation, the periodic boundary conditions are considered, i.e., edges of the tetrahedra can "cross" the boundary. The resulting grid of tetrahedra is a unique, space-filling tessellation of the entire simulation box. For further details on the Delaunay triangulation, see [143].

During (i), a classification of the particles is carried out using the alpha shape method (ii). As a result of (i), each particle is part of several tetrahedra. If the radius of the sphere used for obtaining a certain tetrahedron is greater than a threshold value – the so-called alpha sphere radius r_α – that tetrahedron is labeled as a "low density region", otherwise, it is labeled as a "high density region". In the present chapter, the alpha sphere radius is set to $1.6\,\sigma$. This value was determined from an independent simulation in which the radial distribution function of the pure saturated LJTS liquid was sampled at $T = 0.825\,\varepsilon k_\mathrm{B}^{-1}$ using the open source tool $ms2$ [114] (further details are given in Appendix C). The value $1.6\,\sigma$ corresponds to the first minimum position of that RDF, i.e., the radius of the first solvation shell around a particle. Then, all particles are classified as follows:

(a) A particle is assigned to a liquid region if all tetrahedra that the particle is part of are labeled as a "high density region".

(b) A particle is assigned to a vapor region if all tetrahedra that the particle is part of are labeled as a "low density region".

(c) A particle is assigned to an interfacial region in all other cases.

Figure 17 shows exemplary snapshots from one simulation run. The snapshots are visualized using the open source tool $OVITO$[145]. Particles are colored with respect to the categorization explained above. In all snapshots shown in this chapter as well as the videos provided in Appendix C, a cross section cut through the center of the simulation box perpendicular to the x-axis is shown, allowing for a look into the droplet.

Furthermore, a droplet (drop) is defined as a cluster of interfacial (IF) and liquid region (liq) particles that are contiguously connected by "high density" tetrahedra (cf. Figure 17). The number of particles in a droplet N^drop is therefore defined as

$$N^\mathrm{drop} = N^\mathrm{liq} + N^\mathrm{IF} \; . \tag{16}$$
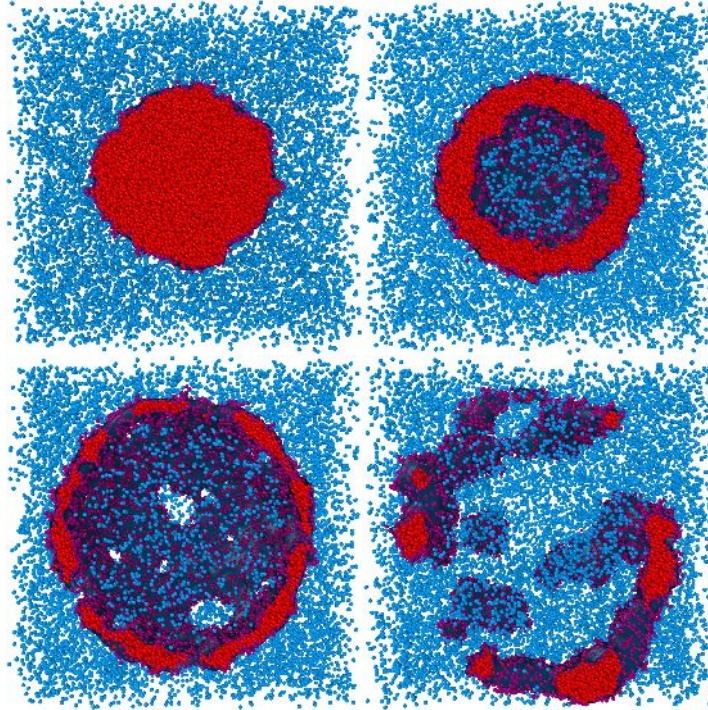
Figure 17: Snapshots of a time sequence of the droplet break-up at the highest investigated set temperature in the droplet center. Top left panel: equilibrium state. Top right panel: the emerging bubble after activating the thermostat in the center. Bottom left panel: the maximum expansion of the liquid film. Bottom right panel: break-up of the droplet. The snapshots show cross-sections through the center of the simulation box, so that the inside of the droplet can be observed. Particle colors: liquid (red), vapor (blue), and interfacial region (purple) (cf. Section 5.2.3). The dark blue area represents the interfacial region and was obtained from adjusting and smoothing a mesh to the positions of the interfacial particles.

Only droplets containing at least 100 particles were considered as droplets to distinguish between local density fluctuations in the vapor phase and fragments of the liquid droplet after its break-up into smaller droplets (in preliminary investigations, high density particle clusters containing up to 30 particles caused by local density fluctuations were identified in the vapor phase).

For quantifying the structure of theses droplets containing only interfacial and liquid region particles, two measures are used. First, the radius of gyration r_{G} is given by

$$r_{\mathrm{G}} = \sqrt{\frac{1}{N^{\mathrm{drop}}} \sum_{k=1}^{N^{\mathrm{drop}}} (r_k^{\mathrm{drop}})^2} \, , \qquad (17)$$

in which r_k^{drop} is the distance of particle k from the center of mass of the droplet.

Second, an "interface position" r^{IF} is defined, i.e., the average distance of the interface to the center of mass of a droplet. It is obtained from calculating the radial density

$\rho^{\mathrm{IF}}(r^{\mathrm{drop}})$ of the particles assigned to interfacial regions as a function of their distance r^{drop} to the center of mass of the droplet, which is defined as

$$\rho^{\mathrm{IF}}(r^{\mathrm{drop}}) = \frac{\mathrm{d}N^{\mathrm{IF}}(r^{\mathrm{drop}})}{4\pi r^{\mathrm{drop}\,2}\mathrm{d}r^{\mathrm{drop}}} \ . \tag{18}$$

Herein, $N^{\mathrm{IF}}(r^{\mathrm{drop}})$ is the number of "interface" particles found in the spherical shell with the thickness $\mathrm{d}r^{\mathrm{drop}}$ at the distance r^{drop} to the center of mass of the corresponding droplet. Two exemplary radial density profiles are shown in Figure 18.
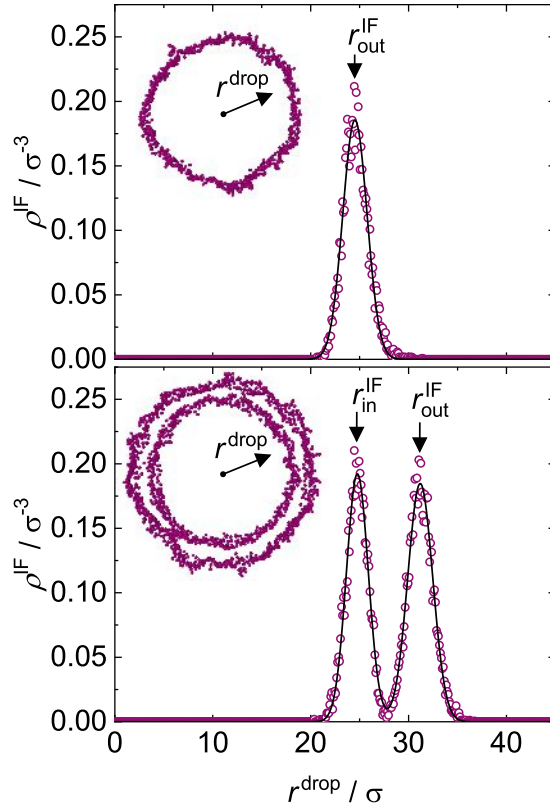
Figure 18: Example of the radial density profile of the interface particles (purple open circles) and the corresponding Gauss model fit (black line). Top panel: equilibrium state with one interface ($\tau = 0$); bottom panel: non-equilibrium state with two interfaces (expanding shell-like droplet, $T^{\mathrm{set}} = 3\,\varepsilon k_{\mathrm{B}}^{-1}$, $\tau = 35\,\sigma(m/\varepsilon)^{1/2}$). Each panel also contains a snapshot showing an exemplary 2D slice through the droplet at the corresponding time step that only contains particles categorized to be part of the interface.

In the top panel, corresponding to an equilibrated droplet surrounded by its vapor, the distribution shows a sharp Gaussian-like peak at the position of the vapor-liquid interface. During the simulations, a vapor bubble nucleates in the inside of the droplet (cf. Figure 17, bottom panels). As a consequence, the corresponding density profile shown in the bottom panel of Figure 18 shows two peaks, representing the inner and outer vapor-liquid interface, respectively. The positions of the interfaces are determined

by fitting a sum of Gaussians, $f_{\mathrm{Gauss}}(r^{\mathrm{drop}})$, to the radial density profile $\rho^{\mathrm{IF}}(r^{\mathrm{drop}})$. The peak positions of the individual Gaussian contributions correspond to the interface positions r^{IF}. The sum of Gaussians is defined as

$$f_{\mathrm{Gauss}}(r^{\mathrm{drop}}) = \sum_{g=1}^{G} a_g \exp\left(-\frac{(r^{\mathrm{drop}} - r_g^{\mathrm{IF}})^2}{2c_g^2} \right), \tag{19}$$

in which a_g is the peak height, r^{IF} is the peak position, and c_g is the standard deviation. The number of Gaussians G is either one or two, depending on the number of interfaces of the droplet. The actual determination of the location of the interfaces and the decision whether there is only one (i.e., a homogeneous spherical droplet, $G = 1$) or two interfaces (i.e., a liquid droplet with a vapor bubble in its center, $G = 2$), is rather technical. Details of the decision procedure are given in Appendix C. The procedure yields the position of the outer interface, denoted $r_{\mathrm{out}}^{\mathrm{IF}}$ in the following, and, if present, that of the inner interface, denoted $r_{\mathrm{in}}^{\mathrm{IF}}$ in the following. The thickness of the liquid film is determined by

$$\Delta r^{\mathrm{IF}} = r_{\mathrm{out}}^{\mathrm{IF}} - r_{\mathrm{in}}^{\mathrm{IF}} \ . \tag{20}$$

5.3 Results and Discussion

5.3.1 Overview of the Droplet Behavior: Three Cases

Videos of the simulations carried out with the proposed scenario are provided in Appendix C and Table 9. The reader is encouraged to first have a look at this video material. Figure 19 shows snapshots of the simulations for all investigated temperatures at different time steps.

Three different cases of the droplet behavior can be distinguished: (i) shrinking droplet, (ii) expanding droplet, and (iii) immediate droplet break-up. An overview of the simulations, the categorization of each simulation into these three cases, and the corresponding video material is given in Table 9.

The first case, the shrinking of the intact droplet, occurred only at the lowest set temperature imposed by the thermostat in the droplet center at $T^{\mathrm{set}} = 1.0\,\varepsilon k_{\mathrm{B}}^{-1}$. The droplet heated up and from time to time, a small vapor bubble formed in its center. However, that bubble quickly collapsed since the interfacial tension of the created vapor-liquid interface inside the droplet worked against the pressure build-up in the bubble and thereby suppressed the growth of the bubble to a size at which it would be stable. As a result, the droplet simply shrunk over time due to evaporation at its surface.

Table 9: Overview of the carried out simulations, the categorization of each simulation into on of the three cases, and the corresponding video files. Video names without a suffix show simulation results in the same fashion as shown in Figures 17 and 19. Videos with the suffix `"*_IF.mp4"` show only the dark blue area adjusted to the interfacial particle positions of the whole droplets. The surface in this footage is transparent so that the processes inside the droplet can be observed. The video with the suffix `"*_Torus.mp4"` show footage specifically of the torus-like droplet. The hyperlinks to the video footage given here are explicitly written out in Table C.1 in Appendix C.

$T^{\text{set}}/\varepsilon k_{\text{B}}^{-1}$	Case categorization	Video files material
1.0	(i) Shrinking droplet	`T10.mp4`, `T10_IF.mp4`
1.5	(ii) Expanding droplet	`T15.mp4`, `T15_IF.mp4`, `T15_Torus.mp4`
2.0		`T20.mp4`, `T20_IF.mp4`
3.0		`T30.mp4`, `T30_IF.mp4`
4.0	(iii) Immediate droplet break-up	`T40.mp4`, `T40_IF.mp4`
5.0		`T50.mp4`, `T50_IF.mp4`

In the second case, the formation of an expanding spherical liquid shell was observed: a vapor bubble nucleates in the center of the droplet, which was surrounded by a thick shell-like liquid film, which expanded as the bubble grows. Over time, due to the expansion of the shell and evaporation, the thickness of the shell decreased and it finally broke up. This case was observed for $T^{\text{set}} = 1.5$ to $3.0\,\varepsilon k_{\text{B}}^{-1}$. As expected, at the higher T^{set} the vapor bubble grew faster and, as a result, also the shell expanded faster. An unexpected behavior was observed: the expansion did not occur monotonously, but in an oscillating way. This can be seen best in the videos in Table 9. The reason for this oscillating behavior must be the interfacial tension that compresses the bubble, but, in contrast to the first case, it is not strong enough to cause the complete collapse of the bubble. Eventually, after several expansion/compression cycles, the bubble tore a hole through the liquid film, leading to a break-up of the droplet. For case (ii), the break-up process of the liquid shell after it tore open showed two variants depending on the set temperature: at high temperatures, the shell simply broke up into smaller droplets, while at low temperatures, the liquid shell formed two holes on opposite sites and formed a temporarily stable torus-like shape, which decayed over time. Interestingly, as seen for $T = 3.0\,\varepsilon k_{\text{B}}^{-1}$ in the middle column of Figure 19, the liquid film can even form tiny holes that "heal" after some time due to the contraction of the liquid film and the action of the surface tension.
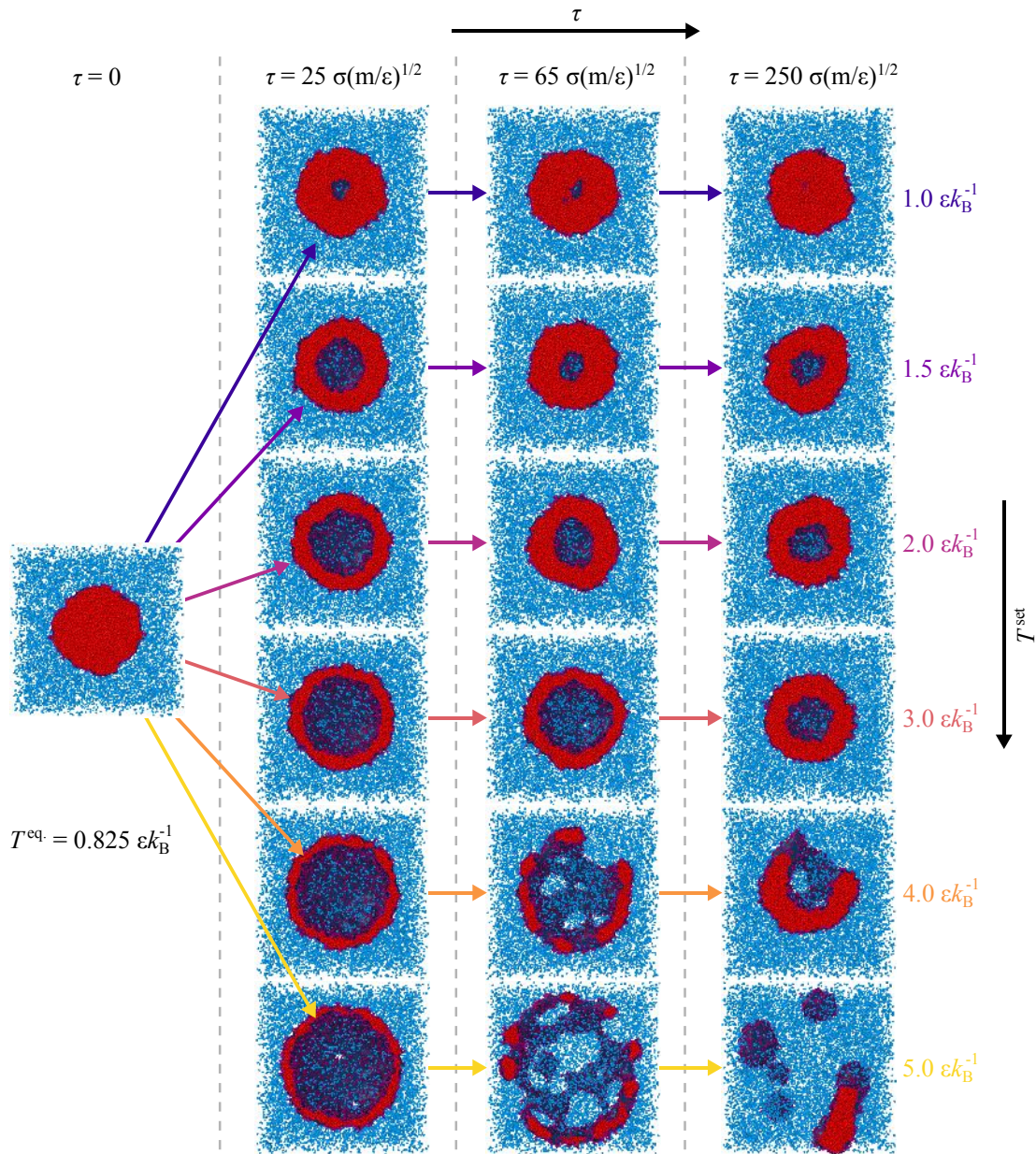
Figure 19: Snapshots from the simulations with different set temperatures at the same three time steps during the production run. The snapshots show cross-sections through the center of the simulation box, so that the inside of the droplet can be observed. Particle colors: liquid (red), vapor (blue), and interfacial region (purple) (cf. Section 5.2.3). The dark blue area represents the interfacial region.

In the third case, the immediate droplet break-up, which occurred at the highest investigated set temperatures $T^{\text{set}} = 4.0$ and $5.0\,\varepsilon k_{\text{B}}^{-1}$, the vapor bubble inside of the droplet grew so quickly that it directly broke the liquid film into smaller droplets.

5.3.2 Number of Particles and Radius of Gyration of the Droplet

In the following, the results for two observables as a function of time are discussed in detail: the number of particles of a droplet N^{drop} and the radius of gyration r_{G}. Figure 20 shows the number of particles in the largest droplet and the corresponding radius of gyration of that droplet as a function of time.
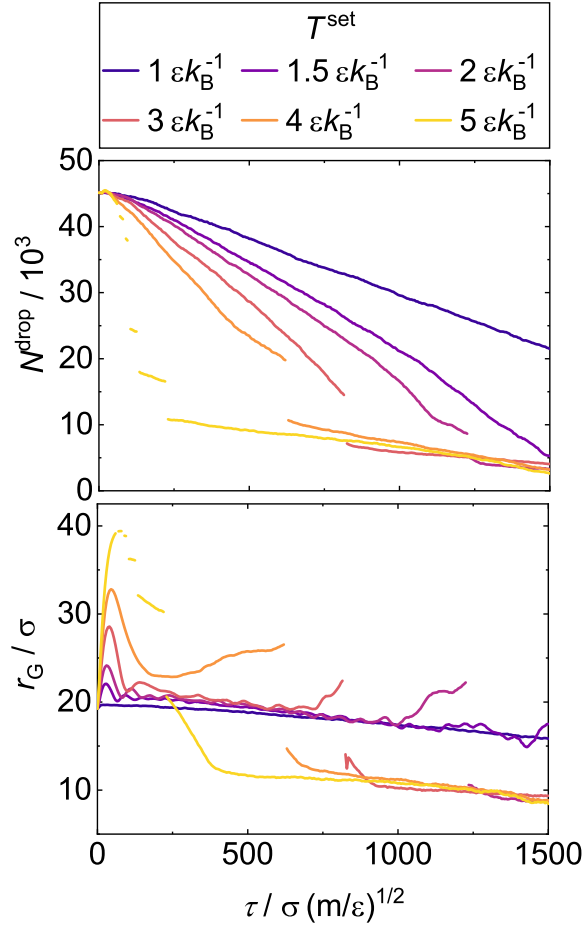
Figure 20: Number of particles (top panel) and the radius of gyration (bottom panel) of the largest droplet as a function of time for different set temperatures. The discontinuities in the curves are related to a break-up of the studied droplet; the curve after the jump is that for the largest remaining droplet after the break-up.

Overall, as expected, the number of particles in the droplet (cf. Figure 20, top panel) decreases faster with increasing set temperature T^{set}, since more heat is supplied to the simulation box, leading to a faster evaporation. At the lowest set temperature, the number of particles remains constant at first and then, after a delay of about $100\,\sigma(m/\varepsilon)^{1/2}$, it decreases nearly linearly. With increasing set temperature, the linear decay becomes faster. When the droplet breaks into smaller droplets, the line that refers only to the

largest droplet shows a discontinuity. For the higher temperatures, several of these break-ups are observed. The size of the new droplets that are formed in the break-up also decays linearly. The following line shows the number of particles of the next largest droplet after the break-up. The break-up into several smaller droplet is most prominent at the highest set temperature (cf. Figure 19, bottom panel). Interestingly, for all studied values of T^{set}, the largest droplet that was observed after the break-up has a similar size, only the time when the curve jumps to the curve of this evaporating droplet differs (cf. Figure 20).

The corresponding results for the radius of gyration are shown in the bottom panel of Figure 20. For the lowest set temperature $T^{\text{set}} = 1.0\,\varepsilon k_{\text{B}}^{-1}$, the radius of gyration decreases basically linearly due to the evaporation. There is a minor increase in the radius of gyration at the beginning of the heating, which is due to thermal expansion of the liquid. For the higher set temperatures, a more complex behavior is observed: first, there is a strong increase in the radius of gyration caused by the formation of a bubble inside the droplet. This is followed by a decrease, which is a result of the interfacial tension, which counteracts the expansion driven by the heating and the evaporation. In the curves for the set temperatures $T^{\text{set}} = 1.5$ to $3.0\,\varepsilon k_{\text{B}}^{-1}$, oscillations occur, which are caused by the interplay of these two effects. The thermostat in the center of the droplet is active over the whole simulation and, after the first nucleation of the vapor bubble, the density of the thermostated region is permanently low, i.e., vapor-like (cf. Appendix C). For a while, the oscillations occur around a trend of decreasing radius of gyration, in which the decline is similar to that observed for the simple droplet evaporation at $T^{\text{set}} = 1.0\,\varepsilon k_{\text{B}}^{-1}$. However, after a certain period of time, the expanding forces start to prevail and the radius of gyration increases again, before a break-up of the spherical shell is observed - except for the results for $T^{\text{set}} = 1.5\,\varepsilon k_{\text{B}}^{-1}$.

This simulation also has the peculiarity that the liquid film did not keep the form of a spherical liquid shell until it broke into parts, as in the other simulations. Rather, a transition from the spherical shell to a torus was observed, which is not evident from the results shown in Figure 20 but clearly visible in the videos presented in Appendix C. At $\tau = 950\,\sigma(m/\varepsilon)^{1/2}$, a first hole punctures the liquid film. This hole grows until $\tau = 1\,280\,\sigma(m/\varepsilon)^{1/2}$, forming a bowl-like shape. Then, a second hole emerges on the opposite site of the first hole and, consequently, the liquid has a torus-like shape. The torus constricts at $\tau = 1\,400\,\sigma(m/\varepsilon)^{1/2}$, forming an elongated, sausage-like object, with constrictions that stayed intact until the end of the simulation. It can be speculated that that object would either have separated into smaller droplets at the constriction, or it would have contracted to a sphere under the influence of the surface tension. The formation of the torus was also observed in the simulations that were carried out with *ls*1 *mardyn*, however, for $T^{\text{set}} = 2.0\,\varepsilon k_{\text{B}}^{-1}$ and not for $T^{\text{set}} = 1.5\,\varepsilon k_{\text{B}}^{-1}$. In these simulations,

the torus broke into smaller droplets. More information on this is given in Appendix C.

Let us come back now to the discussion of the curves with droplet break-up in Figure 20 (T^{set} = 1.5 to $5.0\,\varepsilon k_{\mathrm{B}}^{-1}$). The droplet break-up is indicated by a jump in the radius of gyration; after the jump, the curve shows the results for the largest of the newly formed droplets. The radius of gyration of that droplet first decreases rapidly, as a result of the interfacial tension that brings this droplet into a spherical shape. Once the droplet is spherical, it simply evaporates, leading to a further decrease of the radius of gyration. Interestingly, as in the results for the number of particles in the largest droplet (cf. top panel in Figure 20), a master curve is found, which acts as an attractor for the curves found for the different set temperatures. The slope of that master curve is the same as that for the results for T^{set} = $1.0\,\varepsilon k_{\mathrm{B}}^{-1}$. For T^{set} = $4.0\,\varepsilon k_{\mathrm{B}}^{-1}$ basically no oscillations are observed, indicating that the force exerted by the rapidly expanding bubble prevails after the initial contraction driven by the interfacial tension; for T^{set} = $5.0\,\varepsilon k_{\mathrm{B}}^{-1}$ the expanding liquid spherical shell breaks up very early, probably close to where the maximum radius of gyration would have been found. The break-up happens as follows: first, a droplet containing about 2 000 particles breaks off, shortly after this, the remaining droplet reaches its maximum radius of gyration, before it breaks into about ten smaller droplets.

The magnitude of the first maximum of the radius of gyration and the time when it is reached are shown in Figure 21 for the different set temperatures. As expected, the higher the set temperature is, the higher is the first maximum. The time when the first maximum is reached increases with increasing set temperature. Additionally, Figure 21 shows the results for the time when the droplet breaks apart for the first time. As expected, the higher the set temperature is, the earlier this occurs. At T^{set} = $5.0\,\varepsilon k_{\mathrm{B}}^{-1}$, this time is basically identical with the time when the first maximum is reached, which supports the discussion of this point given above.

The change of the kinetic energy, which is interpreted as the supplied heat to the simulation box, and the density of the thermostated region in the center of the droplet as a function of time are given in Appendix C.
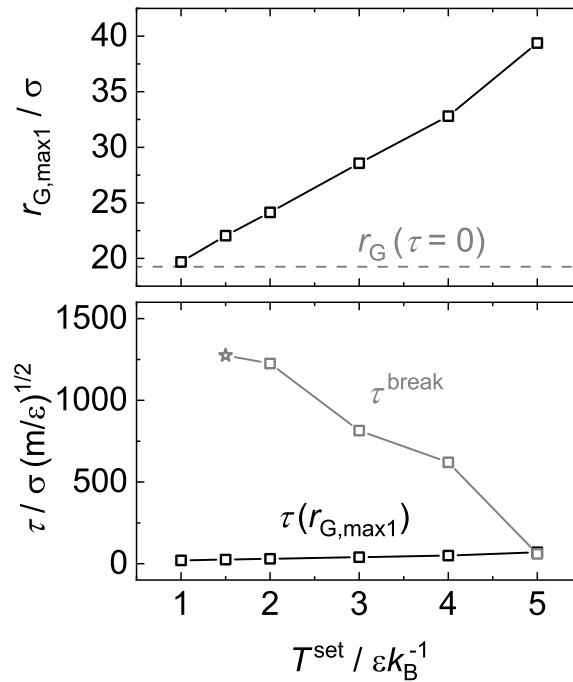
Figure 21: Magnitude (top panel) and time (bottom panel) of the first maximum of the radius of gyration (cf. Figure 20 bottom panel) as a function of the set temperature. Additionally, in the bottom panel, the time at which the liquid droplet breaks up into smaller droplets for the first time is shown (gray symbols). The star simply denotes the temporary maximum at the end of the simulation at $T^{\text{set}} = 1.5\,\varepsilon k_{\text{B}}^{-1}$ in which the droplet does not break apart but instead forms a torus-like shape (cf. Appendix C). The lines connecting the symbols are guides to the eye.

5.3.3 Position of the Interfaces

Figure 22 shows the position of the outer and inner interface as a function of time for all investigated set temperatures. Qualitatively, the curve for the position of the outer interface $r_{\text{out}}^{\text{IF}}$ is similar to that for the radius of gyration (cf. Figure 20). Major differences are observed only in the time span in which the droplet is breaking apart. Here, the radial density function starts to scatter and flattens out, which makes it difficult to identify interface positions in a meaningful way. As soon as the first smaller droplets form after the break-up, the outer interface position is tracked reliably again, which, for example, can be observed for the outer interface position at the highest temperature $T^{\text{set}} = 5\,\varepsilon k_{\text{B}}^{-1}$ starting from $\tau = 400\,\sigma(m/\varepsilon)^{1/2}$ onward. The outer interface of the shrinking droplet case ($T^{\text{set}} = 1\,\varepsilon k_{\text{B}}^{-1}$) follows the d^2 law of droplet evaporation [129]. Moreover, the outer interface of the expanding droplet cases ($T^{\text{set}} = 1.5$ to $3\,\varepsilon k_{\text{B}}^{-1}$) also follows the d^2 law during the time span at which the oscillatory behavior subsided is observed (cf. Figure 20). Details on these findings are given in Appendix C.

Similar to the outer interface position $r_{\text{out}}^{\text{IF}}$ and the radius of gyration r_{G}, the inner
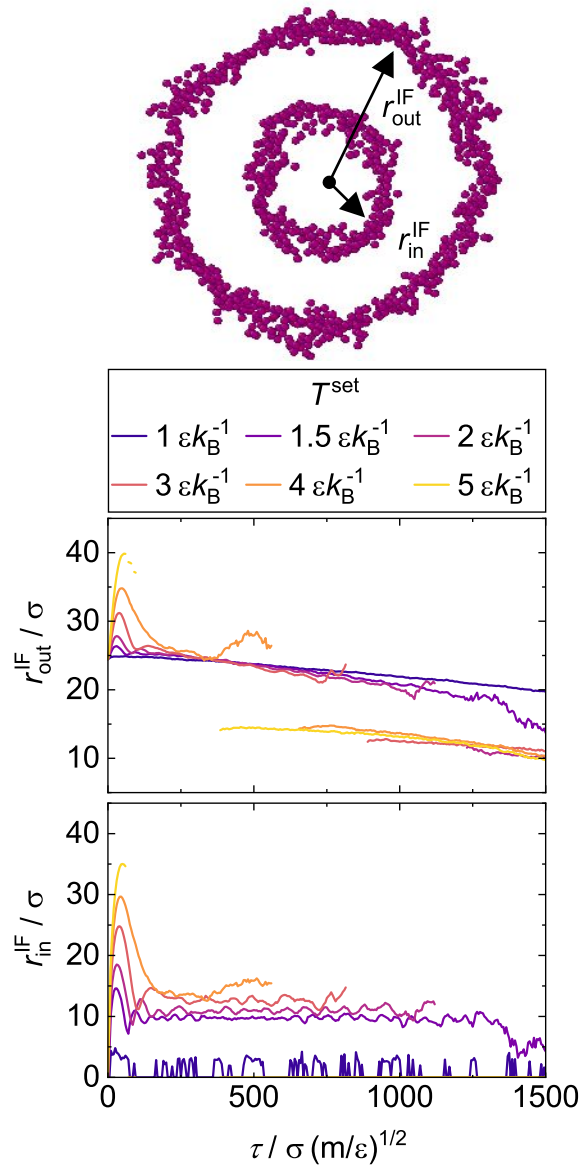
Figure 22: Position of the outer interface (top panel) and position of the inner interface (bottom panel) as a function of time. The discontinuities in the curves are related to a break-up of the studied droplet; the curve after the jump is that for the largest remaining droplet after the break-up. For clarity, a snapshot of a 2D slice through a droplet is included, showing only the interfacial particles. The arrows point to the corresponding interface.

interface position $r_{\mathrm{in}}^{\mathrm{IF}}$ shows a sharp increase after the activation of the thermostat in the droplet center. In the case of the expanding droplet ($T^{\mathrm{set}} = 1.5$ to $3.0\,\varepsilon k_{\mathrm{B}}^{-1}$), after reaching the first maximum, the inner interface position stabilizes and oscillates around a constant value. That constant value increases with increasing temperature and is in all cases larger than the radius of the thermostated region, i.e., the inner interface lies outside of the thermostated region. The oscillating behavior of the inner interface position is more pronounced than that of the outer interface position.

Interestingly, in the case of the expanding droplet, the spherical shell breaks apart when the average thickness of the shell Δr^{IF}, i.e., the distance between the inner and outer interface (cf. Eq. (20)), shrinks below $10\,\sigma$. The thickness of the interfacial region of the initial droplet is about $5.33\,\sigma$ (cf. Appendix C) in equilibrium at $T = 0.825\,\varepsilon k_{\text{B}}^{-1}$. The interfacial thickness of the LJTS fluid increases with increasing temperature [14]. Consequently, the spherical shell of the expanding droplet has to tear when the thickness of the shell leaves no space to sustain a liquid bulk phase in between the two interfacial regions. In summary, two closely linked mechanisms can cause the tearing of the droplet shell: the mechanical force exerted by the expanding vapor bubble or the shrinking of the droplet shell itself due to evaporation.

5.4 Conclusions

The response of a liquid droplet to a sudden temperature increase in its interior is investigated systematically by NEMD simulations. In the studied simulation scenario, the center of an equilibrated droplet is superheated by a thermostat so that a vapor bubble forms. The further evolution depends on the temperature imposed by the thermostat. Two antagonistic effects determine what happens: on the one side, the supplied heat drives the expansion of the bubble, on the other side, the interfacial tension acts against that expansion.

At moderate set temperatures, only small bubbles form in the center of the droplet, which, however, are not large enough to grow and collapse from time to time under the influence of the interfacial tension. The heat supplied by the thermostat is transferred to the surface of the droplet by heat conduction, the droplet evaporates following the well-known d^2 law [146].

Upon increasing the set temperature, a second regime is observed: the heat supply is sufficient to lead to the growth of the bubble, which is surrounded by an expanding spherical shell of liquid. The thickness of the liquid shell decreases as the bubble grows, for geometric reasons, but also due to evaporation. At a certain point in time, the shell is so thin that the interfacial regions on its inside and outside get into contact and the film becomes unstable. Also mechanical instability caused by the pressure difference between the bubble inside the droplet and the surrounding gas may play a role here. Typically, the liquid shell then breaks up, the fragments then contract to form new, smaller droplets, and the entire process may start again. However, also another type of break-up was observed: the transition from the spherical shell to a torus, in which, after the formation of a hole in the shell, a second hole on the opposite side forms and the resulting object becomes a torus under the influence of the interfacial tension. The

torus then continues to evaporate.

At the highest studied set temperatures, the supplied heat is so large that the bubble expands violently, breaking up the droplet mechanically and leading to the formation of smaller objects that contract again to form smaller evaporating droplets. During the expansion of the liquid spherical shell oscillations were observed, which are caused by the antagonistic effects of heat supply and interfacial tension.

6 Molecular Models for Alkali Nitrates in Aqueous Solution

6.1 Introduction

Thermodynamically rigorous modeling of the thermophysical properties of aqueous electrolyte solutions is a difficult task due to the strong long-ranged Coulomb interactions between the ions. Models of the excess Gibbs energy, such as the Pitzer model [147] and its extensions [148–151] or the electrolyte–NRTL [152] model, build on the Debye–Hückel [153] theory but require the adjustment of many parameters and are, thus, mainly used as correlation tools. Also equations of state for electrolytes have been developed, such as ePC-SAFT [154, 155], eCPA [156, 157], and SAFT-γ Mie [158, 159], which, in contrast to the models of the excess Gibbs energy mentioned above, also describe volumetric properties but still do not give access to structural and transport properties. Molecular modeling and simulation based on force fields is a viable route for describing electrolyte solutions. The state of research on molecular modeling and simulation of electrolyte solutions has recently been reviewed by Smith et al. [160] and by Panagiotopoulos [161].

In the present chapter, this model family is extended by a more complex ion model. Due its high practical relevance, the nitrate anion is chosen, i.e., the aim is to add $LiNO_3$, $NaNO_3$, KNO_3, $RbNO_3$, and $CsNO_3$ to the set. Aqueous solutions of nitrate salts are found in nature as well as in many industrial processes. Examples include the production of fertilizers, nutrition, pharmaceuticals, glass, enamel, and explosives [162], as well as the flame spray synthesis [136].

In a previous study of our group [163, 164] a set of molecular models for the alkali halide salts in aqueous solution has been developed. All models of this set consist of a single Lennard-Jones interaction site with a superimposed point charge and are non-polarizable. The alkali halide models were adjusted to thermophysical and structural properties of the aqueous solution in conjunction with the SPC/E water model [165]. For the alkali and halide ion models, the length parameter σ of the LJ potential was adjusted to the density of the solution at 293.15 K [163] and the energy parameter ε

has been adjusted to the self-diffusion coefficients and radial distribution functions at 293.15 K – 298.15 K [164].

Different types of molecular models have been used in the literature for describing the nitrate ion. The focus in this chapter lies on rigid, non-polarizable models based on a combination of LJ and point charge interaction sites, as this is consistent with the alkali ion models. Three models of that class have been proposed in the literature: Vchirawongkwin et al. [166–170], Laaksonen and Kovacs [171, 172], and Krienke and Schmeer [173–176]. Alternative approaches include flexible models [177, 178] and models in which the basic sites are polarizable [179–182] or hard-spheres [183, 184]. Combining different ion models that were developed in conjunction with the same water model seems to be a reasonable approach but this does not guarantee fair predictions and was not possible in the case of these three models: The models by Vchirawongkwin et al. and by Laaksonen and Kovacs were developed and tested in combination with the SPC [185] model, while the model by Krienke and Schmeer was first used in combination with a tailored water model of the authors, that has found no wider applications. The nitrate models from the literature had been expected to serve only as a starting point for a further optimization. However, preliminary tests showed that the nitrate model of Krienke and Schmeer [173] predicted the density of aqueous solutions of alkali nitrates as a function of molality most reliable in conjunction with the set of alkali ions from previous work [163, 164] and the SPC/E water model, without any adjustments. The other two nitrate models overestimated the solution density by far when applied in the same way. Hence, the nitrate model of Krienke and Schmeer in the new model set for alkali nitrates was used without any modifications.

Krienke and Schmeer [173] adopted the LJ parameters of a hybrid quantum-classical nitrate model of Lebrero et al. [186], where the hybrid quantum-classical nitrate model was used in conjunction with the TIP4P [187] and TIP4P-FQ [188] water models. Krienke and Schmeer [173] derived the distances between the nitrogen and the oxygen interaction sites by an *ab initio* approximation of the second order Møller-Plesset perturbation theory (MP2/6-31G(d)) and the partial charges of each interaction site by a Mulliken population analysis. The new nitrate model was used in combination with a tailored water model in Monte Carlo simulations to investigate the hydration of anions with oxygen sites [173]. The nitrate model of Krienke and Schmeer has also been used in conjunction with the SPC/E [165] water model and different cation models from the literature to investigate the hydration [173, 174], structure [175], and the self-diffusion and electric conductivity [176] of nitrate salts in aqueous solutions.

For the choice of the water model, there is a wide range of models available in the literature, e.g., the TIP4P [187], SPC [185], SPC/E [165], or OPC [189] models. These models yield fair descriptions of thermophysical properties such as density and dielectric

constant, and structural properties at near-ambient conditions. As a water model for the alkali nitrate model set, the SPC/E water model was chosen, since the alkali cation model parameters were adjusted in conjunction with the SPC/E water model.

As all models were adopted from the literature and no adjustments were made (the cross interactions were determined from the Lorentz-Berthelot combining rules), all results are predictions. This chapter can also be considered as a case study for the possibility to combine ion models (of different authors) in a building-block like manner. A broad range of properties was studied: the density, the water activity and the mean ionic activity coefficient, the self-diffusion coefficient, and radial distribution functions. The temperature and pressure were always 298.15 K, 1 bar, with the exception of the density (for all studied nitrate salts) and the water activity and the mean ionic activity coefficient (for $NaNO_3$), which were additionally investigated at 333.15 K.

The sampling of entropic properties in molecular dynamics is a demanding task. Different approaches have been developed in the recent years for sampling such properties [190–195]. In this chapter, water activity and related properties such as the osmotic pressure and the mean ionic activity coefficients were determined by the OPAS (*osmotic pressure for the activity of solvents*) method [196–198].

6.2 Molecular Modeling and Simulation

6.2.1 Molecular Models

Figure 23 shows a representation of the molecular model of the nitrate anion that was used in the present chapter, which was taken from Krienke and Schmeer [173], and the corresponding Lewis formula.
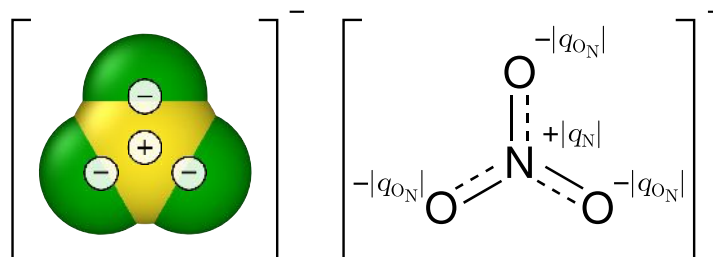
Figure 23: The nitrate anion: depiction of the molecular model used in the present chapter (left panel) and Lewis formula (right panel). The + and − signs in the left panel represent the point charges on the nitrogen (N, yellow) and oxygen (O_N, green) that are placed on the center of the corresponding LJ interaction sites. The model is planar. The dashed lines between nitrogen and oxygen in the Lewis formula represent mesomeric bonds.

The model is planar, rigid, and non-polarizable and consists of one central nitrogen (N) and three identical oxygen (O_N) interaction sites. Each of the interaction sites comprises a LJ site and a point charge that is superimposed in the center of the LJ site. The O_N sites are positioned on an equilateral triangle, with the N in its center. The bond length is r_{N-O_N} = 1.27 Å. All three O_N sites have the same LJ parameters and negative point charge, while the parameters of the N site are different. All four point charges sum up to a net charge of -1 e.

The nitrate model was used together with a set of alkali [163, 164] ion models developed in previous work of our group. All cation models consist of a single LJ site with a superimposed point charge of +1 e in its center. The five alkali cations Li$^+$, Na$^+$, K$^+$, Rb$^+$, and Cs$^+$ are considered.

Throughout this chapter, the SPC/E water model [165] was employed, since the cation models were developed for use together with this water model [164]. The SPC/E water model consists of a single LJ site (O_W) and three partial charges, one of which is placed on the center of O_W, while the other two are located a distance of 1 Å apart from the central O_W site and form a bond angle of 109.47 ° with O_W.

The parameters of all molecular models employed in this chapter are compiled in Table 10.

Table 10: Summary of the parameters of the molecular models used in this chapter. The nitrate model is rigid and flat, the angle between the N and the O_N sites is 120 °, the distance between these sites is r = 1.27 Å. For the SPC/E water model, the angle between the O_W and the H sites is 109.47 ° and the distance between H sites and the O_W is r = 1 Å.

species	site	σ	ε/k_B	q	Ref.
		Å	K	e	
nitrate	N	3.9	100.716	+0.8603	[173]
	O_N	3.154	78.057	−0.6201	
alkaline cations	Li$^+$	1.88	200	+1	[164]
	Na$^+$	1.89			
	K$^+$	2.77			
	Rb$^+$	3.26			
	Cs$^+$	3.58			
water	O_W	3.166	78.198	−0.8476	[165]
	H			+0.4238	

6.2.2 Studied Thermophysical Properties

6.2.2.1 Reduced Density

An essential thermophysical property of electrolyte solutions is their density. Here, we focused on the concentration dependence, i.e., the effect of adding nitrate salts to water at constant temperature and pressure. The overall molality $\tilde{b}_{AB}$ depends linearly on the amount of salt in the solution in contrast to the mole fraction. Following our previous work [163, 164, 199], instead of studying the absolute value of the density ρ, the reduced density ρ^* is studied, which is defined as:

$$\rho^*(T, p, \tilde{b}_{AB}) = \frac{\rho^{(m)}(T, p, \tilde{b}_{AB})}{\rho_W^{(m)}(T, p)} \tag{21}$$

where the density of the solution $\rho^{(m)}$ is divided by the density of pure water $\rho_W^{(m)}$. This definition sets the focus on the concentration dependence and eliminates the influence of the quality of the description of the density of pure water by the water model. It has been found for many salts that the density of the solution increases almost linearly as a function of the overall molality up to quite high salt molalities [58, 163, 200]. The density of pure SPC/E water as determined in molecular simulations under the usage of the Ewald summation as a long range correction from the present chapter is compared to experimental literature data in Table 11 confirming the good quality of the description.

Table 11: Density of pure water determined in this chapter for the SPC/E water model and experimental data from the literature [201] at different temperatures. The values shown here are used as reference for the reduced density, cf. Eq. (21). Statistical uncertainties are given in parentheses.

T / K	$\rho_W^{sim.}$ / kg m^{-3}	$\rho_W^{exp.}$ / kg m^{-3}
298.15	1004.3 (1)	997.05
333.15	982.9 (1)	983.20

For comparison with the present simulation data, experimental data on the density of aqueous alkali nitrate solutions at 298 K and near ambient pressure were taken from the Dortmund Data Bank [202] and correlated as a function $\rho^*(\tilde{b}_{AB})$ using a second order polynomial of the form:

$$\rho^*(\tilde{b}_{AB}) = 1 + \alpha_{AB,1} \, \tilde{b}_{AB} + \alpha_{AB,2} \, \tilde{b}_{AB}^2 \; , \tag{22}$$

where $\alpha_{AB,1}$ and $\alpha_{AB,2}$ are adjustable parameters. The polynomial is only used as a reference for the simulation data of this chapter to the experimental data from the literature. More information on the fitting procedure to the experimental density data

and the handling of outliers is given in Appendix D, where also the values of $\alpha_{AB,1}$ and $\alpha_{AB,2}$ for each nitrate salt considered in this chapter are reported.

6.2.2.2 Water Activity and Mean Ionic Activity Coefficient

The overall chemical potential $\tilde{\mu}_{AB}$ of a salt 'AB' that dissociates into the cation 'A$^+$' and the anion 'B$^-$' in an electrolyte solution is normalized as shown in Eq. (23):

$$\tilde{\mu}_{AB}(T,p,\underline{x}) = \tilde{\mu}_{AB}^{\mathrm{ref\,b}}(T,p,\underline{x}^*) + RT\ln\left(\frac{\tilde{b}_{AB}}{b^0}\ \tilde{\gamma}_{AB}^{\mathrm{b*}}(T,p,\underline{x})\right). \tag{23}$$

Herein, $\tilde{\mu}_{AB}^{\mathrm{ref\,b}}$ is the overall chemical potential of the electrolyte in the reference state, $\tilde{b}_{AB}$ is the overall molality of the salt AB, and b^0 is set to $1\,\mathrm{mol\,kg^{-1}}$. The vectors $\underline{x}$ and $\underline{x}^*$ characterize the composition of the studied mixtures and the mixture in the reference state, respectively. Furthermore, $\tilde{\gamma}_{AB}^{\mathrm{b*}}$ is the mean ionic activity coefficient of the salt AB, which is defined as

$$\tilde{\gamma}_{AB}^{\mathrm{b*}}(T,p,\underline{x}) = \left[\left(\gamma_{A^+}^{\mathrm{b*}}(T,p,\underline{x})\right)^{\nu_{A^+}}\left(\gamma_{B^-}^{\mathrm{b*}}(T,p,\underline{x})\right)^{\nu_{B^-}}\right]^{1/(\nu_{A^+}+\nu_{B^-})}, \tag{24}$$

where $\gamma_{A^+}^{\mathrm{b*}}$ and $\gamma_{B^-}^{\mathrm{b*}}$ as well as ν_{A^+} and ν_{B^-} are the activity coefficients and the stoichiometric coefficients of the cation A$^+$ and the anion B$^-$, respectively. The activity coefficients go to 1 for infinite dilution of the salt.

The water activity a_W, on the other hand, is normalized according to Raoult's law as

$$\tilde{\mu}_W(T,p,\underline{x}) = \tilde{\mu}_W^{\mathrm{ref}}(T,p) + RT\ln\left(a_W(T,p,\underline{x})\right). \tag{25}$$

Herein, the reference state is the pure liquid solvent water at the studied T and p.

The water activity a_W is directly related to the osmotic pressure Π as shown in Eq. (26)

$$\ln(a_W) = -\frac{\Pi}{\rho_W^{(\mathrm{n})}RT}\ , \tag{26}$$

where $\rho_W^{(\mathrm{n})}$ is the molar density of the pure solvent, T is the temperature, and R is the universal gas constant. The osmotic pressure was determined in this chapter by the OPAS method. The water activity a_W as a function of overall molality $\tilde{b}_{AB}$ of an 1:1

electrolyte was correlated by [191, 197, 203]

$$\ln(a_{\mathrm{W}}) = -2M_{\mathrm{W}}(\tilde{b}_{\mathrm{AB}}/b^0) - M_{\mathrm{W}}\ln(10)\Bigg(\beta(\tilde{b}_{\mathrm{AB}}/b^0)^2 + \frac{3}{4}C(\tilde{b}_{\mathrm{AB}}/b^0)^3$$

$$+ \frac{2A}{B^3 + B^4\sqrt{\tilde{b}_{\mathrm{AB}}/b^0}} + \frac{4A\ln(B\sqrt{\tilde{b}_{\mathrm{AB}}/b^0}+1)}{B^3} - \frac{2A\sqrt{\tilde{b}_{\mathrm{AB}}/b^0}}{B^2} - \frac{2A}{B^3}\Bigg), \tag{27}$$

where B, β, and C are adjustable parameters. The parameter A stems from Debye-Hückel theory [194, 196, 203] and is

$$A = \frac{e^3\sqrt{2\rho_{\mathrm{W}}^{(\mathrm{m})}N_{\mathrm{avo}}}}{(4\epsilon_0\epsilon_{\mathrm{r}}k_{\mathrm{B}}T)^{3/2}}\frac{1}{\pi\ln(10)}, \tag{28}$$

where ϵ_{r} is the relative permittivity of the pure solvent, k_{B} is the Boltzmann constant, $\rho_{\mathrm{W}}^{(\mathrm{m})}$ is the mass density of pure water, and N_{avo} is the Avogadro number. In this chapter, for SPC/E water $\epsilon_{\mathrm{r}}(298\ \mathrm{K}) = 71$ [204], $\epsilon_{\mathrm{r}}(333\ \mathrm{K}) = 62.1$ [205], and the densities $\rho_{\mathrm{W}}^{(\mathrm{m})}$ from Table 11 are used, which results in $A(298\ \mathrm{K}) = 0.5938$ and $A(333\ \mathrm{K}) = 0.608$. The correlation shown in Eq. (27) can be used to calculate the mean ionic activity coefficient $\tilde{\gamma}_{\mathrm{AB}}^{\mathrm{b}*}$ as a function of the overall molality $\tilde{b}_{\mathrm{AB}}$ with

$$\ln\tilde{\gamma}_{\mathrm{AB}}^{\mathrm{b}*} = \ln(10)\Bigg(\frac{-A\sqrt{\tilde{b}_{\mathrm{AB}}/b^0}}{1 + B\sqrt{\tilde{b}_{\mathrm{AB}}/b^0}} + \beta(\tilde{b}_{\mathrm{AB}}/b^0) + C(\tilde{b}_{\mathrm{AB}}/b^0)^2\Bigg). \tag{29}$$

6.2.3 Simulation Details

All simulations of this chapter were molecular dynamics simulations and were carried out with the program *ms*2 [204]. The number of particles was 4 000 except for the simulations of self-diffusion coefficients, where it was 16 000, as highly diluted mixtures were studied. The simulation volume was cubic and periodic boundary conditions were applied in all directions. Particle positions were initialized randomly on a cubic grid. The equations of motion were integrated with a fifth order Gear predictor corrector algorithm [35, 206], using a time step of 1.214 fs. A cut-off radius of 15 Å was used for all interactions. Standard tail corrections were applied for the LJ interactions [35]. Ewald summation [47] was applied for the long-range electrostatics, considering up to 10 k-vectors in each Cartesian direction, using the real space convergence parameter κ = 5.6, and conducting boundary conditions. The temperature was controlled using the velocity scaling thermostat [35]. The statistical uncertainties of the simulation results were estimated with the blocking method described by Flyvbjerg and Petersen [207].

The density was determined from NpT simulations in which the pressure was held constant by an Andersen's barostat [208] with a piston mass of $42.65 \cdot 10^6$ kg m^{-4}. The

system was first equilibrated with NVT boundary conditions for 50 000 time steps, followed by an NpT equilibration for 800 000 time steps. The length of the production phase of the NpT simulation run was 1 000 000 time steps.

The osmotic pressure Π was determined with the OPAS method [196–198], and then used for calculating the water activity a_W and the mean ionic activity coefficient $\tilde{\gamma}_{AB}^{b\star}$. The OPAS method is described in detail in Ref. [196]; it has already been applied successfully to aqueous solutions containing the set of alkali and halide ions [197] as well as to mixtures of molecular species [198]. In the present chapter, it is applied to solutions with a multi-center ion, i.e., nitrate, for the first time. In the OPAS method, the osmotic pressure Π of an electrolyte solution is determined from a simulation scenario that introduces a virtual semipermeable membrane through which only water molecules can pass. An OPAS simulation run consists of two steps [196]: first, the volume of the cubic box is determined in a pseudo-NpT run in which a desired pressure in the compartment containing the pure solvent is prescribed. Then, the osmotic pressure Π is sampled in an NVT run with the box volume V obtained in the preceding pseudo-NpT run. The pseudo-NpT run consisted of an equilibration phase of 500 000 time steps followed by a production phase of 2 000 000 time steps. The NVT run consisted of an equilibration phase of 500 000 time steps followed by a production phase of 10 000 000 time steps, in which the osmotic pressure Π was sampled. For further information, the reader is referred to Kohns et al. [196].

The self-diffusion coefficients and the radial distribution functions were calculated in the NVT ensemble. The box volume V and, hence, the density of the NVT simulation run were set according to a preceding NpT simulation run at the same temperature and composition. In the NVT simulation run, the system was first equilibrated for 200 000 time steps before sampling in the production phase for 2 400 000 time steps. The sampling length of the autocorrelation function for the Green-Kubo [53, 54] formalism was set to 10 000 MD steps and the result of every fifth time step was used for calculating the autocorrelation function. A time span of 200 time steps was introduced between the origins of two subsequent auto-correlation functions, so that in total 11 950 auto-correlation functions were sampled per simulation. The radial distribution function was determined and averaged every 10 000 time steps. The radial distribution function was calculated up to the cut-off radius of 15 Å and was divided into 500 equally sized bins.

6.3 Results and Discussion

In the following, the predictive simulation results are compared with experimental data for each of the studied thermophysical and structural properties. For most properties,

experimental data were only available at 298.15 K and 1 bar with the exception of density as well as the water activity of $NaNO_3$ solutions. Hence, almost all simulations were carried out at 298.15 K and 1 bar and, additionally, only some at 333.15 K and 1 bar.

The numerical simulation results are reported in Appendix D.

6.3.1 Reduced Density

Figure 24 shows the reduced densities of all investigated nitrate salt solutions at 298.15 K and 333.15 K.
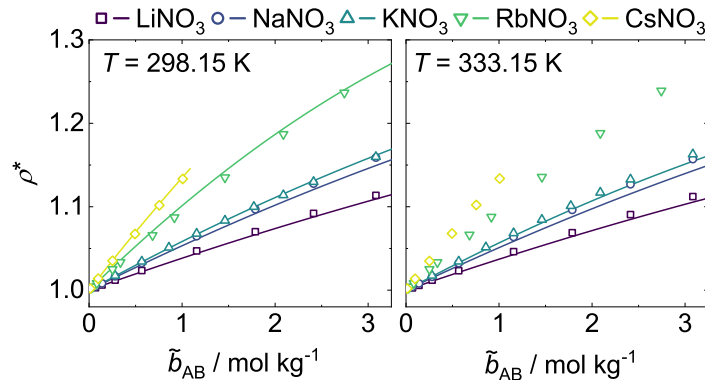
Figure 24: Reduced density $\rho^\star$ as a function of the salt molality $\tilde{b}_{AB}$ for aqueous solutions of the alkali nitrates $LiNO_3$, $NaNO_3$, KNO_3, $RbNO_3$, and $CsNO_3$; at 298.15 K and 333.15 K, 1 bar. Symbols show the simulation results, error bars are within symbol size. The solid lines represent correlations of experimental data from the Dortmund Data Bank [202] (for details, see Appendix D). No experimental data were available for $RbNO_3$ and $CsNO_3$ at 333.15 K.

It is difficult to get reliable information on the solubility of molecular models of salt + solvent systems [160, 161, 195], and no corresponding effort was made here, especially as it is known that models that predict fluid properties of salt solutions well may give poor results for the solubility [195]. The kinetics of the solid formation from liquid solutions are slow and the simulation times that were used in the present study are too low to expect observing solid formation even when the salt concentration is above the solubility (which is not known exactly). Despite this, the concentration range is limited in which the simulation studies were carried out to a range in which the real solutions are still liquid: for $LiNO_3$, $NaNO_3$, KNO_3, and $RbNO_3$ the maximal molality was 3 mol kg^{-1}, for $CsNO_3$ it was 1 mol kg^{-1}.

Figure 24 shows that for all studied solutions and both studied temperatures, the predicted density matches the experimental data well, the deviations are generally below

1 %. Nevertheless, systematic trends of the deviations are observed for both temperatures: the density is slightly underestimated for $LiNO_3$ and $NaNO_3$, while it is slightly overestimated for $RbNO_3$ and $CsNO_3$, i.e., the deviations depend on the mass of the alkali cation. No comparison could be carried out for $RbNO_3$ and $CsNO_3$ at 333 K, as no experimental data were available, but the same trend would be expected as for 298 K. Considering the fact that no adjustments of parameters were made, the predictions for the density are excellent.

6.3.2   Water Activity and Mean Ionic Activity Coefficients

Figure 25 shows the results for the water activity a_W and the mean ionic activity coefficient $\tilde{\gamma}_{AB}^{b*}$ as a function of the overall molality $\tilde{b}_{AB}$ at 298.15 K for all studied alkali nitrate salts. The simulation results are compared in Figure 25 to correlations of experimental data taken from Hamer and Wu [203]. The numerical values of the fit parameters of the correlation to the simulation results (cf. Eqs. (27) and (29)) are given in Table 12.

In contrast to the vast majority of strong electrolytes in aqueous solution, the mean ionic activity coefficients of the alkali nitrates do not have a minimum as a function of concentration, with the exception of $LiNO_3$. The molecular models predict this uncommon behavior well, however, they fail to predict the minimum for $LiNO_3$. This deficiency regarding $LiNO_3$ is not surprising, since the model parameters of Li^+ and Na^+ are very similar. Consequently, no strongly differing behavior in terms of the activity coefficient is to be expected for their nitrate salts. To investigate this more closely, a parameter variation study was conducted for the Li^+ model, the results of which are reported in Appendix D. Regarding the other nitrate salts, also quantitatively, the agreement between experiment and simulation is good, especially for solutions of $NaNO_3$, $RbNO_3$, and $CsNO_3$, considering that activities and related properties are very sensitive and difficult to predict by any other means. With increasing concentrations, it becomes increasingly difficult to correctly model the behavior of water activity and mean ionic activity coefficient for electrolyte solutions. Hence, the simulation results deviate increasingly from the experimental results for higher concentrations. This can be observed especially for $LiNO_3$ and KNO_3. Nonetheless, with the exception of $LiNO_3$, the water activity and the mean ionic activity coefficient are predicted well, especially at low concentrations.

Activity data at temperatures other than 298 K are scarce in the literature, even for important electrolytes such as alkali nitrates. Molecular simulations are an intriguing option to predict these properties. To further assess the predictive capabilities of the model set studied in this chapter, the water activity and mean ionic activity coefficient were studied of $NaNO_3$ solutions at 333 K. This system and temperature were chosen
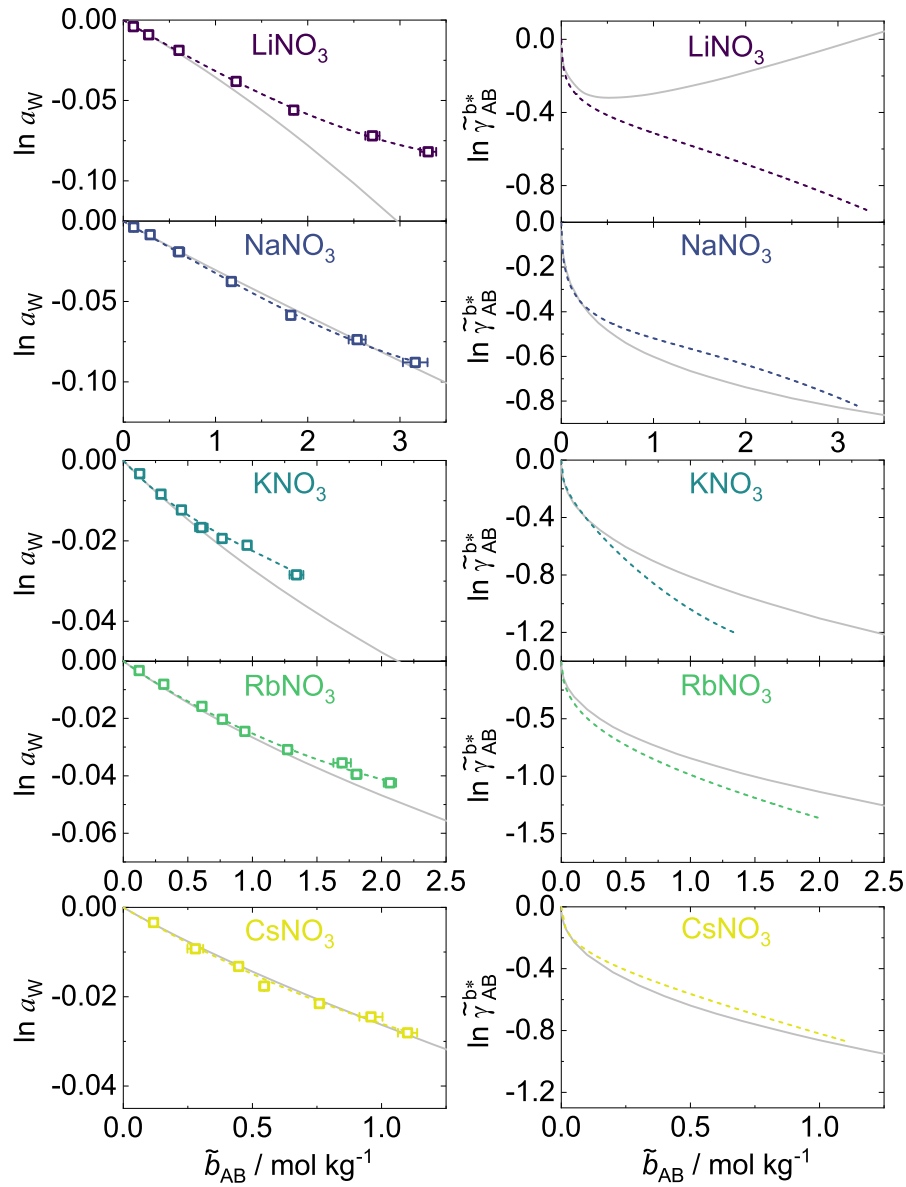
Figure 25: Solvent activity a_W and mean ionic activity coefficients $\tilde{\gamma}_{AB}^{b*}$ as a function of the salt molality $\tilde{b}_{AB}$ for all investigated alkali nitrate salts at 298.15 K and 1 bar. Open squares show the simulation results for the solvent activity a_W. The dashed lines represent the correlations of the simulation data, from which also the mean ionic activity coefficients $\tilde{\gamma}_{AB}^{b*}$ were calculated (cf. Eqs. (27) and (29)). The gray solid lines represent correlations to experimental data taken from Hamer and Wu [203].

because experimental information on the water activity can be derived from the vapor pressure data by Galleguillos et al. [209], when assuming an ideal gas phase of pure water and using the vapor pressure of water of 0.199 bar at that temperature [210]. The results of this study are shown in Figure 26.

The experimental data show almost no temperature influence on the water activity in the studied temperature range up to a molality of about 2.5 mol kg^{-1}. The molecular

Table 12: Summary of the parameters B, β, and C used in Eqs. (27) and (29) for fitting the solvent activity data obtained with the OPAS method for all alkali nitrate salts (cf. Figure 25 and Figure 26). All parameters are valid for 298.15 K, except for those in the last row. For the parameter A, cf. the discussion of Eq. (28).

| salt	B	β	C
LiNO$_3$	2.2331	-0.0309	-0.0082
NaNO$_3$	1.5871	0.0173	-0.0131
KNO$_3$	3.8317	-0.4258	0.0976
RbNO$_3$	0.8255	-0.1045	0.0009
CsNO$_3$	2.5551	-0.1909	0.0019
NaNO$_3$ (333.15 K)	1.2762	0.0386	-0.0117
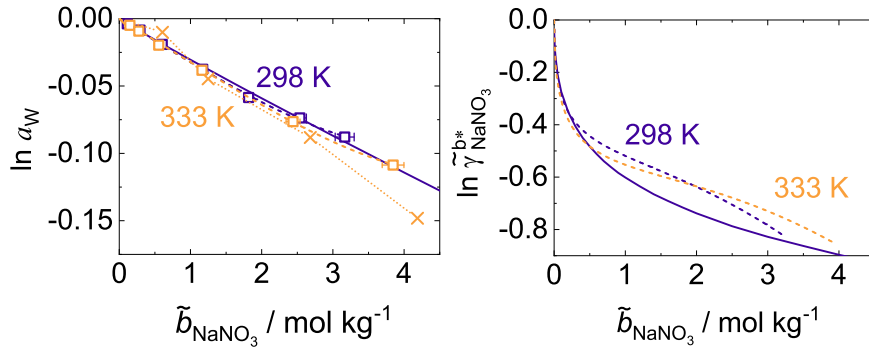
Figure 26: Solvent activity a_W and mean ionic activity coefficient $\tilde{\gamma}_{AB}^{b\ast}$ as a function of the salt molality $\tilde{b}_{AB}$ for aqueous solutions of NaNO$_3$ at 298.15 K and 333.15 K; both at 1 bar. Open squares show the simulation results for the solvent activity a_W. The dashed lines represent correlations of the simulation data, from which also the mean ionic activity coefficients $\tilde{\gamma}_{AB}^{b\ast}$ were calculated (cf. Eqs. (27) and (29)). The solid purple lines represent correlations to experimental data taken from Hamer and Wu [203] at 298.15 K. The orange crosses in the left panel represent points derived from the experimental vapor pressure data of Galleguillos et al. [209] at 333.15 K; the dotted orange lines connect these individual points and are guides to the eye only.

simulations accurately predict this behavior. At higher concentrations, the experiments suggest that the water activity is lower at the higher temperature, which the molecular simulations do not capture. Nevertheless, especially for the lower concentrations the agreement is quite satisfactory considering that the molecular models are used in a strictly predictive manner.

6.3.3 Self-diffusion Coefficients

The predictions of the self-diffusion coefficients of the potassium ion, the nitrate ion and water in aqueous solutions of KNO_3 at 298.15 K and 1 bar are compared to experimental data in Figure 27.
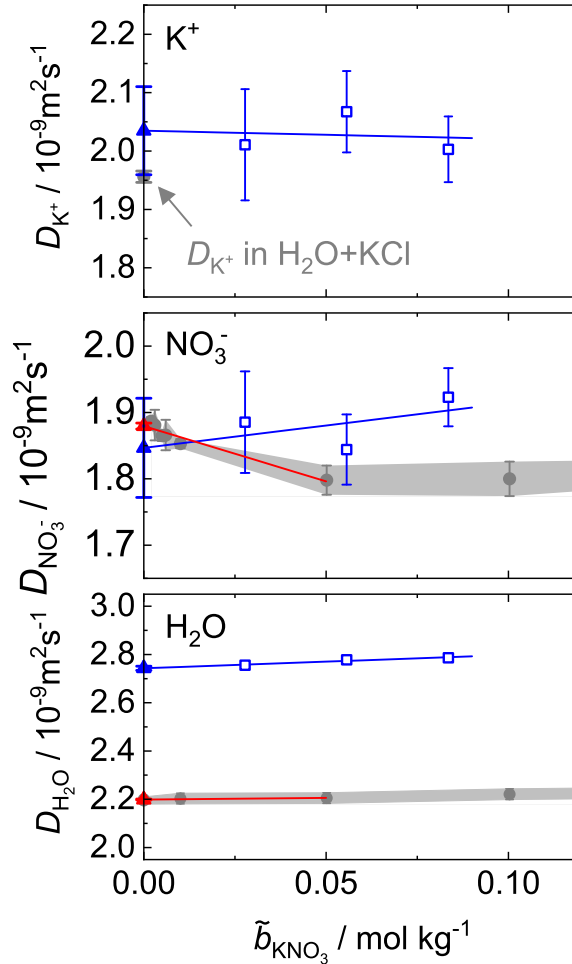
Figure 27: Self-diffusion coefficients of K^+, NO_3^-, and H_2O as a function of salt molality $\tilde{b}_{KNO_3}$ for aqueous solutions of KNO_3 at 298.15 K and 1 bar. Open squares show the simulation results. Solid gray circles show experimental data from the literature (K^+ [211], NO_3^- [212], and H_2O [213]). For K^+, the experimental self-diffusion coefficient at infinite dilution is given for the system $KCl+H_2O$, due to the lack of data for the system KNO_3+H_2O. The areas shaded in light gray are guides to the eye indicating the range of experimental data including uncertainties. The filled triangles represent the self-diffusion coefficient at infinite dilution, which is extrapolated linearly (red line: experimental data, blue line: simulation results).

To the best of the author's knowledge, this is the only alkali nitrate system for which experimental data are available in the literature. The self-diffusion coefficient at infinite dilution was determined in the present chapter from a linear fit. This self-diffusion

coefficient at infinite dilution is of particular interest due to the fact that the influence of the counter ion is negligible. Furthermore, at infinite dilution the self-diffusion coefficient corresponds to the mutual transport diffusion coefficient of the ion.

The simulation result for the self-diffusion coefficient of the nitrate ion is in good agreement with the experimental value, which is only slightly overestimated. In contrast to the experimental trends, the simulation results suggest a slight increase of the self-diffusion coefficient of the nitrate ion with increasing concentration. However, there are considerable uncertainties of the simulation results, which arise from the extremely low concentrations studied, meaning that few ions are present in the simulation box despite large systems containing $16\,000$ particles that were studied. Hence, this finding should not be overinterpreted.

For the potassium ion a comparison to experimental data is only feasible for the infinite dilution due to the lack of experimental data of KNO_3. Again, good agreement between the prediction from the simulation and the experimental data is observed, which, again, is only slightly overestimated.

The results from the present chapter confirm previous findings from the literature [214] that the self-diffusion coefficients of water at 298 K is overestimated by the SPC/E model by about 25 %. This translates directly to the results for the electrolyte solutions. However, the slight increase in the self-diffusion coefficient of water upon adding KNO_3 is correctly predicted. As first pointed out in a study of Kim et al. [215] and summarized in recent reviews by Panagiotopoulos [161] and Panagiotopoulos and Yue [216], many non-polarizable models fail at predicting this trend correctly, but the present model combination for aqueous KNO_3 solutions does.

In summary, the self-diffusion coefficients of the ion models, especially of the NO_3^- ion, at high to infinite dilution are in good agreement with the experimental data. The infinite dilution of NO_3^- ions is of particular interest since it is similar in all aqueous solutions of the alkali nitrate model set. For more information as well as numerical results of the self-diffusion coefficients at infinite dilution, see Appendix D.

6.3.4 Radial Distribution Functions

Figure 28 shows the radial distribution functions of different interaction sites in an aqueous solution of $NaNO_3$ with a molality of $3.084\,\mathrm{mol\,kg^{-1}}$ at 298.15 K and 1 bar. For this system, experimental data are available in the literature for the positions of the first maxima r_{max1} of the radial distribution functions. To the best of the author's knowledge, this is the only alkali nitrate system for which such a comparison can be carried out due to a lack of experimental data for other systems. The molality of the

experimental data from Kameda et al. [217, 218] is at 6.168 mol kg^{-1} and Megyes et al. [175] report data in a range from 2 to 10 mol kg^{-1}. The influence of the concentration on the position of the first maximum is negligible as shown in the work of Megyes et al. [175].
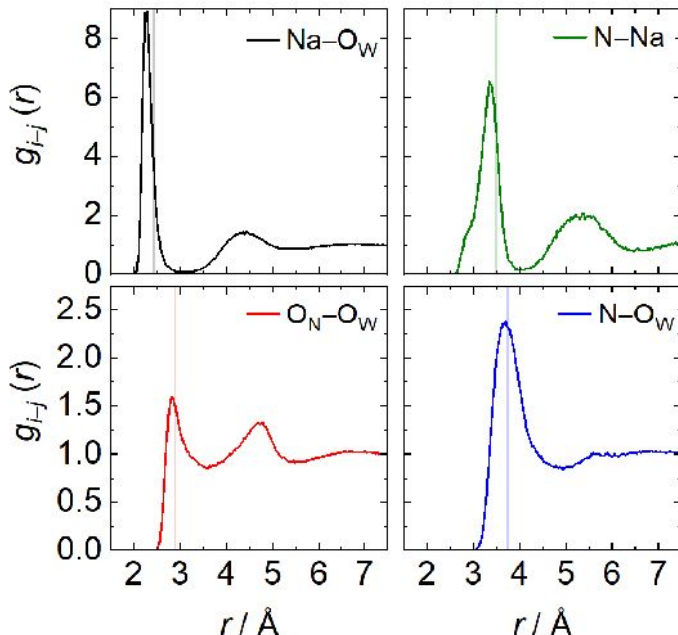
Figure 28: Radial distribution functions of different interaction sites in a NaNO$_3$ solution with a molality of 3.084 mol kg^{-1} at 298.15 K and 1 bar. Solid lines show the simulation results. Experimental data for the position of the first maximum r_{max1} from the literature (g_{Na-O_W}[175], $g_{O_N-O_W}$ [218], g_{N-Na} [175], g_{N-O_W} [217, 218]) are given by the shaded vertical bars including statistical uncertainties.

Overall, favorable agreement is observed between the experimental data for the locations of the first maxima of the different radial distribution functions and the predictions from the molecular simulations. The predictions of the positions of the first maximum in the O$_N$–O$_W$ RDF and the N–O$_W$ RDF are almost within the narrow uncertainty of the experimental results. This indicates that the structure of water around the NO$_3^-$ ion is represented very well by the model. The results for the Na$^+$ ion are less accurate: the position of the first maximum of the Na$^+$–O$_W$ RDF and the N–Na$^+$ RDF are predicted too low. This is not unexpected, as RDF involving the Na$^+$ ion model and SPC/E water have shown similar trends in simulations of aqueous alkali halide systems [164].

A further analysis of the radial distribution functions from molecular simulation reveals two intriguing aspects. First, comparing g_{N-Na} and g_{N-O_W} shows that the Na$^+$ cations get somewhat more closely to the nitrogen atom of the nitrate anion than water molecules do. This is a quite surprising finding since both Na$^+$ and the nitrogen interaction site have positive point charges. Second, there is a shoulder in g_{N-Na} at about $r = 2.9$ Å. The

position of this shoulder in $g_{\text{N-Na}}$ matches the unlike LJ size parameter of the N-Na$^+$ interaction, which is also 2.9 Å. Hence, a small number of Na$^+$ ions coordinate closer to the nitrogen atom of the nitrate anion in that distance, while the majority of the Na$^+$ ions are found at around 3.34 Å in the first maximum.

Both peculiarities can be explained by the fact that the positively charged nitrogen atom on the nitrate anion is surrounded by three negatively charged oxygen atoms, which strongly attract the Na$^+$ ions and shield the positive charge on the nitrogen. In addition, the overall net charge of the nitrate anion is negative, which makes it attractive for Na$^+$. Finally, the size parameter of the employed Na$^+$ model is about 40 % smaller than that of the SPC/E water model, so it has a simple geometric advantage in the competition for the spots closest to the nitrate anion.

In summary, the structure in short range around all investigated interaction sites is well predicted, especially for the NO$_3^-$ ion, which is the main focus of this chapter.

6.4 Conclusions

A set of molecular models for alkali nitrate salts in aqueous solution is proposed. This set is used for predicting thermophysical and structural properties of the aqueous nitrate salt solutions and the results are compared to experimental data. Furthermore, the water activity and the mean ionic activity coefficients are predicted in this study in a broad concentration range by molecular simulations for these five alkali nitrates. The models for the individual species – cations, nitrate, and water – were developed independently of each other by different groups and are deployed in a strictly predictive manner using the Lorentz-Berthelot rules. The alkali cation models were developed for the use in conjunction with halide ions and the SPC/E water model. The nitrate model on the other hand has been derived on the basis of quantum mechanical calculations and developed for the usage with a water model developed by the original authors. Especially the predictions for the density and the radial distribution functions are in good agreement with the available experimental data. The water activity and the mean ionic activity coefficients of the alkali nitrate solutions are in remarkable agreement with experimental data, the only exception being solutions of LiNO$_3$. The self-diffusion coefficients are also predicted well with the exception of water, which is an inherent issue of the SPC/E water model.

7 Molecular Dynamics Study of Ion Clustering in Concentrated Electrolyte Solutions for the Estimation of Salt Solubilities

7.1 Introduction

Molecular modeling and simulation has emerged as a versatile tool for studying the properties of highly concentrated electrolyte solutions. The recent developments in that field with respect to electrolyte solutions have been reviewed by Panagiotopoulos [161] and by Nezbeda et al. [160, 219]. However, irrespective of the recent progress made, with molecular simulations of electrolyte solutions there is always one potential issue: the salt solubility. Taking a look at the few models for which solubility data are available in the literature shows a wide variety of results: as an example, for NaCl in aqueous solution at 298 K, some models vastly underestimate the experimental solubility, while others yield reasonable predictions [57, 195]. This is true for both the well-established class of non-polarizable models and for the class of polarizable models, which have attracted some interest in recent years [192, 220, 221]. The issue of salt solubility is of course closely linked to the parametrization of the investigated molecular models; however, we will not address model parametrization explicitly in the present chapter but rather focus on approaches for determining the solubility for a given model parametrization.

In the present chapter, two types of approaches are distinguished for determining the solubility. The term *solubility calculation* refers to methods that rigorously calculate the solubility for a certain molecular model of an electrolyte solution. Such methods are computationally demanding (see below). The term *solubility estimation* refers to methods that rather yield a rough estimate of the solubility, but which in turn work with much cheaper simulations. The main focus of the present chapter is to propose and assess a new scheme for solubility estimation.

Two methods are available in the literature for rigorous solubility calculations: the

chemical potential method [56, 190–192, 194, 195, 222–227] and the *direct coexistence method* [220, 227–232]. Calculations with the *chemical potential method* consist of two steps. First, the chemical potential of the salt in solution is determined as a function of concentration at constant temperature and pressure. Second, the chemical potential of the solid salt crystal is determined in a separate simulation at the same temperature and pressure. The solubility is then obtained as the concentration at which the chemical potential of the salt in solution equals that of the solid.

However, the chemical potential method requires knowing the structure and stoichiometry of the emerging crystal, i.e., whether a hydrate forms and, if it does, how many water molecules are present in it – only then can the chemical potential of the salt in the correct configuration be calculated. Unfortunately, it is impossible to know this before carrying out simulations, such that the only way is to use a trial-and-error approach that tests different crystal configurations and then considers the one with the lowest free energy. Furthermore, the determination of chemical potentials is not trivial and needs sophisticated evaluation schemes. The chemical potential of the salt in solution is usually obtained from a thermodynamic integration-type calculation that requires a very fine discretization along the chosen path [194]. The chemical potential of the solid salt is typically calculated with techniques based on the Einstein crystal method [233]. Nevertheless, despite the methodological difficulties and challenges, determinations of the solubility of the same model combination by different authors yield similar results with the chemical potential method [56, 190, 191, 194, 195, 227].

In the *direct coexistence method* – as the name suggests – the aqueous solution is simulated in direct coexistence with a solid salt phase and the simulation runs until equilibrium is reached. The solubility then corresponds to the salt concentration in the bulk liquid phase in equilibrium. Even though this method only needs a single simulation to determine the solubility, the time needed to reach equilibrium is on the order of microseconds [227–232]. Considering this slow equilibration process, the initial state of the system has to be chosen close to the final equilibrium state (which is of course usually not known a priori), otherwise risking prohibitively long equilibration times. Additionally, size effects of the bulk phases and the area of the solid-liquid interface are crucial for this method [228]. The first results obtained with the direct coexistence method yielded very different results by different groups of authors even for the same model combination [227–232]. The influence of size effects was investigated in recent years and, as a result, the reproducibility significantly improved [220, 228, 232], reaching mutual agreement with results obtained with the chemical potential method.

As discussed above, both methods for the rigorous calculation of the solubility of a salt in solution possess several pitfalls and are computationally very expensive. Especially during the development of new ion models, their computational cost is prohibitive. Hence,

it is desirable to have empirical rules that allow for making at least a rough estimate of the solubility. Two such rules were proposed by Benavides and co-workers [56, 57]: the *chemical potential difference rule*, which is based on the difference of the chemical potentials of the salt at infinite dilution and of the crystal, and the *ion pairs rule*, which is based on the number of contact ion pairs, i.e., the number of ions in the first coordination shell around the corresponding counter ion. The *chemical potential difference rule*, however, is not readily applicable, as it still requires expensive calculations for obtaining the chemical potential of the electrolyte at infinite dilution in the solvent and that of the emerging solid salt. The use of this rule only circumvents calculating the concentration dependence of the chemical potential of the salt in solution. The *ion pairs rule*, by contrast, is a solubility estimation method: it can be applied easily and on the fly in standard simulations by sampling the cation–anion radial distribution function (RDF). The MD simulations used by Benavides and co-workers for determining that RDF used several hundred to a few thousand particles and took up to 20 ns. For this, the computational demand is several orders of magnitude lower than that needed for calculations of chemical potentials or applying the direct coexistence method. Benavides and co-workers formulated two versions of the ion pairs rule. First, they suggested that the solubility of 1:1 electrolytes with moderate solubility (i.e., lower than $10 \, \mathrm{mol \, kg^{-1}}$) is at the concentration for which the number of contact ion pairs is 0.075 [56]. This did hold for the NaCl models of Joung and Cheatham [234] and Smith and Dang [235] when combined with SPC/E water [165]. In a second publication [57], they redeemed the rule as follows: the solution is most likely supersaturated if the number of contact ion pairs is greater than 0.5, i.e., the concentration range in which the salt is soluble is at a concentration for which the number of contact ion pairs less than or equal to 0.5.

The general idea of the ion pairs rule is that the solubility of a salt should in some way be related to the microscopic structure of the fluid. The formation of ion pairs is of course a logical first and important step in the homogeneous nucleation of a salt crystal from solution. It is widely accepted that the solid phase nucleates in a two-step mechanism [236–243]: in the first step, ion clusters with a short life span and an amorphous structure form. These clusters have to reach a critical size to become stable. In the second step, ions inside of sufficiently large, stable clusters rearrange to form ordered lattice structures of the corresponding salt crystal. These ordered structures inside the cluster are surrounded by an amorphous layer of ions. The focus of this work lies on the early stages of the nucleation process, as the existence of small clusters of a certain size might indicate that, eventually, a salt crystal will form. The studies by Lanaro and Patey [240] and Zimmermann et al. [239, 244] are of particular relevance for the present chapter, since both groups of authors observed that the smallest clusters that can be considered to be stable over an extended period of time contain six ions.

However, both Lanaro and Patey as well as Zimmermann et al. studied only aqueous NaCl solutions as described by combining the Joung-Cheatham NaCl model [234] with the SPC/E water model [165]. It is unclear whether this threshold cluster size also holds for other molecular models of NaCl or other salts.

Following the aforementioned studies on crystal nucleation and inspired by the ion pairs rule, in the present chapter, the structure of aqueous electrolyte solutions at concentrations below, at, and beyond the solubility was investigated systematically. Cation–anion cluster formation were investigated with a neighbor search algorithm [145] to identify the coordination of anions and cations from configurational data, which are readily available from MD simulations. With an observable derived from the cluster size distribution, a new solubility estimation method was developed and compared to the ion pairs rule by Benavides et al. [56, 57]. To anticipate some of the findings from the present chapter, we formulate this new *cluster rule* as follows: when running MD simulations with different salt concentrations at the same temperature and pressure, the estimated salt solubility is the lowest initial composition of the solution for which clusters containing six or more ions are observed.

7.2 Molecular Modeling and Simulation

In the present chapter, MD simulations of aqueous solutions of different alkali halide salts are carried out as described by different molecular models from the literature. The models and some technical simulation details are explained in Sections 7.2.1 and 7.2.2, respectively. The obtained simulation results are evaluated focusing on two aspects: the number of contact ion pairs needed for using the ion pairs rule by Benavides et al., and the distribution of ion cluster sizes for the development and assessment of the cluster rule, see Sections 2.2.3 and 7.2.3, respectively.

7.2.1 Molecular Models

All molecular models for ions studied in this chapter consist of a single LJ interaction site with a superimposed point charge of +1 e (for the Na$^+$ and K$^+$ cations) or −1 e (for the Cl$^-$ and I$^-$ anions). Several ion models from the literature are considered, which only differ in the choice of the two LJ parameters σ and ε. The NaCl models by Smith and Dang (SD) [235], by Joung and Cheatham (JC) [234], and by Reiser et al. (RDVH) [163, 164] are investigated. Additionally, the KCl model by Joung and Cheatham [234] and the NaI model by Reiser et al. [163, 164] are investigated. An overview of the parameters of these ion models is given in Table 13. Throughout the

present chapter, two well-established water models are used: the SPC/E model [165] (for all electrolyte solutions but one) and the TIP4P-Ew model [245] (in combination with the corresponding JC ions for NaCl). This choice of ion models in combination with the water models is motivated by the fact that data on the salt solubility in these systems are available in the literature, which are compiled in Table 14.

Table 13: Parameters of the molecular models of ions studied in this chapter. All ion models consist of a single LJ site with a superimposed point charge. All models are used together with the SPC/E water model, except for the JC-TIP4P-Ew models, which are used together with the TIP4P-Ew water model.

| species | model name | σ | $\varepsilon/k_{\mathrm{B}}$ | q | ref. |
		Å	K	e	
Na$^+$	SD	2.35	65.419	1	[235]
	JC	2.16	177.456	1	[234]
	JC-TIP4P-Ew	2.1845	84.769	1	[234]
	RDVH	1.89	200	1	[163, 164]
K$^+$	JC	2.84	216.236	1	[234]
Cl$^-$	SD	4.4	50.322	-1	[235]
	JC	4.83	6.434	-1	[234]
	JC-TIP4P-Ew	4.9178	5.869	-1	[234]
	RDVH	4.41	200	-1	[163, 164]
I$^-$	RDVH	4.78	200	-1	[163, 164]

Table 14: Solubility of the investigated alkali halide models in water at 298 K. The
water model is SPC/E throughout, except for JC-TIP4P-Ew-NaCl, for which
it is the TIP4P-Ew model. The asterisk (*) indicates the values used as a
benchmark in the figures of this chapter. Statistical uncertainties are given
in parentheses.

salt	model	$x^{\mathrm{sol}}_{\mathrm{A^+}}/$ mol mol^{-1}	ref.
NaCl	SD	0.011	[191]
		0.011(2)	[194]
		0.011(2)	[195] *
		0.012(1)	[56]
		0.016(7)	[227]
NaCl	JC	0.057(1)	[194]
		0.058(4)	[191]
		0.059(1)	[195] *
		0.059(4)	[194]
		0.063(4)	[190]
		0.074(5)	[227]
NaCl	JC-TIP4P-Ew	0.063(5)	[231] *
NaCl	RDVH	0.085(1)	[195] *
KCl	JC	0.044(1)	[195] *
NaI	RDVH	0.166(4)	[195] *

7.2.2 Simulation Details

All simulations in this chapter are molecular dynamics simulations (MD) carried out with the open source program *ms*2 [204]. All simulations are initialized by placing the particles randomly on a cubic grid. Most simulations of the present chapter are carried out with 4 000 particles, but to study the influence of system size, several simulations are repeated using 20 000 particles instead. The simulation box is cubic with periodic boundary conditions. A fifth-order Gear predictor-corrector scheme [35, 206] is used for integrating the equations of motion. The simulation time step is 1.214 fs.

All simulations are carried out in two steps: First, the density is determined with an NpT simulation. In that simulation, the system is first equilibrated for 50 000 time steps in the NVT ensemble and then for 500 000 time steps in the NpT ensemble, before starting the production run of 1 000 000 time steps. The pressure is set using the Andersen barostat [208] and the temperature is set using the velocity scaling thermostat [35]. Second, an NVT simulation is carried out at the density obtained in the NpT run and at the same temperature and composition. That NVT run consists of 500 000 time steps of equilibration and a production phase of 2 000 000 time steps. To study the influence of the duration of the production phase, some simulations are carried out for 20 000 000 time steps instead. In the NVT run, the radial distribution function is sampled (cf. Section 2.2.2) and perform a cluster analysis (cf. Section 7.2.3). The instantaneous particle positions used for the cluster analysis are saved every 100 000 time steps. For sampling the RDF, the range up to the cut-off radius is discretized into 500 equally sized bins for which particle positions were recorded every 10 000 time steps.

All literature solubility data used as a baseline were reported for 298 K and 1 bar. Hence, all molecular simulations in this chapter were carried out at that temperature and pressure. For each salt, several simulations were carried out at different concentrations.

With n_{CIP} defined by Eq. (8), evaluating the ion pairs rule by Benavides et al. [56, 57] is straightforward: if $n_{\mathrm{CIP}} > 0.5$, the solution is supersaturated with the salt, i.e., the composition at which $n_{\mathrm{CIP}} = 0.5$ can be used as an estimate for the salt solubility. That estimate is denoted with the symbol $x_{\mathrm{A^+}}^{\mathrm{sol,CIP}}$ throughout this chapter.

7.2.3 Cluster Analysis

Instantaneous configurations, i.e., snapshots of the simulated system as a function of simulation time, are analyzed with a cluster analysis tool provided by the visualization tool *Ovito* [145]. The employed cluster search algorithm is shown schematically in Figure 29. The cluster algorithm searches for neighboring ions of opposite charge in a radius r^{C} around the central ion. In the present chapter, the value of the first minimum

position in the cation-anion RDF is used as that radius r^C. All particles that are within the search radius are considered to be part of the same cluster. Single ions are counted as a cluster of size 1.
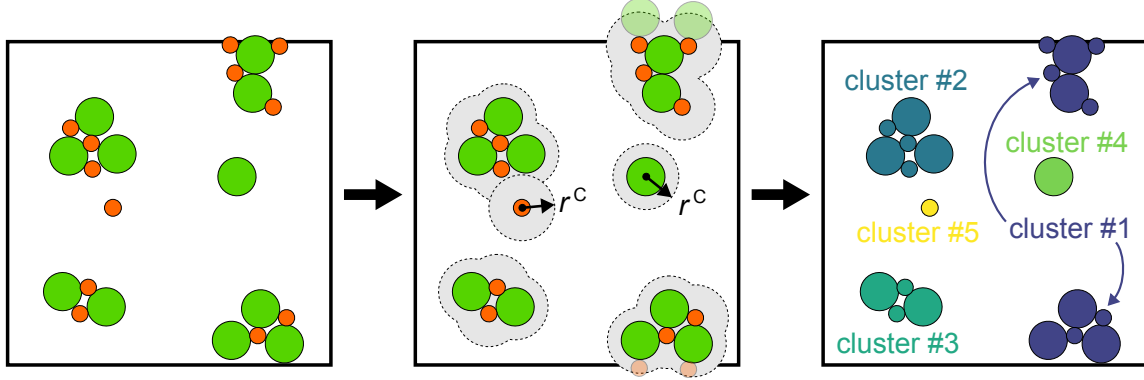

Figure 29: Schematic of the cluster algorithm [145]. Left: a configuration of the ions from a simulation; anions are shown in green, cations in orange. Water molecules are not shown to improve clarity. Middle: neighbor search in the radius r^C around each ion. Around each ion, only the corresponding counter ion is being searched for in the radius r^C and identified neighbors are grouped into a common cluster. The transparent ions represent neighboring counter ions detected on the other side of the periodic boundary conditions. Right: categorization of the ions into clusters of the same color.

In this chapter, the information obtained by the cluster analysis is condensed into a single, intensive observable: the fraction of the number of ions in clusters that contain j or more ions, denoted as $\bar{X}^{C\text{-}j}$ in the following. It is defined as

$$\bar{X}^{C\text{-}j} = \frac{\left\langle \sum_{i=1}^{M^{C\text{-}j}} N_i^C \right\rangle}{N_{A^+} + N_{B^-}} \, , \tag{30}$$

where the summation runs over all ion clusters in the solution, M^{C-j} is the number of clusters with j or more ions, N_i^C is the number of ions in the cluster i, and N_{A^+} and N_{B^-} are the total numbers of cations and anions in the simulation box, respectively. The angular brackets denote the ensemble average, which in this case corresponds to the time average of the investigated length of the production run. For a given state point of an electrolyte solution, the property $\bar{X}^{C\text{-}j}$ depends on three variables: the minimum cluster size j considered in the evaluation, the neighbor search radius r^C (which is equivalent to the first minimum position in the cation–anion RDF), and the length of the production run τ. Furthermore, by virtue of the molecular simulations as such, the cluster distribution might be influenced by the system size. The potential

influences of all these parameters on the outcome of the cluster analysis are investigated in Section 7.3.1.

7.3 Results and Discussion

7.3.1 Influence Parameters on the Property $\bar{X}^{\text{C-}j}$

7.3.1.1 Influence of the Minimal Cluster Size j and the System Size

Figure 30 shows the cluster size distribution of RDVH-NaCl in SPC/E water for three different salt concentrations and two different system sizes: $4\,000$ particles (as used in the remainder of this chapter) and $20\,000$ particles. Note that simulations were carried out at many more concentrations, but only those three are shown here to keep the presentation as simple as possible. Both system sizes show that at the lowest concentration (x_{Na^+} = 0.02 mol mol^{-1}), only single ions, ion pairs, and very few clusters containing three ions are found. At the concentration that is close to the salt solubility (x_{Na^+} = 0.085 mol mol^{-1}), again single ions are predominant, the extent of ion pairing becomes quite noticeable, and clusters of up to six ions are observed. At the highest concentration (x_{Na^+} = 0.15 mol mol^{-1}), corresponding to a highly supersaturated solution, clusters of up to 20 ions are found. In other simulations at similar concentrations, occasionally also somewhat larger clusters were observed. These clusters had an elongated, filamentous, and amorphous shape. One example of such a large cluster is discussed in Appendix E. Similarly shaped clusters have been reported by Lanaro and Patey [240]. In general, for all concentrations, the cluster distribution peaks at 1, which means that most ions are present as single ions, even at high concentrations. Moreover, with increasing cluster size, the cluster size distribution rapidly decreases and approaches zero, resembling an exponential decay.

Qualitatively, irrespective of system size, the cluster distributions are similar if the same salt concentration is investigated. At the same salt concentration, the only difference between the smaller and larger systems is the actual number of clusters of a certain size, which is of course larger for the larger systems. Quite interestingly, at the lowest concentration (x_{Na^+} = 0.02 mol mol^{-1}), the smaller system size tends to favor ion pairing over the larger one, but at and above the solubility, that trend reverses. However, there is considerable uncertainty in this interpretation due to the fluctuations in the cluster size distributions indicated by the error bars, especially at low concentrations. Notwithstanding and most importantly for the remainder of the present chapter, clusters containing six or more ions are only found at or above the salt solubility independent of system size.
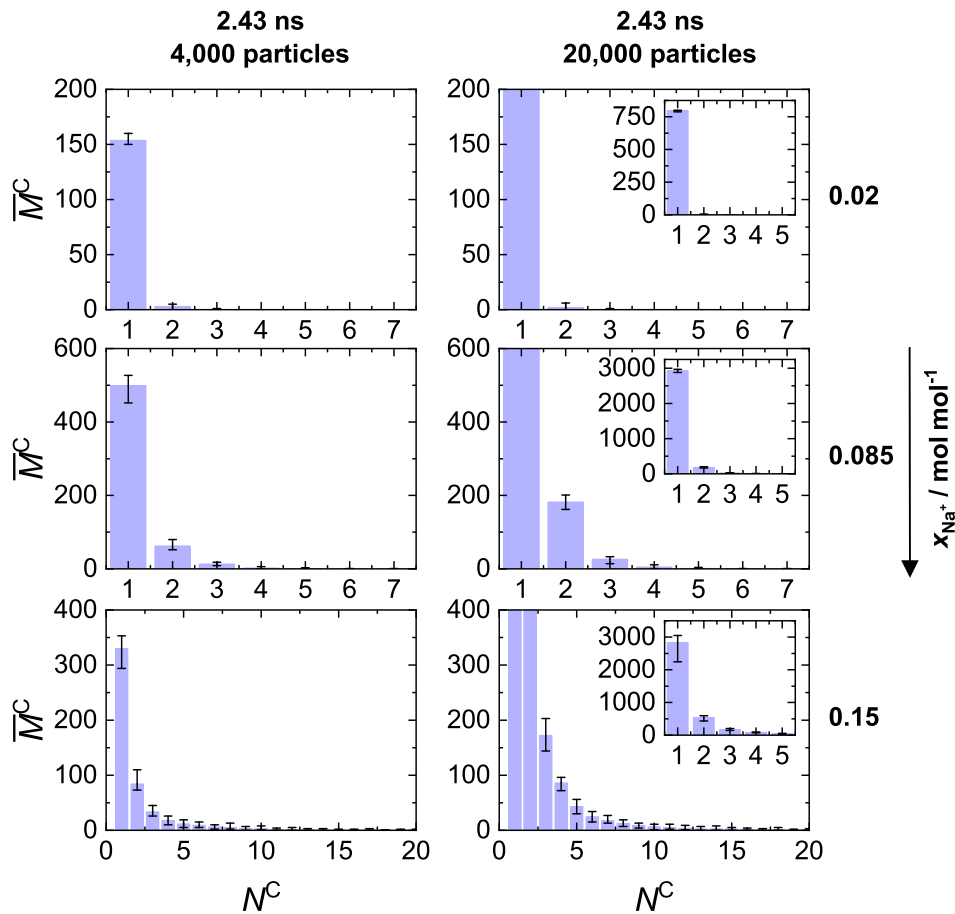
Figure 30: The mean number of clusters $\bar{M}^{\mathrm{C}}$ as a function of the number of ions per cluster N^{C} at 298 K and 1 bar for simulations for different cation mole fractions of the RDVH-NaCl model in SPC/E water. Simulations in the left column had the same system size and the same length of the production run as used in the rest of this chapter. The right column shows simulations with exactly the same simulation settings, only the number of particles is increased five-fold. Plots that are in the same row have the same axis limits for $\bar{M}^{\mathrm{C}}$ to enable a straightforward comparison between the different system sizes, while the insets in the right column focus on the smallest cluster sizes with the highest number of clusters. The concentration shown in the middle row (i.e., 0.085 mol mol^{-1}) corresponds to the salt solubility (cf. Table 14). The error bars contain 98 % of the data points of the respective cluster size obtained over the course of the production run of each simulation. The values of the cluster radius r^{C} are in the range of 3.58 Å – 3.83 Å (cf. Figure 32).

Figure 31 shows the lowest mole fraction $x^{*}_{\mathrm{Na}^{+}}$ at which the property $\bar{X}^{\mathrm{C}\text{-}j}$ (cf. Eq. (30)) is greater than zero as a function of j for a system size of 4 000 particles. In other words, $x^{*}_{\mathrm{Na}^{+}}$ is the lowest mole fraction at which clusters of size j or higher are observed at least once during the simulation.
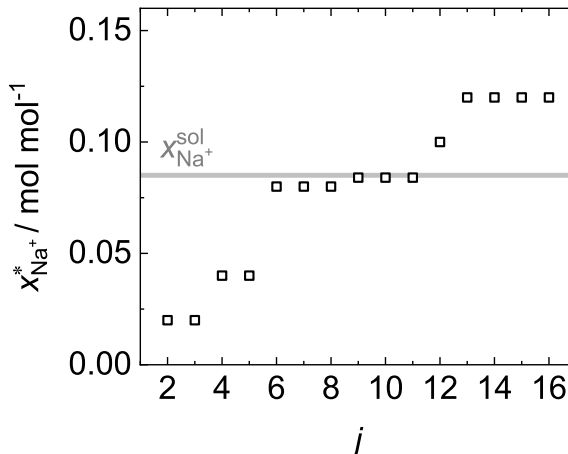
Figure 31: The lowest mole fraction $x^*_{Na^+}$ at which $\bar{X}^{C\text{-}j}$ is greater than zero (i.e., clusters containing j or more ions are found) as a function of j at 298 K and 1 bar for the RDVH-NaCl model in SPC/E water. The investigated systems contained 4 000 particles. The gray shaded area depicts the solubility $x^{sol}_{Na^+}$ by Mester and Panagiotopoulos [195] including uncertainties. The values of the cluster radius r^C are in the range of 3.58 Å – 3.83 Å (cf. Figure 32).

Interestingly, for $6 \leq j \leq 11$, the mole fraction $x^*_{Na^+}$ forms a plateau, the value of which agrees well with the solubility $x^{sol}_{Na^+}$ from the literature [195]. It is gratifying that the value $j = 6$ is in accord with the smallest stable cluster size reported in the literature [239, 240, 244], but for a different NaCl model than the one studied here (JC instead of RDVH) and for much longer simulations. Based on these findings, the empirical *cluster rule* is formulated as follows: it is hypothesized that the lowest cation mole fraction $x^{sol,C\text{-}6}_{A^+}$ for which $\bar{X}^{C\text{-}6}$ is greater than zero, i.e., the concentration for which the first clusters containing six or more ions are observed, can serve as a rough estimate for the salt solubility. The cluster rule is assessed from Section 7.3.2 onwards.

7.3.1.2 Influence of the Ion Mole Fraction on the RDF and the First Minimum

The first minimum position of the cation–anion RDF was chosen as the cluster search radius r^C. This choice obviously has some influence on the obtained cluster size distribution and, in turn, also on $\bar{X}^{C\text{-}6}$. Therefore, the influence of the salt concentration on the RDF was investigated, with a special attention on the position of the first minimum. Figure 32 shows the cation–anion RDFs and the corresponding positions of the first minimum from simulations of RDVH-NaCl in SPC/E water at different salt concentrations.
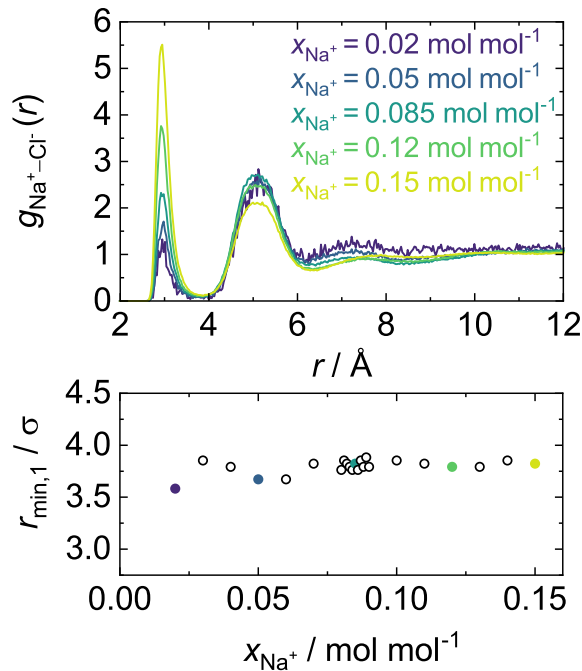
Figure 32: The cation–anion radial distribution functions (top panel) and the corresponding position of the first minimum r_{min1} (bottom panel) as a function of the mole fraction of the cation at 298 K and 1 bar for the RDVH-NaCl model in SPC/E water. The colors of the filled circles in the bottom panel correspond to the radial distribution function shown in the same color in the top panel. r_{min1} is used as the neighbor search radius r^C for the cluster algorithm (cf. Figure 29).

As expected, with increasing concentration the height of the first peak in the cation–anion RDF also increases, which corresponds to an increased number of ion pairs. This furthermore indicates that clustering might be more prevalent at higher concentrations (cf. Figures 30 and 31). The height of the first minimum is roughly the same for all concentrations, while the height of the second maximum decreases with increasing concentration. The positions of the first and second maxima, and, most importantly for the present chapter, the position of the first minimum, are practically independent of composition, even when considering highly supersaturated solutions. Some fluctuations in the first minimum position with increasing salt concentration are evident at low concentrations, but for solutions in the vicinity of the solubility limit or beyond it, practically the same value is obtained for the first minimum position. Hence, the variation of r_{min1} with concentration is small, so that its value – which is used as the neighbor search radius r^C – has no noticeable impact on the outcome of the cluster algorithm.

7.3.1.3 Influence of the Length of the Production Run

Figure 33 shows the running average of the property $\bar{X}^{\text{C-6}}$ as a function of simulation time of RDVH-NaCl in SPC/E water for three different salt concentrations. The simulations shown there were ten times longer than the other simulations shown in the rest of this chapter.
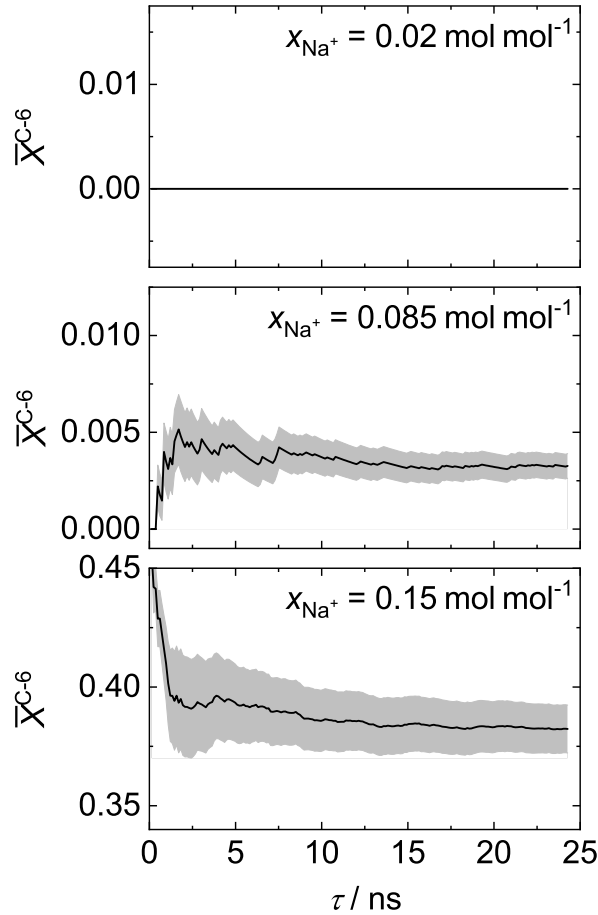
Figure 33: The running average of the property $\bar{X}^{\text{C-6}}$ as a function of production time τ at 298 K and 1 bar for the RDVH-NaCl model in SPC/E water for different salt concentrations. The concentration shown in the middle panel corresponds to the salt solubility (cf. Table 14). The gray shaded area denotes the standard deviation of the data up to the simulation time τ. The values of the cluster radius r^{C} are in the range of 3.58 Å – 3.83 Å (cf. Figure 32).

At the lowest concentration, clusters of size six are never found, even if simulations are run for 24.3 ns. At the salt concentration that is close to the salt solubility (x_{Na^+} = 0.085 mol mol^{-1}), the first clusters containing more than six ions emerge after about 0.4 ns, and $\bar{X}^{\mathrm{C\text{-}6}}$ stays greater than zero and slightly increases with simulation time. At the highest concentration, interestingly, $\bar{X}^{\mathrm{C\text{-}6}}$ starts from a very high value and then slightly decreases with simulation time, but stays well above zero for all times. Hence, once clusters with six or more ions form, they tend to be stable in solution, and/or grow in size with simulation time. Since the definition of the property $\bar{X}^{\mathrm{C\text{-}6}}$ includes all ions in clusters of size six or larger, these growing clusters are explicitly considered in the analysis. Moreover, it seems that a production run of about 2.4 ns is sufficient to determine if clusters with size six or larger will form during a simulation or not.

7.3.2 Results for the NaCl Models with SPC/E water

Figure 34 illustrates the use and the results of the ion pairs rule of Benavides et al. for the three investigated NaCl models with SPC/E water: it shows the number of contact ion pairs as a function of salt concentration. In order to evaluate $x_{\mathrm{Na}^+}^{\mathrm{sol,CIP}}$ from the ion pairs rule, a third order polynomial was fitted to the simulation results and evaluated for the ion mole fraction for which n_{CIP} = 0.5. In the case of the JC model, even at very high concentrations corresponding to highly supersaturated solutions, no values of n_{CIP} in the proximity of 0.5 were obtained, so that the polynomial had to be extrapolated quite considerably. However, for the present discussion it suffices to know that the concentration for which n_{CIP} = 0.5 is much larger than the actual solubility, at least by a factor of two. In principle, in all three cases the general statement of the ion pairs rule holds: the number of contact ion pairs at the solubility reported in the literature is lower than 0.5. In the case of the RDVH model, $x_{\mathrm{Na}^+}^{\mathrm{sol,CIP}}$ is actually quite close to the literature solubility value, such that the ion pairs rule provides a useful estimate of the true solubility. However, for the other two models, $x_{\mathrm{Na}^+}^{\mathrm{sol,CIP}}$ is much larger than the solubility reported in the literature: for the JC model, $x_{\mathrm{Na}^+}^{\mathrm{sol,CIP}}$ is three times greater and for the SD model, it is seven times greater. As a result, since $x_{\mathrm{Na}^+}^{\mathrm{sol,CIP}}$ is the estimated upper limit of the solubility, the ion pairs rule leaves a wide margin for the concentration range in which one may assume that the salt is completely soluble when in fact it is not.

For comparison, Figure 35 shows the results of the evaluation of the cluster analysis algorithm. There, the property $\bar{X}^{\mathrm{C\text{-}6}}$ is depicted as a function of salt concentration for the three investigated NaCl models. Also, the results of the solubility determined with the ion pairs rule is shown (cf. Figure 34).
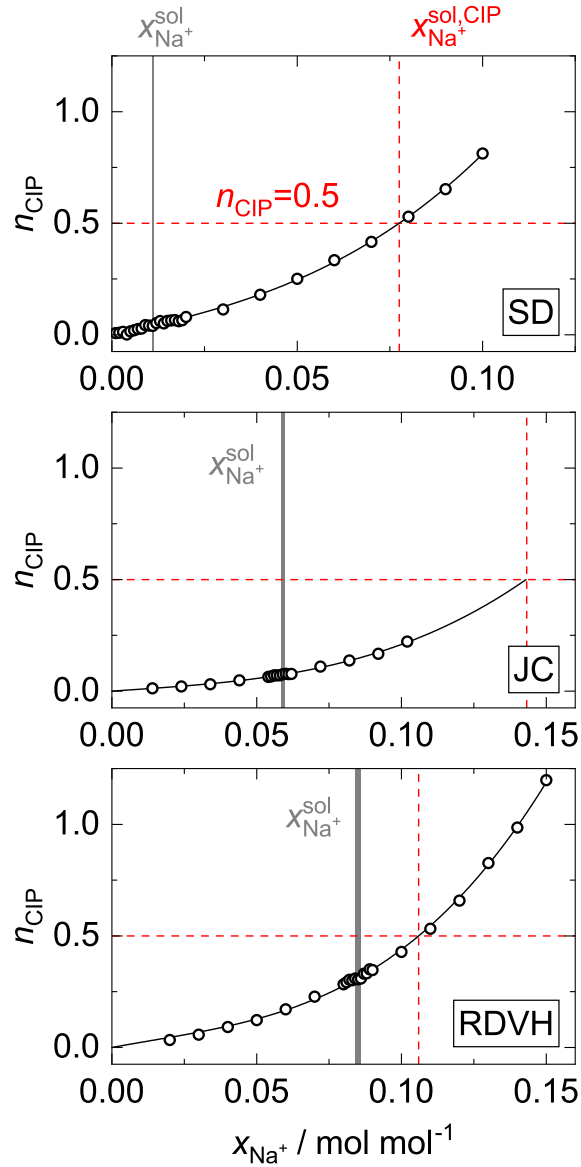
Figure 34: The number of contact ion pairs n_{CIP} as a function of the mole fraction of Na$^+$ at 298 K and 1 bar of all investigated NaCl models (SD, JC, RDVH) in SPC/E water. The vertical red dashed line corresponds to the solubility $x_{\mathrm{Na}^+}^{\mathrm{sol,CIP}}$ determined with the ion pairs rule [56, 57]. The gray shaded area depicts the solubility $x_{\mathrm{Na}^+}^{\mathrm{sol}}$ reported by Mester and Panagiotopoulos [195] including uncertainties. The solid black line corresponds to a third order polynomial used to determine $n_{\mathrm{CIP}} = 0.5$ and hence $x_{\mathrm{Na}^+}^{\mathrm{sol,CIP}}$.
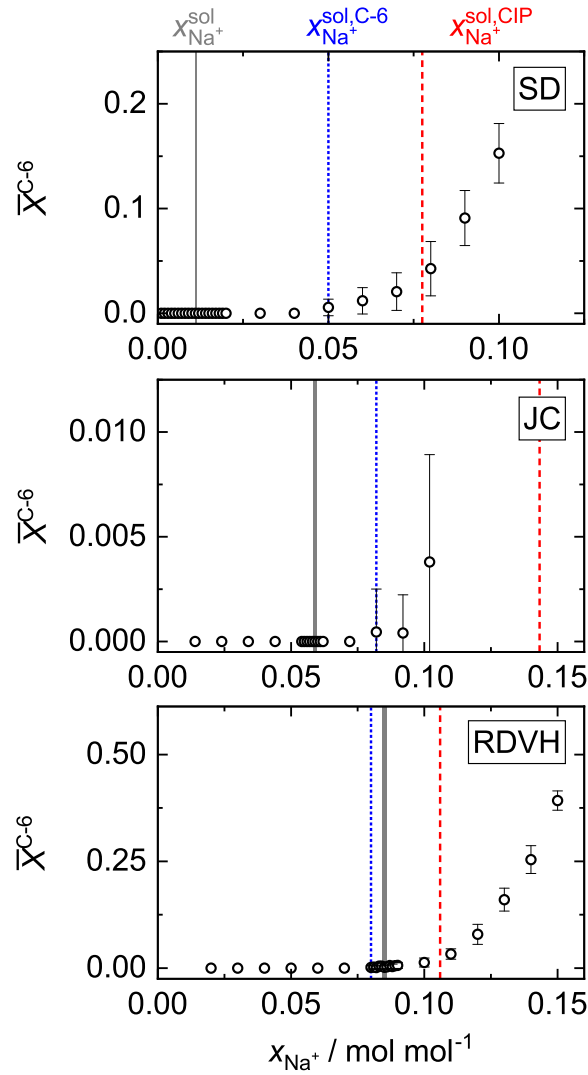
Figure 35: The property $\bar{X}^{\text{C-6}}$ as a function of the mole fraction of Na$^+$ at 298 K and 1 bar of all investigated NaCl models (SD, JC, RDVH) in SPC/E water. The vertical blue dotted line corresponds to the lowest mole fraction at which clusters with six or more ions occur. The vertical red dashed line corresponds to the solubility $x_{\text{Na}^+}^{\text{sol,CIP}}$ determined with the ion pairs rule [56, 57] (cf. Figure 34). The gray shaded area depicts the solubility $x_{\text{Na}^+}^{\text{sol}}$ reported by Mester and Panagiotopoulos [195] including uncertainties.

It is found that for all three NaCl models investigated here, the concentration at which clusters of six or more ions are found is closer to the solubility reported in the literature than the solubility estimated by the ion pairs rule. In the case of the SD and JC models, the cluster rule overestimates the solubility from the literature, while for the RDVH model, the solubility is slightly underestimated. However, slightly underestimating the solubility is actually preferable compared to overestimating it, since that prevents studying state points for which the solution is supersaturated. Furthermore, for the SD model both schemes highly overestimate the solubility reported in the literature. However, the SD model for NaCl is quite different from the other two in that it quite drastically underestimates the solubility of real NaCl.

7.3.3 Results for the JC-TIP4P-Ew-NaCl Model

Figure 36 shows the properties n_{CIP} and $\bar{X}^{\mathrm{C-6}}$ as a function of the salt concentration for the JC-TIP4P-Ew-NaCl model.

Figure 36: The number of contact ion pairs n_{CIP} (top panel) and the property $\bar{X}^{\mathrm{C-6}}$ (bottom panel) as functions of the salt concentration at 298 K and 1 bar for the JC-TIP4P-Ew-NaCl model. The vertical blue dotted line corresponds to the lowest mole fraction at which clusters with six or more ions occur. The vertical red dashed line corresponds to the solubility $x_{\mathrm{Na}^+}^{\mathrm{sol,CIP}}$ determined with the ion pairs rule [56, 57]. The gray shaded area depicts the solubility $x_{\mathrm{Na}^+}^{\mathrm{sol}}$ reported by Manzanilla-Granados [231] including uncertainties.

As for the JC-NaCl model with SPC/E, the number of contact ion pairs had to be extrapolated significantly to reach a concentration for which n_{CIP} reaches 0.5. Thus, the

ion pairs rule overestimates the solubility of JC-NaCl also in TIP4P-Ew water. By contrast, the cluster rule matches the solubility data reported by Manzanilla-Granados [231] well, showing its usefulness irrespective of the used water model.

7.3.4 Results for the JC-KCl Model

Figure 37 shows the properties n_{CIP} and $\bar{X}^{\mathrm{C\text{-}6}}$ as a function of the salt concentration for solutions of the JC-KCl model in SPC/E water.

Figure 37: The number of contact ion pairs n_{CIP} (top panel) and the property $\bar{X}^{\mathrm{C\text{-}6}}$ (bottom panel) as functions of the salt concentration at 298 K and 1 bar for solutions of JC-KCl in SPC/E water. The vertical blue dotted line corresponds to the lowest mole fraction at which clusters with six or more ions occur. The vertical red dashed line corresponds to the solubility $x_{\mathrm{K}^+}^{\mathrm{sol,CIP}}$ determined with the ion pairs rule [56, 57]. The gray shaded area depicts the solubility $x_{\mathrm{K}^+}^{\mathrm{sol}}$ reported by Mester and Panagiotopoulos [195] including uncertainties.

The findings are qualitatively similar to the results obtained for the NaCl models. The ion pairs rule yields a broad concentration range in which the salt is estimated to be soluble and overestimates the solubility reported in the literature. The cluster analysis underestimates the solubility slightly, but as mentioned before this is actually the preferred case from a practical standpoint.

7.3.5 Results for the RVDH-NaI Model

Figure 38 shows the properties n_{CIP} and $\bar{X}^{C\text{-}6}$ as a function of the salt concentration for solutions of the RDVH-NaI model in SPC/E water.
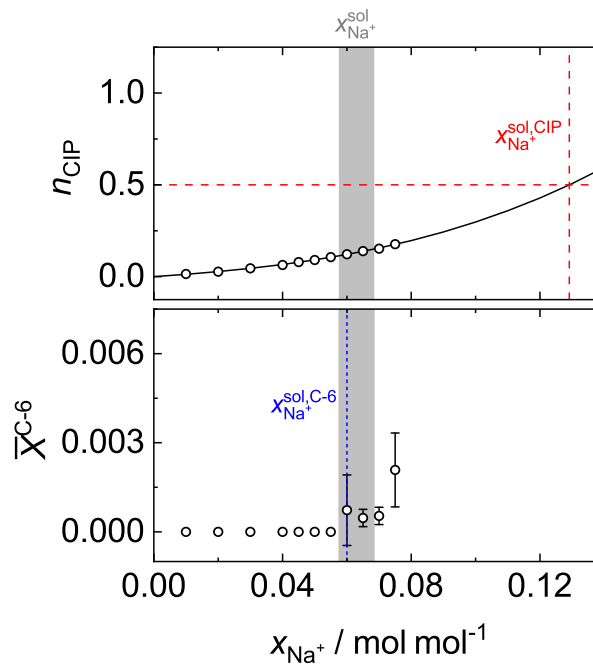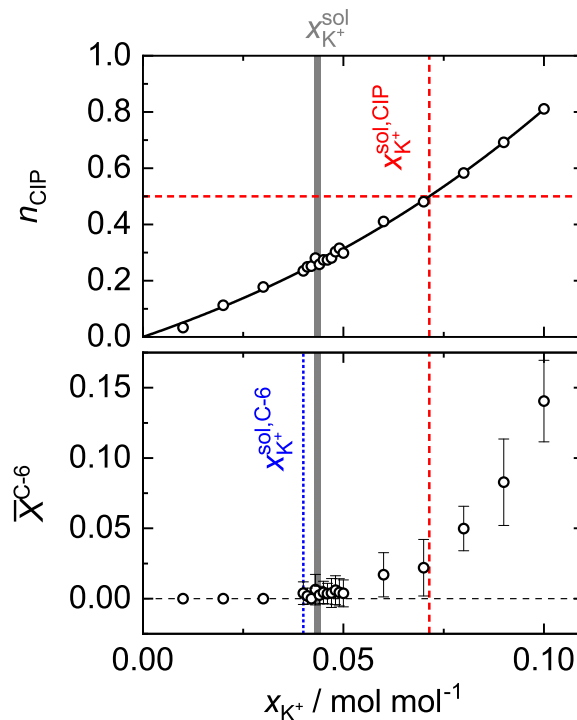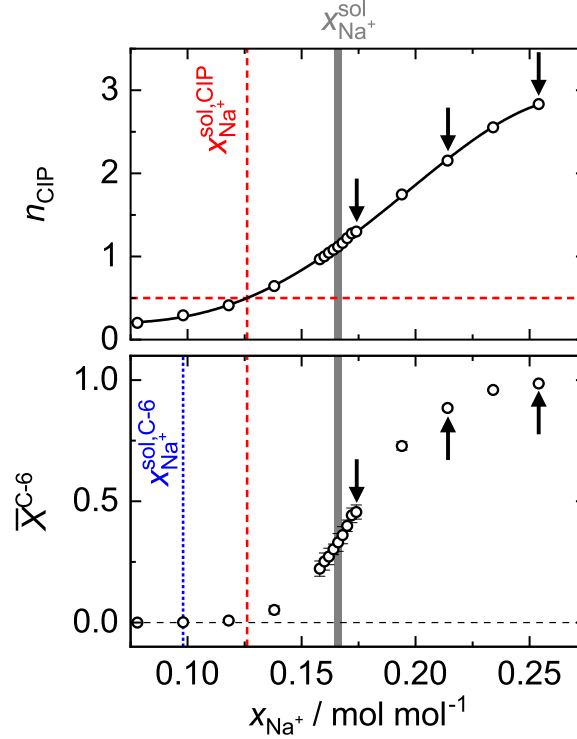

Figure 38: The number of contact ion pairs n_{CIP} (top panel) and the property $\bar{X}^{C\text{-}6}$ (bottom panel) as functions of the mole fraction of Na^+ at 298 K and 1 bar for solutions of RDVH-NaI in SPC/E water. The vertical blue dotted line corresponds to the lowest mole fraction at which clusters with six or more ions occur. The vertical red dashed line corresponds to the solubility $x_{Na^+}^{sol,CIP}$ determined with the ion pairs rule [56, 57]. The gray shaded area depicts the range of the solubility $x_{Na^+}^{sol}$ from the literature [195]. The black arrows indicate the simulations from which the snapshots shown in Figure 39 were captured.

In contrast to the examples discussed before, both rules underestimate the solubility reported in the literature. In agreement with the results reported by Benavides et al. [57] for this model combination, the value of n_{CIP} is about 1.2 to 1.3 at the solubility. In the study of Benavides et al., RDVH-NaI was the only model for which n_{CIP} at the solubility reported in the literature was much larger than 0.5. This finding was attributed to the size difference of the ions, which leads to a lower chemical potential of the NaI crystal.

The values of both n_{CIP} and the property $\bar{X}^{C\text{-}6}$ reach significantly higher values compared to the NaCl and KCl simulations (cf. Figures 34 and 35), which means anions and cations

coordinate closely and large clusters are observed. Beyond the solubility, the slopes of both n_{CIP} and $\bar{X}^{\mathrm{C\text{-}6}}$ decrease with increasing salt concentration, in contrast to what is observed for the NaCl and KCl models. The property $\bar{X}^{\mathrm{C\text{-}6}}$ approaches a value of 1 at the highest cation mole fraction, which means nearly all ions coordinate in clusters of six or more ions.

To elaborate more on this interesting finding, Figure 39 shows snapshots at the end of three simulations with different salt concentrations. The corresponding cation mole fractions are marked with arrows in Figure 38, i.e., $x_{\mathrm{Na^+}}$ = 0.174, 0.214, 0.254 mol mol^{-1}.
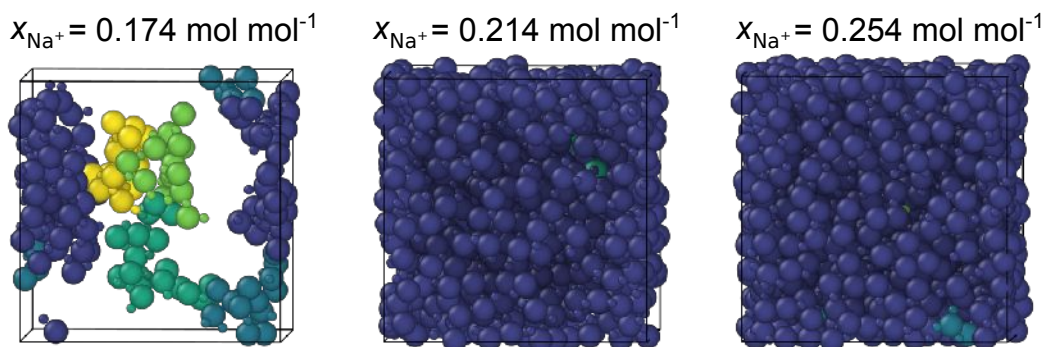
Figure 39: Snapshots taken at the end of the simulation of RDVH-NaI in SPC/E water for three mole fractions beyond the solubility reported in the literature [195] at 298 K and 1 bar (cf. black arrows in Figure 38). Only the five largest ion clusters are shown and categorized by color (dark blue: largest cluster, turquoise: 2$^{\mathrm{nd}}$ largest cluster, dark green: 3$^{\mathrm{rd}}$ largest cluster, light green: 4$^{\mathrm{th}}$ largest cluster, yellow: 5$^{\mathrm{th}}$ largest cluster); water is not shown to improve clarity.

With increasing concentration, more ions coordinate in increasingly bigger clusters, which eventually fill the entire simulation box, as can be seen at the two highest cation mole fractions. At the highest cation mole fraction, at which $\bar{X}^{\mathrm{C\text{-}6}}$ approaches 1, the ratio of NaI to water is 1:2.

While this investigation gives no strict proof for it, these findings support the hypothesis that for the combination of the RDVH-NaI model and SPC/E water, the salt precipitates as the dihydrate $\mathrm{NaI} \cdot 2\,\mathrm{H_2O}$ rather than the pure NaI crystal. It is quite intriguing that also real NaI precipitates as the dihydrate at 298 K and 1 bar [246]. However, the solubility reported by Mester and Panagiotopoulos [195] was determined under the assumption that the pure NaI crystal forms and is therefore not applicable to the dihydrate case. Both methods to calculate the solubility exactly – the direct coexistence method and the chemical potential method – rely on a priori knowledge of the solid phase. The results of this study indicate that investigating the structure of the solution closely,

especially with the help of a cluster algorithm, allows for detecting situations in which the formation of hydrates might occur.

This is an important aspect because in reality, the stable form of the precipitating crystal – i.e., whether a hydrate forms and if it does, with how many water molecules – strongly depends on temperature for many electrolytes in aqueous solution. In the case of NaI investigated here, the dihydrate forms at ambient temperature, but below -12.3 °C the pentahydrate $NaI \cdot 5\,H_2O$ forms [246]. Taking NaCl as a further example, at room temperature the pure NaCl crystal forms, but at temperatures below 0 °C, the dihydrate $NaCl \cdot 2\,H_2O$ is the stable solid form [247]. Many alkali and alkaline earth metal halide salts behave similarly, i.e., they form different hydrates depending on temperature [247].

However, it is not guaranteed that molecular models correctly reproduce this behavior. Molecular models might form different hydrates or non-hydrates that might not be expected when simply looking at what the real electrolyte does in experiments. To the best of the author's knowledge, the only case in which this topic has been thoroughly investigated is the $CaCl_2$ study of Moučka et al. [224]. It is known from experiments that this electrolyte precipitates as the hexahydrate at ambient temperature, but the the dihydrate forms at temperatures above 318 K. However, Moučka et al. found that for the investigated molecular model, only the dihydrate is stable at both temperatures and, hence, the model most likely forms the dihydrate at both temperatures. Investigating the structure of the simulated system closely, e.g., with the help of a cluster algorithm such as the one used in the present chapter, is one way to at least keep this important aspect in mind. In general, hydrate-forming systems are interesting candidates to investigate nucleation kinetics in future works, since nucleation events of hydrates are more probable compared to pure ion crystals because water is part of the forming solid and must not be absent from the nucleation site, which is the case for non-hydrates.

7.4 Conclusions

The structure of electrolyte solutions was investigated with molecular dynamics simulations, using a neighbor search algorithm to identify ion clusters [145]. The information of the cluster size distribution was condensed into a single, intensive property: the fraction $\bar{X}^{\text{C-6}}$ of ions in clusters containing six or more ions. It was found that the lowest concentration at which the first clusters with six or more ions occur, i.e., for which $\bar{X}^{\text{C-6}}$ is greater than zero, is a good indicator to estimate the salt solubility. Together with the ion pairs rule by Benavides et al. [57], this cluster rule was assessed using eight molecular models of alkali halides in water for which solubility data are available in the literature. Overall, reasonable agreement was obtained between these reference data and the two empirical rules, given their simplicity, with the cluster rule slightly outperforming the ion pairs rule. For the case of aqueous NaI, the cluster analysis further revealed that the emerging salt crystal might actually be the dihydrate, as is the case for real NaI in aqueous solution and in contrast to what has been assumed in the literature thus far.

8 Conclusions

In this work, several related research topics from engineering that can only be studied by molecular simulations were tackled.

The results from both the stationary and non-stationary mass transfer scenario developed in this work strongly support the hypothesis that interfacial properties influence mass transfer through fluid interfaces. Even though both investigated LJTS mixtures show similar mass transfer behavior in the bulk phases, there is a significant difference in the interfacial region, i.e., for mixtures with low cross interaction energy, the mass transfer is severely hampered. In the case of the non-stationary scenario, the interfacial mass transfer resistance can eventually become large enough to temporarily reduce or completely stop the flux through the interface and accordingly particles are reflected at the interface. The simulation scenarios proposed in this work are a valuable tool for further investigations, e.g., for studying state points in the vicinity of a critical point, ternary mixtures, real substance mixtures as well as liquid-liquid interfaces.

Furthermore, in this work, the behavior of an LJTS nanodroplet perturbed by a sudden temperature increase in its center was systematically investigated. Depending on the set temperature, three different types of behavior were observed: (i) the shrinking droplet, (ii) expanding droplet, and (iii) the immediate droplet break-up. In case (i), small short-lived vapor bubbles formed in the inside the droplet but overall the droplet remained its spherical shape and shrunk due to continuous evaporation. The first case only occurred at the lowest set temperature, which was still below the critical point of the fluid. In the second case, a vapor bubble nucleated inside of the droplet and pushed the surrounding droplet shell outwards. Here, an oscillatory behavior in the radius of gyration and the interface positions was observed. The oscillations were caused by the interplay of the outwards-pushing vapor bubble and the force exerted by the interface to counteract the increase in its area. Case (ii) occurred at the three intermediate set temperatures. At the two highest set temperatures, the emerging vapor bubble tore the droplet shell immediately apart and the droplet broke into smaller droplets.

The present study was carried out for the LJTS model fluid, which can represent only simple fluids such as noble gases and methane reasonably well. It would be interesting to extend the study to more complex fluids and to mixtures. However, this requires

the availability of reliable molecular models for the components. For such models, the treatment of long-range interactions, which is by definition not needed for the LJTS fluid, is challenging, especially when ionic species are included. The study was motivated by droplet explosions that have been observed in combustion processes and spray flame synthesis. However, in the processes, the superheating does not occur in the center of the droplet, but rather in some shell below the droplet's surface [133]. It would be interesting to extend the present simulation scenario to that case. Furthermore, also a simulation scenario could be considered in which, as in the real processes, the heat is supplied to the gas phase surrounding the liquid, so that the position where the superheating occurs is no longer prescribed. However, also in such scenarios, very large gradients would have to be applied to observe the bubble formation within accessible simulation times. Last but not least, the transfer of the knowledge obtained from studies of nanodroplets by NEMD simulations to larger scales should be addressed. The present study is a starting point for all this.

In addition to simulations of the mass and heat transfer of simple model fluids carried out in this work, a new set of molecular models of the alkali nitrates salts in aqueous solution was presented. The set included the alkali nitrates $LiNO_3$, $NaNO_3$, KNO_3, $RbNO_3$, and $CsNO_3$. The alkali cation models were taken from the model set of Reiser at al. [164] and Deublein et al. [163] and water was represented by the SPC/E water model. No adjustments were made to cross interaction parameters and, hence, the model set was deployed in a strictly predictive manner. Thermophysical and structural properties of the model set, namely the density, the water activity and the mean ionic activity coefficient, the self-diffusion coefficients, and the RDF, were rigorously compared with experimental data from the literature. Especially the predictions of the density and the RDF were in good agreement with experimental data from the literature. For most model combinations, the water activity and the mean ionic activity coefficient also showed remarkable agreement in comparison to the experimental data – the only exception being $LiNO_3$. Overall, the good agreement of all investigated properties with experimental data is surprising, considering the fact that the molecular models for the nitrate anion and the cations were developed independently by different authors and no cross-interactions were adjusted. The presented set of molecular models is a promising tool to further investigate the influence of mixtures of different alkali nitrate salts or mixtures of alkali nitrate and halide salts on thermophysical properties of the aqueous solution, since the set is part of a consistent model family that has provided good predictions for solutions of single salts.

One key physical property of electrolyte models in molecular simulations, such as the alkali nitrates mentioned above, is the solubility. Without knowledge of the solubility of a model combination, one may simulate what could be considered a metastable state

instead of a homogeneous fully solvated solute + solvent mixture. Therefore, the structure of electrolyte solutions and the cluster formation were investigated in this work in a broad concentration range for six different 1:1 electrolyte models. Based on these findings, an empirical rule was proposed for the estimation of the solubility: the solubility is reached at the concentration at which the first clusters containing 6 or more ions are found. This *cluster rule* showed reasonable agreement with the solubility data from the literature and in all cases gave estimates closer the literature data than a similar empirical rule by Benavides and coworkers [56, 57]. Moreover, the cluster simulations implied that one of the models, NaI, may precipitate in the form of the dihydrate $NaI \cdot 2\ H_2O$, while the literature assumed that it precipitates in the form of the pure crystal. Altogether, the insights of the present work provide a point of departure for further investigations on how structuring and clustering of ions in electrolyte solutions relate to the salt solubility. Key advantages of the employed cluster distribution analysis include that it is simple to use, e.g., in post-processing, and does not need any knowledge of the emerging crystal, sophisticated evaluation schemes, or excessive simulation times.

Literature

[1] N. Metropolis, A. W. Rosenbluth, M. N. Rosenbluth, A. H. Teller, E. Teller: Equation of state calculations by fast computing machines, The Journal of Chemical Physics 21 (1953) 1087–1092. DOI:`10.1063/1.1699114`.

[2] B. J. Alder, T. E. Wainwright: Phase transition for a hard sphere system, The Journal of Chemical Physics 27 (1957) 1208–1209. DOI:`10.1063/1.1743957`.

[3] E. J. Maginn, J. R. Elliott: Historical perspective and current outlook for molecular dynamics as a chemical engineering tool, Industrial & Engineering Chemistry Research 49 (2010) 3059–3078. DOI:`10.1021/ie901898k`.

[4] D. N. Theodorou: Progress and outlook in Monte Carlo simulations, Industrial & Engineering Chemistry Research 49 (2010) 3047–3058. DOI:`10.1021/ie9019006`.

[5] S. Becker, S. Werth, M. Horsch, K. Langenbach, H. Hasse: Interfacial tension and adsorption in the binary system ethanol and carbon dioxide: Experiments, molecular simulation and density gradient theory, Fluid Phase Equilibria 427 (2016) 476–487. DOI:`10.1016/j.fluid.2016.08.007`.

[6] W. Li, Z. Jin: Molecular dynamics simulation of natural gas-water interfacial tensions over wide range of pressures, Fuel 236 (2019) 480–492. DOI:`10.1016/j.fuel.2018.09.040`.

[7] W. A. Fouad, L. F. Vega: The phase and interfacial properties of azeotropic refrigerants: the prediction of aneotropes from molecular theory, Physical Chemistry Chemical Physics 19 (2017) 8977–8988. DOI:`10.1039/C6CP08031F`.

[8] O. G. Niño-Amézquita, D. van Putten, S. Enders: Phase equilibrium and interfacial properties of water+CO_2 mixtures, Fluid Phase Equilibria 332 (2012) 40–47. DOI:`10.1016/j.fluid.2012.06.018`.

[9] O. G. Niño-Amézquita, S. Enders: Phase equilibrium and interfacial properties of water+methane mixtures, Fluid Phase Equilibria 407 (2016) 143–151. DOI:`10.1016/j.fluid.2015.05.005`.

[10] F. Llovell, N. M. Dowell, F. J. Blas, A. Galindo, G. Jackson: Application of the SAFT-VR density functional theory to the prediction of the interfacial properties of mixtures of relevance to reservoir engineering, Fluid Phase Equilibria 336 (2012) 137–150. DOI:`10.1016/j.fluid.2012.07.033`.

[11] S. Enders, H. Kahl: Interfacial properties of water + alcohol mixtures, Fluid Phase Equilibria 263 (2008) 160–167. DOI:`10.1016/j.fluid.2007.10.006`.

[12] T.-M. Chang, L. X. Dang: Liquid-vapor interface of methanol-water mixtures: A molecular dynamics study, Journal of Physical Chemistry B 109 (2005) 5759–5765. DOI:`10.1021/jp045649v`.

[13] A. H. Falls, L. E. Scriven, H. T. Davis: Adsorption, structure, and stress in binary interfaces, The Journal of Chemical Physics 78 (1983) 7300–7317. DOI:`10.1063/1.444720`.

[14] S. Stephan, K. Langenbach, H. Hasse: Interfacial properties of binary Lennard-Jones mixtures by molecular simulations and density gradient theory, The Journal of Chemical Physics 150 (2019) 174704. DOI:`10.1063/1.5093603`.

[15] S. Stephan, S. Becker, K. Langenbach, H. Hasse: Vapor-liquid interfacial properties of the system cyclohexane + CO_2: Experiments, molecular simulation and density gradient theory, Fluid Phase Equilibria 518 (2020) 112583. DOI:`10.1016/j.fluid.2020.112583`.

[16] E. A. Müller, A. Mejía: Interfacial properties of selected binary mixtures containing n-alkanes, Fluid Phase Equilibria 282 (2009) 68–81. DOI:`10.1016/j.fluid.2009.04.022`.

[17] C. Miqueu, J. M. Miguez, M. M. Piñeiro, T. Lafitte, B. Mendiboure: Simultaneous application of the gradient theory and Monte Carlo molecular simulation for the investigation of methane/water interfacial properties, Journal of Physical Chemistry B 115 (2011) 9618–9625. DOI:`10.1021/jp202276k`.

[18] S. Stephan, H. Cárdenas, A. Mejía, E. A. Müller: The monotonicity behavior of density profiles at vapor-liquid interfaces of mixtures, Fluid Phase Equilibria 564 (2023) 113596. DOI:`10.1016/j.fluid.2022.113596`.

[19] R. Nagl, P. Zimmermann, T. Zeiner: Interfacial mass transfer in water-toluene systems, Journal of Chemical & Engineering Data 2 (2020) 328–336. DOI:`10.1021/acs.jced.9b00672`.

[20] S. Stephan, K. Langenbach, H. Hasse: Enrichment of components at vapour-liquid interfaces: A study by molecular simulation and density gradient theory, Chemical Engineering Transactions 69 (2018) 295–300. DOI:`10.3303/CET1869050`.

[21] C. Klink, J. Gross: A density functional theory for vapor-liquid interfaces of mixtures using the perturbed-chain polar statistical associating fluid theory equation of state, Industrial & Engineering Chemistry Research 53 (2014) 6169–6178. DOI:`10.1021/ie4029895`.

[22] D. J. Lee, M. M. Telo da Gama, K. E. Gubbins: The vapour-liquid interface for a Lennard-Jones model of argon-krypton mixtures, Molecular Physics 53 (1984) 1113–1130. DOI:`10.1080/00268978400102891`.

[23] M. M. Telo da Gama, R. Evans: The structure and surface tension of the liquid-vapour interface near the upper critical end point of a binary mixture of Lennard-Jones fluids I. the two phase region, Molecular Physics 48 (1983) 229–250. DOI:`10.1080/00268978300100181`.

[24] J. M. Garrido, M. M. Piñeiro, A. Mejía, F. J. Blas: Understanding the interfacial behavior in isopycnic Lennard-Jones mixtures by computer simulations, Physical Chemistry Chemical Physics 18 (2016) 1114–1124. DOI:`10.1039/C5CP06562C`.

[25] B. Karlsson, R. Friedman: Dilution of whisky - the molecular perspective, Scientific Reports 7 (2017) 1–9. DOI:`10.1038/s41598-017-06423-5`.

[26] S. Stephan, D. Schaefer, K. Langenbach, H. Hasse: Mass transfer through vapour-liquid interfaces: a molecular dynamics simulation study, Molecular Physics 119 (2020) e1810798. DOI:`10.1080/00268976.2020.1810798`.

[27] D. Schaefer, S. Stephan, K. Langenbach, M. T. Horsch, H. Hasse: Mass transfer through vapor–liquid interfaces studied by non-stationary molecular dynamics simulations, Journal of Physical Chemistry B 127 (2023) 2521–2533. DOI:`10.1021/acs.jpcb.2c08752`.

[28] C. D. Rosebrock, T. Wriedt, L. Mädler, K. Wegner: The role of microexplosions in flame spray synthesis for homogeneous nanopowders from low-cost metal precursors, AIChE Journal 62 (2015) 381–391. DOI:`10.1002/aic.15056`.

[29] H. Li, C. D. Rosebrock, Y. Wu, T. Wriedt, L. Mädler: Single droplet combustion of precursor/solvent solutions for nanoparticle production: Optical diagnostics on single isolated burning droplets with micro-explosions, Proceedings of the Combustion Institute 37 (2019) 1203–1211. DOI:`10.1016/j.proci.2018.06.133`.

[30] C. Liu, S. Pokhrel, C. Tessarek, H. Li, M. Schowalter, A. Rosenauer, M. Eickhoff, S. Li, L. Mädler: Rare-Earth-Doped $Y_4Al_2O_9$ Nanoparticles for Stable Light-Converting Phosphors, ACS Applied Nano Materials 3 (2020) 699–710. DOI:`10.1021/acsanm.9b02231`.

[31] A. Keller: Thermodynamic Properties of Mixtures for Spray Flame Synthesis of Nanoparticles, Ph.D. thesis, University of Kaiserslautern, 2020.

[32] A. Keller, J. Burger, H. Hasse, M. Kohns: Application of the Pitzer model for describing the evaporation of seawater, Desalination 503 (2021) 114866. DOI:`10.1016/j.desal.2020.114866`.

[33] D. C. Rapaport: The Art of Molecular Dynamics Simulation, Cambridge University Press, 2004. DOI:`10.1017/cbo9780511816581`.

[34] D. Frenkel, B. Smit: Understanding Molecular Simulation: From Algorithms to Applications, Academic Press, 2002. DOI:`10.1016/B978-0-12-267351-1.X5000-7`.

[35] M. P. Allen, D. J. Tildesley: Computer Simulation of Liquids, Oxford University Press, 2017. DOI:`10.1063/1.439486`.

[36] J. Vrabec, G. K. Kedia, G. Fuchs, H. Hasse: Comprehensive study of the vapour-liquid coexistence of the truncated and shifted Lennard-Jones fluid including planar and spherical interface properties, Molecular Physics 104 (2006) 1509–1527. DOI:`10.1080/00268970600556774`.

[37] M. P. Lautenschlaeger, H. Hasse: Transport properties of the Lennard-Jones truncated and shifted fluid from non-equilibrium molecular dynamics simulations, Fluid Phase Equilibria 482 (2019) 38–47. DOI:`10.1016/j.fluid.2018.10.019`.

[38] V. R. Vasquez, E. A. Macedo, M. S. Zabaloy: Lennard-Jones viscosities in wide ranges of temperature and density: Fast calculations using a steady–state periodic perturbation method, International Journal of Thermophysics 25 (2004) 1799–1818. DOI:`10.1007/s10765-004-7736-3`.

[39] D. Fertig, H. Hasse, S. Stephan: Transport properties of binary Lennard-Jones mixtures: Insights from entropy scaling and conformal solution theory, Journal of Molecular Liquids 367 (2022) 120401. DOI:`10.1016/j.molliq.2022.120401`.

[40] S. Stephan, M. Dyga, H. M. Urbassek, H. Hasse: The influence of lubrication and the solid–fluid interaction on thermodynamic properties in a nanoscopic scratching process, Langmuir 35 (2019) 16948–16960. DOI:`10.1021/acs.langmuir.9b01033`.

[41] J. Staubach, S. Stephan: Interfacial properties of binary azeotropic mixtures of simple fluids: Molecular dynamics simulation and density gradient theory, The Journal of Chemical Physics 157 (2022) 124702. DOI:`10.1063/5.0100728`.

[42] A. Lotfi, J. Vrabec, J. Fischer: Evaporation from a free liquid surface, International Journal of Heat and Mass Transfer 73 (2014) 303. DOI:`10.1016/j.ijheatmasstransfer.2014.02.010`.

[43] S. Homes, M. Heinen, J. Vrabec, J. Fischer: Evaporation driven by conductive heat transport, Molecular Physics 119 (2020) e1836410. DOI:`10.1080/00268976.2020.1836410`.

[44] M. Heinen, S. Homes, G. Guevara-Carrion, J. Vrabec: Mass transport across droplet interfaces by atomistic simulations, in: Fluid Mechanics and Its Applications, Springer International Publishing, 2022, pp. 251–268. DOI:`10.1007/978-3-031-09008-0_13`.

[45] P. M. Rauscher, H. C. Öttinger, J. J. de Pablo: Nonequilibrium statistical thermodynamics of multicomponent interfaces, Proceedings of the National Academy of Sciences 119 (2022) e2121405119. DOI:`10.1073/pnas.2121405119`.

[46] G. Rutkai, M. Thol, R. Span, J. Vrabec: How well does the Lennard-Jones potential represent the thermodynamic properties of noble gases?, Molecular Physics 115 (2017) 1104–1121. DOI:`10.1080/00268976.2016.1246760`.

[47] P. P. Ewald: Die Berechnung optischer und elektrostatischer Gitterpotentiale, Annalen der Physik 369 (1921) 253–287. DOI:`10.1002/andp.19213690304`.

[48] H. A. Lorentz: Ueber die Anwendung des Satzes vom Virial in der kinetischen Theorie der Gase, Annalen der Physik 248 (1881) 127–136. DOI:`10.1002/andp.18812480110`.

[49] D. Berthelot: Sur le mélange des gaz, Comptes rendus de l'Académie des Sciences 126 (1898) 1703–1706.

[50] S. Stephan, J. Liu, K. Langenbach, W. G. Chapman, H. Hasse: Vapor-liquid interface of the Lennard-Jones truncated and shifted fluid: Comparison of molecular simulation, density gradient theory, and density functional theory, Journal

of Physical Chemistry C 122 (2018) 24705–24715. DOI:`10.1021/acs.jpcc.8b06332`.

[51] S. Stephan, M. Thol, J. Vrabec, H. Hasse: Thermophysical properties of the Lennard-Jones fluid: Database and data assessment, Journal of Chemical Information and Modeling 59 (2019) 4248–4265. DOI:`10.1021/acs.jcim.9b00620`.

[52] S. Stephan, H. Hasse: Interfacial properties of binary mixtures of simple fluids and their relation to the phase diagram, Physical Chemistry Chemical Physics 22 (2020) 12544–12564. DOI:`10.1039/D0CP01411G`.

[53] M. S. Green: Markoff random processes and the statistical mechanics of time-dependent phenomena. II. Irreversible processes in fluids, The Journal of Chemical Physics 22 (1954) 398–413. DOI:`10.1063/1.1740082`.

[54] R. Kubo: Statistical-mechanical theory of irreversible processes. I. General theory and simple applications to magnetic and conduction problems, Journal of the Physical Society of Japan 12 (1957) 570–586. DOI:`10.1143/jpsj.12.570`.

[55] G. A. Fernández, J. Vrabec, H. Hasse: Self Diffusion and Binary Maxwell–Stefan Diffusion in Simple Fluids with the Green–Kubo Method, International Journal of Thermophysics 25 (2004) 175–186. DOI:`10.1023/b:ijot.0000022333.07168.c4`.

[56] A. L. Benavides, J. L. Aragones, C. Vega: Consensus on the solubility of NaCl in water from computer simulations using the chemical potential route, The Journal of Chemical Physics 144 (2016) 124504. DOI:`10.1063/1.4943780`.

[57] A. Benavides, M. Portillo, J. Abascal, C. Vega: Estimating the solubility of 1:1 electrolyte aqueous solutions: the chemical potential difference rule, Molecular Physics 115 (2017) 1301–1308. DOI:`10.1080/00268976.2017.1288939`.

[58] D. Saric, M. Kohns, J. Vrabec: Dielectric constant and density of aqueous alkali halide solutions by molecular dynamics: A force field assessment, The Journal of Chemical Physics 152 (2020) 164502. DOI:`10.1063/1.5144991`.

[59] M. Lísal, J. K. Brennan, W. R. Smith, F. R. Siperstein: Dual control cell reaction ensemble molecular dynamics: A method for simulations of reactions and adsorption in porous materials, The Journal of Chemical Physics 121 (2004) 4901–4912. DOI:`10.1063/1.1782031`.

[60] G. Arya, H.-C. Chang, E. J. Maginn: A critical comparison of equilibrium, non-equilibrium and boundary-driven molecular dynamics techniques for studying

transport in microporous materials, The Journal of Chemical Physics 115 (2001) 8112–8124. DOI:`10.1063/1.1407002`.

[61] Z.Ható, D. Boda, T. Kristóf: Simulation of steady-state diffusion: Driving force ensured by dual control volumes or local equilibrium monte carlo, The Journal of Chemical Physics 137 (2012) 054109. DOI:`10.1063/1.4739255`.

[62] M. G. Martin, A. P. Thompson, T. M. Nenoff: Effect of pressure, membrane thickness, and placement of control volumes on the flux of methane through thin silicalite membranes: A dual control volume grand canonical molecular dynamics study, The Journal of Chemical Physics 114 (2001) 7174–7181. DOI:`10.1063/1.1360256`.

[63] P. Pohl, G. S. Heffelfinger, D. M. Smith: Molecular dynamics computer simulation of gas permeation in thin silicalite membranes, Molecular Physics 89 (1996) 1725–1731. DOI:`10.1080/002689796173048`.

[64] P. I. Pohl, G. S. Heffelfinger: Massively parallel molecular dynamics simulation of gas permeation across porous silica membranes, Journal of Membrane Science 155 (1999) 1–7. DOI:`10.1016/S0376-7388(98)00283-X`.

[65] J. M. D. MacElroy: Nonequilibrium molecular dynamics simulation of diffusion and flow in thin microporous membranes, The Journal of Chemical Physics 101 (1994) 5274–5280. DOI:`10.1063/1.467381`.

[66] L. Sun, J. F. Ely: Universal equation of state for engineering application: algorithm and application to non-polar and polar fluids, Fluid Phase Equilibria 222-223 (2004) 107–118. DOI:`10.1016/j.fluid.2004.06.028`.

[67] M. Heinen, J. Vrabec, J. Fischer: Communication: Evaporation: Influence of heat transport in the liquid on the interface temperature and the particle flux, The Journal of Chemical Physics 145 (2016) 081101. DOI:`10.1063/1.4961542`.

[68] R. S. Chatwell, M. Heinen, J. Vrabec: Diffusion limited evaporation of a binary liquid film, International Journal of Heat and Mass Transfer 132 (2019) 1296–1305. DOI:`10.1016/j.ijheatmasstransfer.2018.12.030`.

[69] M. Heinen, J. Vrabec: Evaporation sampled by stationary molecular dynamics simulation, The Journal of Chemical Physics 151 (2019) 044704. DOI:`10.1063/1.5111759`.

[70] T. Tsuruta, H. Tanaka, T. Masuoka: Condensation/evaporation coefficient and velocity distributions at liquid–vapor interface, International Journal of Heat

and Mass Transfer 42 (1999) 4107–4116. DOI:`10.1016/S0017-9310(99)00081-2`.

[71] S. Cheng, J. B. Lechman, S. J. Plimpton, G. S. Grest: Evaporation of Lennard-Jones fluids, The Journal of Chemical Physics 134 (2011) 224704. DOI:`10.1063/1.3595260`.

[72] J. M. Simon, D. Bedeaux, S. Kjelstrup, J. Xu, E. Johannessen: Interface film resistivities for heat and mass transfersintegral relations verified by non-equilibrium molecular dynamics, Journal of Physical Chemistry B 110 (2006) 18528–18536. DOI:`10.1021/jp062047y`.

[73] J. Ge, D. Bedeaux, J. Simon, S. Kjelstrup: Integral relations, a simplified method to find interfacial resistivities for heat and mass transfer, Physica A: Statistical Mechanics and its Applications 385 (2007) 421–432. DOI:`10.1016/j.physa.2007.07.033`.

[74] J. Ge, S. Kjelstrup, D. Bedeaux, J. M. Simon, B. Rousseau: Transfer coefficients for evaporation of a system with a Lennard-Jones long-range spline potential, Physical Review E 75 (2007) 061604. DOI:`10.1103/PhysRevE.75.061604`.

[75] M. Matsumoto: Molecular dynamics simulation of interphase transport at liquid surfaces, Fluid Phase Equilibria 125 (1996) 195–203. DOI:`10.1016/S0378-3812(96)03123-8`.

[76] A. Kryukov, V. Levashov: About evaporation–condensation coefficients on the vapor–liquid interface of high thermal conductivity matters, International Journal of Heat and Mass Transfer 54 (2011) 3042–3048. DOI:`10.1016/j.ijheatmasstransfer.2011.02.042`.

[77] M. Kon, K. Kobayashi, M. Watanabe: Kinetic boundary condition in vapor–liquid two-phase system during unsteady net evaporation/condensation, European Journal of Mechanics - B/Fluids 64 (2017) 81–92. DOI:`10.1016/j.euromechflu.2016.12.001`.

[78] E. Bird, Z. Liang: Transport phenomena in the Knudsen layer near an evaporating surface, Physical Review E 100 (2019) 043108. DOI:`10.1103/PhysRevE.100.043108`.

[79] S. Kjelstrup, B. Hafskjold: Nonequilibrium molecular dynamics simulations of steady-state heat and mass transport in distillation, Industrial & Engineering Chemistry Research 35 (1996) 4203–4213. DOI:`10.1021/ie960199h`.

[80] A. Røsjorde, S. Kjelstrup, D. Bedeaux, B. Hafskjold: Nonequilibrium Molecular Dynamics Simulations of Steady-State Heat and Mass Transport in Condensation. II. Transfer Coefficients, Journal of Colloid and Interface Science 240 (2001) 355–364. DOI:`10.1006/jcis.2001.7611`.

[81] A. Røsjorde, D. Fossmo, D. Bedeaux, S. Kjelstrup, B. Hafskjold: Nonequilibrium molecular dynamics simulations of steady-state heat and mass transport in condensation: I. Local equilibrium, Journal of Colloid and Interface Science 232 (2000) 178–185. DOI:`10.1006/jcis.2000.7203`.

[82] I. Inzoli, S. Kjelstrup, D. Bedeaux, J. Simon: Transfer coefficients for the liquid–vapor interface of a two-component mixture, Chemical Engineering Science 66 (2011) 4533–4548. DOI:`10.1016/j.ces.2011.06.011`.

[83] B. Hafskjold, T. Ikeshoji: Non equilibrium molecular dynamics simulation of coupled heat- and mass transport across a liquid/vapor interface, Molecular Simulation 16 (1996) 139–150. DOI:`10.1080/08927029608024068`.

[84] L. van der Ham, R. Bock, S. Kjelstrup: Modelling the coupled transfer of mass and thermal energy in the vapour–liquid region of a nitrogen–oxygen mixture, Chemical Engineering Science 65 (2010) 2236–2248. DOI:`10.1016/j.ces.2009.12.021`.

[85] E. Johannessen, J. Gross, D. Bedeaux: Nonequilibrium thermodynamics of interfaces using classical density functional theory, The Journal of Chemical Physics 129 (2008) 184703. DOI:`10.1063/1.3009182`.

[86] E. Johannessen, D. Bedeaux: Integral relations for the heat and mass transfer resistivities of the liquid–vapor interface, Physica A: Statistical Mechanics and its Applications 370 (2006) 258–274. DOI:`10.1016/j.physa.2006.02.047`.

[87] K. Glavatskiy, D. Bedeaux: Transport of heat and mass in a two-phase mixture: From a continuous to a discontinuous description, The Journal of Chemical Physics 133 (2010) 144709. DOI:`10.1063/1.3486555`.

[88] C. Klink, C. Waibel, J. Gross: Analysis of interfacial transport resistivities of pure components and mixtures based on density functional theory, Industrial & Engineering Chemistry Research 54 (2015) 11483–11492. DOI:`10.1021/acs.iecr.5b03270`.

[89] H. K. Chilukoti, G. Kikugawa, T. Ohara: A molecular dynamics study on transport properties and structure at the liquid-vapor interfaces of alkanes, International Journal of Heat and Mass Transfer 59 (2013) 144–154. DOI:`10.1016/j.ijheatmasstransfer.2012.12.015`.

[90] H. K. Chilukoti, G. Kikugawa, T. Ohara: Structure and mass transport characteristics at the intrinsic liquid–vapor interfaces of alkanes, Journal of Physical Chemistry B 120 (2016) 7207–7216. DOI:`10.1021/acs.jpcb.6b05332`.

[91] H. K. Chilukoti, G. Kikugawa, T. Ohara: Self-diffusion coefficient and structure of binary n-alkane mixtures at the liquid-vapor interfaces, Journal of Physical Chemistry B 119 (2015) 13177–13184. DOI:`10.1021/acs.jpcb.5b07189`.

[92] D. Duque, P. Tarazona, E. Chacón: Diffusion at the liquid-vapor interface, The Journal of Chemical Physics 128 (2008) 134704. DOI:`10.1063/1.2841128`.

[93] C. Braga, J. Muscatello, G. Lau, E. A. Müller, G. Jackson: Nonequilibrium study of the intrinsic free-energy profile across a liquid-vapour interface, The Journal of Chemical Physics 144 (2016) 044703. DOI:`10.1063/1.4940137`.

[94] P. Liu, E. Harder, B. J. Berne: On the calculation of diffusion coefficients in confined fluids and interfaces with an application to the liquid-vapor interface of water, Journal of Physical Chemistry B 108 (2004) 6595–6602. DOI:`10.1021/jp0375057`.

[95] C. Braga, A. Galindo, E. A. Müller: Nonequilibrium molecular dynamics simulation of diffusion at the liquid-liquid interface, The Journal of Chemical Physics 141 (2014) 154101. DOI:`10.1063/1.4897159`.

[96] B. C. Garrett, G. K. Schenter, A. Morita: Molecular simulations of the transport of molecules across the liquid/vapor interface of water, Chemical Reviews 106 (2006) 1355–1374. DOI:`10.1021/cr040370w`.

[97] V. G. Baidakov, S. P. Protsenko: Molecular-dynamics simulation of relaxation processes at liquid–gas interfaces in single- and two-component Lennard-Jones systems, Colloid Journal 81 (2019) 491–500. DOI:`10.1134/S1061933X19040021`.

[98] V. G. Baidakov, S. P. Protsenko, V. M. Bryukhanov: Relaxation processes at liquid-gas interfaces in one- and two-component Lennard-Jones systems: Molecular dynamics simulation, Fluid Phase Equilibria 481 (2019) 1–14. DOI:`10.1016/j.fluid.2018.10.012`.

[99] G. S. Heffelfinger, F. van Swol: Diffusion in Lennard-Jones fluids using dual control volume grand canonical molecular dynamics simulation (DCV-GCMD), The Journal of Chemical Physics 100 (1994) 7548–7552. DOI:`10.1063/1.466849`.

[100] G. Heffelfinger, D. Ford: Massively parallel dual control volume grand canonical molecular dynamics with LADERA II. Gradient driven diffusion through polymers, Molecular Physics 94 (1998) 673–683. DOI:10.1080/002689798167836.

[101] G. S. Heffelfinger, D. M. Ford: Massively parallel dual control volume grand canonical molecular dynamics with LADERA I. Gradient driven diffusion in Lennard-Jones fluids, Molecular Physics 94 (1998) 659–671. DOI:10.1080/002689798167827.

[102] S. Stephan, H. Hasse: Enrichment at vapour-liquid interfaces of mixtures: Establishing a link between nanoscopic and macroscopic properties, International Reviews in Physical Chemistry 39 (2020) 319–349. DOI:10.1080/0144235X.2020.1777705.

[103] S. Stephan, H. Hasse: Molecular interactions at vapor-liquid interfaces: Binary mixtures of simple fluids, Physical Review E 101 (2020) 012802. DOI:10.1103/PhysRevE.101.012802.

[104] S. Stephan, H. Hasse: Influence of dispersive long range interactions on properties of vapour-liquid interfaces of binary Lennard-Jones mixtures, Molecular Physics 118 (2020) e1699185. DOI:10.1080/00268976.2019.1699185.

[105] P. M. Cornelisse: The Square Gradient Theory Applied Simultaneous Modelling of Interfacial Tension and Phase Behaviour, Ph.D. thesis, Technische Universiteit Delft, 1997.

[106] B. Carey: The Gradient Theory of Fluid Interfaces, Ph.D. thesis, University of Minnesota, Minneapolis, 1979.

[107] A. Mejía, M. Cartes, H. Segura, E. A. Müller: Use of equations of state and coarse grained simulations to complement experiments: Describing the interfacial properties of carbon dioxide + decane and carbon dioxide + eicosane mixtures, Journal of Chemical & Engineering Data 59 (2014) 2928–2941. DOI:10.1021/je5000764.

[108] J. M. Garrido, M. Cartes, A. Mejía: Coarse-grained theoretical modeling and molecular simulations of nitrogen + n-alkanes: (n-pentane, n-hexane, n-heptane, n-octane), Journal of Supercritical Fluids 129 (2017) 83–90. DOI:10.1016/j.supflu.2017.01.001.

[109] A. Mejía, J. C. Pàmies, D. Duque, H. Segura, L. F. Vega: Phase and interface behaviors in type-I and type-V Lennard-Jones mixtures: Theory and simulations, The Journal of Chemical Physics 123 (2005) 034505. DOI:10.1063/1.1955529.

[110] J. M. Garrido, A. Mejía, M. M. Piñeiro, F. J. Blas, E. A. Müller: Interfacial tensions of industrial fluids from a molecular-based square gradient theory, AIChE Journal 62 (2016) 1781–1794. DOI:`10.1002/aic.15190`.

[111] D. Fertig, S. Stephan: Influence of dispersive long-range interactions on transport and excess properties of simple mixtures, Molecular Physics (2023) e2162993. DOI:`10.1080/00268976.2022.2162993`.

[112] M. Heier, S. Stephan, J. Liu, W. G. Chapman, H. Hasse, K. Langenbach: Equation of state for the Lennard-Jones truncated and shifted fluid with a cut-off radius of 2.5σ based on perturbation theory and its applications to interfacial thermodynamics, Molecular Physics 116 (2018) 2083–2094. DOI:`10.1080/00268976.2018.1447153`.

[113] R. Taylor, R. Krishna: Multicomponent Mass Transfer, John Wiley & Sons, 1993.

[114] C. Niethammer, S. Becker, M. Bernreuther, M. Buchholz, W. Eckhardt, A. Heinecke, S. Werth, H.-J. Bungartz, C. W. Glass, H. Hasse, J. Vrabec, M. Horsch: ls1 mardyn: The massively parallel molecular dynamics code for large systems, Journal of Chemical Theory Computation 10 (2014) 4455–4464. DOI:`10.1021/ct500169q`.

[115] B. E. Poling, J. M. Prausnitz, J. P. O'Connell: The Properties of Gases and Liquids, 5 ed., McGraw-Hill, New York, 2001. DOI:`10.1036/0070116822`.

[116] G. Rutkai, A. Köster, G. Guevara-Carrion, T. Janzen, M. Schappals, C. W. Glass, M. Bernreuther, A. Wafai, S. Stephan, M. Kohns, S. Reiser, S. Deublein, M. Horsch, H. Hasse, J. Vrabec: ms2: A molecular simulation tool for thermodynamic properties, release 3.0, Computer Physics Communications 221 (2017) 343–351. DOI:`10.1016/j.cpc.2017.07.025`.

[117] G. A. Fernández, J. Vrabec, H. Hasse: Self-diffusion and binary Maxwell–Stefan diffusion coefficients of quadrupolar real fluids from molecular simulation, International Journal of Thermophysics 26 (2005) 1389–1407. DOI:`10.1007/s10765-005-8093-6`.

[118] G. Guevara-Carrion, J. Vrabec, H. Hasse: Prediction of self-diffusion coefficient and shear viscosity of water and its binary mixtures with methanol and ethanol by molecular simulation, The Journal of Chemical Physics 134 (2011) 074508. DOI:`10.1063/1.3515262`.

[119] D. Bellaire, H. Kiepfer, K. Münnemann, H. Hasse: PFG-NMR and MD simulation study of self-diffusion coefficients of binary and ternary mixtures containing

cyclohexane, ethanol, acetone, and toluene, Journal of Chemical & Engineering Data 65 (2020) 793–803. DOI:`10.1021/acs.jced.9b01016`.

[120] S. Pařez, G. Guevara-Carrion, H. Hasse, J. Vrabec: Mutual diffusion in the ternary mixture of water + methanol + ethanol and its binary subsystems, Physical Chemistry Chemical Physics 15 (2013) 3985–4001. DOI:`10.1039/c3cp43785j`.

[121] K. Bucior, L. Yelash, K. Binder: Molecular-dynamics simulation of evaporation processes of fluid bridges confined in slitlike pores, Physical Review E 79 (2009) 031604. DOI:`10.1103/PhysRevE.79.031604`.

[122] L. Casalino, Z. Gaieb, J. A. Goldsmith, C. K. Hjorth, A. C. Dommer, A. M. Harbison, C. A. Fogarty, E. P. Barros, B. C. Taylor, J. S. McLellan, et al.: Beyond shielding: the roles of glycans in the SARS-CoV-2 spike protein, ACS Central Science 6 (2020) 1722–1734. DOI:`10.1021/acscentsci.0c01056`.

[123] S. Stephan, M. Dyga, I. A. Alhafez, J. Lenhard, H. M. Urbassek, H. Hasse: Reproducibility of atomistic friction computer experiments: a molecular dynamics simulation study, Molecular Simulation 47 (2021) 1509–1521. DOI:`10.1080/08927022.2021.1987430`.

[124] Y. Zhang, A. Otani, E. J. Maginn: Reliable viscosity calculation from equilibrium molecular dynamics simulations: A time decomposition method, Journal of Chemical Theory and Computation 11 (2015) 3537–3546. DOI:`10.1021/acs.jctc.5b00351`.

[125] A. P. Thompson, D. M. Ford, G. S. Heffelfinger: Direct molecular simulation of gradient-driven diffusion, The Journal of Chemical Physics 109 (1998) 6406–6414. DOI:`10.1063/1.477284`.

[126] S. Werth, M. Kohns, K. Langenbach, M. Heilig, M. Horsch, H. Hasse: Interfacial and bulk properties of vapor-liquid equilibria in the system toluene + hydrogen chloride + carbon dioxide by molecular simulation and density gradient theory + PC-SAFT, Fluid Phase Equilibria 427 (2016) 219–230. DOI:`10.1016/j.fluid.2016.07.016`.

[127] M. Roeselová, J. Vieceli, L. X. Dang, B. C. Garrett, D. J. Tobias: Hydroxyl radical at the air-water interface, Journal of the American Chemical Society 126 (2004) 16308–16309. DOI:`10.1021/ja045552m`.

[128] J. Vieceli, M. Roeselova, N. Potter, L. X. Dang, B. C. Garrett, D. J. Tobias: Molecular dynamics simulations of atmospheric oxidants at the air-water interface: solvation and accommodation of OH and O_3, Journal of Physical Chemistry B 109 (2005) 15876–15892. DOI:`10.1021/jp051361+`.

[129] C. K. Law: Internal boiling and superheating in vaporizing multicomponent droplets, AIChE Journal 24 (1978) 626–632. DOI:`10.1002/aic.690240410`.

[130] J. C. Lasheres, A. C. Fernandez-Pello, F. L. Dryer: Experimental observations on the disruptive combustion of free droplets of multicomponent fuels, Combustion Science and Technology 22 (1980) 195–209. DOI:`10.1080/00102208008952383`.

[131] M. Mikami, T. Yagi, N. Kojima: Occurrence probability of microexplosion in droplet combustion of miscible binary fuels, Symposium (International) on Combustion 27 (1998) 1933–1941. DOI:`10.1016/s0082-0784(98)80037-4`.

[132] Y. Zeng, C. fon F. Lee: Modeling droplet breakup processes under microexplosion conditions, Proceedings of the Combustion Institute 31 (2007) 2185–2193. DOI:`10.1016/j.proci.2006.07.237`.

[133] B. Kunstmann, I. Wlokas, M. Kohns, H. Hasse: Simulation study of superheating in evaporating droplets of (TTIP + p-xylene) in sprayflame synthesis, Applications in Energy and Combustion Science, under review (2023).

[134] A. Keller, I. Wlokas, M. Kohns, H. Hasse: Thermophysical properties of solutions of iron(III) nitrate-nonahydrate in mixtures of ethanol and water, Journal of Chemical & Engineering Data 65 (2020) 3519–3527. DOI:`10.1021/acs.jced.0c00105`.

[135] A. Keller, I. Wlokas, M. Kohns, H. Hasse: Thermophysical properties of mixtures of titanium(IV) isopropoxide (TTIP) and p-xylene, Journal of Chemical & Engineering Data 65 (2020) 869–876. DOI:`10.1021/acs.jced.9b01059`.

[136] A. Keller, I. Wlokas, M. Kohns, H. Hasse: Thermophysical properties of solutions of iron(III) nitrate nonahydrate in mixtures of 1-propanol and water, Journal of Chemical & Engineering Data 65 (2020) 5413–5420. DOI:`10.1021/acs.jced.0c00531`.

[137] A. Keller, I. Wlokas, M. Kohns, H. Hasse: Solid-liquid Equilibria in Mixtures of Iron(III) Nitrate Nonahydrate and Ethanol or 1-Propanol, Fluid Phase Equilibria 536 (2021) 112987. DOI:`10.1016/j.fluid.2021.112987`.

[138] A. Keller, I. Wlokas, M. Kohns, H. Hasse: Thermophysical properties of mixtures of titanium(IV) isopropoxide (TTIP) and 2-propanol (iPOH), Journal of Chemical & Engineering Data 66 (2021) 1296–1304. DOI:`10.1021/acs.jced.0c00941`.

[139] A. P. Thompson, H. M. Aktulga, R. Berger, D. S. Bolintineanu, W. M. Brown, P. S. Crozier, P. J. in 't Veld, A. Kohlmeyer, S. G. Moore, T. D. Nguyen, R. Shan, M. J.

Stevens, J. Tranchida, C. Trott, S. J. Plimpton: LAMMPS - a flexible simulation tool for particle-based materials modeling at the atomic, meso, and continuum scales, Computer Physics Communications 271 (2022) 108171. DOI:`10.1016/j.cpc.2021.108171`.

[140] S. Nosé: A unified formulation of the constant temperature molecular dynamics methods, The Journal of Chemical Physics 81 (1984) 511–519. DOI:`10.1063/1.447334`.

[141] W. G. Hoover: Canonical dynamics: Equilibrium phase-space distributions, Physical Review A 31 (1985) 1695–1697. DOI:`10.1103/physreva.31.1695`.

[142] L. Verlet: Computer "experiments" on classical fluids. I. thermodynamical properties of Lennard-Jones molecules, Physical Review 159 (1967) 98–103. DOI:`10.1103/physrev.159.98`.

[143] B. Delaunay: Sur la sphere vide, Izvestia Akademii Nauk SSSR, Otdelenie Matematicheskii i Estestvennyka Nauk 7 (1934) 1–2.

[144] H. Edelsbrunner, E. P. Mücke: Three-dimensional alpha shapes, ACM Transactions on Graphics 13 (1994) 43–72. DOI:`10.1145/174462.156635`.

[145] A. Stukowski: Visualization and analysis of atomistic simulation data with OVITO – the open visualization tool, Modelling and Simulation in Materials Science and Engineering 18 (2009) 015012. DOI:`10.1088/0965-0393/18/1/015012`.

[146] C. K. Law: Combustion Physics, Cambridge University Press, Cambridge, 2010.

[147] K. S. Pitzer: Thermodynamics of electrolytes. I. Theoretical basis and general equations, Journal of Physical Chemistry 77 (1973) 268–277. DOI:`10.1021/j100621a026`.

[148] K. S. Pitzer, J. J. Kim: Thermodynamics of electrolytes. IV. activity and osmotic coefficients for mixed electrolytes, Journal of the American Chemical Society 96 (1974) 5701–5707. DOI:`10.1021/ja00825a004`.

[149] T. J. Edwards, G. Maurer, J. Newman, J. M. Prausnitz: Vapor-liquid equilibria in multicomponent aqueous solutions of volatile weak electrolytes, AIChE Journal 24 (1978) 966–976. DOI:`10.1002/aic.690240605`.

[150] C.-C. Chen, H. I. Britt, J. F. Boston, L. B. Evans: Extension and application of the pitzer equation for vapor-liquid equilibrium of aqueous electrolyte systems with molecular solutes, AIChE Journal 25 (1979) 820–831. DOI:`10.1002/aic.690250510`.

[151] P. de Alcântara Pessôa Filho, G. Maurer: An extension of the pitzer equation for the excess gibbs energy of aqueous electrolyte systems to aqueous polyelectrolyte solutions, Fluid Phase Equilibria 269 (2008) 25–35. DOI:`10.1016/j.fluid.2008.04.019`.

[152] C.-C. Chen, L. B. Evans: A local composition model for the excess gibbs energy of aqueous electrolyte systems, AIChE Journal 32 (1986) 444–454. DOI:`10.1002/aic.690320311`.

[153] P. D. E. Hückel: Zur Theorie der Elektrolyte, Physikalische Zeitschrift 24 (1923) 185–206.

[154] C. Held, L. F. Cameretti, G. Sadowski: Modeling aqueous electrolyte solutions, Fluid Phase Equilibria 270 (2008) 87–96. DOI:`10.1016/j.fluid.2008.06.010`.

[155] C. Held, T. Reschke, S. Mohammad, A. Luza, G. Sadowski: ePC-SAFT revised, Chemical Engineering Research and Design 92 (2014) 2884–2897. DOI:`10.1016/j.cherd.2014.05.017`.

[156] A. Schlaikjer, K. Thomsen, G. M. Kontogeorgis: eCPA: An ion-specific approach to parametrization, Fluid Phase Equilibria 470 (2018) 176–187. DOI:`10.1016/j.fluid.2017.12.008`.

[157] M. D. Olsen, G. M. Kontogeorgis, X. Liang, N. von Solms: Investigation of the performance of e-CPA for a wide range of properties for aqueous NaCl solutions, Fluid Phase Equilibria 548 (2021) 113167. DOI:`10.1016/j.fluid.2021.113167`.

[158] M. Kohns, G. Lazarou, S. Kournopoulos, E. Forte, F. A. Perdomo, G. Jackson, C. S. Adjiman, A. Galindo: Predictive models for the phase behaviour and solution properties of weak electrolytes: nitric, sulphuric, and carbonic acids, Physical Chemistry Chemical Physics 22 (2020) 15248–15269. DOI:`10.1039/c9cp06795g`.

[159] A. J. Haslam, A. González-Pérez, S. D. Lecce, S. H. Khalit, F. A. Perdomo, S. Kournopoulos, M. Kohns, T. Lindeboom, M. Wehbe, S. Febra, G. Jackson, C. S. Adjiman, A. Galindo: Expanding the applications of the SAFT-γ Mie group-contribution equation of state: Prediction of thermodynamic properties and phase behavior of mixtures, Journal of Chemical & Engineering Data 65 (2020) 5862–5890. DOI:`10.1021/acs.jced.0c00746`.

[160] W. R. Smith, I. Nezbeda, J. Kolafa, F. Moučka: Recent progress in the molecular simulation of thermodynamic properties of aqueous electrolyte solutions, Fluid Phase Equilibria 466 (2018) 19–30. DOI:`10.1016/j.fluid.2018.03.006`.

[161] A. Z. Panagiotopoulos: Simulations of activities, solubilities, transport properties, and nucleation rates for aqueous electrolyte solutions, The Journal of Chemical Physics 153 (2020) 010903. DOI:`10.1063/5.0012102`.

[162] B. Elvers: Ullmann's Encyclopedia of Industrial Chemistry, Wiley, Hoboken, 2000. DOI:`10.1002/14356007`.

[163] S. Deublein, J. Vrabec, H. Hasse: A set of molecular models for alkali and halide ions in aqueous solution, The Journal of Chemical Physics 136 (2012) 084501. DOI:`10.1063/1.3687238`.

[164] S. Reiser, S. Deublein, J. Vrabec, H. Hasse: Molecular dispersion energy parameters for alkali and halide ions in aqueous solution, The Journal of Chemical Physics 140 (2014) 044504. DOI:`10.1063/1.4858392`.

[165] H. J. C. Berendsen, J. R. Grigera, T. P. Straatsma: The missing term in effective pair potentials, Journal of Physical Chemistry 91 (1987) 6269–6271. DOI:`10.1021/j100308a038`.

[166] V. Vchirawongkwin, H. Sato, S. Sakaki: RISM-SCF-SEDD study on the symmetry breaking of carbonate and nitrate anions in aqueous solution, Journal of Physical Chemistry B 114 (2010) 10513–10519. DOI:`10.1021/jp101700d`.

[167] V. Vchirawongkwin, C. Kritayakornupong, A. Tongraar, B. M. Rode: Symmetry breaking and hydration structure of carbonate and nitrate in aqueous solutions: A study by ab initio quantum mechanical charge field molecular dynamics, Journal of Physical Chemistry B 115 (2011) 12527–12536. DOI:`10.1021/jp204809f`.

[168] J. Thøgersen, J. Réhault, M. Odelius, T. Ogden, N. K. Jena, S. J. K. Jensen, S. R. Keiding, J. Helbing: Hydration dynamics of aqueous nitrate, Journal of Physical Chemistry B 117 (2013) 3376–3388. DOI:`10.1021/jp310090u`.

[169] S. Matsunaga: Molecular simulation study of structure and dynamical properties of nitrate anion in sodium chloride aqueous solution, Molecular Simulation 41 (2014) 913–917. DOI:`10.1080/08927022.2014.976637`.

[170] P. Banerjee, S. Yashonath, B. Bagchi: Coupled jump rotational dynamics in aqueous nitrate solutions, The Journal of Chemical Physics 145 (2016) 234502. DOI:`10.1063/1.4971864`.

[171] A. Laaksonen, H. Kovacs: Silver nitrate in aqueous solution and as molten salt: A molecular dynamics simulation and NMR relaxation study, Canadian Journal of Chemistry 72 (1994) 2278–2285. DOI:`10.1139/v94-290`.

[172] G. Lu, Y. Li, W. Sun, C. Li: Molecular Dynamics Simulation of Hydration Structure of KNO$_3$ Electrolyte Solution, Chinese Journal of Chemical Physics 20 (2007) 22–30. DOI:`10.1360/cjcp2007.20(1).22.9`.

[173] H. Krienke, G. Schmeer: Hydration of Molecular Anions with Oxygen Sites – a Monte Carlo Study, Zeitschrift für Physikalische Chemie 218 (2004) 749–764. DOI:`10.1524/zpch.218.6.749.33456`.

[174] H. Krienke, D. Opalka: Hydration of Molecular Ions: A Molecular Dynamics Study with a SPC/E Water Model, Journal of Physical Chemistry C 111 (2007) 15935–15941. DOI:`10.1021/jp073721u`.

[175] T. Megyes, S. Bálint, E. Peter, T. Grósz, I. Bakó, H. Krienke, M.-C. Bellissent-Funel: Solution structure of NaNO$_3$ in water: Diffraction and molecular dynamics simulation study, Journal of Physical Chemistry B 113 (2009) 4054–4064. DOI:`10.1021/jp806411c`.

[176] Krienke: On the influence of molecular structure on the conductivity of electrolyte solutions - sodium nitrate in water, Condensed Matter Physics 16 (2013) 43006. DOI:`10.5488/cmp.16.43006`.

[177] S. Jayaraman, A. P. Thompson, O. A. von Lilienfeld, E. J. Maginn: Molecular simulation of the thermal and transport properties of three alkali nitrate salts, Industrial & Engineering Chemistry Research 49 (2009) 559–571. DOI:`10.1021/ie9007216`.

[178] W. J. Xie, Z. Zhang, Y. Q. Gao: Ion pairing in alkali nitrate electrolyte solutions, Journal of Physical Chemistry B 120 (2016) 2343–2351. DOI:`10.1021/acs.jpcb.5b10755`.

[179] L. X. Dang, T.-M. Chang, M. Roeselova, B. C. Garrett, D. J. Tobias: On NO$_3$- –H$_2$O interactions in aqueous solutions and at interfaces, The Journal of Chemical Physics 124 (2006) 066101. DOI:`10.1063/1.2171375`.

[180] B. Minofar, R. Vácha, A. Wahab, S. Mahiuddin, W. Kunz, P. Jungwirth: Propensity for the air/water interface and ion pairing in magnesium acetate vs magnesium nitrate solutions: molecular dynamics simulations and surface tension measurements, Journal of Physical Chemistry B 110 (2006) 15939–15944. DOI:`10.1021/jp060627p`.

[181] P. Salvador, J. E. Curtis, D. J. Tobias, P. Jungwirth: Polarizability of the nitrate anion and its solvation at the air/water interface, Physical Chemistry Chemical Physics 5 (2003) 3752. DOI:`10.1039/b304537d`.

[182] J. L. Thomas, M. Roeselová, L. X. Dang, D. J. Tobias: Molecular dynamics simulations of the solution-air interface of aqueous sodium nitrate, Journal of Physical Chemistry A 111 (2007) 3091–3098. DOI:`10.1021/jp0683972`.

[183] G. Lu, C. Li, W. Wang, Z. Wang: Structure of KNO_3 electrolyte solutions: a Monte Carlo study, Fluid Phase Equilibria 225 (2004) 1–11. DOI:`10.1016/j.fluid.2004.06.055`.

[184] G.-W. Lu, C.-X. Li, W.-C. Wang, Z.-H. Wang: A Monte Carlo simulation on structure and thermodynamics of potassium nitrate electrolyte solution, Molecular Physics 103 (2005) 599–610. DOI:`10.1080/00268970410001683834`.

[185] H. J. C. Berendsen, J. P. M. Postma, W. F. van Gunsteren, J. Hermans: Interaction models for water in relation to protein hydration, in: The Jerusalem Symposia on Quantum Chemistry and Biochemistry, The Jerusalem Symposia on Quantum Chemistry and Biochemistry, Springer Netherlands, Dordrecht, 1981, pp. 331–342. DOI:`10.1007/978-94-015-7658-1_21`.

[186] M. C. G. Lebrero, D. E. Bikiel, M. D. Elola, D. A. Estrin, A. E. Roitberg: Solvent-induced symmetry breaking of nitrate ion in aqueous clusters: A quantum-classical simulation study, The Journal of Chemical Physics 117 (2002) 2718–2725. DOI:`10.1063/1.1490578`.

[187] W. L. Jorgensen, J. Chandrasekhar, J. D. Madura, R. W. Impey, M. L. Klein: Comparison of simple potential functions for simulating liquid water, The Journal of Chemical Physics 79 (1983) 926–935. DOI:`10.1063/1.445869`.

[188] S. W. Rick, S. J. Stuart, B. J. Berne: Dynamical fluctuating charge force fields: Application to liquid water, The Journal of Chemical Physics 101 (1994) 6141–6156. DOI:`10.1063/1.468398`.

[189] S. Izadi, R. Anandakrishnan, A. V. Onufriev: Building water models: A different approach, Journal of Physical Chemistry Letters 5 (2014) 3863–3871. DOI:`10.1021/jz501780a`.

[190] F. Moučka, M. Lísal, J. Škvor, J. Jirsák, I. Nezbeda, W. R. Smith: Molecular simulation of aqueous electrolyte solubility. 2. Osmotic ensemble Monte Carlo methodology for free energy and solubility calculations and application to NaCl, Journal of Physical Chemistry B 115 (2011) 7849–7861. DOI:`10.1021/jp202054d`.

[191] F. Moučka, I. Nezbeda, W. R. Smith: Molecular simulation of aqueous electrolytes: Water chemical potential results and Gibbs-Duhem equation consistency tests, The Journal of Chemical Physics 139 (2013) 124505. DOI:`10.1063/1.4821153`.

[192] F. Moučka, I. Nezbeda, W. R. Smith: Chemical potentials, activity coefficients, and solubility in aqueous NaCl solutions: Prediction by polarizable force fields, Journal of Chemical Theory and Computation 11 (2015) 1756–1764. DOI:`10.1021/acs.jctc.5b00018`.

[193] M. Lísal, W. R. Smith, J. Kolafa: Molecular simulations of aqueous electrolyte solubility: 1. The expanded-ensemble osmotic molecular dynamics method for the solution phase, Journal of Physical Chemistry B 109 (2005) 12956–12965. DOI:`10.1021/jp0507492`.

[194] Z. Mester, A. Z. Panagiotopoulos: Mean ionic activity coefficients in aqueous NaCl solutions from molecular dynamics simulations, The Journal of Chemical Physics 142 (2015) 044507. DOI:`10.1063/1.4906320`.

[195] Z. Mester, A. Z. Panagiotopoulos: Temperature-dependent solubilities and mean ionic activity coefficients of alkali halides in water from molecular dynamics simulations, The Journal of Chemical Physics 143 (2015) 044505. DOI:`10.1063/1.4926840`.

[196] M. Kohns, S. Reiser, M. Horsch, H. Hasse: Solvent activity in electrolyte solutions from molecular simulation of the osmotic pressure, The Journal of Chemical Physics 144 (2016) 084112. DOI:`10.1063/1.4942500`.

[197] M. Kohns, M. Schappals, M. Horsch, H. Hasse: Activities in aqueous solutions of the alkali halide salts from molecular simulation, Journal of Chemical & Engineering Data 61 (2016) 4068–4076. DOI:`10.1021/acs.jced.6b00544`.

[198] M. Kohns, M. Horsch, H. Hasse: Activity coefficients from molecular simulations using the OPAS method, The Journal of Chemical Physics 147 (2017) 144108. DOI:`10.1063/1.4991498`.

[199] S. Reiser, M. Horsch, H. Hasse: Temperature dependence of the density of aqueous alkali halide salt solutions by experiment and molecular simulation, Journal of Chemical & Engineering Data 59 (2014) 3434–3448. DOI:`10.1021/je500420g`.

[200] S. Deublein, S. Reiser, J. Vrabec, H. Hasse: A set of molecular models for alkaline-earth cations in aqueous solution, Journal of Physical Chemistry B 116 (2012) 5448–5457. DOI:`10.1021/jp3013514`.

[201] W. Wagner, A. Pruß: The IAPWS formulation 1995 for the thermodynamic properties of ordinary water substance for general and scientific use, Journal of Physical and Chemical Reference Data 31 (2002) 387–535. DOI:`10.1063/1.1461829`.

[202] Dortmund data bank, 2022. URL: `www.ddbst.com`.

[203] W. J. Hamer, Y.-C. Wu: Osmotic coefficients and mean activity coefficients of uni-univalent electrolytes in water at 25°C, Journal of Physical and Chemical Reference Data 1 (1972) 1047–1100. DOI:`10.1063/1.3253108`.

[204] R. Fingerhut, G. Guevara-Carrion, I. Nitzke, D. Saric, J. Marx, K. Langenbach, S. Prokopev, D. Celný, M. Bernreuther, S. Stephan, M. Kohns, H. Hasse, J. Vrabec: ms2: A molecular simulation tool for thermodynamic properties, release 4.0, Computer Physics Communications 262 (2021) 107860. DOI:`10.1016/j.cpc.2021.107860`.

[205] R. Fuentes-Azcatl, N. Mendoza, J. Alejandre: Improved SPC force field of water based on the dielectric constant: SPC/ϵ, Physica A: Statistical Mechanics and its Applications 420 (2015) 116–123. DOI:`10.1016/j.physa.2014.10.072`.

[206] C. W. Gear: The numerical integration of ordinary differential equations of various orders, Technical Report #ANL-7126, Argonne National Lab., Ill., 1966. URL: `http://refhub.elsevier.com/S0378-3812(23)00083-3/sb44`.

[207] H. Flyvbjerg, H. G. Petersen: Error estimates on averages of correlated data, The Journal of Chemical Physics 91 (1989) 461–466. DOI:`10.1063/1.457480`.

[208] H. C. Andersen: Molecular dynamics simulations at constant pressure and/or temperature, The Journal of Chemical Physics 72 (1980) 2384–2393. DOI:`10.1063/1.439486`.

[209] H. Galleguillos, D. Salavera, P. Vargas, A. Coronas: Experimental determination and prediction of the vapor pressure of some binary and quaternary aqueous solutions of alkaline nitrites and nitrates, Fluid Phase Equilibria 291 (2010) 208–211. DOI:`10.1016/j.fluid.2009.12.028`.

[210] E. W. Lemmon, I. H. Bell, M. Huber, M. McLinden: NIST standard reference database 23: reference fluid thermodynamic and transport properties-REFPROP, version 10.0, Standard Reference Data Program, Gaithersburg (2018). DOI:`10.18434/T4/1502528`.

[211] R. Mills, V. M. M. Lobo: Self-diffusion in Electrolyte Solutions, Elsevier, Amsterdam, 1989.

[212] T. Hashitani, K. Tanaka: Measurements of self-diffusion coefficients of the nitrate ion in aqueous solutions of potassium nitrate and calcium nitrate, Journal of the Chemical Society, Faraday Transactions 1: Physical Chemistry in Condensed Phases 79 (1983) 1765–1768. DOI:`10.1039/f19837901765`.

[213] K. Tanaka: Measurements of self-diffusion coefficients of water in pure water and in aqueous electrolyte solutions, Journal of the Chemical Society, Faraday Transactions 1: Physical Chemistry in Condensed Phases 71 (1975) 1127–1131. DOI:`10.1039/f19757101127`.

[214] I. N. Tsimpanogiannis, O. A. Moultos, L. F. M. Franco, M. B. de M. Spera, M. Erdős, I. G. Economou: Self-diffusion coefficient of bulk and confined water: a critical review of classical molecular simulation studies, Molecular Simulation 45 (2018) 425–453. DOI:`10.1080/08927022.2018.1511903`.

[215] J. S. Kim, Z. Wu, A. R. Morrow, A. Yethiraj, A. Yethiraj: Self-diffusion and viscosity in electrolyte solutions, Journal of Physical Chemistry B 116 (2012) 12007 − 12013. DOI:`10.1021/jp306847t`.

[216] A. Z. Panagiotopoulos, S. Yue: Dynamics of aqueous electrolyte solutions: Challenges for simulations, Journal of Physical Chemistry B 127 (2023) 430 − 437. DOI:`10.1021/acs.jpcb.2c07477`.

[217] Y. Kameda, H. Saitoh, O. Uemura: The Hydration Structure of NO_3^- in Concentrated Aqueous Sodium Nitrate Solutions, Bulletin of the Chemical Society of Japan 66 (1993) 1919–1923. DOI:`10.1246/bcsj.66.1919`.

[218] Y. Kameda, K. Sugawara, T. Usuki, O. Uemura: Hydration Structure of Na^+ in Concentrated Aqueous Solutions, Bulletin of the Chemical Society of Japan 71 (1998) 2769–2776. DOI:`10.1246/bcsj.71.2769`.

[219] I. Nezbeda, F. Moučka, W. R. Smith: Recent progress in molecular simulation of aqueous electrolytes: force fields, chemical potentials and solubility, Molecular Physics 114 (2016) 1665–1690. DOI:`10.1080/00268976.2016.1165296`.

[220] J. Kolafa: Solubility of NaCl in water and its melting point by molecular dynamics in the slab geometry and a new BK3-compatible force field, The Journal of Chemical Physics 145 (2016) 204509. DOI:`10.1063/1.4968045`.

[221] J. Dočkal, M. Lísal, F. Moučka: Molecular force field development for aqueous electrolytes: 2. Polarizable models incorporating crystalline chemical potential and their accurate simulations of halite, hydrohalite, aqueous solutions of NaCl, and solubility, Journal of Chemical Theory and Computation 16 (2020) 3677–3688. DOI:`10.1021/acs.jctc.0c00161`.

[222] E. Sanz, C. Vega: Solubility of KF and NaCl in water by molecular simulation, The Journal of Chemical Physics 126 (2007) 014507. DOI:`10.1063/1.2397683`.

[223] S. H. Saravi, A. Z. Panagiotopoulos: Activity coefficients and solubilities of NaCl in water–methanol solutions from molecular dynamics simulations, Journal of Physical Chemistry B 126 (2022) 2891–2898. DOI:`10.1021/acs.jpcb.2c00813`.

[224] F. Moučka, J. Kolafa, M. Lísal, W. R. Smith: Chemical potentials of alkaline earth metal halide aqueous electrolytes and solubility of their hydrates by molecular simulation: Application to $CaCl_2$, antarcticite, and sinjarite, The Journal of Chemical Physics 148 (2018) 222832. DOI:`10.1063/1.5024212`.

[225] A. S. Paluch, S. Jayaraman, J. K. Shah, E. J. Maginn: A method for computing the solubility limit of solids: Application to sodium chloride in water and alcohols, The Journal of Chemical Physics 133 (2010) 124504. DOI:`10.1063/1.3478539`.

[226] L. Li, T. Totton, D. Frenkel: Computational methodology for solubility prediction: Application to sparingly soluble organic/inorganic materials, The Journal of Chemical Physics 149 (2018) 054102. DOI:`10.1063/1.5040366`.

[227] J. L. Aragones, E. Sanz, C. Vega: Solubility of NaCl in water by molecular simulation revisited, The Journal of Chemical Physics 136 (2012) 244508. DOI:`10.1063/1.4728163`.

[228] J. R. Espinosa, J. M. Young, H. Jiang, D. Gupta, C. Vega, E. Sanz, P. G. Debenedetti, A. Z. Panagiotopoulos: On the calculation of solubilities via direct coexistence simulations: Investigation of NaCl aqueous solutions and Lennard-Jones binary mixtures, The Journal of Chemical Physics 145 (2016) 154111. DOI:`10.1063/1.4964725`.

[229] I. S. Joung, T. E. Cheatham: Molecular dynamics simulations of the dynamic and energetic properties of alkali and halide ions using water-model-specific ion parameters, Journal of Physical Chemistry B 113 (2009) 13279–13290. DOI:`10.1021/jp902584c`.

[230] K. Kobayashi, Y. Liang, T. Sakka, T. Matsuoka: Molecular dynamics study of salt–solution interface: Solubility and surface charge of salt in water, The Journal of Chemical Physics 140 (2014) 144705. DOI:`10.1063/1.4870417`.

[231] H. M. Manzanilla-Granados, H. Saint-Martín, R. Fuentes-Azcatl, J. Alejandre: Direct coexistence methods to determine the solubility of salts in water from numerical simulations. Test case NaCl, Journal of Physical Chemistry B 119 (2015) 8389–8396. DOI:`10.1021/acs.jpcb.5b00740`.

[232] T. Yagasaki, M. Matsumoto, H. Tanaka: Lennard-Jones parameters determined to reproduce the solubility of NaCl and KCl in SPC/e, TIP3p, and TIP4p/2005 water, Journal of Chemical Theory and Computation 16 (2020) 2460–2473. DOI:`10.1021/acs.jctc.9b00941`.

[233] D. Frenkel, A. J. C. Ladd: New Monte Carlo method to compute the free energy of arbitrary solids. Application to the fcc and hcp phases of hard spheres, The Journal of Chemical Physics 81 (1984) 3188–3193. DOI:`10.1063/1.448024`.

[234] I. S. Joung, T. E. Cheatham: Determination of alkali and halide monovalent ion parameters for use in explicitly solvated biomolecular simulations, Journal of Physical Chemistry B 112 (2008) 9020–9041. DOI:`10.1021/jp8001614`.

[235] D. E. Smith, L. X. Dang: Computer simulations of NaCl association in polarizable water, The Journal of Chemical Physics 100 (1994) 3757–3766. DOI:`10.1063/1.466363`.

[236] P. R. ten Wolde, D. Frenkel: Enhancement of protein crystal nucleation by critical density fluctuations, Science 277 (1997) 1975–1978. DOI:`10.1126/science.277.5334.1975`.

[237] V. J. Anderson, H. N. W. Lekkerkerker: Insights into phase transition kinetics from colloid science, Nature 416 (2002) 811–815. DOI:`10.1038/416811a`.

[238] D. Erdemir, A. Y. Lee, A. S. Myerson: Nucleation of crystals from solution: Classical and two-step models, Accounts of Chemical Research 42 (2009) 621–629. DOI:`10.1021/ar800217x`.

[239] N. E. R. Zimmermann, B. Vorselaars, D. Quigley, B. Peters: Nucleation of NaCl from aqueous solution: Critical sizes, ion-attachment kinetics, and rates, Journal of the American Chemical Society 137 (2015) 13352–13361. DOI:`10.1021/jacs.5b08098`.

[240] G. Lanaro, G. N. Patey: Birth of NaCl crystals: Insights from molecular simulations, Journal of Physical Chemistry B 120 (2016) 9076–9087. DOI:`10.1021/acs.jpcb.6b05291`.

[241] H. Jiang, A. Haji-Akbari, P. G. Debenedetti, A. Z. Panagiotopoulos: Forward flux sampling calculation of homogeneous nucleation rates from aqueous NaCl solutions, The Journal of Chemical Physics 148 (2018) 044505. DOI:`10.1063/1.5016554`.

[242] H. Jiang, P. G. Debenedetti, A. Z. Panagiotopoulos: Nucleation in aqueous NaCl solutions shifts from 1-step to 2-step mechanism on crossing the spinodal, The Journal of Chemical Physics 150 (2019) 124502. DOI:`10.1063/1.5084248`.

[243] D. James, S. Beairsto, C. Hartt, O. Zavalov, I. Saika-Voivod, R. K. Bowles, P. H. Poole: Phase transitions in fluctuations and their role in two-step nucleation, The Journal of Chemical Physics 150 (2019) 074501. DOI:`10.1063/1.5057429`.

[244] N. E. R. Zimmermann, B. Vorselaars, J. R. Espinosa, D. Quigley, W. R. Smith, E. Sanz, C. Vega, B. Peters: NaCl nucleation from brine in seeded simulations: Sources of uncertainty in rate estimates, The Journal of Chemical Physics 148 (2018) 222838. DOI:`10.1063/1.5024009`.

[245] H. W. Horn, W. C. Swope, J. W. Pitera, J. D. Madura, T. J. Dick, G. L. Hura, T. Head-Gordon: Development of an improved four-site water model for biomolecular simulations: TIP4P-Ew, The Journal of Chemical Physics 120 (2004) 9665 – 9678. DOI:`10.1063/1.1683075`.

[246] T. R. Briggs, W. F. Geigle: Note on the system sodium iodide–water, Journal of Physical Chemistry 44 (1940) 373–377. DOI:`10.1021/j150399a009`.

[247] R. Cohen-Adad, J. W. Lorimer: Alkali Metal and Ammonium Chlorides in Water and Heavy Water (Binary Systems) (IUPAC Solubility Data Series), Pergamon, Oxford, 1991. URL: `http://refhub.elsevier.com/S0378-3812(23)00083-3/sb49`.

[248] S. Stephan, M. Horsch, J. Vrabec, H. Hasse: MolMod - an open access database of force fields for molecular simulations of fluids, Molecular Simulation 45 (2019) 806–814. DOI:`10.1080/08927022.2019.1601191`.

[249] A. R. Imre, G. Mayer, G. Házi, R. Rozas, T. Kraska: Estimation of the liquid-vapor spinodal from interfacial properties obtained from molecular dynamics and lattice boltzmann simulations, The Journal of Chemical Physics 128 (2008) 114708. DOI:`10.1063/1.2837805`.

[250] I. Van de Ven-Lucassen, T. Vlugt, A. Van der Zanden, P. Kerkhof: Using molecular dynamics to obtain Maxwell-Stefan diffusion coefficients in liquid systems, Molecular Physics 94 (1998) 495–503. DOI:`10.1080/00268979809482342`.

[251] P. D. Neufeld, A. Janzen, R. Aziz: Empirical equations to calculate 16 of the transport collision integrals $\omega^{(l,s)*}$ for the Lennard-Jones (12–6) potential, The Journal of Chemical Physics 57 (1972) 1100–1102. DOI:`10.1063/1.1678363`.

[252] M. Schappals, A. Mecklenfeld, L. Kröger, V. Botan, A. Köster, S. Stephan, E. J. García, G. Rutkai, G. Raabe, P. Klein, K. Leonhard, C. W. Glass, J. Lenhard, J. Vrabec, H. Hasse: Round robin study: Molecular simulation of thermodynamic properties from models with internal degrees of freedom, Journal of Chemical Theory and Computation 13 (2017) 4270–4280. DOI:`10.1021/acs.jctc.7b00489`.

[253] T. R. Merton: The viscosity and density of caesium nitrate solutions, Journal of the Chemical Society, Transactions 97 (1910) 2454–2463. DOI:`10.1039/ct9109702454`.

[254] P. W. Holland, R. E. Welsch: Robust regression using iteratively reweighted least-squares, Communications in Statistics - Theory and Methods 6 (1977) 813–827. DOI:`10.1080/03610927708827533`.

[255] S. Lloyd: Least squares quantization in PCM, IEEE Transactions on Information Theory 28 (1982) 129–137. DOI:`10.1109/tit.1982.1056489`.

[256] M. Ester, H.-P. Kriegel, J. Sander, X. Xu: A density-based algorithm for discovering clusters in large spatial databases with noise, Proceedings of the 2nd ACM International Conference on Knowledge Discovery and Data Mining (KDD) 96 (1996) 226–231.

A Supporting Information for Chapter 3

The Appendix for Chapter 3 contains the following supporting information:

- Simulation details of the mass transfer simulations of the Lennard-Jones mixtures.

- Additional results for mixture B.

- Additional numerical values from the mass transfer simulations from both mixtures and all studied temperatures.

- Details and numerical values on the bulk diffusion coefficients.

A.1 Simulation Details

Figure A.1 shows details of the simulations that were carried out for both mixtures at the temperature $T = 0.715\,\varepsilon k_{\mathrm{B}}^{-1}$. Only results from the production phase are shown. In the diagrams on the left side, the number of inserted and deleted particles of component 2 in the two control volumes is shown as a function of the simulation time. Note that the control volumes regulate the chemical potential, which can result in the fact that each control volume inserts and deletes particles in some times steps. However, the cumulative number of inserted particles in the control volume CV+ and deleted particles in the control volume CV- during the production phase yield increasing and decreasing trends, respectively, cf. Figure A.1. The statistical uncertainty of the mass flux j_2 was determined from the average deviation of the lines through the origin with the slope $\frac{\Delta N_2}{\Delta \tau}$ and $-\frac{\Delta N_2}{\Delta \tau}$ and the corresponding primary data for $N_2^+(\tau)$ and $N_2^-(\tau)$, cf. Figure A.1.

For mixture B, the results are as expected: symmetric straight lines through the origin for $N_2^+(\tau)$ and $N_2^-(\tau)$. The rate of low-boiling particles inserted in the left control volume approximately equals the rate of low-boiling particles being removed in the right control volume. The results for mixture A scatter much more than those for mixture B. This is mainly due to the higher vapor density and pressure in mixture A. Hence, the

uncertainty obtained for the flux j_2 in mixture A is significantly larger than in mixture B (see main body of this work).

Since the insertion is the more difficult step in a sense that also unfavorable configurations are sometimes accepted, the fluctuations are more pronounced for the inserting control volume, cf. Figure A.1. Still, both shown cases can be considered quasi-stationary.

The interface positions shown in Figure A.1 – right indicate that the liquid slab remains fairly constant in the simulation box. However, in the case of mixture B, the liquid slab slightly moves towards the inserting control volume during the production phase.
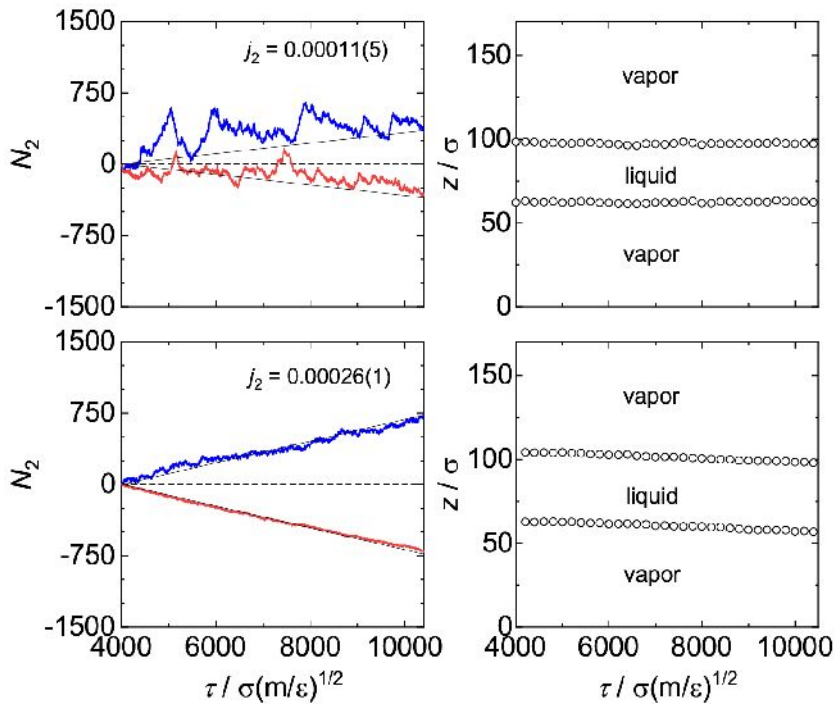

Figure A.1: Results from the production phase of the mass transfer simulations at $T = 0.715\,\varepsilon k_{\mathrm{B}}^{-1}$. Left: cumulative inserted and removed particles of the component 2 in the control volumes $N_2^+(\tau)$ (blue) and $N_2^-(\tau)$ (red); right: position of the interfaces as a function of the simulation time. Results of the mixture A are in the top; results of mixture B are bottom. Symbols indicate the z-position where the total density at the interface is $\rho_{50} = \rho_{\mathrm{V}} + 0.5\,(\rho^{\mathrm{liq}} - \rho^{\mathrm{vap}})$. The black lines indicate the obtained slopes $\frac{\Delta N_2}{\Delta \tau}$ and $-\frac{\Delta N_2}{\Delta \tau}$.

Several challenges were observed during the preliminary testing of the simulation method that are briefly summarized here. The choice of an appropriate difference of the chemical potential was particularly challenging. Large values of the difference of the chemical potential were found to cause strong perturbations – especially in the vapor phases – and, hence, cause nucleation of droplets or bubbles and also require long equilibration times to reach a quasi-stationary state. Furthermore, large differences of the chemical potential favor movements of the liquid film in the box. Small values of the differences

of the chemical potential will on the other hand result in small values of the flux.

The number and frequency of GCMC steps applied in the control volumes (see main body of this work) were chosen based on preliminary tests. On the one side, the amount of MC steps has to be large enough to ensure that the prescribed chemical potential is regulated in the control volumes. On the other side, the number of Monte Carlo steps should be small as it significantly influences the required computational time and causes perturbations in the vapor phase. Also the frequency of MC and MD calculations has to be balanced between computational effort and the stability of the simulation.

A.2 Individual State Points in the Profiles

Figure A.2 depicts a detailed comparison of the sampled state points from each bin (excluding the vicinity of the control volumes) from all profiles during the production phase from the mass transfer simulation with mixture A and mixture B at $T = 0.715\,\varepsilon k_{\mathrm{B}}^{-1}$. In the case of mixture A, the averaged state points for the two vapor domains and the liquid domain agree very well with the equilibrium phase envelope computed from the PeTS EOS [14, 112]. The liquid bulk domain state points are connected to the two vapor domains by the state points in the interface. For the liquid bulk domain, the state points show an elliptic scatter pattern around a point on the phase equilibrium envelope. The scattering is dominated by a scattering in the pressure, which is simply due to the fact that the pressure shows stronger fluctuations in the liquid bulk than the vapor bulk, cf. the pressure profiles in Figure 4. On the contrary, for vapor bulk domains V_{left} and V_{right}, where the scattering of the individual bin state points is dominated by a scattering in the concentration. This is due to the fact that the relatively low number of particles in the vapor bins yields stronger fluctuations compared to the liquid bulk bins. Nevertheless, the three averaged state points from the bins in the respective bulk domain from all profiles during the production phase (blue squares in Figure A.2) are in excellent agreement with the phase equilibrium computed from the PeTS EOS [14, 112], which is known to give an excellent description of the phase equilibrium of LJTS mixtures [52, 103, 248]. Following Ref. [249], the local scalar pressure p in the heterogeneous system was simply computed by averaging the trace of the pressure tensor. The pressure across the interfaces smoothly connects the three bulk domains $V_{\mathrm{left}} - L - V_{\mathrm{right}}$. The pressure transition in the two interfaces differs, which is in line with differences in the enrichment, cf. Figure 5.

For mixture B (cf. Figure A.2, right panel), the magnitude of the pressure and composition scattering in the bulk domains is similar to that for mixture A: the state points in the vapor bulk domains (yellow and dark blue circles) exhibit stronger fluctuations
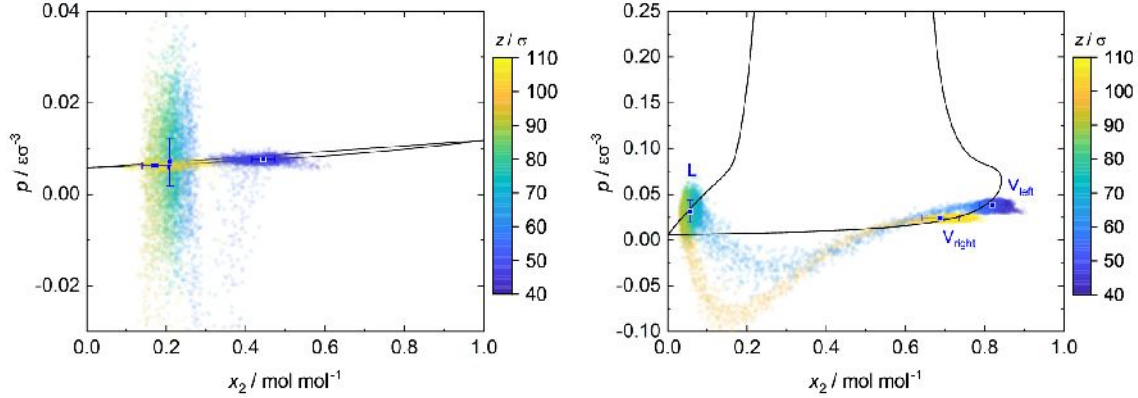
Figure A.2: Pressure – composition diagram for mixture A (left) and mixture B (right) at $T = 0.715\,\varepsilon k_{\mathrm{B}}^{-1}$. The black line indicates the phase equilibrium computed with the PeTS EOS [14, 112]. The circles indicate state points sampled during the stationary phase of the simulation in the individual bins of the profiles – excluding the vicinity of the control volumes. The color corresponds to the z-position in the profile. The squares indicate the averaged state points computed in each bulk domain (liquid as well as left and right vapor).

in the composition, whereas the liquid bulk domain exhibits more pronounced pressure fluctuations (turquoise circles). Also the scalar pressure across the interfaces has a similar behavior as found for mixture A. Also for mixture B, the pressure range in the interface and the scattering in the liquid domain exceeds the pressure range of the phase equilibrium.

A.3 Definition of Mass Fluxes and Reference Systems

Velocities and fluxes reported in the main part of the paper refer to the fixed laboratory frame. The flux of component 2 is related to the mean directed velocity u_2 by

$$j_2 = \rho x_2 u_2\,. \tag{A.1}$$

Due to the chosen boundary conditions, the mean directed velocity of component 1 is zero here ($u_1 = 0$), which results in a zero corresponding net flux of component 1 ($j_1 = 0$). Hence, the diffusive and convective mass flux of component 1 cancel each other in the stationary state

$$j_1^{\mathrm{D}} = -j_1^{\mathrm{conv}}\,. \tag{A.2}$$

The velocity u_2 is also the diffusion velocity of component 2 when the reference velocity

is that of component 1.

$$u_2^{D,1} = u_2 \tag{A.3}$$

However, often other reference velocities are used for defining the diffusive velocity and the corresponding diffusive fluxes, namely mole-averaging (or, equivalently particle number-averaging) and mass-averaging. As the mass of all components is the same, there is no difference between these averages here. The mole-averaged velocity is:

$$u_0^n = x_1 u_1 + x_2 u_2 \tag{A.4}$$

or, using $u_1 = 0$:

$$u_0^n = x_2 u_2 \tag{A.5}$$

Hence, using that reference velocity, the diffusion velocity of component 2 $u_2^{D,n}$ is

$$u_2^{D,n} = u_2 - u_0 = u_2 - x_2 u_2 = x_1 u_2 . \tag{A.6}$$

The corresponding diffusive flux is

$$j_2^{D,n} = \rho x_2 x_1 u_2 . \tag{A.7}$$

Comparing these results for the diffusion in the molar reference frame with the corresponding results in the fixed laboratory frame yields:

$$u_2^{D,n}/u_2 = j_2^{D,n}/j_2 = x_1 \tag{A.8}$$

As the liquid bulk considered here consists mainly of the high-boiling component 1, the diffusive contributions (in the molar reference frame) are small in the liquid bulk. On the contrary, they are important in the vapor domain.

A.4 Additional Results for Mixture B

Figure A.3 shows the density profiles and isothermal $p-x$ diagrams of mixture B during the production phase of the mass transfer simulations at different temperatures. In all cases, no enrichment is found at the interface. The state points averaged for the three bulk domains are in excellent agreement with the respective phase equilibrium envelope.
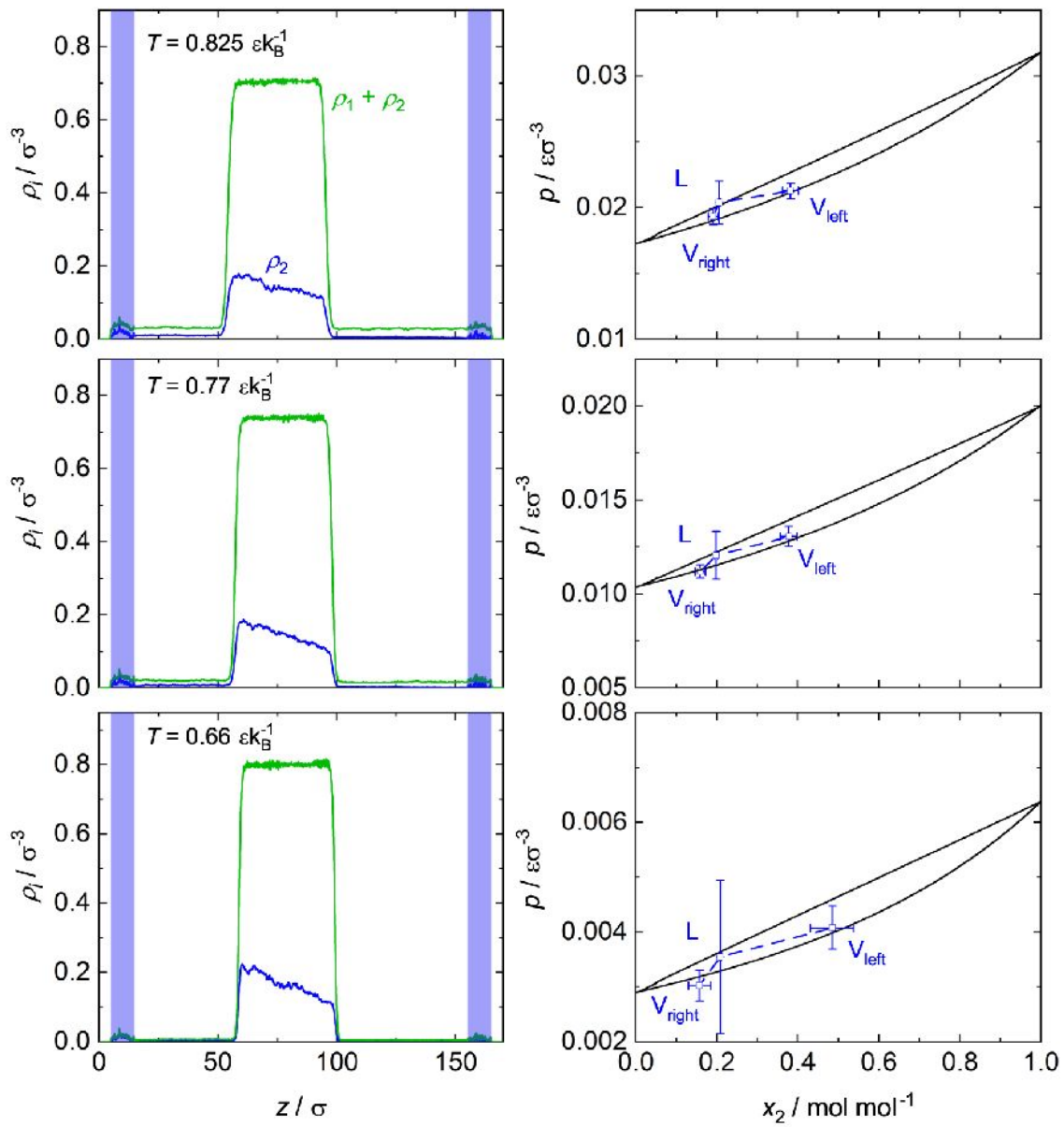
Figure A.3: Density profiles (left panels) and state points in the bulk domains (right panels) sampled during the production phase of the mass transfer simulations for mixture B at different temperatures. The blue shaded area indicates the elongation of the control volumes in z-direction.

A.5 Numerical Values from the Mass Transfer Simulations

Table A.1 reports the numerical values for the pressure, density, mole fraction, and velocity of component 2 obtained for all three bulk domains for both studied mixtures and the four considered temperatures.

Table A.1: Numerical values for the results from the mass transfer simulations in the three bulk domains V_{left}, L, and V_{right} (as defined in the main body of this work). Results for mixture A and mixture B. Results for all four studied temperatures: pressure p; total density ρ in the bulk domains; mole fraction of the low-boiling component x_2 in the bulk domains; and average velocity u_2 of the component 2 particles in the fixed laboratory frame.

$T/\varepsilon k_{\text{B}}^{-1}$	V_{left} A	B	L A	B	V_{right} A	B
			$p/\varepsilon\sigma^{-3}$			
0.66	0.0335(25)	0.0041(4)	0.0262(19)	0.0036(14)	0.0187(7)	0.0030(3)
0.715	0.0387(15)	0.0077(5)	0.0316(21)	0.0071(13)	0.0239(14)	0.0063(3)
0.77	0.0440(21)	0.0131(5)	0.0376(20)	0.0121(13)	0.0300(15)	0.0112(4)
0.825	0.048(3)	0.0213(6)	0.0436(22)	0.0204(16)	0.0382(17)	0.0193(6)
			ρ/σ^{-3}			
0.66	0.06576(3)	0.00660(1)	0.79691(3)	0.80062(3)	0.03292(1)	0.00484(1)
0.715	0.06718(3)	0.01176(1)	0.76706(3)	0.77081(2)	0.04325(8)	0.00944(1)
0.77	0.07236(3)	0.01937(1)	0.73398(2)	0.73935(2)	0.04623(3)	0.01630(1)
0.825	0.07376(3)	0.03112(1)	0.69914(2)	0.70425(2)	0.05838(7)	0.02791(1)
			$x_2/\text{mol}\,\text{mol}^{-1}$			
0.66	0.895(10)	0.48(5)	0.057(5)	0.208(3)	0.81(4)	0.16(3)
0.715	0.829(9)	0.44(3)	0.056(3)	0.209(2)	0.68(6)	0.171(22)
0.77	0.711(13)	0.378(21)	0.058(4)	0.198(4)	0.60(3)	0.159(12)
0.825	0.567(22)	0.382(20)	0.055(3)	0.206(3)	0.49(4)	0.191(12)
			$u_2/\sqrt{\varepsilon/\text{M}}$			
0.66	0.0011(1)	0.0719(1)	0.0014(1)	0.0014(1)	0.0024(2)	0.3023(1)
0.715	0.0020(1)	0.0497(1)	0.0026(1)	0.0016(1)	0.0038(1)	0.1609(1)
0.77	0.0020(2)	0.0287(1)	0.0024(2)	0.0014(2)	0.0037(2)	0.0810(2)
0.825	0.0045(2)	0.0202(2)	0.0049(3)	0.0017(1)	0.0066(3)	0.0451(2)

Table A.2 reports the interface positions averaged during the production phase. The interface position was defined as the point in the interface with the total density $\rho_{\text{interface}} = \rho_{\text{V}} + 0.5\,(\rho_{\text{L}} - \rho_{\text{V}})$, cf. Figure A.1. The interface position was computed from each block averaged density profile; the reported values in Table A.2 are their mean values. The uncertainty was estimated as three times the standard deviation of the block average values, which confirms the assumption of a quasi-stationary state of the simulations.

Table A.2: Average position of the two vapor-liquid interfaces during the mass transfer simulations. Results for mixture A and mixture B. Results for all four studied temperatures. The uncertainty was estimated as three times the standard deviation of the block averages obtained during the simulation.

$T\,/\,\varepsilon k_{\text{B}}^{-1}$	z_{left}/σ		z_{right}/σ	
	A	B	A	B
0.66	59(1)	58(1)	96(1)	98(1)
0.715	62(1)	56(2)	97(1)	99(2)
0.77	61(1)	56(2)	94(1)	96(2)
0.825	63(1)	52(2)	95(2)	94(2)

A.6 Comparison of Equilibrium and Mass Transfer Density Profiles

Figure A.4 shows the comparison of density profiles sampled from equilibrium (i.e., no mass transfer present) and density profiles during the production phase with a stationary mass transfer being established. Results are shown for both mixtures at $T = 0.66\,\varepsilon k_{\text{B}}^{-1}$. The results are as expected: the equilibrium density profiles are constant in the bulk phases – neglecting the fluctuations, whereas the mass transfer density profiles exhibit a distinct gradient in the bulk phases (see the main body of this work for a detailed discussion).
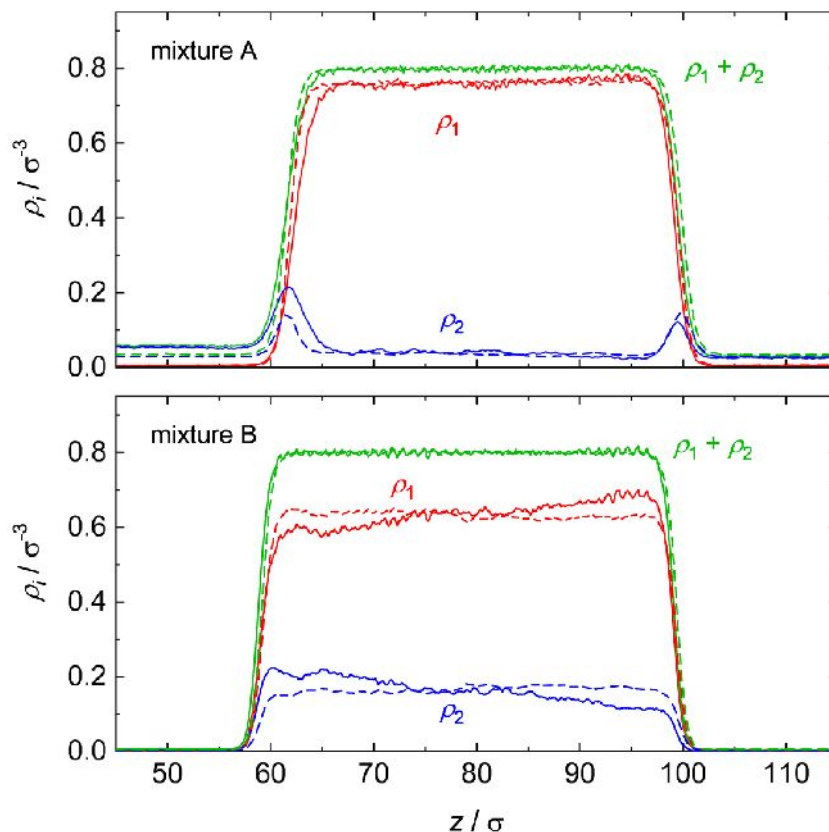
Figure A.4: Density profiles for mixtures A and B at $T = 0.66\,\varepsilon k_{\mathrm{B}}^{-1}$ sampled under equilibrium, i.e., no mass transfer present (dashed lines), and density profiles during the production phase with a stationary mass transfer being present (solid lines). The blue lines indicate the low-boiling component 2, the red lines the high-boiling component 1, and the green lines the total density. The average liquid phase composition (definition is given in the main body of this work) is $x_2' = 0.06\,\mathrm{mol\,mol^{-1}}$ for mixture A and $x_2' = 0.21\,\mathrm{mol\,mol^{-1}}$ for mixture B (cf. Table A.1).

A.7 Determination of Bulk Diffusion Coefficients

Diffusion coefficients were computed for both mixtures in the liquid and the vapor phase. For the liquid phase, molecular simulations were performed at state points slightly above the bubble line. For the vapor phase, diffusion coefficients were determined from the Chapman-Enskog theory [115]. The methodology and the results are discussed in the following.

Liquid Phase Simulations

The diffusion coefficients of the liquid bulk phases were determined with the molecular simulation code *ms*2 [116, 204], using molecular dynamics simulations at given temperature and pressure. For both mixtures, simulations were carried out at $T/\varepsilon k_{\mathrm{B}}^{-1} = 0.66$, 0.715, 0.77, 0.825. The pressure was chosen $p = 0.4\,\varepsilon\sigma^{-3}$ for mixture A and $p = 0.1\,\varepsilon\sigma^{-3}$ for mixture B at a given composition and temperature. The pressures were chosen, such

that the state points were above the bubble line of the phase equilibrium for all studied temperatures. Due to the steep bubble line and the presence of a critical point in mixture A, simulations in the liquid phase were only performed up to $x_2' \approx 0.15 \, \text{mol} \, \text{mol}^{-1}$ for that mixture.

For all *ms*2 simulations, the box was a cubic volume with periodic boundary conditions, containing 4000 particles. The simulation time step was $\Delta \tau = 0.001 \, \sigma (m/\varepsilon)^{1/2}$ using a leapfrog integration scheme. The temperature was controlled using velocity scaling and the pressure with Andersen's barostat [35]. In a first step, the isobaric-isothermal ensemble (NpT) was used to determine the density at a given temperature, pressure and composition. The simulations in the NpT ensemble consisted of 9x10^5 equilibration time steps and 1x10^6 production time steps. The density determined by the NpT simulations was then used in a second simulation in the canonical ensemble (NVT) at the same temperature, density and composition. The NVT simulations consisted of 8x10^4 equilibration time steps and 1x10^6 production time steps. The diffusion coefficients were sampled during the production phase of the NVT runs using the velocity autocorrelation function.

The binary Maxwell-Stefan diffusion coefficient $Ð_{12}$ was sampled using the Green-Kubo formalism [53–55, 250]:

$$Ð_{12} = \frac{x_2}{3N_1} \left(\frac{x_1 M_1 + x_2 M_2}{x_2 M_2} \right)^2 \int_0^\infty \left\langle \sum_{k=1}^{N_1} v_{1,k}(\tau = 0) \cdot \sum_{l=1}^{N_1} v_{1,l}(\tau) \right\rangle \mathrm{d}\tau \,, \qquad (A.9)$$

where x_1 represents the mole fraction, M_1 and M_2 the molar mass of the two components, respectively, N_1 the number of particles and $v_{1,k}(\tau)$ the velocity of component 1 at time τ. The notation $\langle ... \rangle$ indicates the ensemble average. The choice of the component 1 and 2 in the binary mixture is arbitrary. The auto correlation functions were sampled at a length of 1x10^4 time steps at 5x10^3 different time origins. Statistical uncertainties were estimated using the block averaging method [207].

Vapor Phase Calculations

Diffusion coefficients for the vapor bulk phases were determined using the Chapman-Enskog theory [115]. Fickian mutual diffusion coefficients D_{12} in a binary mixture are related to the Maxwell-Stefan diffusion coefficients $Ð_{12}$ by the thermodynamic factor, i.e., $D_{12} = Ð_{12} \Gamma$. In the present work, the thermodynamic factor Γ is assumed to be unity in the vapor phase. Hence, the Maxwell-Stefan diffusion coefficients are computed as [115]

$$Ð_{12} = D_{12} = \frac{3}{8\pi^{1/2}} \frac{(k_\mathrm{B} T)^{1/2}}{M_{12}^{1/2} \rho \sigma_{12}^2 \Omega} \,, \qquad (A.10)$$

where ρ is the density, Ω is the collision integral, σ_{12} is the cross interaction Lennard-Jones size parameter and M_{12} a mass parameter, which is defined as

$$M_{12} = \frac{1}{\left(\dfrac{1}{M_1} + \dfrac{1}{M_2}\right)^{1/2}} .$$ (A.11)

The collision Integral Ω in Eq. (A.10) of the Lennard-Jones fluid was computed from an empirical correlation [251].

The density in Eq. (A.10) was taken as the total density of the left vapor bulk domain in the respective mass transfer simulation, cf. Table A.1.

Results for the Bulk Diffusion Coefficients

The numerical values of the Maxwell-Stefan diffusion coefficients obtained from the Green-Kubo molecular simulations are reported in Tables A.3 and A.4. Figure A.5 shows the results for the diffusivity ρD_{12} for the liquid phase for both mixtures. Figure A.6 shows the diffusivity ρD_{12} for the vapor phase for both mixtures computed from the Chapman-Enskog theory.

The values of the diffusivity for both mixtures are approximately the same. This holds for both the liquid and the vapor phase. For the liquid and the vapor phase, there is a tendency that the diffusivity ρD_{12} for mixture A slightly exceeds that of mixture B.
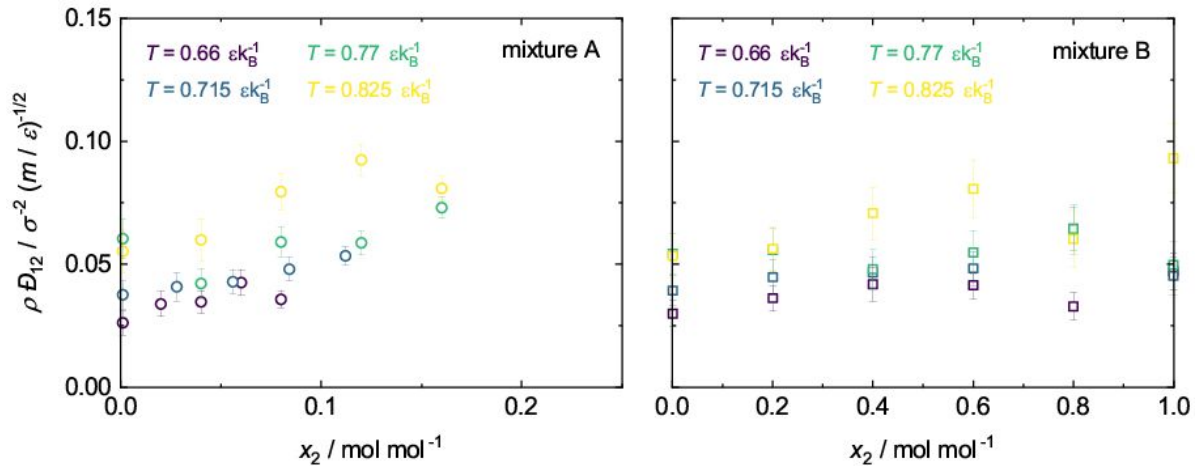

Figure A.5: Diffusivity ρD_{12} of the liquid phase at different temperatures. Results for mixture A (left) and mixture B (right). The color indicates the temperature.

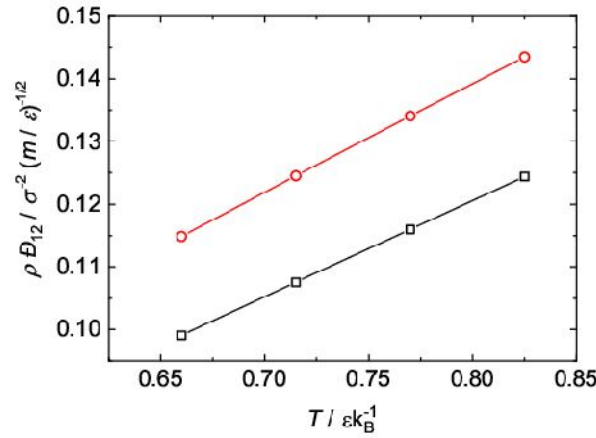**Figure A.6:** Diffusivity ρD_{12} of the vapor phase for mixture A (circles) and B (squares).

Table A.3: Maxwell-Stefan diffusion coefficients of the liquid phase of mixture A at different density, temperature and mole fraction computed using the Green-Kubo formalism [53–55, 250].

$T \ / \ \varepsilon k_{\mathrm{B}}^{-1}$	$\rho \ / \ \sigma^{-3}$	$p \ / \ \varepsilon \sigma^{-3}$	$x_2 \ / \ \mathrm{mol\,mol^{-1}}$	$D_{12} \ / \ \sigma \, \varepsilon^{0.5} \, m^{-0.5}$
0.66	0.838	0.39994(21)	0.001	0.031(5)
	0.835	0.39999(21)	0.02	0.041(6)
	0.831	0.39999(20)	0.04	0.042(6)
	0.828	0.40001(23)	0.06	0.051(7)
	0.824	0.40000(20)	0.08	0.043(5)
0.715	0.814	0.40000(13)	0.001	0.046(6)
	0.809	0.40000(14)	0.028	0.051(7)
	0.804	0.39997(14)	0.056	0.053(7)
	0.799	0.40001(13)	0.084	0.060(7)
	0.793	0.40000(13)	0.112	0.067(7)
0.77	0.790	0.40000(13)	0.001	0.077(8)
	0.782	0.39999(14)	0.04	0.054(7)
	0.773	0.39999(14)	0.08	0.076(9)
	0.765	0.40000(15)	0.12	0.077(10)
	0.755	0.40000(14)	0.16	0.097(11)
0.825	0.765	0.40000(21)	0.001	0.072(9)
	0.756	0.39999(15)	0.04	0.079(10)
	0.747	0.39999(15)	0.08	0.107(11)
	0.737	0.39996(20)	0.12	0.125(12)
	0.727	0.40000(15)	0.16	0.111(13)

Table A.4: Maxwell-Stefan diffusion coefficients of the liquid phase of mixture B at different density, temperature and mole fraction computed using the Green-Kubo formalism [53–55, 250].

T / εk_B^{-1}	ρ / σ^{-3}	p / $\varepsilon\sigma^{-3}$	x_2 / $\mathrm{mol\,mol^{-1}}$	$Đ_{12}$ / $\sigma\,\varepsilon^{0.5}\,m^{-0.5}$
0.66	0.816	0.10002(13)	0.001	0.037(5)
	0.810	0.09999(13)	0.2	0.045(5)
	0.803	0.10000(13)	0.4	0.052(7)
	0.796	0.10002(13)	0.6	0.052(5)
	0.788	0.09998(14)	0.8	0.042(6)
	0.781	0.09999(13)	0.999	0.060(7)
0.715	0.789	0.10000(14)	0.001	0.050(6)
	0.781	0.10000(14)	0.2	0.057(7)
	0.774	0.10000(13)	0.4	0.060(6)
	0.765	0.09999(14)	0.6	0.063(7)
	0.757	0.10003(14)	0.8	0.085(9)
	0.748	0.09999(15)	0.999	0.060(8)
0.77	0.760	0.09999(15)	0.001	0.071(8)
	0.751	0.09999(14)	0.2	0.074(9)
	0.742	0.10000(14)	0.4	0.065(8)
	0.733	0.09999(17)	0.6	0.075(9)
	0.723	0.10000(20)	0.8	0.089(10)
	0.713	0.10001(14)	0.999	0.070(10)
0.825	0.729	0.10000(15)	0.001	0.073(9)
	0.719	0.09998(15)	0.2	0.078(9)
	0.708	0.10000(15)	0.4	0.100(11)
	0.697	0.10001(14)	0.6	0.116(12)
	0.685	0.09999(15)	0.8	0.088(12)
	0.672	0.10000(15)	0.999	0.139(14)

B Supporting Information for Chapter 4

The Appendix for Chapter 4 contains the following supporting information:

- Details on the statistics of two sets of replicas at $T = 0.715\,\varepsilon k_{\mathrm{B}}^{-1}$.

- Details on the determination of the interface position and thickness.

- Pressure, density, and flux sampled in the measurement volumes as a function of time at the temperatures $T = 0.66, 0.77, 0.825\,\varepsilon k_{\mathrm{B}}^{-1}$. The results at $T = 0.715\,\varepsilon k_{\mathrm{B}}^{-1}$ are shown in the main body of this work.

- Pressure-composition diagrams as a function of time at the temperatures $T = 0.66, 0.77, 0.825\,\varepsilon k_{\mathrm{B}}^{-1}$. The results at $T = 0.715\,\varepsilon k_{\mathrm{B}}^{-1}$ are shown in the main body of this work.

- Response of the system at the vapor-liquid interfaces for simulations at temperatures $T = 0.66, 0.77, 0.825\,\varepsilon k_{\mathrm{B}}^{-1}$ for both mixtures. The results at $T = 0.715\,\varepsilon k_{\mathrm{B}}^{-1}$ are shown in the main body of this work.

B.1 Details on the Statistics of a Set of Replicas

The initial number of particles and their initial configuration, the box size as well as the temperature were the same for all simulations in a set of replicas. The simulations from a set of replicas differ only in the initial velocities of the particles in the box at the beginning of the simulation. The initial velocity of each particle is randomly drawn from the Maxwell-Boltzmann distribution by using a random number generator. This ensures that the simulations from a set of replicas pass different trajectories in the phase space and representative and significant measures can be obtained from the simulations.

The stochastic nature of the Grand Canonical Monte Carlo algorithm utilized in the simulation method results in the fact that the number of inserted particles in the *In* phase differs among the simulations of a set of replicas. The variation of the number of inserted particles in a set of replicas and its influence on observables is briefly discussed

here. Figure B.1 shows the results from a set of replicas from mixtures A and one from mixtures B at $T = 0.715\,\varepsilon k_{\mathrm{B}}^{-1}$. The distribution of simulations, the density $\rho'_{2,\mathrm{Eq2}}$ and the delay time $\Delta\tau_{\mathrm{d}}$ as functions of the number of inserted particles N_2 are shown. The number of simulations with a certain number of inserted particles (cf. Figure B.1 (a)) shows that the distribution approximately follows a Gaussian distribution. For both mixtures the peak of the distribution is at about $1\,200$ and the scattering lies in the range $1\,075$ to $1\,425$. The standard deviation of the distributions is 46 for mixtures A and 64 for mixtures B. Hence, the set of replicas from mixtures B has a slightly broader distribution of the number of inserted particles compared to mixtures A.
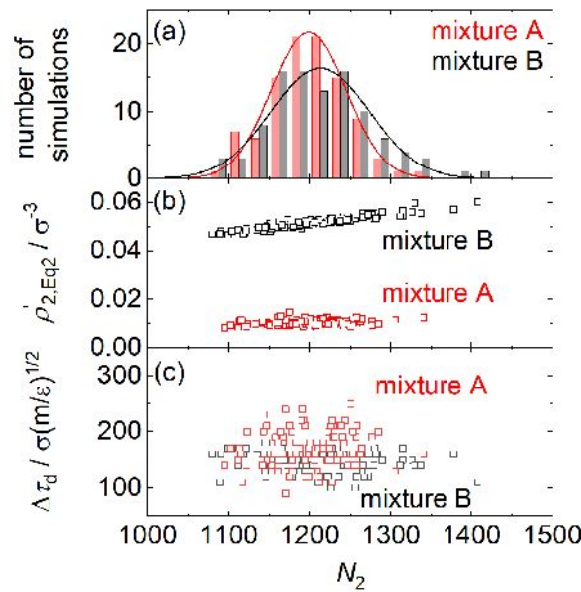

Figure B.1: Statistics from two exemplar sets of replicas with 100 simulations each: One for mixtures A (red) and one for mixture B (black) at $T = 0.715\,\varepsilon k_{\mathrm{B}}^{-1}$. Histogram of the number of simulations (top), density of component 2 at equilibrium state *Eq2* $\rho'_{2,\mathrm{Eq2}}$ in the measurement volume in the liquid phase $\mathrm{MV_{liq}}$ (middle), and the delay time $\Delta\tau_{\mathrm{d}}$ (bottom) as functions of the number of inserted particles N_2. Red and black lines in the top represent Gaussian distribution functions fitted to the respective data.

Figure B.1 (b) shows that the variation of N_2 has only a minor influence on the density $\rho'_{2,\mathrm{Eq2}}$ in the equilibrium state after the relaxation process of component 2 in the liquid phase measurement volume $\mathrm{MV_{liq}}$. For mixtures B, a tendency can observed that $\rho'_{2,\mathrm{Eq2}}$ slightly increases with increasing N_2, which is simply due to the fact that a slightly different state point of the binary mixtures is obtained if more component 2 particles are inserted. The density $\rho'_{2,\mathrm{Eq2}}$ obtained for mixtures B is stronger influenced by N_2 than mixtures A, since the majority of inserted component 2 particles end up in the liquid phase in the equilibrium *Eq2* in the case of mixtures B. This is simply a result of the large differences in the gas solubility of the two mixtures [103, 104].

The delay time $\Delta\tau_{\mathrm{d}}$ is defined as the time span between the start of the insertion phase at $\tau = 1\,000\,\sigma(m/\varepsilon)^{1/2}$ and the time at which the density of component 2 exceeds $\rho'_2(\tau) \geq 0.0001\,\sigma^{-3}$ in the liquid phase measurement volume. For both mixtures, the number of inserted particles N_2 has no significant influence on the delay time $\Delta\tau_{\mathrm{d}}$. Furthermore, the delay time is the same for both mixtures within the scattering, which is also seen in density response in the liquid phase in Figures B.2 (b),B.3 (b), and B.4 (b) and the corresponding Figure in the main body of this work at $T = 0.715\,\varepsilon k_{\mathrm{B}}^{-1}$.

Overall, the scattering of the number of inserted particles N_2 within a set of replicas has a small effect on the response of the system. Thus, the method of set of replicas gives a clearer view of the dynamic processes within the system. The set of replicas helps to distinguish between physically relevant processes and noise.

B.2 Simulation Details: Determination of the Interface Position and Thickness

For the determination of the density ρ' and ρ'' of the liquid and vapor bulk, first the z-position of the global minimum and maximum of the gradient $\partial\rho/\partial z$ is determined. The maximum is the initial guess for the position of the right interface, the minimum is the initial guess for the left interface. Based on the initial guesses of the interface position, the bulk density ρ' and ρ'' are sampled in a distance of $1/3$ of the size of the liquid phase in z-direction to the minimum and maximum position of the gradient $\partial\rho/\partial z(z)$ in the liquid and vapor phase. Bulk density are averaged over a length of $1/3$ of the size of the liquid phase in z-direction. With the bulk density ρ' and ρ'', the position z_{10}, z_{50}, and z_{90} can be precisely determined as the position where the density corresponds to

$$
\begin{aligned}
\rho_{10} &= \rho'' + 0.1(\rho' - \rho'') \\
\rho_{50} &= \rho'' + 0.5(\rho' - \rho'') \\
\rho_{90} &= \rho'' + 0.9(\rho' - \rho'')
\end{aligned}
\tag{B.1}
$$

B.3 Response in the Liquid and Vapor Phases for Various Temperatures

Figures B.2, B.3, and B.4 show pressure, density, and net flux sampled in the measurement volumes as a function of time at temperatures $T = 0.66, 0.77, 0.825\,\varepsilon k_{\mathrm{B}}^{-1}$. The results are qualitatively similar to the results shown for $T = 0.715\,\varepsilon k_{\mathrm{B}}^{-1}$. The negative

net flux in the vapor phase observable, which is only observed for mixture A, decreases with increasing temperature, which can be attributed the enrichment that is known to decreases with increasing temperature [103, 104].

Figure B.5 shows the pressure as a function of composition and time at the temperatures $T = 0.66, 0.77, 0.825\, \varepsilon k_\mathrm{B}^{-1}$. Results sampled in the measurement volumes for both mixtures A and B are shown. For all studied temperatures, the vapor and liquid equilibrium state points of *Eq1* and *Eq2* obtained from the NEMD simulations are in good agreement with the results from the PeTS EOS [14, 112]. Furthermore, in all studied cases, the vapor and liquid phase pressure are in excellent agreement – as expected in equilibrium. The pressure $p(x_2, \tau)$ sampled in the liquid and vapor phase follows a similar course over time as shown for $T = 0.715\, \varepsilon k_\mathrm{B}^{-1}$ in the main body of this work for each mixture. In the case of mixture B, the pressure sampled in the vapor phase intersect the dew line for the first time at $1,200 \leq \tau / \sigma (m/\varepsilon)^{1/2} \leq 1,250$ at all temperatures. From the intersection point, the pressure and composition sampled in the measurement volume of the vapor phase follows the dew line towards *Eq2* at all temperatures. The vapor phase of mixture B is close to equilibrium states but is continuously shifted out of equilibrium by the mass transfer in the liquid phase, which is observed at all temperatures. For mixture A, the pressure and composition sampled in the vapor phase first intersects the dew line at higher pressure and composition than *Eq2* state point with the exception of the results for $T = 0.825\, \varepsilon k_\mathrm{B}^{-1}$, for which the dew line is intersected at lower pressure and composition.
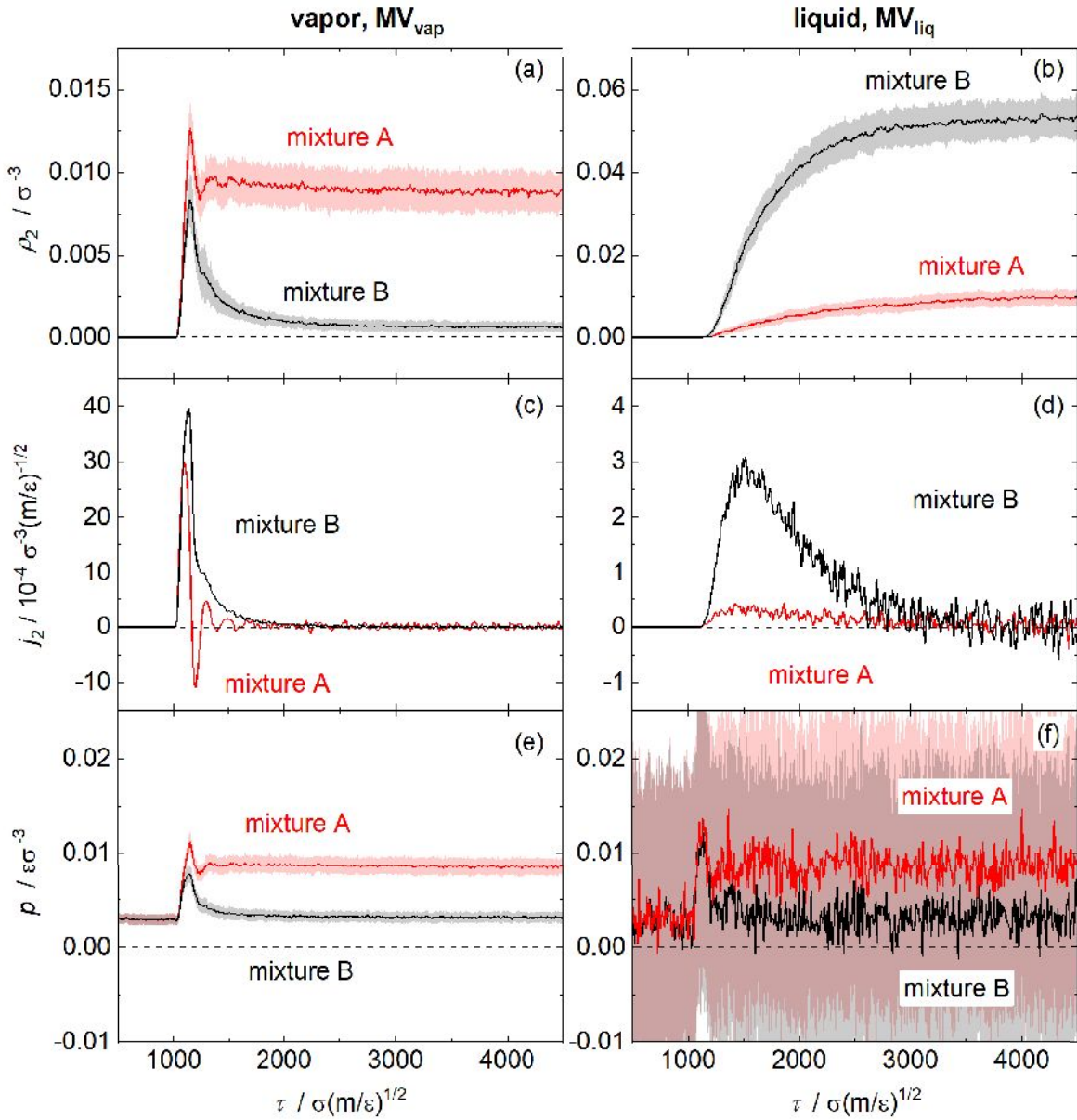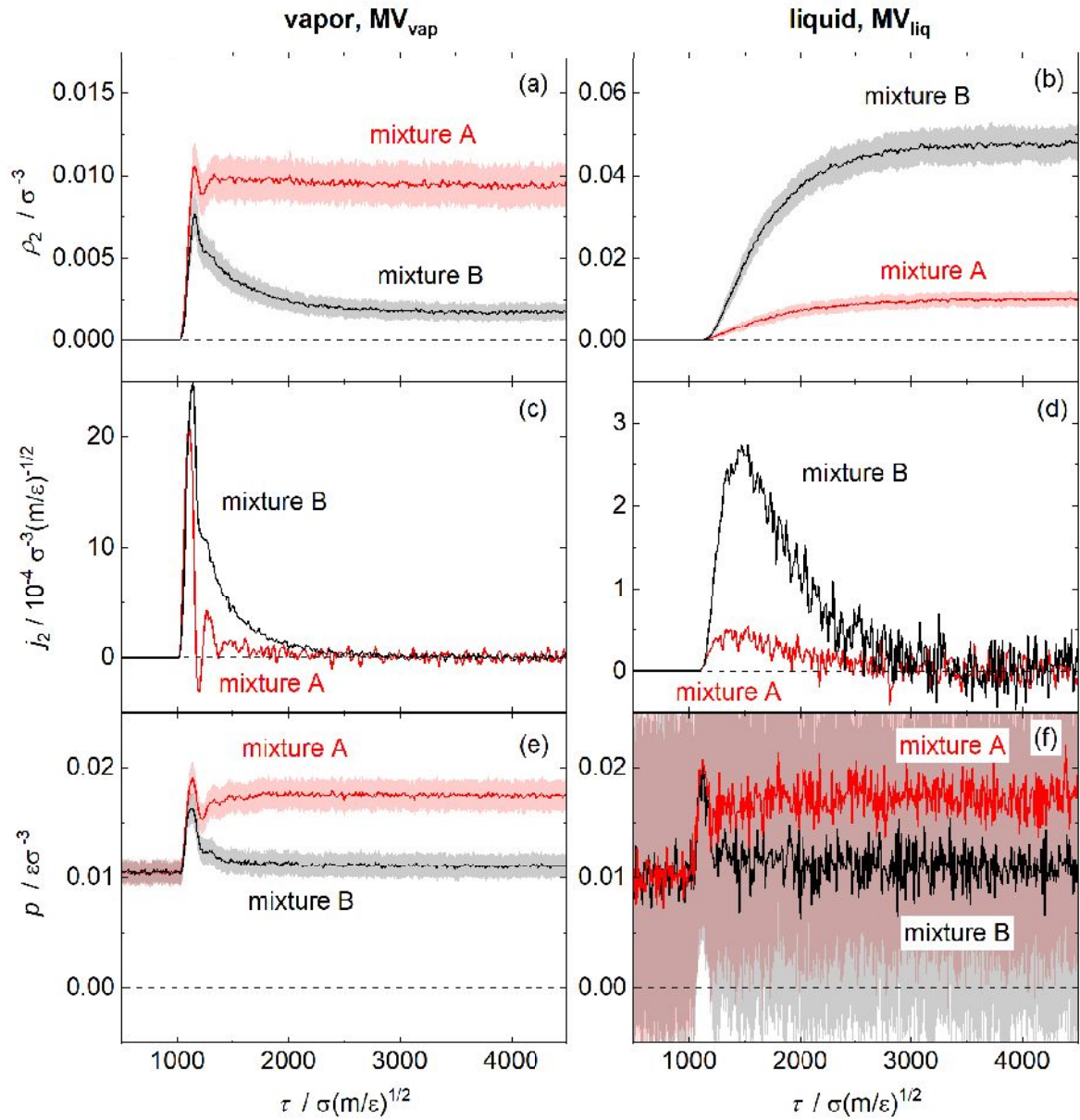
Figure B.2: Observables sampled in the replica NEMD simulations in the measurement volumes in the vapor phase MV_{vap} (left) and in the liquid phase MV_{liq} (right), respectively, as a function of the simulation time: density of component 2 ρ_2, flux of component 2 j_2, and pressure p. The temperature was $T = 0.66\,\varepsilon k_B^{-1}$. Results for mixtures A are indicated in red; results for mixtures B in black. Solid lines indicate the mean value obtained from the set of replicas, the shaded area indicates standard deviation. The standard deviation is only given for the two properties that were sampled directly (ρ_2 and p); j_2 was calculated from ρ_2.
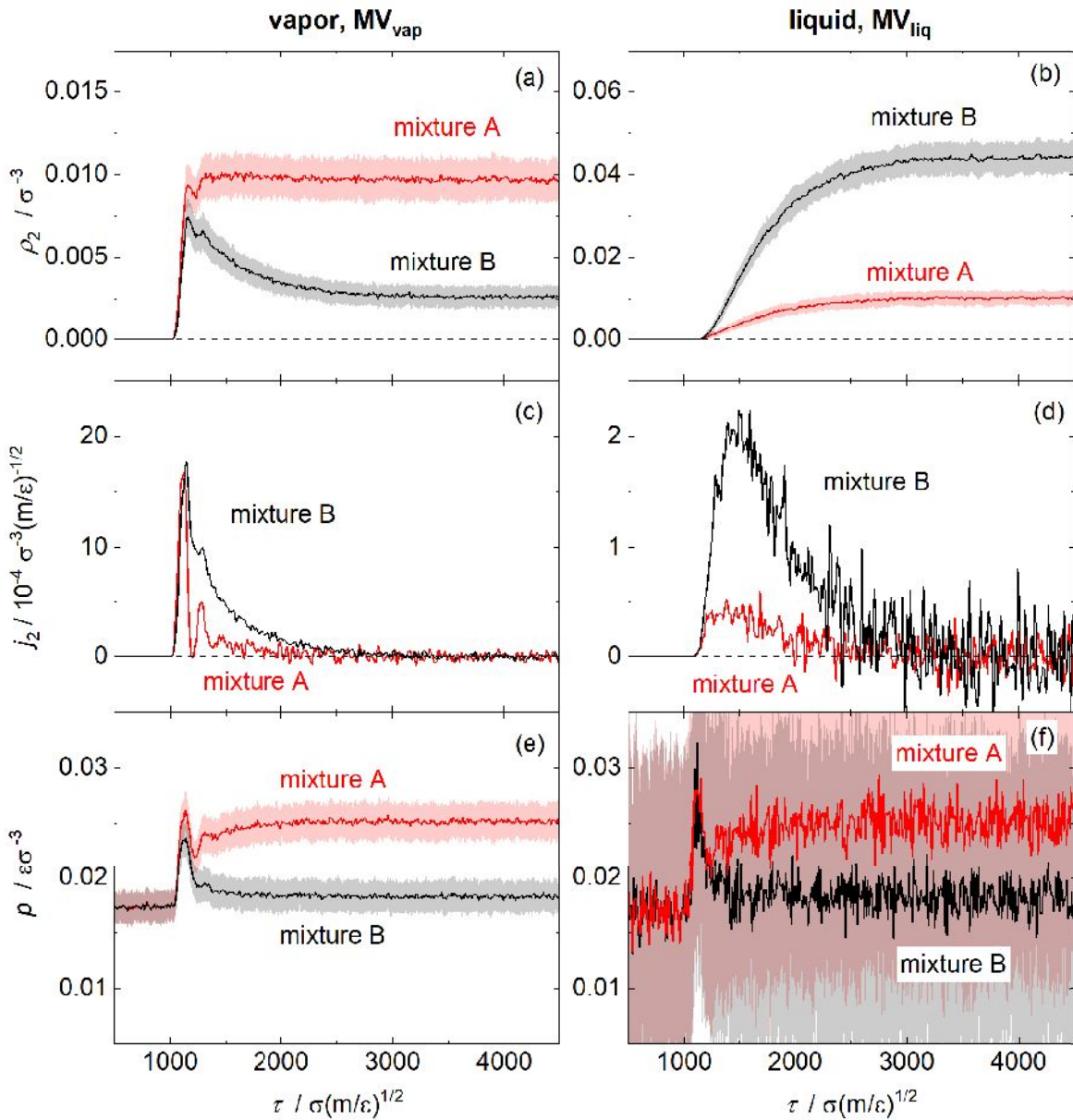
Figure B.3: Observables sampled in the replica NEMD simulations in the measure-
ment volumes in the vapor phase MV_{vap} (left) and in the liquid phase
MV_{liq} (right), respectively, as a function of the simulation time: density
of component 2 ρ_2, flux of component 2 j_2, and pressure p. The tempera-
ture was $T = 0.77\,\varepsilon k_B^{-1}$. Results for mixtures A are indicated in red; results
for mixtures B in black. Solid lines indicate the mean value obtained from
the set of replicas, the shaded area indicates standard deviation. The
standard deviation is only given for the two properties that were sampled
directly (ρ_2 and p); j_2 was calculated from ρ_2.

Figure B.4: Observables sampled in the replica NEMD simulations in the measurement volumes in the vapor phase MV_{vap} (left) and in the liquid phase MV_{liq} (right), respectively, as a function of the simulation time: density of component 2 ρ_2, flux of component 2 j_2, and pressure p. The temperature was $T = 0.825\,\varepsilon k_B^{-1}$. Results for mixtures A are indicated in red; results for mixtures B in black. Solid lines indicate the mean value obtained from the set of replicas, the shaded area indicates standard deviation. The standard deviation is only given for the two properties that were sampled directly (ρ_2 and p); j_2 was calculated from ρ_2.
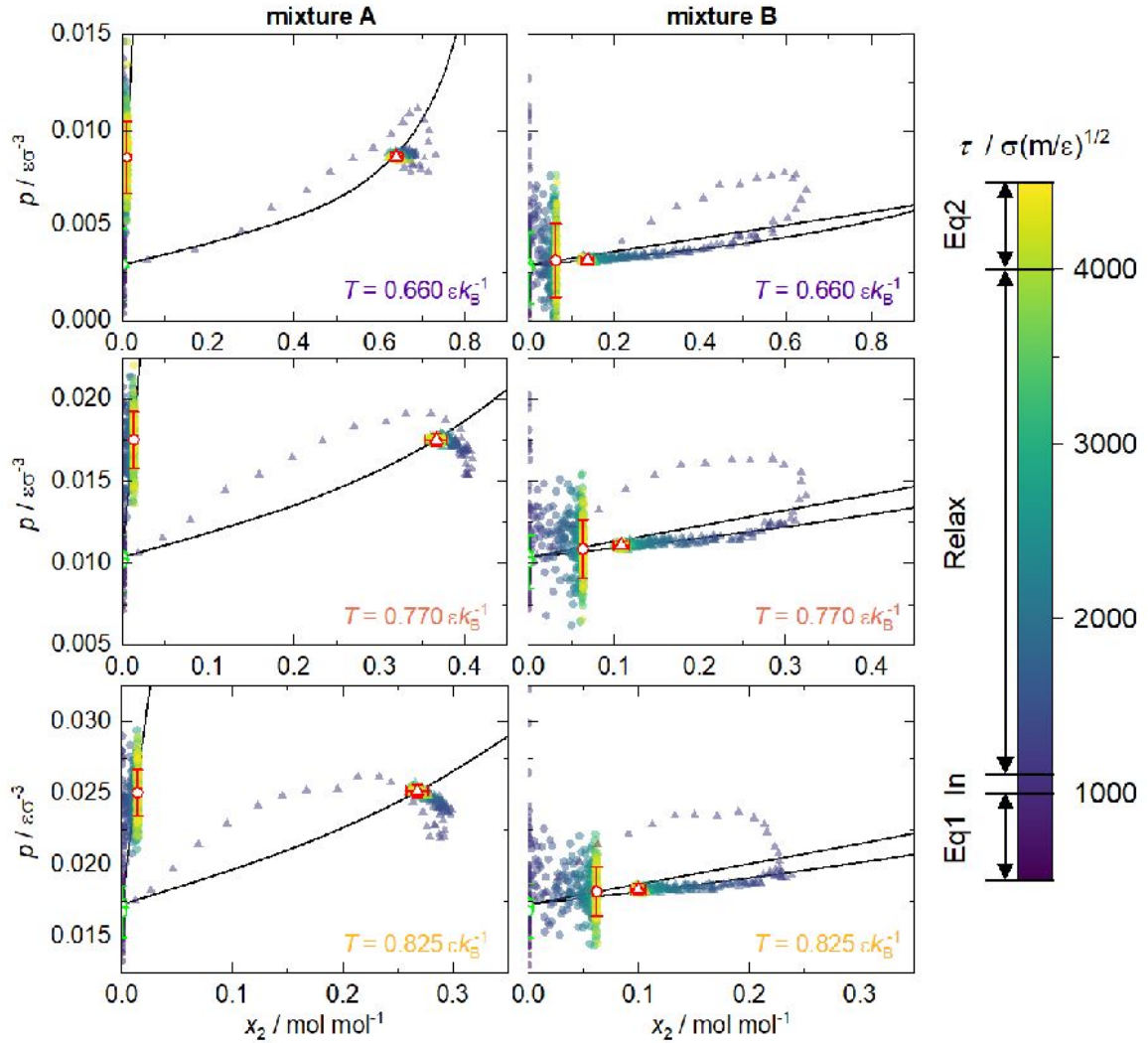
Figure B.5: Pressure-composition diagrams for mixtures A (left) and mixtures B (right). Results for at $T = 0.66\,\varepsilon k_{\mathrm{B}}^{-1}$ (top), at $T = 0.77\,\varepsilon k_{\mathrm{B}}^{-1}$ (middle), and at $T = 0.825\,\varepsilon k_{\mathrm{B}}^{-1}$ (bottom). Circles indicate state points sampled in the measurement volume MV_{liq}; triangles indicate state points sampled in the measurement volume MV_{vap}. The color scale indicates the simulation time. Each data point represents the mean value obtained from a set of replicas at a given simulation time τ. The white filled symbols indicate pressure and composition in *Eq1* (green) and in *Eq2* (red) phases. The error bars are the standard deviation obtained from a set of replicas. The black line indicates the phase equilibrium computed with the PeTS EOS [14, 112].

B.4 Response at the Vapor-Liquid Interface

Figures B.6, B.7, and B.8 show the response of the system in the interfacial region and the neighboring bulk phases for simulations at temperatures $T = 0.66, 0.77, 0.825 \, \varepsilon k_{\mathrm{B}}^{-1}$ for both mixtures. The temporary density peak of component 2 at the interface of mixture B decreases in height with increasing temperature. At the highest temperature, it vanishes nearly completely. This can be explained by a lower mass transfer resistance in the interface and the liquid phase at higher temperatures in mixture B. For mixture A at all temperatures, the density of component 2 at the interface is reaching its equilibrium value very quickly ($\Delta\tau = 200 \, \sigma(m/\varepsilon)^{1/2}$), immediately forming the characteristic symmetric enrichment peak.
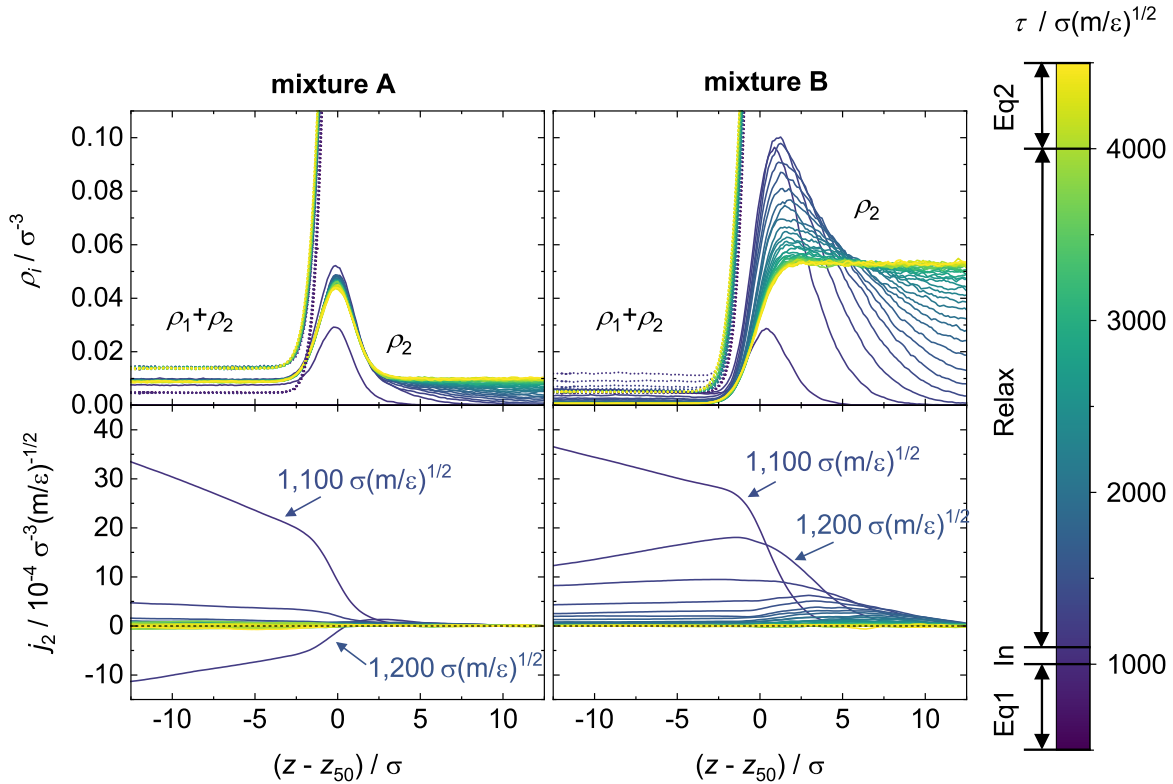

Figure B.6: Spatial profiles of the observables sampled in the vicinity of the interface and the neighboring bulk phases for mixture A (left) and mixture B (right). Results for the temperature $T = 0.66 \, \varepsilon k_{\mathrm{B}}^{-1}$ from set of replicas. Top: density of the low-boiling component 2 (——) and total density (·····); Bottom: molar flux of component 2 j_2. The simulation time τ is indicated by the color. The shown profiles were measured at time intervals of $\Delta\tau = 100 \, \sigma(m/\varepsilon)^{1/2}$.
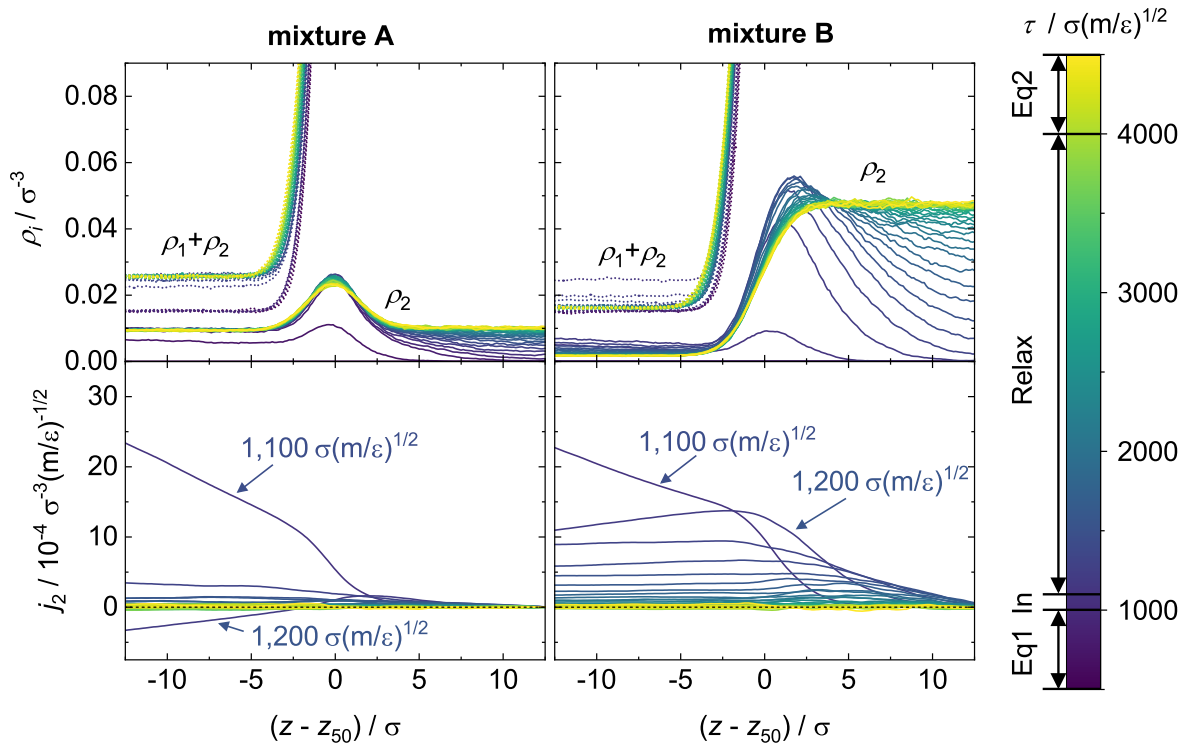
Figure B.7: Spatial profiles of the observables sampled in the vicinity of the interface and the neighboring bulk phases for mixture A (left) and mixture B (right). Results for the temperature $T = 0.77\,\varepsilon k_{\mathrm{B}}^{-1}$ from set of replicas. Top: density of the low-boiling component 2 (—) and total density (·····); Bottom: molar flux of component 2 j_2. The simulation time τ is indicated by the color. The profiles shown were measured at time intervals of $\Delta\tau = 100\,\sigma(m/\varepsilon)^{1/2}$.
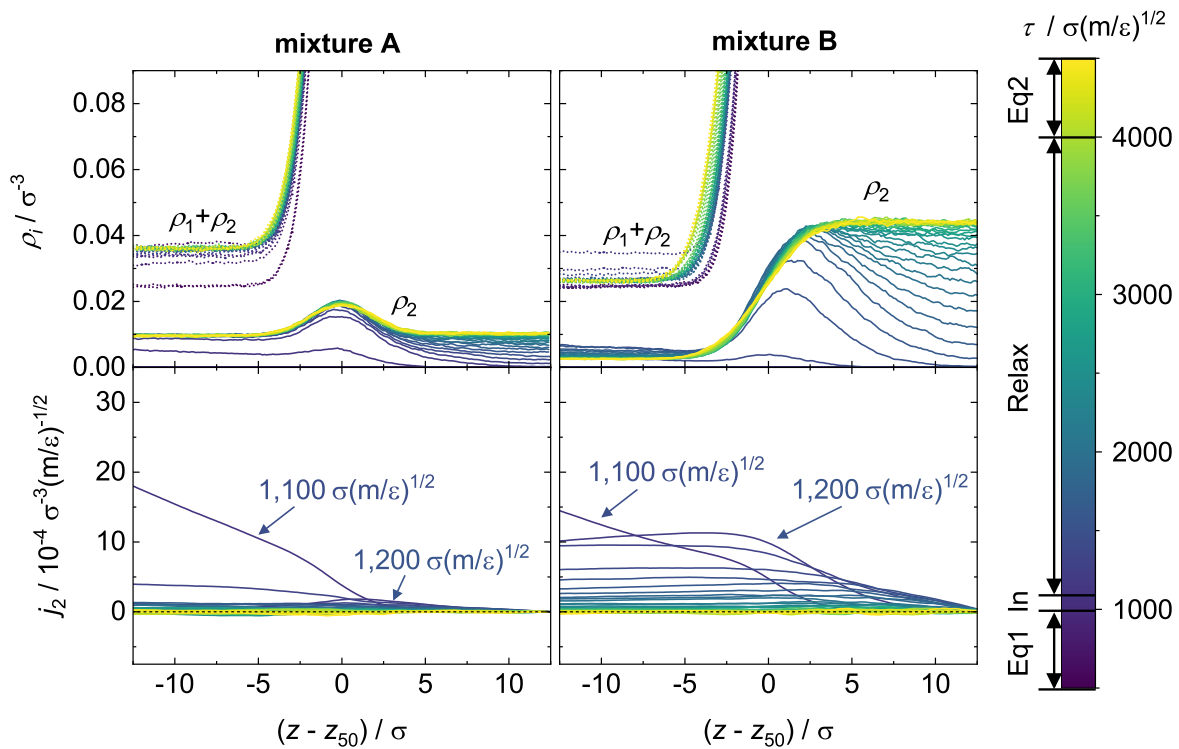
Figure B.8: Spatial profiles of the observables sampled in the vicinity of the interface and the neighboring bulk phases for mixture A (left) and mixture B (right). Results for the temperature $T = 0.825 \, \varepsilon k_{\mathrm{B}}^{-1}$ from set of replicas. Top: density of the low-boiling component 2 (——) and total density (·····); Bottom: molar flux of component 2 j_2. The simulation time τ is indicated by the color. The profiles shown were measured at time intervals of $\Delta \tau = 100 \, \sigma(m/\varepsilon)^{1/2}$.

C Supporting Information for Chapter 5

The Appendix for Chapter 5 contains the following supporting information:

- The decision tree for the determination of the interface positions.

- Determination of the alpha sphere radius r_α.

- Radial density profiles of droplets in equilibrium at $T = 0.825\,\varepsilon k_{\mathrm{B}}^{-1}$.

- URL links to the video footage from the *LAMMPS* [139] simulations shown in the main body of this work.

- Additional results from the *LAMMPS* [139] simulations.

- Results from the *ls*1 *mardyn* [114] simulations.

C.1 Decision Tree for the Determination of the Interface Positions

The positions of the interfaces are determined by fitting a sum of Gaussians, $f_{\mathrm{Gauss}}(r^{\mathrm{drop}})$, to the radial density profile $\rho^{\mathrm{IF}}(r^{\mathrm{drop}})$. Two cases are considered: there is only the outer interface (i.e., a simple droplet) or there is an inner and an outer interface (i.e., a vapor bubble inside a droplet). The function f_{Gauss} is adjusted twice to the simulation data for $\rho^{\mathrm{IF}}(r^{\mathrm{drop}})$ – one fit considers only one peak, i.e., $G = 1$, and one fit considers two peaks, i.e., $G = 2$. The decision tree shown in Figure C.1 is used to decide whether the unimodal (one peak, $G = 1$) or bimodal (two peaks, $G = 2$) Gaussian model is used for a single frame:

1. If the root mean square error (RMSE) of the unimodal fit is lower, the unimodal model is taken.

2. If the peaks of the bimodal Gaussian are closer than $3.6\,\sigma$ (which corresponds to three times the standard deviation of the Gauss peak of the density profile of the equilibrated droplet), the unimodal model is used.

3. If the peak areas A_g (estimated to be $A_g = c_g \cdot a_g$) of the two peaks of the bimodal function differ by more than $90\,\%$, the unimodal model is taken.

The root mean square error RMSE is defined as

$$\text{RMSE} = \sqrt{\frac{\sum_{i=1}^{M}(\hat{y}_i - y_i)^2}{M}} \; , \qquad (\text{C.1})$$

in which i is the index of the measurement data y_i containing M samples and $\hat{y}_i$ is the value of the adjusted function corresponding to the same input values as for y_i. In the first step the quantitatively best fit is considered. If the bimodal Gaussian model is chosen, the bimodal fit is checked for overlapping peaks in the second step and for significant differences in the peak area in the third step, both of which should not occur when the radial density function shows to two distinguishable peaks.
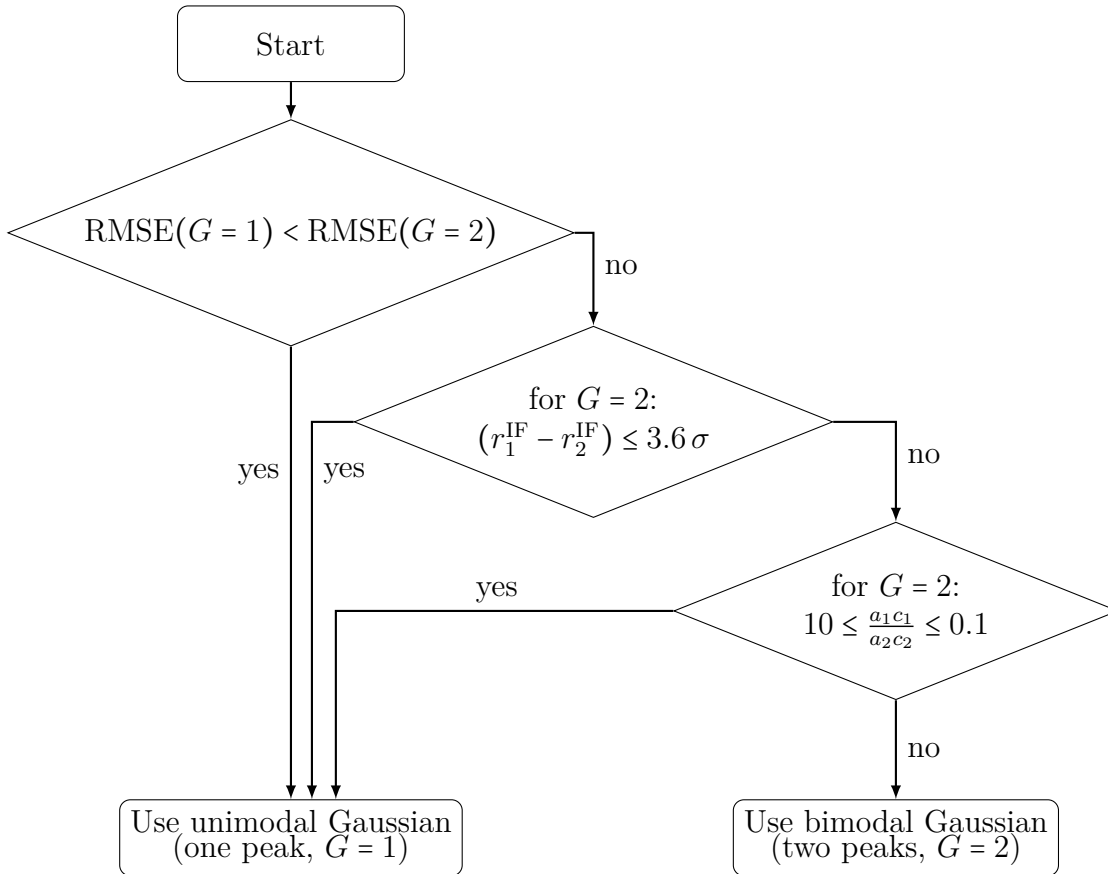

Figure C.1: Decision tree used to decide whether the unimodal or bimodal Gaussian function is used to determine the interface positions from the radial density profile.

C.2 Determination of the Alpha Sphere Radius r_α

The alpha sphere radius r_α [144] is used in conjunction with the Delaunay triangulation [143] to categorize particles according to their local density belonging to the liquid phase, vapor phase, and interfacial region. The alpha sphere radius r_α used in this work is set to the first minimum of the radial distribution function (RDF) of the homogeneous liquid phase of the model fluid, i.e., the first coordination shell around a particle. The corresponding RDF is shown in Figure C.2.
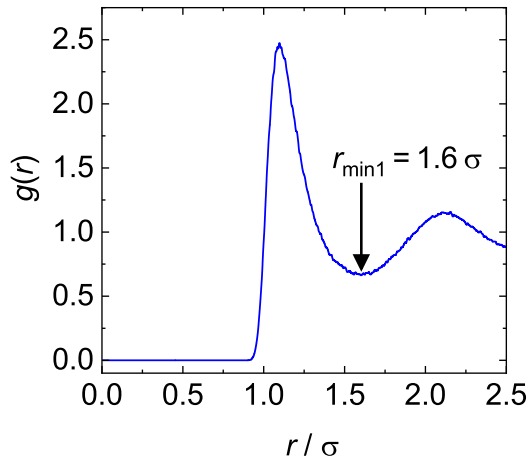

Figure C.2: Radial distribution function of the homogeneous liquid of the LJTS fluid at $\rho = 0.7149\,\sigma^{-3}$ and $T = 0.825\,\varepsilon k_{\mathrm{B}}^{-1}$.

To this end, a single molecular dynamics simulation in the NVT ensemble at $\rho = 0.7149\,\sigma^{-3}$, $N = 4\,000$, and $T = 0.825\,\varepsilon k_{\mathrm{B}}^{-1}$ is carried out using the open source simulation tool *ms*2 [204]. The density corresponds to the saturated liquid density of the LJTS fluid as calculated from the PeTS equation of state [112]. The system is equilibrated for 500 000 time steps before a production run of 2 000 000 time steps. The leapfrog scheme [35] is used to integrate the equations of motion. The RDF is determined up the cut-off radius of $2.5\,\sigma$. The investigated range is divided into 500 equally sized bins.

C.3 Radial Density Profile of Droplets in Equilibrium at $T = 0.825\,\varepsilon k_{\mathrm{B}}^{-1}$

To validate the method for determining the interfacial position, in Figure C.3, the interface position $r_{\mathrm{out}}^{\mathrm{IF}}$ is shown together with the mean overall density profile of the equilibrated droplet. Density profiles calculated from both molecular simulation codes, *LAMMPS* and *ls*1 *mardyn*, are shown.
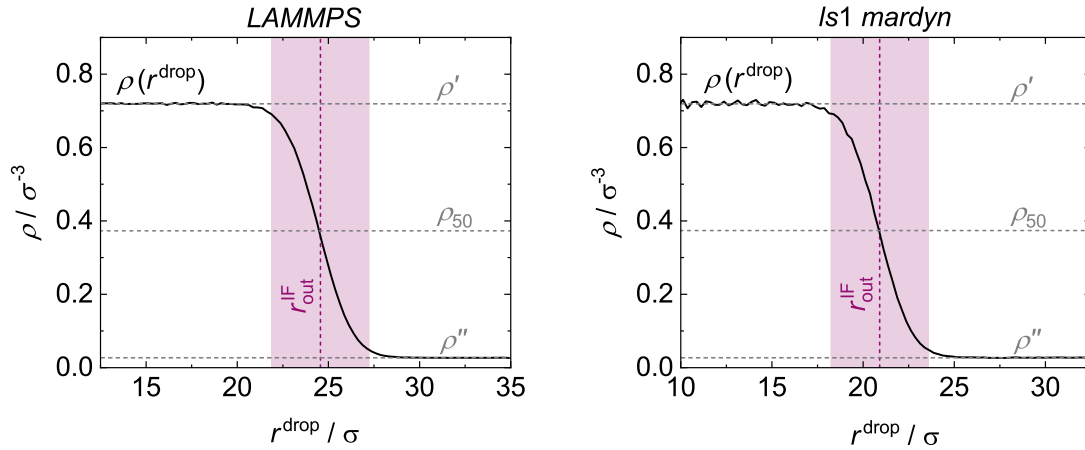
Figure C.3: Density profile of equilibrated droplets: density as a function of the distance to the droplet center averaged at $T^{\text{eq.}} = 0.825\,\varepsilon k_{\text{B}}^{-1}$ from simulations using *LAMMPS* (left panel) and *ls*1 *mardyn* (right panel). The density profiles are averaged over a time span of $1\,000\,\sigma(m/\varepsilon)^{1/2}$. The vertical purple dashed line represents the average position of the interface $r_{\text{out}}^{\text{IF}}$ determined with a single Gauss model fit. The purple shaded area represents twice the average standard deviation of the adjusted Gauss model fits, i.e., about 95 % of data points used in the Gauss fit are contained in the purple shaded area. The gray horizontal dashed lines represent the average bulk densities of the vapor and liquid phase as well as ρ_{50} (cf. Eq. (C.2)).

Additionally, the vapor-liquid interface position is evaluated using another method [26, 27, 40]: the position $r^{\text{drop}}(\rho_{50})$ at which the density threshold value

$$\rho_{50} = \rho^{''} + 0.5(\rho^{'} - \rho^{''}) \tag{C.2}$$

is reached, in which $\rho^{'}$ is the liquid and $\rho^{''}$ is the vapor bulk density. The position $r^{\text{drop}}(\rho_{50})$ and $r_{\text{out}}^{\text{IF}}$ in Figure C.3 are in remarkable agreement. Moreover, the range of the double standard deviation coincides reasonably with the thickness of the interface in between the two bulk phases. This holds also for the *ls*1 *mardyn* results (cf. Figure C.3 right panel). Even though both profiles were averaged over the same simulation time, the *ls*1 *mardyn* density profile shows slight fluctuations in the liquid bulk phase in comparison to the *LAMMPS* results because the output frequency of configurational data were set lower for the *ls*1 *mardyn* simulations, i.e., less density profiles were evaluated in the case of *ls*1 *mardyn*. For more details on the *ls*1 *mardyn* simulations and its results, cf. Chapter C.6.

C.4 Video Footage from the *LAMMPS* Simulations

URL links to the video footage of the LAMMPS simulations are given in Table C.1.

Table C.1: Explicitly written out links to the video footage from the *LAMMPS* simulations. Video names without a suffix show simulation results in the same fashion as shown in Figures 17 and 19 in the main body of this work. Videos with the suffix `"*_IF.mp4"` show only the dark blue area adjusted to the interfacial particle positions of the whole droplets. The surface in this footage is transparent so that the processes inside the droplet can be observed. The video with the suffix `"*_Torus.mp4"` show footage specifically of the torus-like droplet.

Video name	URL
`T10.mp4`	`https://youtu.be/9dnsW-Nb5oY`
`T10_IF.mp4`	`https://youtu.be/5rngSfFR534`
`T15.mp4`	`https://youtu.be/F28muenMe00`
`T15_IF.mp4`	`https://youtu.be/dVN7_Of4G5E`
`T15_Torus.mp4`	`https://youtu.be/UCjgJUILFOE`
`T20.mp4`	`https://youtu.be/TKAPPP39Xuk`
`T20_IF.mp4`	`https://youtu.be/msF7Lqe9KaY`
`T30.mp4`	`https://youtu.be/JKkCa9w0aQQ`
`T30_IF.mp4`	`https://youtu.be/OiInsMXtGIw`
`T40.mp4`	`https://youtu.be/33se2Wsmmow`
`T40_IF.mp4`	`https://youtu.be/nIAfh8qYoaA`
`T50.mp4`	`https://youtu.be/GA325cSBmhc`
`T50_IF.mp4`	`https://youtu.be/mqrgZvPVS3M`

C.5 Additional Results from the *LAMMPS* Simulations

Snapshots of the Torus-like Shape

Figure C.4 shows snapshots of the formation and decay of the torus-like shape at $T^{\text{set}} = 1.5\,\varepsilon k_{\text{B}}^{-1}$.
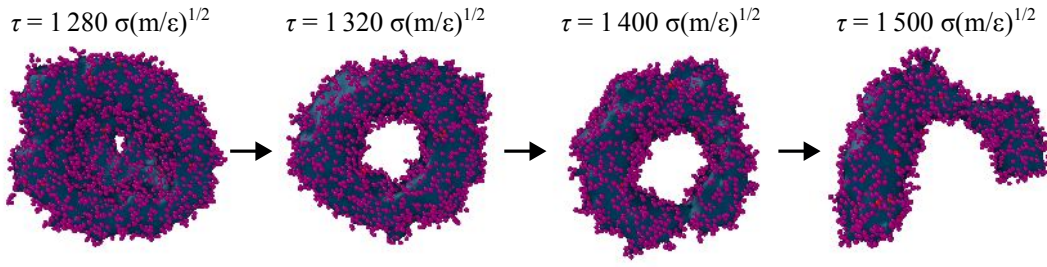
$\tau = 1\,280\;\sigma(m/\varepsilon)^{1/2}$ $\qquad$ $\tau = 1\,320\;\sigma(m/\varepsilon)^{1/2}$ $\qquad$ $\tau = 1\,400\;\sigma(m/\varepsilon)^{1/2}$ $\qquad$ $\tau = 1\,500\;\sigma(m/\varepsilon)^{1/2}$

Figure C.4: Snapshots of different time steps during the formation of the torus-like shape at $T^{\mathrm{set}} = 1.5\,\varepsilon k_{\mathrm{B}}^{-1}$. From left to right: (1) The droplet forms a bowl-like shape (top view into the bowl), while a second hole is forming at the bottom of the bowl. (2) Snapshot of the torus. (3) The torus is about to rip at the bottom. (4) The torus has broken apart and forms a sausage-like object. Only interface and liquid particles are shown for clarity.

Squared Droplet Radius as a Function of Time

Figure C.5 shows the squared outer droplet radius normalized with the radius of the initial, equilibrated droplet $r_{\mathrm{out},0}^{\mathrm{IF}}$ as a function of time. The squared droplet radius at the lowest temperature $T^{\mathrm{set}} = 1\,\varepsilon k_{\mathrm{B}}^{-1}$ decreases linearly after a short delay. At this temperature, the droplet follows the d^2 law of droplet evaporation [146], i.e., the droplet diameter squared decreases linearly over time during evaporation. This is peculiar, since the d^2 law is developed under the assumption of an initially cold droplet that evaporates due to a hot, surrounding vapor phase, while in the presented simulation scenario, the situation is vice versa: the liquid phase is heated up from the inside, while the vapor phase at the start of the simulation is colder. An interesting behavior can be observed in the case of the expanding droplet surrounding the vapor bubble ($T^{\mathrm{set}} = 1.5\,\varepsilon k_{\mathrm{B}}^{-1}$, $2.0\,\varepsilon k_{\mathrm{B}}^{-1}$, and $3.0\,\varepsilon k_{\mathrm{B}}^{-1}$): during the time span between the fading of the oscillatory behavior after the bubble nucleation and before the break-up of the liquid film, the squared outer droplet radius decreases linearly, also following the d^2 law of droplet evaporation [146]. The time range of the linear fits are chosen so that they incorporate the visibly linear time range and are a guide to the eye. The slope of the linear fit is lower with increasing temperature, which means that the droplet is shrinking faster with increasing temperature, as would be expected.
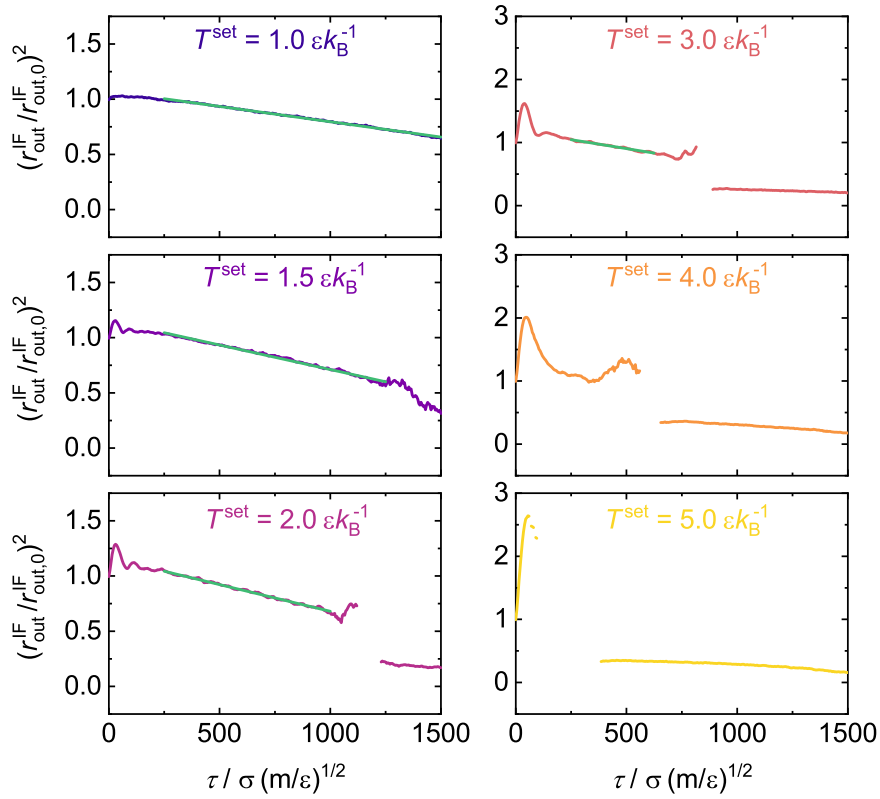
Figure C.5: The squared outer droplet radius normalized by the radius of the equilibrated droplet as a function of time for all investigated set temperatures. The green solid lines are linear fits to the simulation data, illustrating that the radius follows the d^2 law of droplet evaporation [146] and are a guide to the eye. The discontinuities in the curves are related to a break-up of the studied droplet; the curve after the jump is that for the largest remaining droplet after the break-up.

Cumulative Supplied Heat and Density of the Thermostated Region

Figure C.6 shows the cumulative heat supplied to the simulation box and the density of the thermostated region as a function of time.

At $\tau = 0$, the heat increases stepwise because the velocity of all particles in the thermostated region is increased towards the set temperature value instantaneously. The magnitude of the stepwise increase depends on the set temperature and with increasing set temperatures, as expected. In the case of the lowest temperature, which corresponds to the continuous evaporation case, the heat increases linearly after the first stepwise increase. The other set temperatures also show an approximately linear trend overall, which is at times interrupted by different events during the simulation, e.g., the oscillatory behavior or break-up of the liquid film. The higher the set temperature, the higher the overall slope of the cumulative heat, as expected. In the case of the expanding droplet, the cumulative heat shows an increased slope until the liquid film surrounding the vapor bubble breaks apart at which the slope of the cumulative heat generally de-
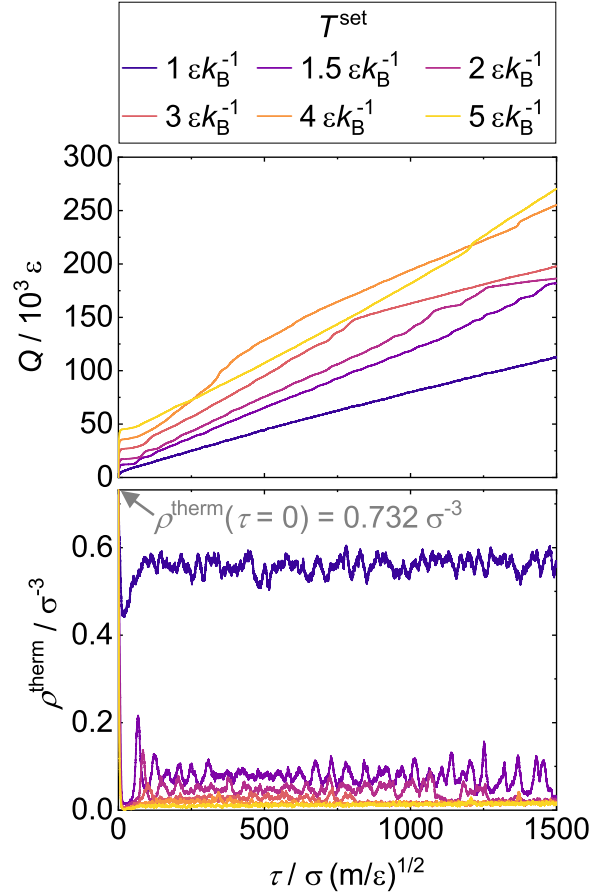
Figure C.6: Heat supplied to the simulation box (top panel) and particle density (bottom panel) of the thermostated region as a function of the time.

clines. In the time span of $0 < \tau/\sigma(m/\varepsilon)^{1/2} < 250$, slight oscillations can be observed for $T^{\text{set}} > 1.0\,\varepsilon k_{\text{B}}^{-1}$, which corresponds to the oscillating behavior of the surrounding liquid film.

The bulk liquid density calculated with the PeTS EOS [112] at $T^{\text{set}} = 1.0\,\varepsilon k_{\text{B}}^{-1}$ is $\rho = 0.5701\,\sigma^{-3}$ compared to the average density of the thermostated region during the time range $250 < \tau/\sigma(m/\varepsilon)^{1/2} < 1\,500$ of $0.561(17)\,\sigma^{-3}$ at the same set temperature. This indicates that the density is continuously striving towards its equilibrium value at $T = 1.0\,\varepsilon k_{\text{B}}^{-1}$. The density in the thermostated region in the case of the shrinking droplet case $(T^{\text{set}} = 1.0\,\varepsilon k_{\text{B}}^{-1})$ and the expanding droplet $(T^{\text{set}} = 1.5$ to $3.0\,\varepsilon k_{\text{B}}^{-1})$ show more pronounced oscillations, which decrease with increasing temperature. The oscillation in the density is attributed also to the interplay of the emerging vapor bubble and the counteracting force exerted due to extension of the inner and outer interface: when the density in the thermostated region increases, more particles have to be corrected, and heat can be dissipated faster by molecular interactions. Hence, more heat is put into the simulation, which increases the vapor bubble and decreases the density. Due to the decreasing density, less heat is put into the simulation and the counteracting forces exerted by

the expansion of the two interfaces decreases the bubble again, which in turn increases density in the vapor phase. This phenomenon is therefore an artifact of the simulation scenario.

Interestingly, during the time span of $250 < \tau / \sigma(m/\varepsilon)^{1/2} < 1\,250$, the cumulative heat at $T^{\mathrm{set}} = 4\,\varepsilon k_{\mathrm{B}}^{-1}$ is higher than for $T^{\mathrm{set}} = 5\,\varepsilon k_{\mathrm{B}}^{-1}$, which at first glance seems counter-intuitive. The heat input at $T^{\mathrm{set}} = 4\,\varepsilon k_{\mathrm{B}}^{-1}$ is higher because during the time span of $125 < \tau / \sigma(m/\varepsilon)^{1/2} < 500$, the average density in the thermostated region is $0.019(5)\,\sigma^{-3}$, which is almost twice the value at $T^{\mathrm{set}} = 5\,\varepsilon k_{\mathrm{B}}^{-1}$ in the same time span $(0.010(2)\,\sigma^{-3})$. The higher the density the more particles are thermostated and the heat input of the thermostat is transferred faster outside the thermostated region due to more particle interactions. After $\tau = 500\,\sigma(m/\varepsilon)^{1/2}$, the density in the thermostated region at $T^{\mathrm{set}} = 4\,\varepsilon k_{\mathrm{B}}^{-1}$ decreases towards a similar value as for $T^{\mathrm{set}} = 5\,\varepsilon k_{\mathrm{B}}^{-1}$, and the slope of the cumulative heat at $T^{\mathrm{set}} = 4\,\varepsilon k_{\mathrm{B}}^{-1}$ started to decline and eventually decreased below the value at $T^{\mathrm{set}} = 5\,\varepsilon k_{\mathrm{B}}^{-1}$.

First Maxima and Minima of the Position of the Inner and Outer Interface
The magnitude and time of the first minimum and maximum of the inner and outer interface position as a function of the set temperature are shown in Figure C.7.
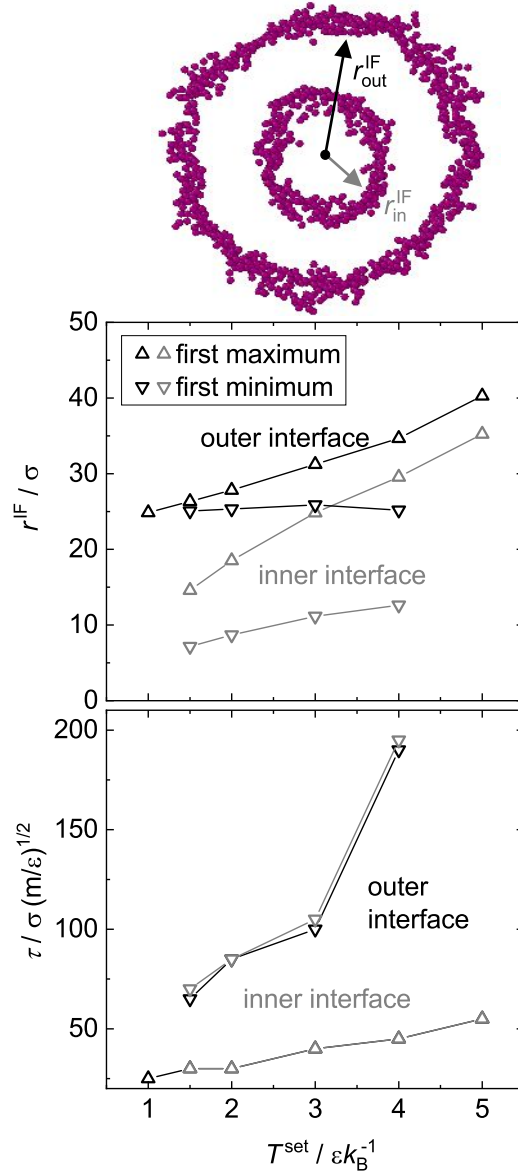

Figure C.7: Position (top panel) and time (bottom panel) of the first maximum and minimum of the two interface positions as a function of the set temperature of the thermostat. Results are shown for the outer interface (black) and inner interface (gray). No results for the first minimum at the highest temperature $T^{\mathrm{set}} = 5\,\varepsilon k_{\mathrm{B}}^{-1}$ are shown because the droplet immediately breaks apart at this temperature. The lines connecting the symbols are a guides to the eye. For clarity, a snapshot of a 2D slice through a droplet is included, showing only the interfacial particles. The arrows point to the corresponding interface.

The magnitude of the first maximum of both interfaces increase linearly with increasing temperature. The maxima of the outer interface increase more slowly with increasing

temperature than the maxima of the inner interface. Qualitatively, the course of the first minima of the two interfaces show the same behavior: for both interfaces, the temperature dependence is nearly linear and the slope is lower for the outer interface. This could also be explained by the stretching of the liquid film due to the vapor bubble pushing outwards. For both interfaces, the first minima have a significantly lower slope than the slope of the first maxima. The maxima and minima occur almost at the same time (cf. Figure C.7, bottom panel).

C.6 Results from the *ls*1 *mardyn* Simulations

The simulations presented in the main body of this work were reproduced with the open source MD code *ls*1 *mardyn* [114]. The simulation settings and procedure in these simulations were basically identical with those in the *LAMMPS* simulations. The main differences are summarized in Table C.2. Hence, it cannot be expected that the results obtained with the two codes match quantitatively. It also has to be considered, that it cannot be expected in such complex non-stationary simulations that, even when using the same code, reproduction simulations yield the same results [27, 40, 93, 123, 252].

Table C.2: Compilation of the key differences in the simulation settings of the *ls*1 *mardyn* and *LAMMPS* simulations.

Setting	*ls*1 *mardyn* [114]	*LAMMPS* [139]
Equilibration time steps	15 000 000	5 000 000
Equilibration thermostat	Andersen [208]	Nosé-Hoover [140, 141]
Thermostat in droplet	velocity-scaling [35], cubic, side length $l^{\text{therm}} = 12\,\sigma$, 4.5 % of the droplet volume	velocity-scaling [35], spherical, diameter $d^{\text{therm}} = 18\,\sigma$, 4.9 % of the droplet volume
Integration scheme	leapfrog [35]	velocity-Verlet [35, 142]
d_0^{drop}	$41.82(5)\,\sigma$	$49.06(2)\,\sigma$
l^{box}	$140\,\sigma$	$150\,\sigma$
N	102 337	134 425
Output of configurations	every 10 000 time steps	every 2 000 time steps

However, it turned out that the results obtained with *LAMMPS* were basically confirmed by the *ls*1 *mardyn* simulations and similar behavior was found:

(i) $T^{\text{set}} = 1.0\,\varepsilon k_{\text{B}}^{-1}$: shrinking droplet with nucleation of small, short-lived vapor bubbles in the inside of the droplet.

(ii) $T^{\text{set}} = 1.5\,\varepsilon k_{\text{B}}^{-1}$, $2.0\,\varepsilon k_{\text{B}}^{-1}$, and $3.0\,\varepsilon k_{\text{B}}^{-1}$: a vapor bubble nucleates inside of the droplet. The spherical droplet shell surrounding the emerged vapor bubble expands and eventually breaks apart.

(iii) $T^{\text{set}} = 4.0\,\varepsilon k_{\text{B}}^{-1}$ and $5.0\,\varepsilon k_{\text{B}}^{-1}$: a vapor bubble nucleates inside of the droplet. The emerging vapor bubble immediately tears the surrounding droplet apart.

The higher the temperature, the wider and faster the liquid film is pushed outwards by the emerging vapor bubble (cf. Figures C.8, C.9, C.10, C.11, C.12, and C.13). Oscillations in the radius of gyration and interface positions (cf. Figures C.9 and C.11 at $T^{\text{set}} = 1.5$ to $4.0\,\varepsilon k_{\text{B}}^{-1}$) can be observed shortly after the emergence of the vapor bubble and shortly before the liquid film breaks up, which is similar to the *LAMMPS* simulations. These oscillations are caused by the interplay of the emerging vapor bubble pushing outwards and the counteracting forces exerted by the interfaces due to the extension of the interfacial area and its tension. At $T^{\text{set}} = 2.0\,\varepsilon k_{\text{B}}^{-1}$, the liquid film surrounding the vapor bubble does not break apart, but instead forms a torus-like shape as seen in the main body of this work at $T^{\text{set}} = 1.5\,\varepsilon k_{\text{B}}^{-1}$ (cf. Figure C.14). The shrinking droplet case at the lowest temperature at $T^{\text{set}} = 1.0\,\varepsilon k_{\text{B}}^{-1}$ follows the d^2 law of droplet evaporation [146] (cf. Figure C.13). In the case of the expanding droplet ($T^{\text{set}} = 1.5$ to $3.0\,\varepsilon k_{\text{B}}^{-1}$), after the oscillatory behavior at the start subsided and before the liquid film breaks apart, the droplet is also following the d^2 law of droplet evaporation [146].
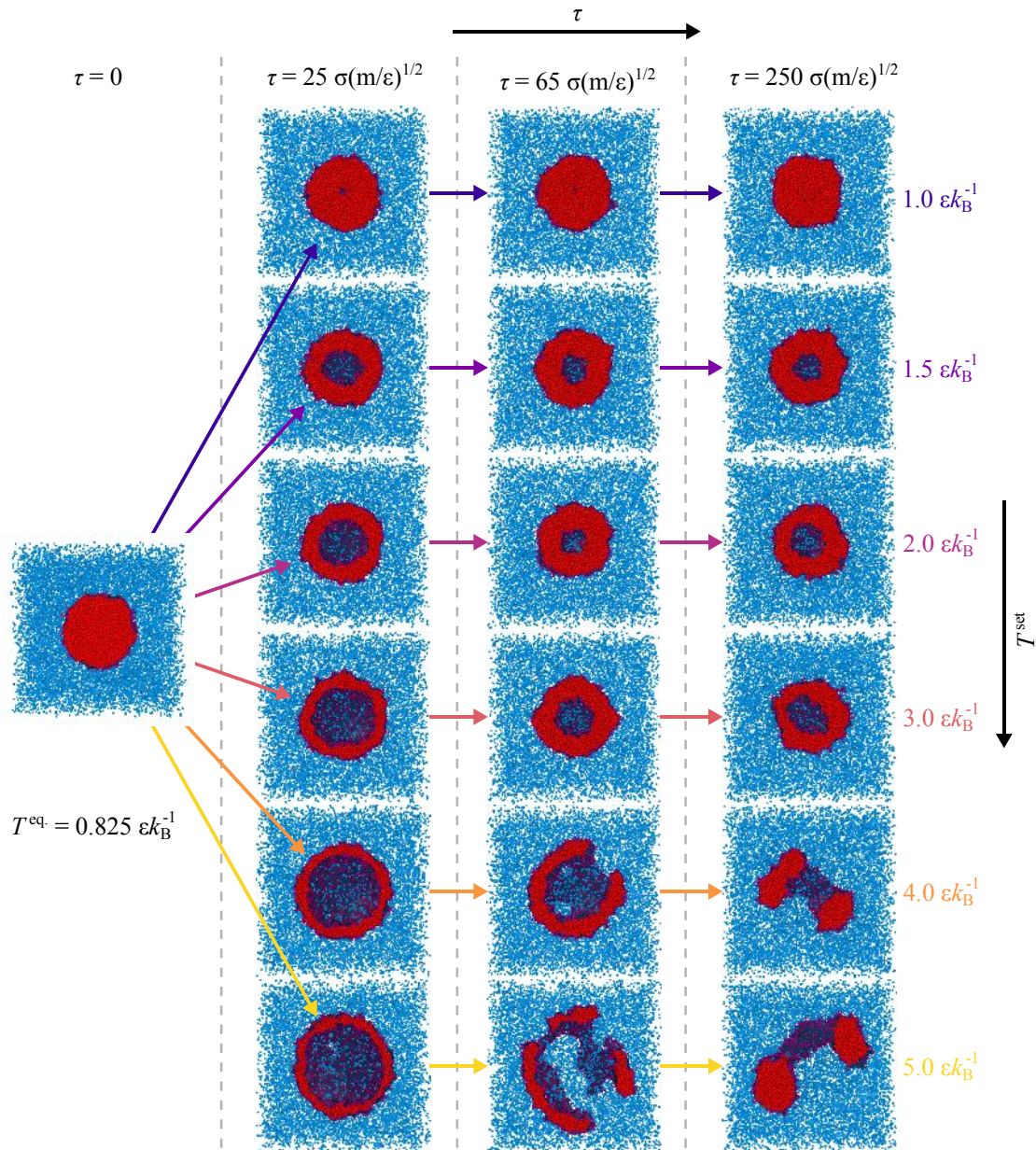
Figure C.8: Snapshots from the simulations with different set temperatures at the same three time steps during the production run from the *ls*1 *mardyn* [114] simulations. The snapshots show cross-sections through the center of the simulation box, so that the inside of the droplet can be observed. Particle colors: liquid (red), vapor (blue), and interfacial region (purple) (cf. to the section on data processing the main body of this work). The dark blue area represents the interfacial region.
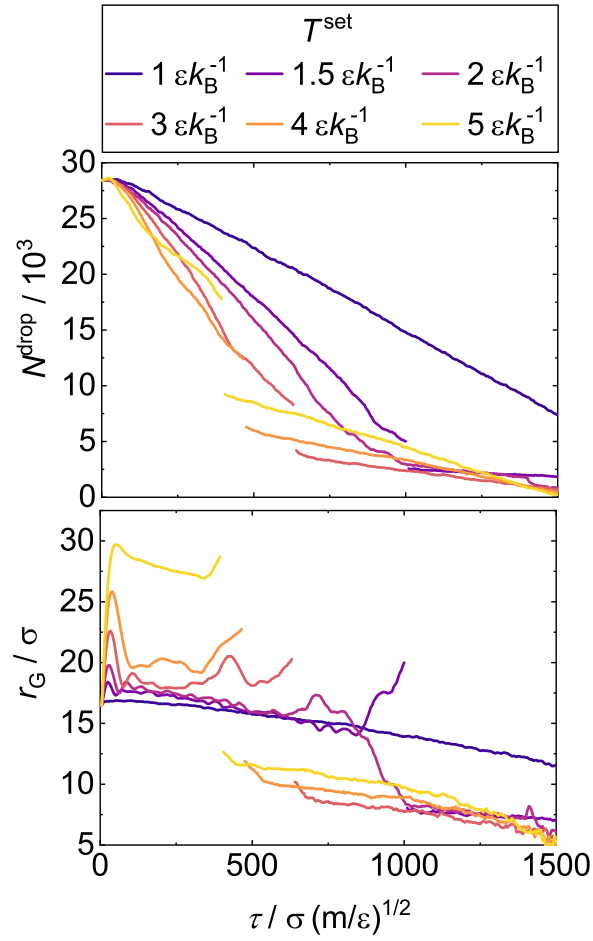
Figure C.9: Number of particles (top panel) and the radius of gyration (bottom panel) of the largest droplet as a function of time for different set temperatures from the *ls*1 *mardyn* [114] simulations. The discontinuities in the curves are related to a break-up of the studied droplet; the curve after the jump is that for the largest remaining droplet after the break-up.
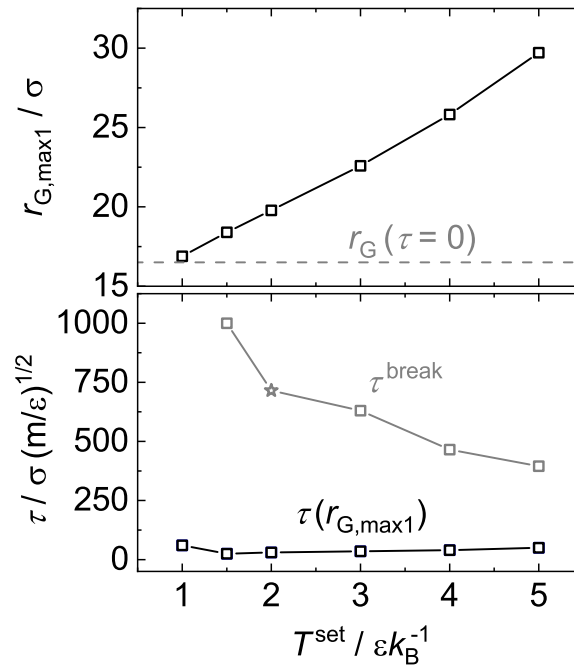
Figure C.10: Magnitude (top panel) and time (bottom panel) of the first maximum of the radius of gyration (cf. Figure C.9 bottom panel) as a function of the set temperature from the *ls1 mardyn* [114] simulations. Additionally in the bottom panel, the time at which the liquid droplet breaks up into smaller droplets for the first time is shown (gray symbols). The star simply denotes the temporary maximum at the end of the simulation at $T^{\text{set}} = 2.0\,\varepsilon k_{\text{B}}^{-1}$ in which the droplet does not break apart but instead forms a torus-like shape (cf. Figure C.14). The lines connecting the symbols are guides to the eye.
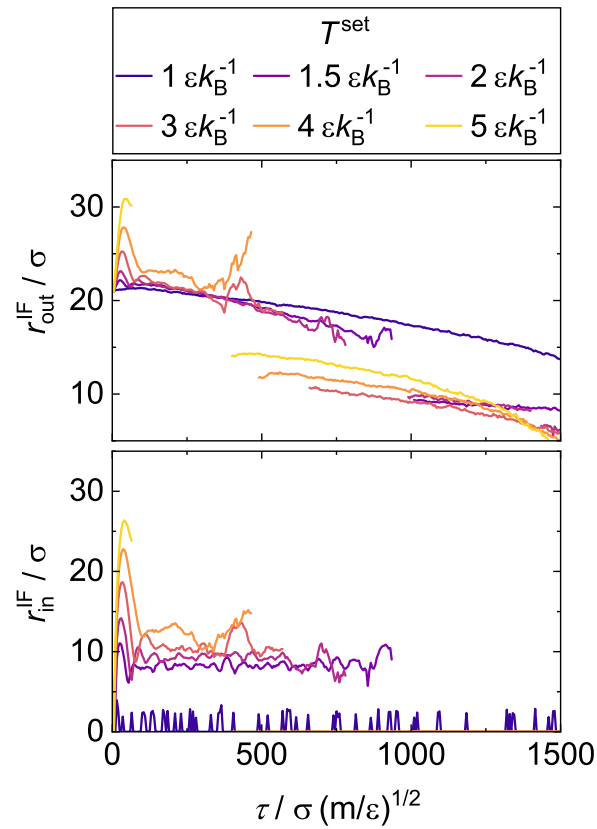
Figure C.11: Position of the outer interface (top panel) and position of the inner interface (bottom panel) as a function of time from the *ls*1 *mardyn* [114] simulations. The discontinuities in the curves are related to a break-up of the studied droplet; the curve after the jump is that for the largest remaining droplet after the break-up.
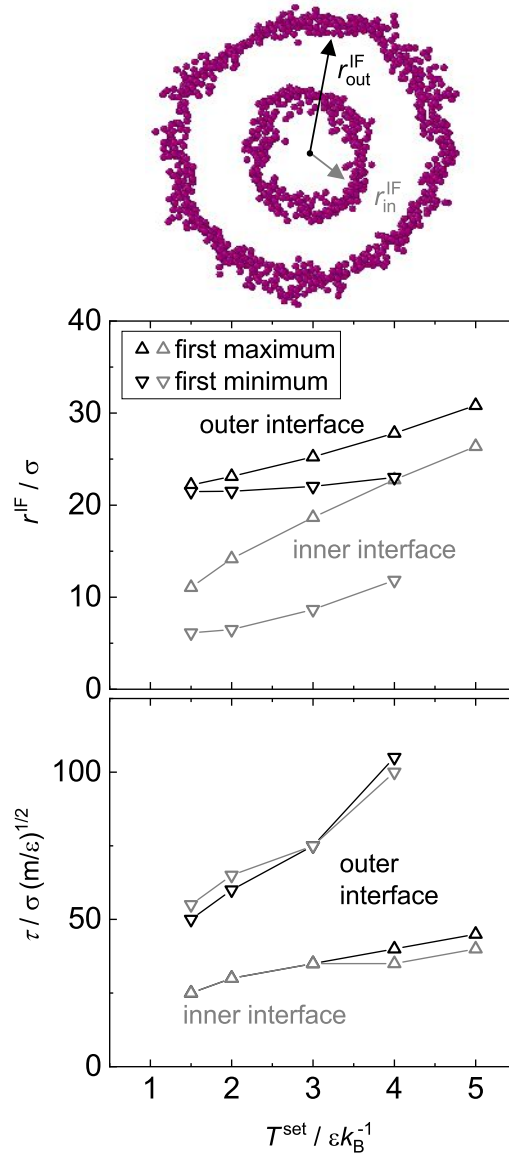
Figure C.12: Position (top panel) and time (bottom panel) of the first maximum and minimum of the two interface positions as a function of the set temperature of the thermostat from the *ls1 mardyn* [114] simulations. Results are shown for the outer interface (black) and inner interface (gray). No results for the first minimum at the highest temperature $T^{\text{set}} = 5\,\varepsilon k_{\text{B}}^{-1}$ are shown because the droplet immediately breaks apart at this temperature. The lines connecting the symbols are a guides to the eye. For clarity, a snapshot of a 2D slice through a droplet is included, showing only the interfacial particles. The arrows point to the corresponding interface.
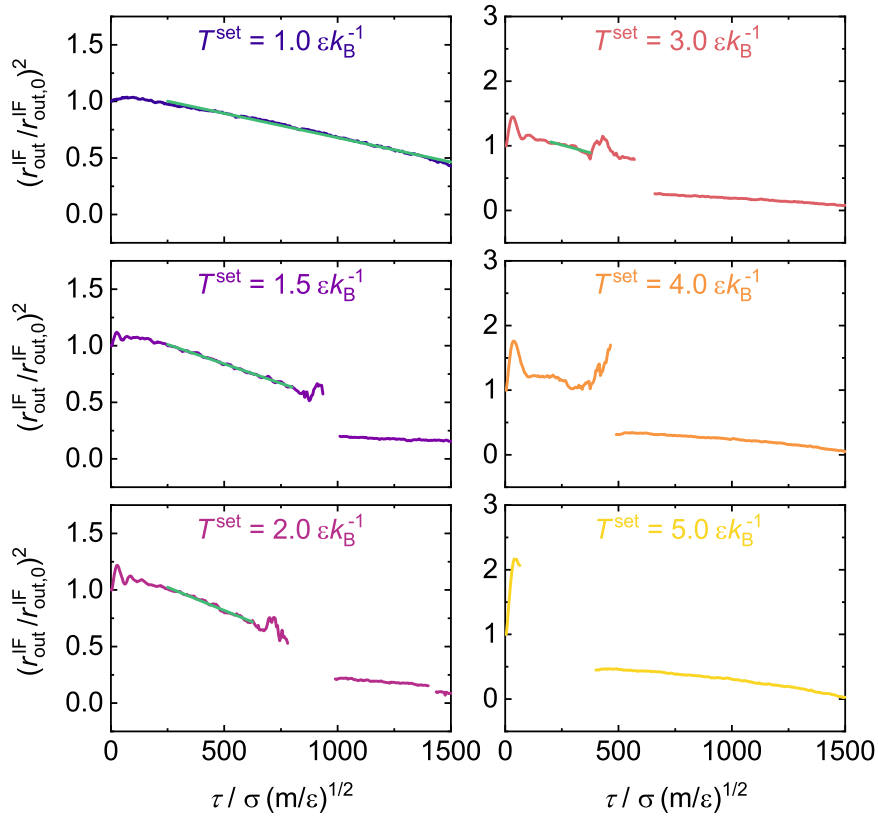
Figure C.13: The squared outer droplet radius normalized by the radius of the equilibrated droplet as a function of time for all investigated set temperatures from the *ls*1 *mardyn* [114] simulations. The green solid lines are linear fits to the simulation data, illustrating that the radius follows the d^2 law of droplet evaporation [146] and are a guide to the eye. The discontinuities in the curves are related to a break-up of the studied droplet; the curve after the jump is that for the largest remaining droplet after the break-up.
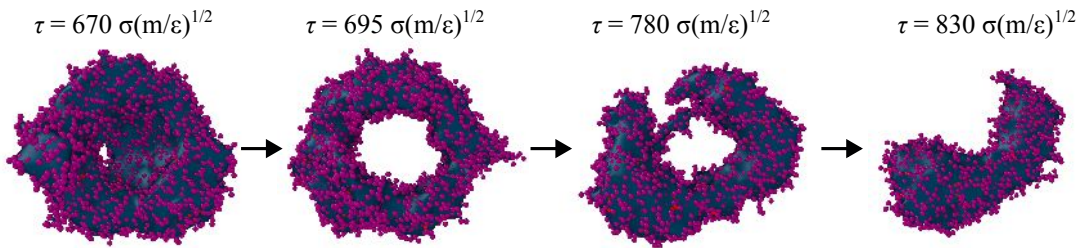
Figure C.14: Snapshots of different time steps during the formation of the torus-like shape at $T^{\text{set}} = 2.0\,\varepsilon k_{\text{B}}^{-1}$ from the *ls*1 *mardyn* [114] simulations. From left to right: (1) The droplet forms a bowl-like shape (top view into the bowl), while a second hole is forming at the bottom of the bowl. (2) Snapshot of the torus. (3) The torus is about to rip at the bottom. (4) The torus has broken apart and forms a sausage-like object. Only interface and liquid particles are shown for clarity.

D Supporting Information for Chapter 6

The Appendix for Chapter 6 contains the following supporting information:

- Details on the procedure and parameters of the polynomial fit to the experimental density data for all considered nitrate salts.

- Results from an OPAS simulation study in which the LJ parameters of the Li^+ cation model were varied in aqueous solutions of $LiNO_3$ and the influence of said parameters on the solvent activity and the mean ionic activity coefficient was investigated.

- Details on the determination of the standard error for the extrapolated self-diffusion coefficient at infinite dilution.

- Compilations of the numerical values of the simulation results of all nitrate salts considered in the main body of this work for the observables:

    - density $\rho^{(m)}$

    - self-diffusion coefficients D_i of K^+, NO_3^-, and H_2O as well as the corresponding density $\rho^{(m)}$

    - osmotic pressure Π and the water activity $\ln a_W$ determined with the OPAS method [196–198]

D.1 Iteratively Reweighted Polynomial Fit to the Experimental Density Data

A second order polynomial for the reduced density ρ^* was adjusted to the experimental density data of the literature for all considered nitrate salts. The experimental data were taken from the Dortmund Data Bank [202]. However, for aqueous $CsNO_3$ solutions, the Dortmund Data Bank contained only data sets reporting the density for low salt concentrations. Hence, an additional literature search was carried out and the data

by Merton [253] was added. The data set of Merton is from the year 1910 and agrees well with the data at low concentrations available in the Dortmund Data Bank. The polynomial for the density adjusted in this work is given as:

$$\rho^*(\tilde{b}_{AB}) = 1 + \alpha_{AB,1}\,\tilde{b}_{AB} + \alpha_{AB,2}\,\tilde{b}_{AB}^2 \ . \tag{D.1}$$

$\alpha_{AB,1}$ and $\alpha_{AB,2}$ are adjustable parameters and AB indicates the nitrate salt of interest. The parameters $\alpha_{AB,1}$ and $\alpha_{AB,2}$ were adjusted independently fo the two temperatures considered in this work, i.e., 298.15 K and 333.15 K. Experimental density values were reduced with the corresponding density of pure water, which is $\rho_W^{(m)}$ = 997.05 kg m^{-3} at 298.15 K and 1 bar [201] and $\rho_W^{(m)}$ = 983.20 kg m^{-3} at 333.15 K and 1 bar [201]. For the fit of the polynomial, also data points that lie within ±0.5 K of the desired temperature were considered. The polynomial was adjusted to density data up to a molality of 4 mol kg^{-1} with the exception of CsNO$_3$, which was adjusted in a range up to the experimental data point with the highest available molality, which was 0.853 mol kg^{-1} at 298.15 K [253].

The two parameters $\alpha_{AB,2}$ and $\alpha_{AB,1}$ of the polynomial of each salt were adjusted using iteratively reweighted least-squares [254] to reduce the impact of outliers. In the iteratively reweighted least-squares algorithm [254], every data point y_i of a data set is associated with a weight w_i. The weight has a value between 0 and 1. Data points with a weight of 1 are fully taken into account in the regression, while data points with a weight of 0 are not considered in the regression. The algorithm iteratively fits the polynomial to the available density data by using a weighted sum of least squares, then adjusts the weights according to the residuals, and repeats the fitting procedure. This is done until the fit converges, which took typically less than 30 iterations. The weighted sum of least squares is given as

$$S = \sum_{i=1}^{M} w_i (y_i - \hat{y}_i)^2 \ , \tag{D.2}$$

in which $\hat{y}_i$ is the value of the polynomial function for the same x_i value as the data point y_i and M is the number of available data points. The standardized adjusted residual is given as

$$r_i = \frac{y_i - \hat{y}_i}{k\ \text{MAD}\ \sqrt{1 - h_i}} \ , \tag{D.3}$$

where k = 4.685 is a tuning constant specific for the here used bisquare weights (cf. Eq. (D.4)), MAD is the median absolute deviation of the residuals from the residual median divided by 0.6745, and h_i is the leverage value of the weight. The median absolute deviation of the residuals is divided by the constant 0.6745 to make the estimate unbiased for the normal distribution. The leverage value h_i can range from 0 to 1 and is

a measure of wether a data point is an outlier regarding its x_i value and therefore could have an overly large effect on the regression result. The bisquare weights are adjusted by r_i according to

$$w_i = \begin{cases} (1 - r_i^2)^2 & , |r_i| < 1 \\ 0 & , |r_i| \geq 1 \end{cases} . \tag{D.4}$$

The parameters adjusted to the experimental density data of each salt is given in Table D.1. In addition to the parameters of the polynomial, the mean absolute error MAE is given in Table D.1, which is defined as

$$\text{MAE} = \frac{1}{M} \sum_{i=1}^{M} |y_i - \hat{y}_i| . \tag{D.5}$$

Furthermore, in Table D.1 the number of data points as well as the number of data sets are given. A data set is defined as a set of data points taken from the same publication. For $CsNO_3$ and $RbNO_3$ at 333.15 K, no experimental data were available in the Dortmund Data Bank [202].

Table D.1: Overview of the parameters of the polynomial (cf. Eq. (D.1)) for the reduced density adjusted to experimental density data. Additionally, the mean absolute error (MAE) as well as the number of data points and the number of data sets used in the fitting procedure are given.

salt	$10^2 \, \alpha_{\text{AB},1}$ mol kg^{-1}	$10^3 \, \alpha_{\text{AB},2}$ $\text{mol}^2 \, \text{kg}^{-2}$	10^3 MAE	number of data points	number of data sets
		$T = 298.15$ K			
$LiNO_3$	3.969	−1.382	0.164	155	8
$NaNO_3$	5.551	−2.291	1.193	129	20
KNO_3	6.113	−2.822	0.690	188	27
$RbNO_3$	10.906	−7.855	6.699	31	3
$CsNO_3$	14.361	−8.873	0.030	25	3
		$T = 333.15$ K			
$LiNO_3$	3.848	−1.387	0.191	3	2
$NaNO_3$	5.316	−2.193	0.281	8	2
KNO_3	5.980	−3.144	0.228	13	2

In Figure D.1, the results using the iteratively reweighted least-squares algorithm are shown for the available experimental density data of all considered nitrate salts at 298.15 K and 1 bar. For all salts, the adjusted polynomial is in good agreement with the bulk of the experimental data. Only for $RbNO_3$, at increasing concentrations the experimental density data fork into two branches, of which the branch with lower increase in density as a function of molality is weighted more heavily by the the algorithm. The high deviation of experimental data at higher concentration causes that the adjusted

polynomial for RbNO$_3$ has the highest MAE of all nitrate salts at 298.15 K (cf. Table D.1). For NaNO$_3$, the relative number of outliers is higher compared to the other nitrate salts. 21.7 % of data points are given a weight of zero for NaNO$_3$ compared to 6.3 % in the case of LiNO$_3$, 12.8 % for KNO$_3$, 9.7 % for RbNO$_3$ and 4.0 % for CsNO$_3$.
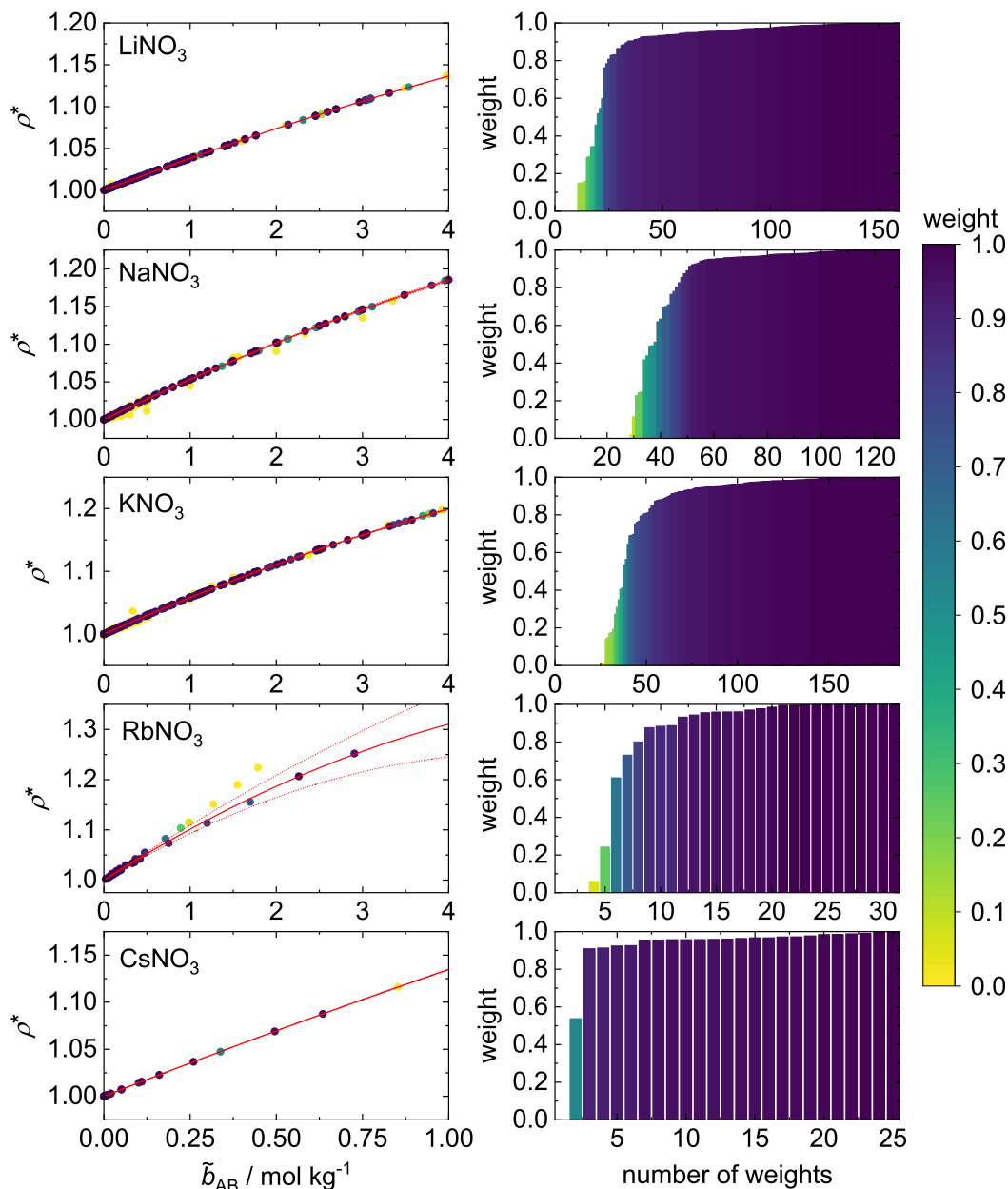

Figure D.1: Experimental density data [202, 253] as a function of molality with the corresponding polynomial fit (left panel) and the corresponding weights (right panel) using the iteratively reweighted least-squares algorithm [254] for all considered nitrate salts at 298.15 K and 1 bar. The experimental data points (circles) are colored according to their corresponding weight. The polynomial fit (solid red line) as well as the 95 % confidence interval (dotted red line) are shown. The 95 % confidence interval of the fit is within the thickness of the line for all nitrates except RbNO$_3$.

D.2 Influence of the Li$^+$ Cation LJ Parameters on the Solvent Activity and the Mean Ionic Activity Coefficient of LiNO$_3$.

To investigate the most interesting case with regards to the activity properties, LiNO$_3$, more closely, three additional series of OPAS simulations were conducted, varying the LJ parameters of the Li$^+$ cation while keeping all other model parameters constant. To this end, the Li$^+$ cation from the popular model set by Joung and Cheatham [234] was considered (denoted JC in the following), for which $\sigma_{\mathrm{Li}^+}^{\mathrm{JC}}$ = 1.44 Å and $\varepsilon_{\mathrm{Li}^+}^{\mathrm{JC}}/k_{\mathrm{B}}$ = 52.4 K. Both LJ parameters are considerably lower than those of the Li$^+$ model from previous work of our group [164] (denoted RDVH in the following, $\sigma_{\mathrm{Li}^+}^{\mathrm{RDVH}}$ = 1.88 Å and $\varepsilon_{\mathrm{Li}^+}^{\mathrm{RDVH}}/k_{\mathrm{B}}$ = 200 K). In the first series of simulations, the JC parameters were used directly. In the second series of simulations, the JC size parameter was combined with the RDVH energy parameter. Finally, in the third series of simulations, the same was done – but vice versa. The results of that parameter variation study are presented in Figure D.2. The numerical values of the fit parameters of the correlation to the simulation results are given in Table D.2.
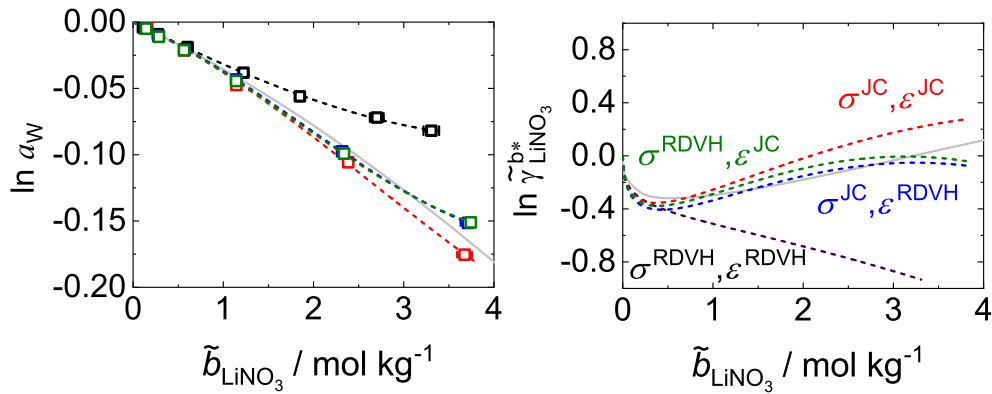

Figure D.2: Solvent activity a_{W} and mean ionic activity coefficient $\tilde{\gamma}_{\mathrm{AB}}^{\mathrm{b*}}$ as a function of the salt molality $\tilde{b}_{\mathrm{AB}}$ for aqueous solutions of LiNO$_3$ at 298.15 K and 1 bar. Four different variants of LJ parameters for the Li$^+$ cation are studied and shown with different colors as indicated in the right panel. Open squares show the simulation results for the solvent activity a_{W}. The dashed lines represent the correlations of the simulation data, from which also the mean ionic activity coefficients $\tilde{\gamma}_{\mathrm{AB}}^{\mathrm{b*}}$ were calculated (cf. Eqs. (11) and (13) in the main body of this work). The gray solid line represents the correlation to experimental data taken from Hamer and Wu [203].

It is apparent from Figure D.2 that changing either of the two LJ parameters from the RDVH value to the JC value (or doing both) drastically improves the water activity prediction. At the same time, when doing so a minimum appears for the mean ionic

activity coefficient as a function of molality. Interestingly, when using both JC parameters, the water activity is slightly underpredicted at higher concentrations, while using either of the 'hybrid' Li$^+$ model parametrizations leads to an almost perfect agreement with the experimental data. This underlines that it is obviously worthwhile to consider activity coefficient data in the development of the ion models. The present results show that the LJ energy parameter has a strong influence on the activity coefficient. This is remarkable, as it has only little influence on the density, so that it was sufficient to use a single, common value for all alkali ions when parameterizing the models based on density data [164].

Table D.2: Summary of the parameters B, β, and C used in Eqs. (11) and (13) in the main body of this work for fitting the solvent activity data obtained with the OPAS method for the variation of the LJ parameters of the Li$^+$ cation in aqueous solutions of LiNO$_3$ (cf. Figure D.2). The parameter A was 0.5938 throughout.

LJ parameter combination		B	β	C
$\sigma_{\text{Li}^+}^{\text{JC}}$	$\varepsilon_{\text{Li}^+}^{\text{JC}}$	0.8902	0.2249	-0.0216
$\sigma_{\text{Li}^+}^{\text{JC}}$	$\varepsilon_{\text{Li}^+}^{\text{RDVH}}$	0.5005	0.2871	-0.0372
$\sigma_{\text{Li}^+}^{\text{RDVH}}$	$\varepsilon_{\text{Li}^+}^{\text{JC}}$	0.6178	0.2807	-0.0387

D.3 Determination of the Standard Error of the Self-Diffusion Coefficient at Infinite Dilution

The self-diffusion coefficient at infinite dilution was extrapolated by using a first order polynomial adjusted to the experimental data or simulation results. The mean squared error MSE of the self-diffusion coefficient at infinite dilution was determined as follows:

$$\text{MSE} = \frac{\sum_{i=1}^{M}(y_i - \hat{y}_i)^2}{M-2} \ , \tag{D.6}$$

where M is the number of data points. The sum of squared errors is divided by the number of degrees of freedom, which is the difference of the number of data points and the number of adjustable parameters. The standard error SE at infinite dilution was determined with the MSE according to

$$\text{SE} = \sqrt{\text{MSE} \ \frac{\sum_{i=1}^{M} x_i^2}{M \sum_{i=1}^{M}(x_i - \bar{x})^2}} \ , \tag{D.7}$$

where $\bar{x}$ denotes the mean value of x_i.

D.4 Simulation Results

In the following, the numerical results from the simulations considered in the main body of this work are given for the density $\rho^{(\mathrm{m})}$, the self-diffusion coefficients D_i of K^+, NO_3^-, and H_2O, and the osmotic pressure Π and the water activity $\ln a_W$.

Table D.3: Simulation results for the density of all considered alkali nitrate solutions at 298.15 K and 1 bar. Statistical uncertainties are given in parentheses.

LiNO$_3$		NaNO$_3$		KNO$_3$	
$\tilde{b}_{\mathrm{AB}}$	$\rho^{(\mathrm{m})}$	$\tilde{b}_{\mathrm{AB}}$	$\rho^{(\mathrm{m})}$	$\tilde{b}_{\mathrm{AB}}$	$\rho^{(\mathrm{m})}$
mol kg^{-1}	mol kg^{-1}	mol kg^{-1}	mol kg^{-1}	mol kg^{-1}	mol kg^{-1}
0.07	1,007.2(1)	0.07	1,008.4(1)	0.28	1,021.7(1)
0.14	1,010.5(1)	0.14	1,012.5(1)	0.566	1,038.8(1)
0.28	1,016.4(1)	0.28	1,020.9(1)	0.858	1,055.6(1)
0.566	1,027.9(1)	0.566	1,037.0(1)	1.156	1,072.4(1)
1.156	1,051.5(1)	1.156	1,069.2(1)	1.461	1,088.1(1)
1.787	1,074.7(2)	1.787	1,101.7(2)	1.772	1,104.6(1)
2.413	1,096.7(2)	2.413	1,132.5(2)	2.089	1,118.7(1)
3.084	1,118.4(1)	3.084	1,163.8(2)	2.413	1,134.6(2)
				3.084	1,164.8(2)

RbNO$_3$		CsNO$_3$	
$\tilde{b}_{\mathrm{AB}}$	$\rho^{(\mathrm{m})}$	$\tilde{b}_{\mathrm{AB}}$	$\rho^{(\mathrm{m})}$
mol kg^{-1}	mol kg^{-1}	mol kg^{-1}	mol kg^{-1}
0.042	1,008.5(1)	0.014	1,006.3(1)
0.084	1,012.6(1)	0.098	1,018.1(1)
0.252	1,029.4(2)	0.252	1,039.6(1)
0.337	1,037.9(2)	0.494	1,072.0(2)
0.683	1,070.3(2)	0.756	1,106.5(1)
0.918	1,091.8(2)	1.007	1,138.2(2)
1.461	1,139.9(1)		
2.089	1,192.0(2)		
2.745	1,241.9(2)		

Table D.4: Simulation results for the density of all considered alkali nitrate solutions at 333.15 K and 1 bar. Statistical uncertainties are given in parentheses.

$\tilde{b}_{AB}$ LiNO$_3$	$\rho^{(m)}$	$\tilde{b}_{AB}$ NaNO$_3$	$\rho^{(m)}$	$\tilde{b}_{AB}$ KNO$_3$	$\rho^{(m)}$
mol kg^{-1}	mol kg^{-1}	mol kg^{-1}	mol kg^{-1}	mol kg^{-1}	mol kg^{-1}
0.07	985.6(1)	0.07	986.8(1)	0.28	1,000.1(1)
0.14	988.6(1)	0.14	990.8(1)	0.566	1,016.8(1)
0.28	994.7(1)	0.28	998.6(1)	0.858	1,033.5(1)
0.566	1,005.8(1)	0.566	1,014.8(1)	1.156	1,050.1(1)
1.156	1,028.4(1)	1.156	1,045.6(1)	1.461	1,065.9(1)
1.787	1,050.6(1)	1.787	1,077.5(1)	1.772	1,082.2(1)
2.413	1,071.9(1)	2.413	1,107.7(1)	2.089	1,098.0(1)
3.084	1,093.2(2)	3.084	1,137.3(1)	2.413	1,113.4(1)
				3.084	1,143.0(2)

$\tilde{b}_{AB}$ RbNO$_3$	$\rho^{(m)}$	$\tilde{b}_{AB}$ CsNO$_3$	$\rho^{(m)}$
mol kg^{-1}	mol kg^{-1}	mol kg^{-1}	mol kg^{-1}
0.042	987.0(1)	0.014	984.8(1)
0.084	991.1(1)	0.098	996.2(1)
0.252	1,007.5(1)	0.252	1,017.3(1)
0.337	1,015.7(1)	0.494	1,049.7(1)
0.683	1,048.1(1)	0.756	1,083.2(1)
0.918	1,069.2(1)	1.007	1,114.4(1)
1.461	1,116.2(1)		
2.089	1,167.8(1)		
2.745	1,217.8(2)		

Table D.5: Simulation results for the self-diffusion coefficients of the potassium ion, the nitrate ion, and water in an aqueous solution of KNO$_3$ at 298.15 K and 1 bar as well as the corresponding density. The results in the last row (denoted by a star) are the results for the linear extrapolation at infinite dilution. Statistical uncertainties are given in parentheses.

$\tilde{b}_{AB}$	$\rho^{(m)}$	D_{K^+}	$D_{NO_3^-}$	D_W
mol kg^{-1}	mol kg^{-1}	10^{-9} m s^{-2}	10^{-9} m s^{-2}	10^{-9} m s^{-2}
0.028	1,006.8(1)	2.01(9)	1.89(8)	2.756(5)
0.056	1,008.6(1)	2.07(6)	1.84(5)	2.778(6)
0.084	1,010.4(1)	2.00(5)	1.92(4)	2.786(6)
0.0*		2.03(8)	1.85(7)	2.743(8)

Table D.6: Simulation results for the osmotic pressure and the water activity of all considered alkali nitrate solutions at 298.15 K and 1 bar. Statistical uncertainties are given in parentheses.

$\tilde{b}_{AB}$	LiNO$_3$ Π	$\ln a_{W}$	$\tilde{b}_{AB}$	NaNO$_3$ Π	$\ln a_{W}$
mol kg^{-1}	MPa		mol kg^{-1}	MPa	
0.11(2)	0.56(1)	$-0.004\,07(7)$	0.11(3)	0.528(7)	$-0.003\,82(5)$
0.27(2)	1.26(1)	$-0.009\,14(9)$	0.29(3)	1.17(2)	$-0.0085(1)$
0.60(2)	2.60(3)	$-0.0188(2)$	0.60(6)	2.64(3)	$-0.0191(2)$
1.22(3)	5.3(1)	$-0.0382(9)$	1.17(5)	5.19(7)	$-0.0376(5)$
1.85(4)	7.7(2)	$-0.056(1)$	1.82(4)	8.09(7)	$-0.0585(5)$
2.70(8)	9.9(2)	$-0.072(2)$	2.54(9)	10.2(1)	$-0.074(1)$
3.31(9)	11.3(2)	$-0.082(1)$	3.2(1)	12.1(3)	$-0.088(2)$

$\tilde{b}_{AB}$	KNO$_3$ Π	$\ln a_{W}$	$\tilde{b}_{AB}$	RbNO$_3$ Π	$\ln a_{W}$
mol kg^{-1}	MPa		mol kg^{-1}	MPa	
0.13(2)	0.454(2)	$-0.003\,29(2)$	0.12(1)	0.463(4)	$-0.003\,35(3)$
0.29(3)	1.16(2)	$-0.0084(1)$	0.31(3)	1.12(1)	$-0.008\,10(7)$
0.45(2)	1.70(2)	$-0.0123(1)$	0.61(3)	2.19(4)	$-0.0158(3)$
0.60(5)	2.30(3)	$-0.0167(2)$	0.77(3)	2.80(2)	$-0.0203(2)$
0.77(2)	2.68(4)	$-0.0194(3)$	0.94(2)	3.39(5)	$-0.0245(3)$
0.96(2)	2.91(4)	$-0.0211(3)$	1.27(3)	4.27(5)	$-0.0309(4)$
1.34(5)	3.93(5)	$-0.0284(3)$	1.69(7)	4.90(4)	$-0.0355(3)$
			1.81(4)	5.45(8)	$-0.0395(6)$
			2.06(5)	5.9(1)	$-0.0424(7)$

$\tilde{b}_{AB}$	CsNO$_3$ Π	$\ln a_{W}$
mol kg^{-1}	MPa	
0.12(1)	0.467(1)	$-0.003\,381(8)$
0.28(3)	1.281(2)	$-0.009\,27(2)$
0.45(2)	1.826(6)	$-0.013\,22(4)$
0.55(2)	2.44(1)	$-0.0176(1)$
0.76(1)	2.975(8)	$-0.021\,53(6)$
0.96(4)	3.39(1)	$-0.024\,51(8)$
1.10(4)	3.88(1)	$-0.0281(1)$

Table D.7: Simulation results for the osmotic pressure and the water activity of $NaNO_3$ solutions at 333.15 K and 1 bar. Statistical uncertainties are given in parentheses.

$\tilde{b}_{AB}$	Π	$\ln a_W$
mol kg^{-1}	MPa	
0.149(7)	0.744(5)	−0.004 92(4)
0.275(5)	1.39(1)	−0.009 21(7)
0.55(3)	2.97(2)	−0.0196(2)
1.16(2)	5.78(6)	−0.0383(4)
2.4(1)	11.5(1)	−0.076(1)
3.8(2)	16.4(2)	−0.109(1)

NaNO$_3$, 333.15 K

Table D.8: Simulation results for the osmotic pressure and the water activity from the parameter variation of the LiNO$_3$ solutions at 298.15 K and 1 bar (cf. Figure D.2). Statistical uncertainties are given in parentheses.

	$\sigma_{Li^+}^{JC}$, $\varepsilon_{Li^+}^{JC}$			$\sigma_{Li^+}^{JC}$, $\varepsilon_{Li^+}^{RDVH}$	
$\tilde{b}_{AB}$	Π	$\ln a_W$	$\tilde{b}_{AB}$	Π	$\ln a_W$
mol kg^{-1}	MPa		mol kg^{-1}	MPa	
0.16(2)	0.620(6)	−0.004 48(4)	0.14(1)	0.685(3)	−0.004 95(2)
0.29(1)	1.47(2)	−0.0106(1)	0.28(1)	1.431(7)	−0.010 35(5)
0.57(2)	2.96(2)	−0.0214(1)	0.57(2)	2.85(3)	−0.0206(2)
1.14(3)	6.55(3)	−0.0474(2)	1.14(5)	5.98(8)	−0.0433(6)
2.38(4)	14.6(2)	−0.106(1)	2.32(4)	13.5(2)	−0.098(2)
3.67(8)	24.2(2)	−0.175(2)	3.71(8)	20.9(1)	−0.151(1)

	$\sigma_{Li^+}^{RDVH}$, $\varepsilon_{Li^+}^{JC}$	
$\tilde{b}_{AB}$	Π	$\ln a_W$
mol kg^{-1}	MPa	
0.144(7)	0.680(4)	−0.004 92(3)
0.28(2)	1.529(8)	−0.011 06(6)
0.56(1)	2.94(3)	−0.0213(2)
1.14(6)	6.14(6)	−0.0444(5)
2.34(5)	13.7(2)	−0.099(1)
3.74(9)	20.9(1)	−0.151(1)

E Supporting Information for Chapter 7

The Appendix for Chapter 6 contains the following supporting information:

- Information on the structure of large ion clusters observed at high salt concentrations.

E.1 Structure of Large Clusters Observed at High Salt Concentrations

As stated in Section 7.3.1.1, among all simulations carried out in the present work, clusters containing more than 20 ions were rare and clusters of this size were not long-lived. Figure E.1 shows the largest cluster observed in this work (excluding the RDVH-NaI simulations), which was found at the highest investigated concentration, $x_{\mathrm{Na^+}}$ = 0.15 mol mol^{-1}, of RDVH-NaCl in SPC/E water. This cluster contains 147 ions out of the total of 1 200 for that simulation and has an elongated, filamentous, and amorphous shape. Upon closer investigation, the cluster consists of at least two sub-clusters connected by a single cation (cf. Figure E.1, bottom panel). The left sub-cluster consists of 85 ions and the right sub-cluster consists of 62 ions. The merging of several sub-clusters by a chain of single ions is caused by the neighbor-based cluster algorithm used in this work. Other cluster approaches, such as centroid-based clustering (e.g., k-means algorithm [255]) or density-based clustering (e.g., DBSCAN [256]), may have identified the two individual sub-clusters instead. Notwithstanding, for the topic investigated in the present work, this makes essentially no difference since both cases still yield the same value for the property $\bar{X}^{\mathrm{C\text{-}6}}$.
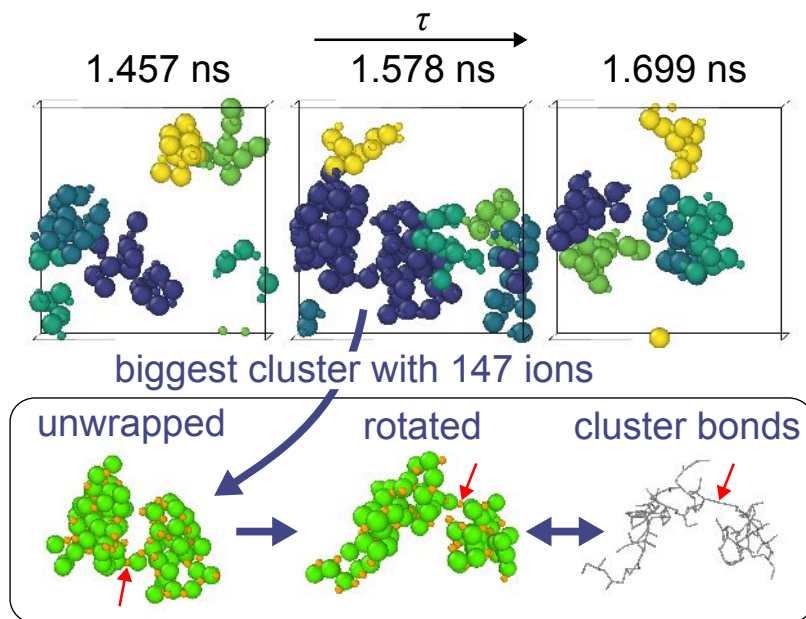
Figure E.1: Snapshots from the simulation at the highest concentration of RDVH-NaCl in SPC/E water (x_{Na^+} = 0.15 mol mol^{-1}). Top panels: snapshots showing the five biggest clusters in three consecutive frames with coloring as in Figure 39 of the main text; the frame that contains the biggest overall cluster with 147 ions is shown in the middle panel, while snapshots of the previous and subsequent configurations are shown to its left and right, respectively. Bottom panels, from left to right: the largest cluster containing 147 ions unwrapped (i.e., depicted as a coherent object without visual disconnections arising from the periodic boundary conditions), the same unwrapped cluster rotated for improved visualization, and the corresponding cluster bounds used by the cluster algorithm. The red arrows indicate the single cation that connects the two sub-clusters, which build up the large cluster.

Declaration

This dissertation contains material that has been published previously or that is included in submitted publications. In the following, these publications are listed together with a statement on the contributions of the author of the present dissertation.

- D. Schaefer, B. Kunstmann, S. Schmitt, H. Hasse, M. Kohns: Explosions of Nano-droplets Studied with Molecular Dynamics Simulations, New Journal of Physics, *to be submitted* (2023).
  The author developed the simulation scenario, carried out the MD simulations, post-processing, video production, evaluated the results, and wrote the manuscript.

- D. Schaefer, M. Kohns, H. Hasse: Molecular Modeling and Simulation of Aqueous Solutions of Alkali Nitrates, The Journal of Chemical Physics 158 (2023) 134508. DOI: 10.1063/5.0141331.
  The author carried out the MD simulations, post-processing, and evaluated the results. The author wrote the manuscript.

- D. Schaefer, M. Kohns: Molecular Dynamics Study of Ion Clustering in Concentrated Electrolyte Solutions for the Estimation of Salt Solubilities, Fluid Phase Equilibria 571 (2023) 113802. DOI: 10.1016/j.fluid.2023.113802.
  The author carried out the MD simulations, post-processing, and evaluated the results. The author wrote the manuscript.

- D. Schaefer, S. Stephan, K. Langenbach, Martin T. Horsch, H. Hasse: Mass Transfer through Vapor–Liquid Interfaces Studied by Non-Stationary Molecular Dynamics Simulations, The Journal of Physical Chemistry B 127 (2023) 2521-2533. DOI: 10.1021/acs.jpcb.2c08752.
  The author developed the simulation scenario and carried out the MD simulations, post-processing, and evaluated the results. The author wrote the manuscript.

- S. Stephan, D. Schaefer, K. Langenbach, H. Hasse: Mass Transfer through Vapour–liquid Interfaces: a Molecular Dynamics Simulation Study, Molecular Physics (2020) e1810798, DOI: 10.1080/00268976.2020.1810798.
  The author developed the simulation scenario and carried out the MD simulations, post-processing, and evaluated the results together with Simon Stephan. The author wrote the corresponding parts of the manuscript.

Student Theses

The following student theses were prepared under the supervision of the author of the present doctoral thesis in the frame of his research:

- Agathe Cazade: Molecular Simulation of Mass Transport through Vapour-Liquid Interfaces, Master thesis, Laboratory of Engineering Thermodynamics (LTD), TU Kaiserslautern (2019).

- Yannik Sinnwell: Development of Molecular Models for Nitrate Ions in Aqueous Solution, Bachelor thesis, Laboratory of Engineering Thermodynamics (LTD), TU Kaiserslautern (2020).

- Yannick Mang: Development of Molecular Models for Ammonium and Sulfate Ions in Aqueous Solution, Bachelor thesis, Laboratory of Engineering Thermodynamics (LTD), TU Kaiserslautern (2020).

- Yunus Sari: Molecular Simulation Study of the Structure of Highly Concentrated Aqueous Electrolyte Solutions, Student thesis, Laboratory of Engineering Thermodynamics (LTD), TU Kaiserslautern (2021).

- Yannik Sinnwell: Calculation of Gas and Energy Balances for an Integrated Steel Plant for Evaluation of Different Technologies for Carbon Dioxide Emission Reduction, Student thesis, Laboratory of Engineering Thermodynamics (LTD), TU Kaiserslautern & Paul Wurth GmbH, Luxembourg (2021).

- Kai-Henrik Müller: Molecular Simulation of Mass Transport through Vapour-Liquid Interfaces, Student thesis, Laboratory of Engineering Thermodynamics (LTD), TU Kaiserslautern (2022).

- Kai-Henrik Müller: Study of Mass Transport through Vapour-Liquid Interfaces in Azeotropic Mixtures by Molecular Simulations, Bachelor thesis, Laboratory of Engineering Thermodynamics (LTD), TU Kaiserslautern (2022).

- Rebecca Loubet: Investigation of the Physical and Chemical Absorption of CO_2 Gas in Liquids - Investigation of Diffusivity Parameters and Reaction Kinetics within a Lewis Cell, Student thesis, Laboratory of Engineering Thermodynamics (LTD), RPTU Kaiserslautern & INSA Rouen, Normandie, France (2023).

- Maximilian Koch: Thermodynamic Modeling of the Influence of Salts on the Vapor Pressure of Alcohol-Water Mixtures for Safety Applications in Alkoxylations, Master thesis, Laboratory of Engineering Thermodynamics (LTD), RPTU Kaiserslautern & BASF SE, Ludwigshafen am Rhein (2023).

Curriculum Vitae

Name:	Dominik Schaefer
Place of birth:	Koblenz
Nationality:	German

Education

2016 – 2018	Master studies at TU Kaiserslautern Program: Biochemical and Chemical Engineering Sciences Degree: Master of Science
2011 – 2016	Bachelor studies at TU Kaiserslautern Program: Biochemical and Chemical Engineering Sciences Degree: Bachelor of Science
2002 – 2011	Bischöfliches Cusanus Gymnasium in Koblenz Degree: Allgemeine Hochschulreife
1998 – 2002	Elementary school in Mülheim-Kärlich

Professional

2018 – 2023	Research Associate at the Laboratory of Engineering Thermodynamics (LTD), RPTU Kaiserslautern Prof. Dr.-Ing. Hans Hasse